COMPUTER-ASSISTED PROOFS FOR PARTIAL DIFFERENTIAL EQUATIONS IN MULTIPLE SPATIAL DIMENSIONS

Lindsey Johanna Wilhelmina van der Aalst



VRIJE UNIVERSITEIT

Computer-assisted proofs for partial differential equations in multiple spatial dimensions

ACADEMISCH PROEFSCHRIFT

ter verkrijging van de graad Doctor
aan de Vrije Universiteit Amsterdam,
op gezag van de rector magnificus
prof.dr. J.J.G. Geurts,
volgens besluit van de decaan
van de Faculteit der Bètawetenschappen
in het openbaar te verdedigen
op dinsdag 17 november 2026 om 13.45 uur
in de universiteit

door

Lindsey Johanna Wilhelmina van der Aalst

geboren te Geldrop

promotoren:	prof.dr. G.J.B. van den Berg prof.dr. B.W. Rink
promotiecommissie:	prof.dr. D. Avitabile dr. M. Breden prof.dr. J.-P. Lessard prof.dr. M. Plum dr. E. Queirolo

Deze publicatie maakt deel uit van het project *Fully 3D periodic motions in the forced Navier-Stokes equations* met dossiernummer 613.009.132 van het onderzoeksprogramma *Mathematics Clusters – PhD positions 2019* dat (mede) is gefinancierd door de Nederlandse Organisatie voor Wetenschappelijk Onderzoek (NWO).

Contents

Acknowledgements **5**

1 Introduction **7**
1.1 Motivation: From simulation to proof . . . 7
1.1.1 Simulation . . . 8
1.1.2 Computer-assisted proofs . . . 8
1.1.3 Toy problem . . . 11
1.1.4 The cost of rigor . . . 13
1.2 Challenges in high-dimensional nonlinear dynamics . . . 14
1.2.1 Computational costs . . . 14
1.3 Thesis outline . . . 16
1.3.1 Suspension bridge equation (2D) . . . 16
1.3.2 The Navier-Stokes equations (3D) . . . 19

2 Traveling waves in SB equation **23**
2.1 Introduction . . . 23
2.2 Setup and notation . . . 28
2.3 Determining the Fourier coefficients of the nonlinear term . . . 31
2.3.1 Enclosure for the tail . . . 32
2.3.2 Aliasing error . . . 34
2.4 Bounds . . . 36
2.4.1 Computing Y . . . 37
2.4.2 Computing Z . . . 38
2.4.3 Computing W . . . 44
2.5 Results . . . 46
2.6 An alternative method: power series . . . 50
Appendix 2.A Overview of computational parameters N . . . 53
Appendix 2.B Estimation of the constant in Lemma 2.3.2 . . . 54
Appendix 2.C Two-dimensional discrete Poisson summation formula . . 55

3 SB equation on an infinite strip **57**
3.1 Introduction . . . 57
3.2 Set-up . . . 60
3.2.1 Zero-finding problem for functions . . . 60
3.2.2 Fourier series representation . . . 62
3.3 Constructive proof of existence . . . 64
3.3.1 Construction of an approximate solution . . . 65
3.3.2 Computing the nonlinearity . . . 66
3.3.3 Approximate inverse . . . 67
3.4 Computation of the bounds . . . 67
3.5 Stability Analysis . . . 74

3.5.1 Enclosure of the spectrum of $D\mathbb{F}(\tilde{u})$ . . . 76
3.5.2 Enclosure of θ . . . 81
3.6 Results . . . 83
Appendix 3.A Technical results . . . 86

4 Traveling waves in NS equations **89**
4.1 Introduction . . . 89
4.2 Setup . . . 92
4.3 Symmetries . . . 94
4.3.1 Reflection symmetry in x_1 and x_2 (Sx_1Sx_2) . . . 94
4.3.2 Shift and reflection symmetry in x_1 (DSx_1) . . . 94
4.3.3 Rotation and shift symmetry (P_4Sx_1R) . . . 94
4.4 Existence theorem . . . 95
4.4.1 Symmetry-reduced existence theorem . . . 97
4.5 Bounds . . . 99
4.5.1 Y_0-bound . . . 99
4.5.2 Z_0-bound . . . 100
4.5.3 Z_1-bound . . . 100
4.5.4 Z_2-bound . . . 102
4.6 Results . . . 103
4.7 Acknowledgements . . . 104

5 Hopf bifurcation analysis in NS equations **105**
5.1 Introduction . . . 105
5.1.1 Context and motivation . . . 105
5.1.2 Chapter roadmap and objectives . . . 105
5.2 Proof of the Hopf bifurcation point . . . 106
5.2.1 Setup . . . 106
5.2.2 Eigenvalue problem . . . 109
5.2.3 Spaces and existence theorem . . . 112
5.2.4 Bounds . . . 113
5.2.5 Results . . . 120
5.3 Toward three-dimensional solutions away from the bifurcation . . . 121
5.3.1 The zero-finding formulation . . . 122
5.3.2 The Jacobian matrix . . . 125
5.3.3 The approximate inverse A . . . 126
5.3.4 Bounds . . . 132
5.3.5 Future work . . . 136

Summary **139**

Bibliography **141**

Acknowledgements

During my PhD journey, I quickly discovered that while coding algorithms and deriving estimates is a challenge in itself, the real struggle is convincing others that a computer can actually produce a rigorous proof. Hopefully, if you are reading this thesis, it means you are convinced. Writing this thesis was only possible because of the incredible network of people who supported and inspired me along the way.

First and foremost, I would like to express my sincere thanks to my supervisor, Jan Bouwe. Thank you for trusting me with this project and for all the discussions, help and invaluable guidance. I truly enjoyed our meetings and greatly appreciated your feedback. Your insights and attention to detail really helped me keep this project on track.

I would also like to thank my copromotor, Bob, and the rest of the committee (Daniele, Maxime, Jean-Philippe, Michael, Elena) for taking the time to read my thesis and for their helpful comments.

Moreover, thank you Matthieu and Jean-Philippe for being fantastic co-authors and for our mathematical discussions.

Next, I want to thank my paranymphs, Aafje and Eric. I'm grateful to Aafje for always being there to listen to me about my PhD, but perhaps more importantly, for knowing exactly when to force me to think about literally anything else. Thank you Eric, for not only being my academic brother, but for all the humor and jokes you brought into the department and to our conference trips.

I also want to thank the rest of my VU colleagues. The lunch breaks were so much more fun with you. A special shout-out must go to the PhDs for crowning me *PhD student of the Month* in February 2026. Being recognized as a *cool woman in the cool wing* is easily the highest honor I will ever achieve and I will carry that title with immense pride.

Furthermore, I want to thank my family, my family-in-law, Suze, the *Wiskids* (Aafje, Noëlle, Jordi, Rick) and Lynn. A special thank you goes out to Sharon: your willingness to read through my papers, despite your dislike of mathematics, is a true definition of friendship.

Last but definitely not least, thank you Stefan. Thank you for always believing in me and helping me during my PhD and everything beyond it. Besides your emotional support, I appreciate you designing the cover of this book. I only had to say two sentences and you completely captured what I had in mind, as you always do. I simply could not imagine my life, or this thesis, without you.

1 Introduction

1.1 Motivation: From simulation to proof

The ambition of applied mathematics is to reliably describe, understand and predict the behavior of the physical world. When we observe physical phenomena, we immediately recognize two dependencies: space and time. The study of how these systems evolve over time is what we call *dynamics*. As for the spatial dependence, to model systems that vary continuously across space, where neighboring points are connected and not independent of one another, we treat them as continuous media. In such media, the physical state at one location pulls and pushes against its neighbors. To capture this spatial interconnectedness alongside the dynamics in time, we use *Partial Differential Equations (PDEs)*.

Historically, linear PDEs have provided a good starting point to study continuous media. In the linear world, the output is proportional to the input: if you double the input, you double the output. However, physical reality is inherently nonlinear as nature is dominated by complicated interactions that linear models alone cannot capture.

The origins of these nonlinearities are tied to physical mechanisms. For example, in the suspension bridge model studied in this thesis, the force is asymmetric: an upward displacement of the deck slackens the suspension cables, while a downward displacement stretches them. A linear model cannot capture this difference in behavior depending on the direction of movement. In the context of fluid dynamics, the Navier-Stokes equations describe how the velocity of fluid particles changes. As the fluid transports its own momentum, the particles move through a velocity field that they themselves dictate. This physical self-interaction mathematically translates to a nonlinear transport term in the PDEs.

Hence, nonlinear models serve as the language of the physical sciences. Equations such as the Navier-Stokes equations for fluid dynamics or the nonlinear wave equations in elasticity are not purely abstract mathematical concepts. They are the products of fundamental physical laws like the conservation of mass, momentum and energy. However, the expressive power of these nonlinear PDEs comes at a price: solvability. Unlike their linear counterparts, for which we often possess general theories and closed-form analytical solutions, nonlinear PDEs rarely admit explicit formulas. There is no general formula for the behavior of a turbulent fluid or a collapsing bridge. While classical analysis can often predict qualitative behaviors such as whether a solution exists or remains smooth, mapping the precise quantitative dynamics of these systems requires us to turn to computational methods. This transition marks the shift from the search for exact formulas to the investigation of approximate solutions, for which we need numerical simulation.

1.1.1 Simulation

Since explicit analytical solutions are rarely available for nonlinear systems, numerical simulations have become the standard tool in engineering and applied sciences. In this process, infinite-dimensional operators acting on function spaces are replaced by finite-dimensional approximations through discretization methods, such as finite differences and finite elements.

In many practical contexts, particularly in engineering, these approximate solutions are sufficient. If a numerical simulation predicts that a bridge will remain stable and these results align with experimental data within a safety margin, the method is often considered successful. However, a simulation, no matter how high the precision, does not constitute a mathematical proof. A numerical solution is a finite sequence of numbers satisfying a discretized equation, rather than a continuous function satisfying the original differential equation.

The distinction between simulation and proof becomes critical when studying nonlinear systems. In such regimes, standard numerical methods face two fundamental limitations:

1. *Truncation errors:* The errors introduced by discretizing a continuous operator.
2. *Rounding errors:* The errors introduced by the finite precision of floating-point arithmetic.

Due to the nonlinear nature of equations, these errors can be amplified, potentially leading the numerical trajectory far away from the true solution. This phenomenon can result in "ghost" solutions: numerical artifacts that appear stable in the simulation, but are not solutions to the continuous mathematical model. On the other hand, unstable phenomena might not be visible in numerical simulations. Consequently, while simulations are invaluable for observing behavior, they cannot, by themselves, guarantee the existence of the solutions they predict.

1.1.2 Computer-assisted proofs

To overcome the limitations of numerical simulation alone and to provide mathematical certainty, we turn to the field of *Computer-Assisted Proofs (CAPs)*. This thesis explores the boundaries of what is currently possible via CAPs for nonlinear PDEs in multiple spatial dimensions. The use of these computer-assisted techniques for rigorously verifying numerical simulations of dynamical systems has seen immense growth during the last decades. For comprehensive overviews of the field, see [30, 49]. The philosophy of a CAP is to combine the computational power of numerical methods with the rigor of functional analysis. Unlike standard simulations, CAPs yield rigorous verification of the existence, local uniqueness and error bounds of numerical approximations.

To ensure the rigor of the computer calculations that constitute the proof, we use *interval arithmetic* (see e.g. [46, 64]). During the validation phase, after a candidate solution has been found via floating-point numerical computations, we replace single floating-point numbers in computations with intervals guaranteed

to contain the true values. Every arithmetic operation in this process is rounded outwards to preserve the rigor. For example, for $a, b, c, d \in \mathbb{R}$, addition between two intervals is done as follows:

$$[a, b] + [c, d] = [a + c, b + d].$$

While this guarantees mathematical rigor, it introduces the challenge that interval bounds can grow overly pessimistic if the computation is not carefully structured. Furthermore, note that an interval representation of a real number is not unique: a true value can be enclosed by infinitely many valid intervals of varying widths. For instance, the true value of π is contained in $[3.1, 3.2]$, but also in the tighter interval $[3.14, 3.15]$. In a CAP, interval arithmetic is used to guarantee that computer calculations are rigorously justified in the mathematical sense. Keeping the interval representations sufficiently tight ensures that these computations do not unnecessarily squander the careful pen-and-paper analysis invested in deriving the analytic formulas.

While interval arithmetic successfully resolves the rounding errors introduced by finite-precision hardware, it alone does not address the truncation errors. Such errors naturally arise in numerical approximations. Truncation is already an issue in *Ordinary Differential Equations (ODEs)*, where it can occur due to discrete time-stepping. However, this challenge is amplified in the context of PDEs, where the phase space is infinite-dimensional. Truncating this space to a finite number of modes for a computer calculation introduces a truncation error that is typically much more significant than rounding errors. An essential challenge of a CAP is to use functional analysis to derive rigorous, analytical bounds for the infinite tail modes. These tail modes represent the infinitely many high-frequency (Fourier) coefficients that are excluded from the finite computer representation. Interval arithmetic is then utilized to safely evaluate these analytical bounds on the computer. By combining rigorous functional analysis to manage the infinite dimensions with interval arithmetic to evaluate all associated computations, we can fully complete CAPs.

Historical context

The concept of using computers to prove mathematical theorems has gained recognition with Lanford's proof of the Feigenbaum conjectures in 1982 [39]. He rigorously verified the existence of a fixed point of a renormalization operator, which in this case was not a single numerical value, but an entire function. Since the calculation needed to prove this was inaccessible to pen-and-paper analysis due to the complexity of the required estimates, Lanford relied on a computer. His work demonstrated that computers could manage the "bookkeeping" of bounds required for functional analysis estimates.

Another major milestone was the verification of the strange attractor originally observed numerically by Edward Lorenz, which was proven using computer-assisted means in [63]. This conjecture stated that, for certain parameters, the Lorenz equations support a robust strange attractor. By combining rigorous computations and normal form theory, the existence of the strange attractor was proven

and geometric properties were established, settling a debate that had persisted since the 1960s. These results indicated that CAPs are a useful tool in the study of finite-dimensional dynamical systems.

However, the application of CAPs to PDEs presents new challenges due to the infinite-dimensional nature of the phase space. Broadly speaking, the approaches to addressing these infinite-dimensional problems have split into two main categories: topological and analytical methods.

Topological methods rely on tools such as the Conley index and covering relations. For ODEs and maps, these techniques have been successfully applied to prove the existence of (un)stable manifolds for hyperbolic fixed points [90]. Furthermore, they have been useful in verifying chaotic dynamics, including further rigorous studies of the aforementioned Lorenz equations [44]. These topological arguments have also been extended to PDEs by combining them with rigorous integration of the infinite-dimensional flow, originating with works such as [4, 89] and continuing with more recent results like [85], which proves chaotic dynamics in the Kuramoto-Sivashinsky PDE.

Analytical methods, which are the focus of this thesis, are based on contraction mapping principles. Specifically, they rely on Newton-Kantorovich type theorems (e.g. [7, 8]). These methods are a useful tool for proving specific solutions with high precision. Early existence theorems for solutions to elliptic PDEs using this approach were presented in [48, 53], leading to analytical methods becoming a regular tool for verifying various structures, such as boundary value problems for PDEs [10, 62, 87], periodic orbits for PDEs [18, 27, 68], equilibrium solutions for PDEs [3, 22, 26] and Hopf bifurcation points [70, 72]. Furthermore, these analytical techniques, often combined with parameterization methods, have been instrumental in rigorously computing invariant stable and unstable manifolds in PDEs [37] and connecting orbits [40, 71].

The Newton-Kantorovich framework

For the differential equations studied in this thesis, Fourier transformations are a natural tool, which allows us to apply a Newton-Kantorovich type theorem. We specifically follow the *radii polynomial approach* [22].

The methodology follows a four-step recipe to convert a numerical approximation into a proven solution:

1. *Reformulation*: We rewrite the differential equation as a zero-finding problem $F(x) = 0$ on a Banach space X. In our context, X is typically a weighted space of Fourier coefficients.

2. *Approximation*: We compute a numerical approximation $\bar{x}$ using Newton iterations such that the residual is small, i.e., $\|F(\bar{x})\|_X \approx 0$.

3. *Linearization*: We compute an injective linear operator A that acts as an approximate inverse of the Fréchet derivative $DF(\bar{x})$.

4. *Validation*: We construct a Newton-like operator $T(x) = x - AF(x)$ and prove that it is a contraction on a ball $B_r(\bar{x})$ centered at our approximation.

To prove the contraction property, we compute three bounds Y_0, Z_1, Z_2, which, provided they are sufficiently small, together guarantee that the Newton-like operator maps a local neighborhood into itself and is a contraction.

The residual bound Y_0 bounds the defect $\|AF(\bar{x})\|_X \leq Y_0$. This measures how close the numerical approximation is to being a zero of F.

The inverse bound Z_1 bounds the error $\|I - ADF(\bar{x})\|_{B(X)} \leq Z_1$ where I denotes the identity map. This measures how good of an approximate inverse A is to $DF(\bar{x})$.

Lastly, *the nonlinearity bound* Z_2 estimates how the nonlinearity behaves as we move away from $\bar{x}$. Via $\|A[DF(\bar{x}+w) - DF(\bar{x})]\|_{B(X)} \leq Z_2\|w\|_X$, for all perturbations w up to a maximum radius $r^* \in (0, \infty]$, we bound the second derivative. This parameter r^* acts as an *a priori* chosen computational boundary. For quadratic nonlinearities, this bound holds globally, meaning we can set $r^* = \infty$. However, for rapidly growing nonlinearities, we must restrict our analysis to a finite maximum radius r^* to ensure Z_2 does not become uncontrollably large.

The radii polynomial approach transforms these three bounds into an algebraic condition. To guarantee that T maps the ball $B_r(\bar{x})$ into itself and acts as a contraction, we require that $Y_0 + Z_1 r + Z_2 r^2 < r$. By rearranging this inequality, we arrive at the condition $p(r) < 0$, where the *radii polynomial* $p(r)$ is defined as

$$p(r) = Z_2 r^2 - (1 - Z_1)r + Y_0.$$

Through this approach, the (infinite-dimensional) functional analysis problem is reduced to checking the negativity of a quadratic polynomial. Specifically, the existence result holds if we can find $r > 0$, adhering to the restriction $r \leq r^*$, such that $p(r) < 0$. This is formalized in the existence theorem below, of which we will use variants to obtain the CAPs in this thesis.

Theorem 1.1.1 (e.g. [9, 22])**.** *Let $F : X \to \hat{X}$ be a Fréchet differentiable map between Banach spaces X and $\hat{X}$. Furthermore, let $A \in B(\hat{X}, X)$ be injective, $\bar{x} \in X$ and $r^* \in (0, \infty]$. Let $Y_0, Z_1, Z_2 \in \mathbb{R}^+$ satisfy*

$$\begin{aligned} \|AF(\bar{x})\|_X &\leq Y_0, \\ \|I - ADF(\bar{x})\|_{B(X)} &\leq Z_1, \\ \|A[DF(\bar{x}+w) - DF(\bar{x})]\|_{B(X)} &\leq Z_2\|w\|_X \quad \text{for all } \|w\|_X \leq r^*. \end{aligned}$$

If there exists $r_0 > 0$, where $r_0 \leq r^*$, such that $p(r_0) < 0$, then there exists a unique $\hat{x} \in B_{r_0}(\bar{x})$ satisfying $F(\hat{x}) = 0$.

1.1.3 Toy problem

To understand the methodology of CAPs without the complexity of nonlinear differential equations or working in infinite-dimensional function spaces, we consider

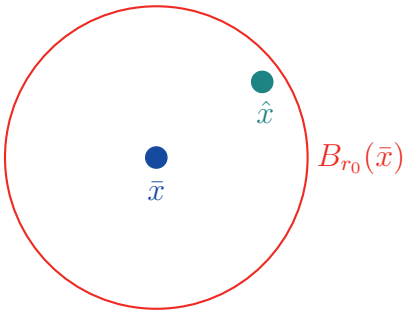


Figure 1.1.1: Visualization of Theorem 1.1.1. The true solution $\hat{x}$ is guaranteed to exist within the ball $B_{r_0}(\bar{x})$ around the approximate solution $\bar{x}$ if the conditions of the theorem are met.

a simple scalar zero-finding problem. The goal is to rigorously prove the existence of a solution to the equation

$$F(x) = x^2 - 3 = 0.$$

While we can immediately see that one of the exact solutions is $\sqrt{3}$, we will purposely treat this solution as unknown to demonstrate how the proof technique operates in practice. By proceeding as if the true solution is undiscovered, we can clearly illustrate the CAP methodology, showing how a numerical guess can lead to a proof.

To achieve certainty, our goal is to use a numerical approximation to prove that the true solution exists within a tight, rigorous error bound. Specifically, we aim to find an explicit radius $r > 0$ such that the exact solution is guaranteed to lie within the interval $[\bar{x} - r, \bar{x} + r]$ around our approximate solution $\bar{x}$.

We demonstrate this using an initial numerical guess $\bar{x} = 1.7$. Typically, such guesses are obtained using Newton iterations to maximize accuracy. However, in this case we did not use Newton's algorithm, as for illustration purposes it is useful to have a less optimal approximation.

Remark 1.1.2. *Note that* 1.7 *does not have a finite binary representation and must be enclosed in an interval during actual computations. However, for the sake of clarity in this demonstration, we will proceed as if numbers with finite decimal expansions can be represented exactly in computers. We will omit the explicit interval bounds for such values to maintain readability.*

Next, we compute an approximate inverse A for the derivative $DF(\bar{x})$. The derivative is $DF(x) = 2x$ and evaluating this at our numerical approximation gives $DF(1.7) = 3.4$. We choose our linear operator A to be an approximate inverse of this value, i.e., $A = 0.294$.

Subsequently, we compute the three estimates Y_0, Z_1 and Z_2 from Theorem 1.1.1. As

$$|AF(\bar{x})| = \left|0.294 \cdot (1.7^2 - 3)\right| = 0.032...,$$

we can set $Y_0 = 0.033$.

In this simplified scalar case, the inverse is almost exact at the point $\bar{x}$, which means that Z_1 is relatively close to zero. We can see this from the following computation:

$$|I - ADF(\bar{x})| = |1 - 0.294(2 \cdot 1.7)| = 4 \cdot 10^{-4}.$$

Therefore, we set $Z_1 = 4 \cdot 10^{-4}$. However, typically it is not the case that we can compute such a good approximation of the inverse. In fact, in the PDE problems in this thesis, the Z_1-bound is often the most difficult bound to compute and to make sufficiently small.

For the last bound, we compute

$$|A[DF(\bar{x} + w) - DF(\bar{x})]| = |A| \cdot |2(\bar{x} + w) - 2\bar{x}| = 0.588|w|.$$

Hence, we set $Z_2 = 0.588$.

Computing the radii polynomial $p(r) = Z_2 r^2 - (1 - Z_1)r + Y_0$ for these values, we get that $p(r) < 0$ for $r \in [0.033, 1.66]$. The theorem now guarantees that a unique exact solution $\hat{x}$ exists within the interval $[\bar{x} - r, \bar{x} + r]$. For $r = 0.033$, this yields

$$\hat{x} \in [1.667, 1.733].$$

Indeed, $\sqrt{3} = 1.73205...$, which lies within our proven bounds. Note that the better the approximate solution and the tighter the estimates, the smaller r and thus, the more precise the statement will be.

This simple example demonstrates the power of the method of CAPs. By checking a few algebraic inequalities on a numerical guess, we obtain a mathematical proof of existence of a true solution. While the application to PDEs follows the same logic, deriving the estimates and doing the computations is definitely not as straightforward as in this scalar example.

One reason for this is that we have to shift from scalar bounds to norms in infinite-dimensional Banach spaces. Furthermore, to capture complicated physical phenomena, such as localized traveling waves in the two-dimensional suspension bridge equation or in the three-dimensional Navier-Stokes equations, we must overcome severe analytical and computational hurdles. These include managing unbounded domains, controlling the extreme growth of exponential nonlinearities and handling the large amplitudes of the localized waves.

1.1.4 The cost of rigor

While CAPs provide a level of mathematical certainty that simulations alone cannot achieve, this rigor comes at a significant price, which manifests as both an analytical and a computational cost.

First, there is a substantial mathematical "pen-and-paper" cost. A CAP relies on using finite computations to make statements about infinite-dimensional Banach spaces. To justify this, we must derive explicit, analytical estimates to bound the

infinite-dimensional tails of the operators. Hence, a CAP demands deep *a priori* analytical work before any computational validation can even begin.

Second, to ensure that these analytical bounds are sufficiently small to satisfy the validation inequalities, the finite-dimensional projection must be highly accurate. For high-dimensional and strongly nonlinear PDEs, the number of modes N required to succeed at the proof is large. This high dimensionality directly translates into a major computational cost: the approximate inverse A. This inverse operator is often dense and massive. Thus, computing and storing it explicitly requires immense memory. As a result, it is important to find efficient ways to represent A in the computer or to avoid storing it explicitly to find a good balance between memory usage and computational time.

Finally, the proofs are computationally heavy due to the use of interval arithmetic. Arithmetic operations on these intervals are more expensive than standard arithmetic. For example, multiplying two intervals requires calculating the products of all combinations of their endpoints to find the new minimum and maximum.

1.2 Challenges in high-dimensional nonlinear dynamics

Historically, the development of both analytical and numerical tools for dynamical systems has focused extensively on one-dimensional spatial models. While one-dimensional reductions, such as modeling a bridge as a line or a fluid flow as a unidirectional stream, offer valuable qualitative insights, they rely on assumptions that discard essential spatial structure. In practice, physical reality typically operates in two and three spatial dimensions.

Indeed, many critical physical systems are intrinsically higher-dimensional. For instance, the twisting of the deck of a suspension bridge cannot be captured by a one-dimensional vertical displacement model. Similarly, in fluid dynamics, mechanisms such as vortex stretching (lengthening of vortices) are fundamentally three-dimensional phenomena that vanish in two-dimensional reductions. It is important to note that the higher-dimensional partial differential equations studied in this thesis, such as the two-dimensional suspension bridge equation, remain simplified mathematical idealizations of reality. Nevertheless, they incorporate the multidimensional interactions absent in their one-dimensional versions. To move toward descriptions that better suit the geometry of the physical world, we must therefore face the challenges of multidimensional nonlinear dynamics.

1.2.1 Computational costs

While CAPs provide a robust framework for analyzing dynamical systems, their extension to higher-dimensional spatial domains presents several computational and analytical hurdles. The transition from ODEs or one-dimensional PDEs to problems defined on two- or three-dimensional domains is not merely a matter of adding variables; it fundamentally increases the computational cost of their verification. Consequently, rather than a straightforward application of existing

techniques, verifying solutions in higher dimensions requires the derivation of new quantifiable bounds and computational methods.

Applying the Newton-Kantorovich framework to higher-dimensional PDEs implies that the computational complexity grows severely. This manifests itself in two distinct, but interconnected, ways: the massive data storage required, especially for the Jacobian matrix, and the algebraic complexity of evaluating nonlinearities.

Remark 1.2.1. *Before a proof can even be attempted, we must find a suitable numerical approximation $\bar{x}$ that converges when applying Newton iterations. In one-dimensional spatial problems, the phase space is relatively constrained and techniques like "trial and error", shooting methods and continuing an initial condition or a known solution segment across a domain are highly effective. However, in two or three spatial dimensions, the phase space is more complicated and the discretized state space is larger. As a result, these traditional techniques typically break down.*

A possible strategy to overcome this, is to find a solution to a simplified problem and use numerical continuation to reach the system of interest. Nevertheless, in multidimensional settings, bifurcation diagrams become more complicated, making these continuation paths difficult to find or track. Alternative approaches, such as numerical implementations of the mountain pass algorithm (e.g., see [32]), can be employed to locate specific saddle-point solutions of the associated energy functional. However, these algorithms are computationally demanding and often difficult to implement in high-dimensional settings. While this section focuses on computational costs of the proof, it is important to acknowledge that the numerical investigation required to find $\bar{x}$ prior to the proof is a significant challenge in itself in higher dimensions.

Data storage

The first hurdle is the amount of data required to represent the solution and its corresponding linear operators. When discussing dimensionality, it is important to distinguish between spatial and spatiotemporal dimensions. For instance, a spatiotemporal problem involving two spatial dimensions plus time has a complexity similar to a stationary or traveling wave problem in three spatial dimensions.

Consider a solution represented by a truncated Fourier series. If constructing a suitable spatial profile in one dimension requires N modes, a comparable resolution in d dimensions requires N^d coefficients. For a high-precision proof where $N = 10^2$ is a modest requirement, a one-dimensional solution requires storing $N = 10^2$ coefficients. However, increasing to two or three dimensions requires $N^2 = 10^4$ or $N^3 = 10^6$ coefficients, respectively. While storing the solution vector itself remains manageable on modern hardware, its size dictates the size of the Jacobian matrix, which is the primary contributor to the data storage bottleneck. If the discretized solution has N^d degrees of freedom, the Jacobian matrix is of size $N^d \times N^d$. Hence, revisiting our case of $N = 10^2$ modes per spatial direction, the Jacobian matrix for a three-dimensional problem contains $(10^6)^2 = 10^{12}$ entries. Storing a dense matrix of this size explicitly is computationally ineffective and impractical.

Consequently, high-dimensional proofs require specialized techniques to handle the linearization without reaching the limit of the available memory. Instead of explicitly forming and storing the full Jacobian matrix for all high-dimensional modes, we can find an approximate inverse without ever storing it fully. A standard approach is to explicitly compute and store the dense inverse only on a relatively small, finite-dimensional subspace containing the dominant low-frequency modes. For the infinite, high-frequency tail, the matrix is never stored. Instead, the action of A is applied implicitly by exploiting the analytic structure of the differential operators, such as utilizing the fact that the Laplacian acts diagonally in Fourier space. Finding an efficient representation of A that balances the requirement of the Z_1-bound (the accuracy of the inverse) with the limitations of available memory (and computation time) is a challenge addressed in the upcoming chapters in this thesis.

Algebraic complexity

The second challenge arises from the evaluation of nonlinear terms. Algebraic operations in physical space correspond to convolutions in Fourier space. For example, the advective term $u \cdot \nabla u$ in the Navier-Stokes equations requires computing discrete convolutions, of which the cost increases severely with the spatial dimension, despite using Fast Fourier Transform (FFT) algorithms. In high dimensions, computing such nonlinear terms with rigorous error bounds becomes a significant bottleneck in the verification process.

1.3 Thesis outline

To push the boundaries of computer-assisted verification for nonlinear PDEs in multiple spatial dimensions, the investigation in this thesis is structured by increasing complexity. Specifically, the research is divided into two parts: Chapters 2 and 3 focus on localized traveling wave solutions in the two-dimensional suspension bridge equation and Chapters 4 and 5 transition to fluid dynamics by analyzing the Navier-Stokes equations in three spatial dimensions.

1.3.1 Suspension bridge equation (2D)

The mathematical investigation of suspension bridge dynamics was historically catalyzed by engineering observations. In 1938, significant movement was noted in the Golden Gate Bridge during strong winds [80]. However, the field gained even more mathematical interest following the collapse of the Tacoma Narrows Bridge in 1940, where wind-induced waves grew until the construction failed [1].

In this work, the bridge deck is modeled as a two-dimensional beam or plate hinged by cables. We emphasize that this formulation represents a simplified mathematical model. Our goal is not to derive a fully realistic engineering representation of a bridge, but rather to isolate and rigorously analyze the multidimensional nonlinear dynamics that such structures exhibit. Let $U = U(X_1, X_2, t)$ represent the downward deflection (perturbation) of the height of the road and Δ^2 denote the

bilaplacian operator in two spatial dimensions. Following Newton's second law of motion ($F = ma$), a regular beam satisfies $\partial_t^2 U = -\Delta^2 U$, where the right-hand side represents the internal elastic force. To model the suspension, we add a smooth nonlinearity $-e^U + 1$ [20, 47]. Note that $U > 0$ denotes displacement in the downward direction, such as when a vehicle drives over the bridge deck and bends it downward. The situation is visualized in Figure 1.3.1. The spatiotemporal suspension bridge model studied in Chapters 2 and 3 is (e.g. [20, 47])

$$\partial_t^2 U = -\Delta^2 U - e^U + 1.$$

We are specifically interested in dynamical structures that can propagate along the longitudinal axis X_1 of the bridge at a constant speed without altering their fundamental shape. This focus is motivated by the emergence of such traveling patterns within computational simulations of this PDE ([9, 20, 32]). To analyze these phenomena, we apply the traveling wave ansatz

$$U(X_1, X_2, t) = u(X_1 - ct, X_2) = u(x_1, x_2),$$

where c denotes the wave speed and u the wave profile. This reduces the equation to the elliptic problem

$$\Delta^2 u + c^2 \partial_{x_1}^2 u + e^u - 1 = 0.$$

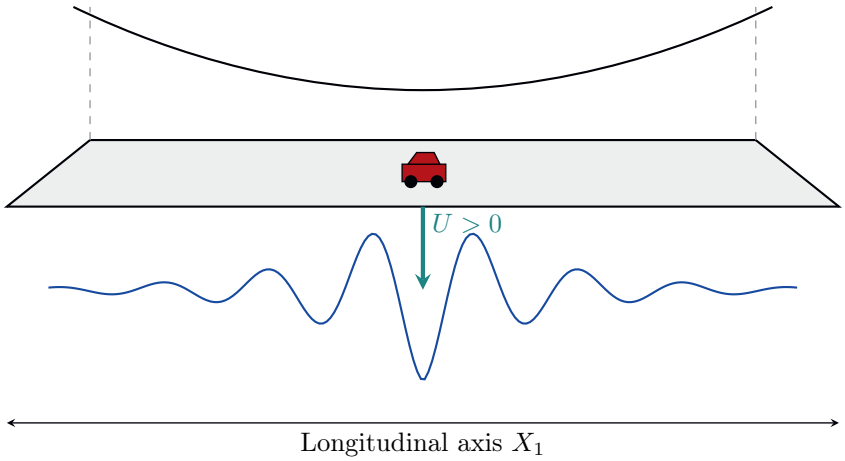


Figure 1.3.1: Physical interpretation of the displacement U. The road deck is at equilibrium at $U = 0$. The core of the localized wave represents the symmetric perturbation U in the downward direction.

The existing literature on the suspension bridge equation has predominantly focused on the one-dimensional spatial case, for which the corresponding traveling wave equation simplifies to an ODE. These one-dimensional models have successfully provided valuable mathematical insights into the existence and behavior of longitudinal waves. However, to capture more complex physical phenomena such as twisting of the deck, it is necessary to study the model in multiple spatial dimensions. Historically, these traveling structures in two spatial dimensions have

only been studied via numerical simulations. This thesis builds upon the foundation of the one-dimensional research by introducing proofs for the two-dimensional PDE, bringing the mathematical analysis a step closer to the geometry of an actual bridge deck.

In particular, **Chapter 2**, based on the publication [79], proves the existence of periodic localized traveling wave solutions on a bounded two-dimensional domain. The proof relies on a Newton-Kantorovich approach applied to a high-dimensional Fourier-cosine series discretization. A major mathematical challenge overcome in this chapter is the analytical management of the exponential nonlinearity. Unlike polynomial nonlinearities, which map a finite Fourier expansion to a strictly finite number of output modes, evaluating the term e^u on a finite number of input coefficients generates an infinite sequence of nonzero output modes and none of them can be evaluated exactly within a finite computation. To address this, we develop a framework to strictly control the resulting multidimensional aliasing errors, yielding small, explicit bounds that confirm the existence of the exact PDE solutions (see Figure 1.3.2 for a visualization of such a wave profile).

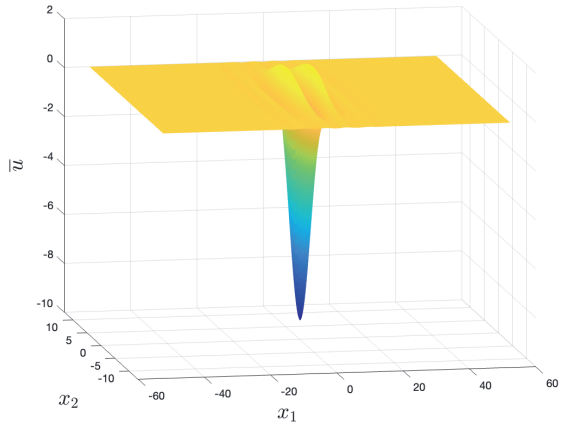


Figure 1.3.2: Visualization of an approximate localized traveling wave $\bar{u}$ for wave speed $c = 1.2$. The approximation is truncated to a finite domain in this plot.

Building on these techniques, **Chapter 3**, based on the publication [77], extends these existence results to an infinite strip $\Omega = \mathbb{R} \times (-d_2, d_2)$ for $d_2 > 0$. Transitioning to an unbounded domain fundamentally alters the functional analytic setting, necessitating the use of more advanced estimates. Furthermore, this chapter goes beyond mere existence by providing a rigorous computer-assisted proof for the orbital stability of these traveling waves. By enclosing the spectrum of the Fréchet derivative evaluated at the proven traveling wave solution, we verify that these multidimensional wave structures are stable or unstable, depending on the type of solution and the wave speed. In particular, the solution of which the approxima-

tion is visualized in Figure 1.3.2 is orbitally stable.

1.3.2 The Navier-Stokes equations (3D)

The second part of the thesis shifts to the Navier-Stokes equations in three spatial dimensions. These equations describe the motion of viscous fluids and are frequently studied in science and engineering, modeling phenomena ranging from ocean currents and weather patterns to blood flow and airflow over an aircraft wing.

The importance of the Navier-Stokes equations is underscored by their status as one of the seven Millennium Prize Problems stated by the Clay Mathematics Institute. The problem of proving the existence and smoothness of solutions in three dimensions remains a significant open challenge in mathematics. While we do not attempt to solve the Millennium Prize problem, we contribute to the field of fluid equations by rigorously verifying specific dynamical structures within the three-dimensional flow.

We investigate solutions to the incompressible Navier-Stokes equations

$$\begin{cases} \partial_t u + (u \cdot \nabla)u - \nu \Delta u + \nabla p = f, \\ \nabla \cdot u = 0, \end{cases}$$

where u is the velocity field, p is the pressure, ν is the viscosity and f is a time-independent forcing.

As standard analytical methods fall short of capturing specific nonlinear solutions to this system, we use CAPs. In the specific context of fluid dynamics, the application of CAPs has evolved from the verification of basic stationary states to the analysis of complicated three-dimensional flows. Early foundational results, such as those described in [84], successfully established the existence of stationary solutions for the Navier-Stokes equations. A few years later, the methodology was expanded to analyze hydrodynamic stability, leading to proofs of fluid instabilities governed by the Orr-Sommerfeld equation [38, 83], which is directly derived from the Navier-Stokes equations. Building upon these early stationary and linear stability results, CAP techniques were subsequently adapted to capture complex nonlinear dynamics in planar flows. For instance, the authors in [5] proved the existence of a Hopf bifurcation and an emerging branch of periodic solutions in the two-dimensional Navier-Stokes equations. Furthermore, the existence of spontaneous periodic orbits was verified in [68].

Beyond these major breakthroughs, the scope of verified computations has recently expanded to include the analytical challenges posed by three spatial dimensions and nontrivial geometries. Rigorous frameworks have been established to verify the existence of stationary solutions to the Navier-Stokes equations over general three-dimensional domains [41]. Furthermore, the field has increasingly pushed beyond standard bounded domains to tackle unbounded spatial domains. A prime example is [86], in which computer-assisted existence proofs are provided for Navier-Stokes flows on an unbounded strip with an obstacle. These methods also continue to

be successfully adapted to other fluid configurations, such as rigorously bounding viscous fluid flow between parallel disks [82].

We also note that the reach of CAPs in fluid dynamics extends beyond the Navier-Stokes equations. For instance, these methods have recently been used to prove the existence of finite time singularities for the two-dimensional free boundary incompressible Euler equations [19], which are the inviscid limit of the Navier-Stokes equations. CAPs continue to push the boundaries of fluid mechanics, leading to results such as the rigorous verification of smooth self-similar imploding solutions for three-dimensional compressible fluids [12]. Furthermore, the combination of machine learning and CAPs is opening new doors. For example, by utilizing neural networks to find the profiles, families of unstable singularities in the three-dimensional Euler equations were recently discovered in [81].

While these recent developments show the versatility of CAPs across different fluids, this thesis focuses only on the incompressible Navier-Stokes equations. Specifically, we build on the techniques developed in [68] to explore the three-dimensional flow generated by the Taylor-Green forcing. As the viscosity parameter ν is varied, this system exhibits various dynamical behaviors, transitioning from stationary states to periodic orbits and traveling waves. This behavior is summarized in the bifurcation diagram in Figure 1.3.3. The three light blue dots indicate numerical Hopf bifurcations: for these values of ν, a branch of non-trivial solutions numerically seems to exist. The first dot marks a bifurcation that leads to a branch of solutions independent of x_3. Proofs for points along this two-dimensional branch, up to the secondary bifurcation indicated by the red dot, can be found in [68].

In contrast, the present work focuses on the three-dimensional phenomena arising at the subsequent bifurcations. Specifically, the second light blue dot ($\nu \approx 0.2112$) and the third light blue dot ($\nu \approx 0.1234$) mark symmetry-breaking Hopf bifurcations. The Navier-Stokes equations possess an $O(2)$ symmetry with respect to the x_3-direction, meaning the equations are invariant under both continuous spatial translations and discrete mirror reflections along this axis. Following Chapter XVII of the book [29], such $O(2)$-Hopf bifurcations generically result in the simultaneous emergence of two distinct primary branches of solutions: standing waves (three-dimensional periodic solutions that preserve the reflectional symmetry) and traveling waves (which break the reflectional symmetry). The latter are called rotating waves in [29].

Consequently, both a traveling wave and a three-dimensional periodic branch originate from each of these two bifurcation points. Since numerical continuation typically tracks a single solution path, our computations isolated one distinct branch per point. Specifically, we observed the traveling wave branch emerging from the second bifurcation point and the three-dimensional periodic branch emerging from the third. Guided by these numerical observations, the thesis is dedicated to the existence results for these specific branches.

In **Chapter 4**, we adapt the techniques from [68] to prove the existence of a three-dimensional traveling wave solution (indicated by the orange dot in Figure 1.3.3) located on the second branch. While previous proofs focused mainly on solutions that are essentially two-dimensional (independent of x_3), the wave proven

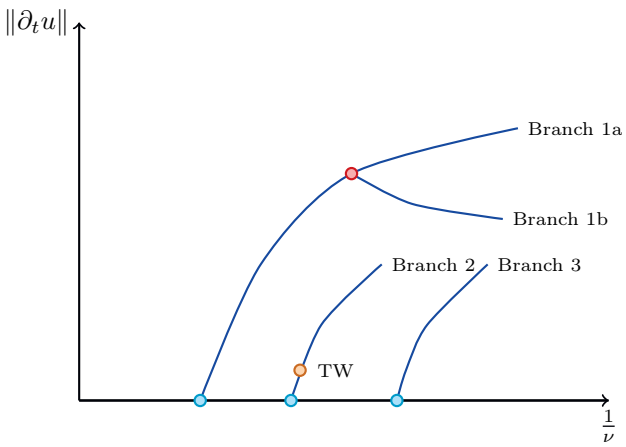


Figure 1.3.3: Schematic bifurcation diagram illustrating branches of solutions emerging as the inverse viscosity $\frac{1}{\nu}$ increases. The light blue dots represent Hopf bifurcations from the stationary state. The red dot indicates a secondary bifurcation on the first branch, while the orange dot highlights a traveling wave solution on the second branch.

here possesses a non-trivial, fully three-dimensional spatial structure, as visualized by the vorticity level set in Figure 1.3.4. By applying a traveling wave ansatz, the time-dependent problem is reduced to a stationary boundary value problem, effectively eliminating the temporal variable. Furthermore, by taking advantage of the symmetries present in the Navier-Stokes equations, we are able to reduce the number of required Fourier modes, helping us to successfully execute the Newton-Kantorovich argument despite the high dimensionality.

Chapter 5 aims to extend this framework to detect and verify both the exact Hopf bifurcation point and the emerging branches of three-dimensional periodic solutions, focusing specifically on the third light blue dot in Figure 1.3.3. We first formulate the zero-finding eigenvalue problem for the bifurcation point and derive the corresponding bounds (Y_0, Z_1 and Z_2). At this third bifurcation point, the viscosity parameter ν is significantly smaller ($\nu \approx 0.1234$). This leads to more complicated fluid dynamics. To accurately capture these dynamics such that the Newton-Kantorovich bounds are satisfied, the spatial truncation parameter N must be substantially increased. As the Jacobian matrix required for the full three-dimensional bifurcation analysis scales as $N^3 \times N^3$, this necessary increase in modes causes the dense matrix operations to rapidly exceed the memory capacity of standard hardware (exhausting 256 GB of RAM), constituting a computational boundary for the execution of the proof.

Looking beyond these current hardware limitations, the remainder of the chapter provides a blueprint for proving the existence of periodic solutions emerging from this bifurcation. While we do not computationally implement the problem away from the Hopf bifurcation point, we formulate the fully three-dimensional zero-

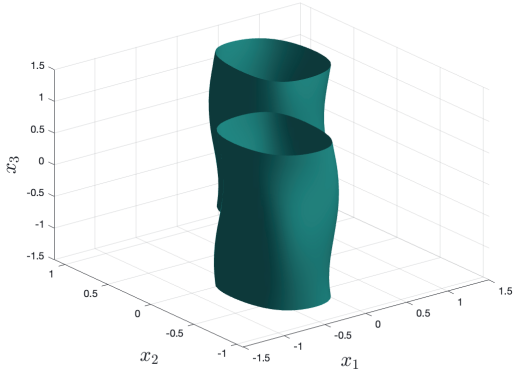


Figure 1.3.4: Level set at value 4 of the vorticity of the third component of a traveling wave approximation to the Navier-Stokes equations.

finding problem. Furthermore, we outline a step-by-step methodology for how a CAP could proceed. By linking the theoretical structure of the approximate inverse back to the Jacobian matrix of the implemented Hopf problem, we specify the analytical conditions, such as a bound on the approximate inverse A, that are required to satisfy $Z_1 < 1$. Although a full computational verification is currently out of reach due to memory constraints, this framework provides a roadmap for an existence proof of fully three-dimensional periodic solutions of small amplitude.

The concrete next steps to complete the fully three-dimensional proofs will involve the large-scale computational implementation of this blueprint. Specifically, future work must focus on efficient evaluations for the finite blocks of the Jacobian matrix, the derivation of the analytical convolution constants for the tail estimates and the development of highly parallelized or matrix-free evaluation techniques to explicitly construct and bound the approximate inverse without exhausting available memory.

2 Periodic localized traveling waves in the two-dimensional suspension bridge equation

2.1 Introduction

The purpose of this chapter is to find and prove suitably localized traveling wave solutions to the suspension bridge equation in two spatial dimensions. Historically, one of the stimuli for studying suspension bridges was the collapse of the Tacoma Narrows Bridge in 1940 [1]. The collapse was caused by the blowing of a strong wind, creating waves in the bridge, which eventually resulted in failure of the construction. This catastrophic event motivated the development of mathematical models of suspension bridges. Overviews of the history of various mathematical models for suspension bridges can be found in [23] and [28]. As argued in [23], in essence there are two type of models of suspension bridges: very realistic, advanced ones (e.g. [2, 42, 45]) and more simplistic models, which are better suitable for mathematical analysis. In this chapter, we study the relatively simple model (see e.g. [20, 47])

$$\partial_t^2 U = -\Delta^2 U - e^U + 1, \tag{2.1}$$

where $U = U(X_1, X_2, t) \in \mathbb{R}$ denotes the deflection of the bridge surface in the downward direction, depending on spatial variables $X_1, X_2 \in \mathbb{R}$ and time $t \geq 0$. The bilaplacian Δ^2 in (2.1) is given by $\Delta^2 = \left(\partial_{X_1}^2 + \partial_{X_2}^2\right)^2$.

In numerical simulations of this partial differential equation (PDE), traveling localized structures are frequently observed (e.g. [9, 20, 32]). To study these, we introduce the parameter $c \in \mathbb{R}$, representing the wave speed in the X_1-direction, and we reduce (2.1) further by substituting the traveling wave ansatz

$$U(X_1, X_2, t) = u(X_1 - ct, X_2) = u(x_1, x_2), \tag{2.2}$$

where the traveling wave profile u satisfies

$$\Delta^2 u + c^2 \partial_{x_1}^2 u + e^u - 1 = 0. \tag{2.3}$$

In one spatial dimension, the traveling wave equation is an ordinary differential equation (ODE) rather than a PDE, i.e.,

$$u'''' + c^2 u'' + e^u - 1 = 0. \tag{2.4}$$

This chapter reproduces the content of the published paper *Periodic localized traveling waves in the two-dimensional suspension bridge equation* [79], co-authored with Jan Bouwe van den Berg and Jean-Philippe Lessard. Minor modifications have been made to match the formatting of this thesis.

This one-dimensional suspension bridge equation has been studied extensively (e.g. [9, 20, 43, 47, 61]). In [61], it was proven that for *almost all* $c \in (0, \sqrt{2})$ there exist at least one homoclinic solution of (2.4). These homoclinic solutions correspond to planar traveling wave solutions of (2.1) that are localized in the X_1-direction. In addition, existence of at least one homoclinic solution was proven for all $c \in [0.71, 1.37]$ in [67] using computer-assisted means and for all $c \in (0, 0.74)$ in [60] using variational methods. Complementing these findings, 36 homoclinic solution were proven for $c = 1.3$ in [9]. Orbital (in)stability of these solutions was investigated in [47].

In [52], existence of periodic, instead of homoclinic, solutions of (2.4) was proven. The authors developed a method for proving existence of two families of (multi-bump) periodic solutions for all $c \in (0, \sqrt{2})$. Both families consist of sets of distinct periodic traveling patterns.

It is observed in many of the above mentioned chapters that for c approaching $\sqrt{2}$, the amplitudes of the waves tend to zero, leading to oscillatory solutions. On the other hand, when c approaches zero, the amplitudes of the waves go to infinity. Indeed this behavior is known to hold in any dimension [59]. At $c = 0$, solutions no longer exist [52, 59].

In contrast to the many analytic results for the one-dimensional case summarized above, the two-dimensional traveling wave problem has so far only been studied numerically. The simulations presented in [32] suggest that localized (in both spatial directions) traveling structures appear in the dynamics of (2.1). However, to our knowledge, an existence proof is lacking.

Rather than studying the idealized setting of localized solutions of (2.3) on an unbounded two-dimensional domain, which is certainly mathematically interesting but for now out of reach, we reduce technical difficulties by considering a large domain with periodic boundary conditions. We are interested in the situation where the bridge is much longer than the characteristic length scale of the observed localized traveling patterns. Physically, the length scale along the X_1-direction of the bridge is of primary importance. To reduce the influence of the boundary condition in the X_2-direction, we focus on solutions which are localized in both spatial dimensions, as was done in [32]. Of course, both an infinitely long bridge and a long "periodic" bridge are merely mathematical idealizations.

To be precise, we introduce constants $L_1, L_2 > 0$. We set out to prove traveling wave solutions on a bridge of width $2L_2$ (in the X_2-direction) that are $2L_1$ periodic in the X_1-direction. By using computer-assisted techniques we will be able to inspect that the localization length scale of the solution found is indeed much smaller than L_1 and L_2.

The natural "free" boundary conditions in the X_2-direction for the bilaplacian are $\Delta U(\,\cdot\,, \pm L_2) = 0 = \partial_{X_2} \Delta U(\,\cdot\,, \pm L_2)$. In this chapter, we idealize the setting by imposing Neumann boundary conditions $\partial_{X_2} U(\,\cdot\,, \pm L_2) = 0 = \partial_{X_2} \Delta U(\,\cdot\,, \pm L_2)$, which are easier to deal with in our approach. Finally, we take advantage of the symmetry ($x_1 \mapsto -x_1$, $x_2 \mapsto -x_2$) and consider solutions on a rectangle

$[0, L_1] \times [0, L_2]$ with Neumann boundary conditions on all sides:

$$\partial_{x_1} u\,(0, x_2) = 0, \quad \partial_{x_1} u\,(L_1, x_2) = 0, \quad \partial^3_{x_1} u\,(0, x_2) = 0, \quad \partial^3_{x_1} u\,(L_1, x_2) = 0, \tag{2.5a}$$

$$\partial_{x_2} u\,(x_1, 0) = 0, \quad \partial_{x_2} u\,(x_1, L_2) = 0, \quad \partial^3_{x_2} u\,(x_1, 0) = 0, \quad \partial^3_{x_2} u\,(x_1, L_2) = 0. \tag{2.5b}$$

The symmetries allow a natural extension of a solution u on $[0, L_1] \times [0, L_2]$ satisfying the boundary conditions (2.5) to a solution of (2.3) on $\mathbb{R} \times [-L_2, L_2]$ through

$$u(x_1, x_2) = u(-x_1, x_2) = u(x_1, -x_2) = u(2L_1 + x_1, x_2).$$

This extended profile u then constitutes, via (2.2), a periodic traveling wave solution of (2.1) on $\mathbb{R} \times [-L_2, L_2]$ satisfying Neumann boundary conditions in the X_2-direction.

In this chapter, we develop a computer-assisted method for proving existence of solutions to (2.3) with boundary conditions (2.5). An example of the type of result we obtain is stated in Theorem 2.1.1 and illustrated in Figure 2.1.1. The method yields an explicit approximation of a *periodically localized* traveling wave, i.e., periodic in the X_1-direction and localized in space when viewed on a fundamental domain of periodicity, together with an also explicit and very small error bound on the distance between the proven solution and the depicted approximation.

Theorem 2.1.1. *For $c = 1.1$ and $L = (50, 40)$, there exists a solution $\hat{u}$ to (2.3) with boundary conditions (2.5) such that $\|\hat{u} - \bar{u}\|_\infty \leq 4 \cdot 10^{-8}$, where $\bar{u}$ is the numerical approximation visualized in Figure 2.1.1. The finitely many non-vanishing Fourier-cosine coefficients of $\bar{u}$ can be found in the code at [78].*

We argue that, by comparing the size of the error bound in Theorem 2.1.1 with (the amplitude of) the graph of $\bar{u}$ in Figure 2.1.1, we can convincingly claim that the solution $\hat{u}$ describes a traveling pattern that localized in space on a fundamental domain (as well as periodic in the X_1-direction). Concerning regularity of the solution, although Theorem 2.1.1 provides an error estimate in terms of the supremum norm only, it follows immediately from the proof method that the solution $\hat{u}$ is real-analytic.

We prove this theorem using a computer-assisted proof (CAP). The use of CAPs for rigorously verifying numerical simulations of dynamical systems has seen tremendous growth during the last decades. To ensure rigor of the computer calculations that are part of the proof, interval arithmetic is used (see e.g. [46]). Examples of existence theorems for solutions to elliptic PDEs using computer-assisted means can be found in [48, 53], which mark some of the earliest instances of CAPs for PDEs. The developed techniques were part of the foundation for later studies on CAPs for PDEs described in [10, 50, 62]. For periodic patterns such as the ones studied in this chapter, Fourier transformations are a natural tool. This bring us in a setting where a Newton-Kantorovich type theorem can be applied, which is a standard tool when constructing CAPs for PDEs and beyond (e.g. [7, 8, 35, 56, 69, 75]). One of the Newton-Kantorovich approaches is known as the radii polynomial approach [22], which we follow in this chapter. We note that a different powerful

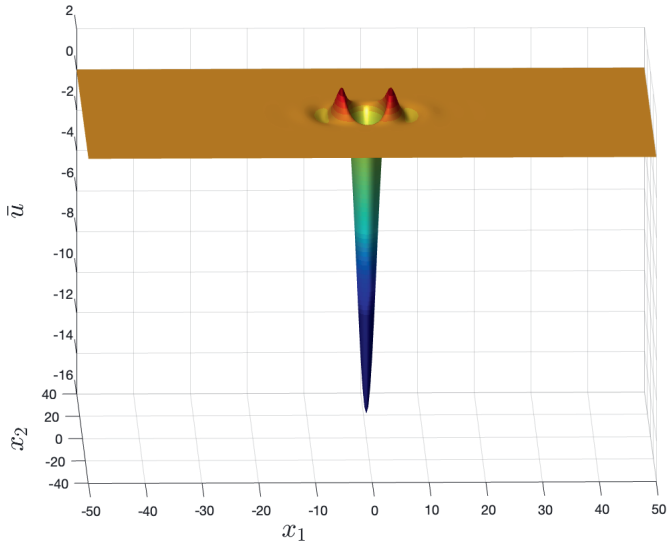


Figure 2.1.1: Plot of the approximate solution $\bar{u}$ to (2.3) with boundary conditions (2.5), justified in Theorem 2.1.1. The approximation is extended to the domain $[-L_1, L_1] \times [-L_2, L_2]$ in this plot, i.e., we visualize a single period.

computer-assisted technique for finding periodic orbits in time is to use rigorous integration of the infinite dimensional flow combined with a topological argument (e.g. [4, 89]). More extensive overviews of CAPs for PDEs can be found in the book [49] and the survey article [30].

This chapter builds on the aforementioned results and introduces several novel aspects. Indeed, as far as we know our approach is the first one to enable proving the existence of periodically localized traveling waves in the two-dimensional suspension bridge equation, confirming numerical indications from simulations that go two decades back [32]. As already stated, there is a stark contrast with the results in one spatial dimension, where a multitude of techniques is available. We note in particular that the computer-assisted techniques for the one-dimensional case as presented in [67] are not readily extendable to two dimensions. Namely, the method in [67] is based on introducing the variable $v = e^u$, so that v and u and its derivatives satisfy a system of polynomial ODEs, for which powerful CAP techniques are available. However, in two dimensions there is, to our knowledge, no convenient analogue of this nonlinear change of variables.

To overcome this obstacle, we extend a recent method outlined in [66] to higher dimensions. This method is based on the techniques introduced in [25] for controlling the aliasing error. We present the method in this chapter in two dimensions in such a way that the analogue for dimensions three and higher is also clear,

essentially without any additional difficulties. In this chapter, we limit ourselves to an exponential nonlinearity, but the method can be applied to other analytic nonlinearities, polynomial or nonpolynomial, as well, and the presentation makes this apparent (see also [66]). We hasten to add that there are certainly alternatives to our approach. In particular, Example 9.7 in [49], which is based on [54], considers the Gelfand equation, a second-order elliptic PDE with an exponential nonlinearity, on a two dimensional domain. Using computer-assisted means and a finite element approach, smooth solution branches are proven for that problem. We note that the same book also covers the suspension bridge equation (based on the work in [9]), but only in one spatial dimension.

Finally we mention a more technical point. Any CAP combines human effort with computations delegated to a computer. In an infinite dimensional setting this usually means that the computations are done on a finite dimensional approximation of the full problem, and the truncation dimension is one of the crucial parameters in such a method. To deal with the resulting "projection" or "truncation" error, complementary estimates are derived using pen-and-paper analysis. In our construction, there are multiple steps where we need to choose the dimension of a Galerkin projection determining the amount of modes of a Fourier series that are represented in the computer. The projection dimensions should be chosen judiciously and do not need to be the same in each step of the proof. We highlight the independence of these choices in this chapter. The main advantage of this distinction is that by choosing the parameters independently, we create more flexibility, which we can exploit to decrease computation time as well as memory requirements, hence bringing a proof within practical range. This is especially important in higher dimensions.

The techniques outlined in this chapter open the door for future work: they can be used for studying PDEs in higher dimensions with general analytic nonlinear terms (that may be polynomial or not). Furthermore, our results provide the first proof of periodic localized solutions of the two-dimensional suspension bridge equation. These may serve as a starting point for proving existence of solutions that decay to 0 as $X_1 \to \pm\infty$ by combining our techniques with those developed recently in [16] and [17]. Another follow-up study would be the investigation of (in)stability of the solutions, as was done for the one-dimensional case in [47].

The rest of the chapter is organized as follows. In Section 2.2, we introduce notation that will be convenient later on. Furthermore, we transform our problem to a fixed-point problem which prepares us for applying the Newton-Kantorovich type existence Theorem 2.2.6. In Section 2.3, we describe how to rigorously compute intervals containing the Fourier coefficients corresponding to the nonlinear term of (2.3). These intervals are essential for computing the bounds necessary to apply the existence Theorem 2.2.6. Explicit expressions for these bounds are derived in Section 2.4. Subsequently, the proof of Theorem 2.1.1 is presented in Section 2.5. We also explore some other solutions, see Figure 2.5.1. In the closing section 2.6, we outline and discuss an alternative computer-assisted method for proving solutions to the suspension bridge equation based on a power series expansion of the nonlinearity. Finally, in Appendix 2.A an overview of the different projection dimensions is presented, in Appendix 2.B we describe how to establish in practice

a rigorous computational bound on certain constant that appears in the estimates, and in Appendix 2.C the theorem and short proof of the two-dimensional discrete Poisson summation formula are presented.

2.2 Setup and notation

We start by transforming (2.3) with boundary conditions (2.5) to a zero-finding problem in Fourier space. To shorten notation, we introduce frequency parameters $q_1, q_2 > 0$ such that $L_1 = \frac{\pi}{q_1}$ and $L_2 = \frac{\pi}{q_2}$. For $a_{|n|} = a_{|n_1|,|n_2|} = a_{n_1,n_2} = a_n$, we use the Fourier series expansion

$$u(x_1, x_2) = \sum_{n \in \mathbb{Z}^2} a_{|n|} e^{i(n_1 q_1 x_1 + n_2 q_2 x_2)}. \tag{2.6}$$

Remark 2.2.1. *The absolute values in* (2.6) *appear because of our focus on symmetric solutions. Hence, we can also write u as the cosine series*

$$u = \sum_{n \in \mathbb{N}^2} \gamma_n a_n \cos(n_1 q_1 x_1) \cos(n_2 q_2 x_2),$$

where

$$\gamma_n = \gamma_{n_1,n_2} := \begin{cases} 1 & \text{for } n_1 = n_2 = 0, \\ 2 & \text{for } n_1 = 0, n_2 > 0, \\ 2 & \text{for } n_1 > 0, n_2 = 0, \\ 4 & \text{for } n_1 > 0, n_2 > 0. \end{cases} \tag{2.7}$$

We denote the nonlinear part of (2.3) by $\mathcal{G}(u) = e^u - u - 1$ and let $a = (a_n)_{n \in \mathbb{Z}^2}$. Furthermore, let

$$G_n(a) = (G(a))_n = (G(a))_{n_1,n_2} = (G(a))_{|n_1|,|n_2|} = (G(a))_{|n|}$$

denote the Fourier coefficients of $\mathcal{G} \circ u$. We will not always explicitly mention the dependence of G_n on a. The relation between G_n and a_n is defined via

$$\mathcal{G}\left(\sum_{n \in \mathbb{Z}^2} a_{|n|} e^{i(n_1 q_1 x_1 + n_2 q_2 x_2)} \right) = \sum_{n \in \mathbb{Z}^2} G_{|n|} e^{i(n_1 q_1 x_1 + n_2 q_2 x_2)}.$$

We will use similar notation for the derivative compositions $\mathcal{G}' \circ u$ and $\mathcal{G}'' \circ u$.

To represent the linear part of (2.3) in Fourier space, we introduce

$$\lambda_n = \lambda_{n_1,n_2} := \left(n_1^2 q_1^2 + n_2^2 q_2^2\right)^2 - c^2 n_1^2 q_1^2 + 1. \tag{2.8}$$

Remark 2.2.2. *In this splitting into a linear and nonlinear part we have made the choice to use the linearization of* (2.3) *around* 0 *as the linear part. We also explored the alternative where the nonlinearity is $\widehat{\mathcal{G}}(u) = e^u - 1$ with corresponding $\widehat{\lambda}_n = \left(n_1^2 q_1^2 + n_2^2 q_2^2\right)^2 - c^2 n_1^2 q_1^2$. This did not significantly influence the applicability of our method.*

Plugging the Fourier series expansion, as given in (2.6), into (2.3) leads to the zero-finding problem $F(a) = 0$ where

$$F_n(a) := \lambda_n a_n + (G(a))_n \qquad \text{for all } n \in \mathbb{N}^2.$$

To keep track of finite truncations and corresponding (Galerkin) projections, for any $N \in \mathbb{N}^2$ we introduce the index sets

$$\begin{aligned} I_N &:= \{n \in \mathbb{Z}^2 : |n_1| \le N_1, |n_2| \le N_2\}, \\ I_N^+ &:= I_N \cap \mathbb{N}^2 = \{0 \le n_1 \le N_1, 0 \le n_2 \le N_2\}. \end{aligned}$$

To shorten notation, when we write $n \notin I_N^+$ we mean $n \in \mathbb{N}^2 \setminus I_N^+$, and when we write $n \notin I_N$ we mean $n \in \mathbb{Z}^2 \setminus I_N$.

The amount of (nonzero) Fourier coefficients used in the numerical approximation of a solution is denoted by $N^{\mathrm{Gal}} \in \mathbb{N}^2$. The size of the numerically approximated part of the Fréchet derivative of F is denoted by $N^{\mathrm{Jac}} \in \mathbb{N}^2$. An overview of the different computational truncation parameters N used in this chapter can be found in Appendix 2.A.

Remark 2.2.3. *Later on we work with the reciprocal of λ_n. In particular, we will need that $\lambda_n \neq 0$ for $n \notin I_{N^{\mathrm{Jac}}}^+$. For $c^2 < 2$ (which in practice is always the case) this is automatic, while for $c^2 \ge 2$ an elementary calculation shows that we require $(N_1^{\mathrm{Jac}} + 1)^2 q_1^2 > \frac{c^2}{2} + [\frac{c^4}{4} - 1]^{1/2}$ and $(N_2^{\mathrm{Jac}} + 1)^2 q_2^2 > \frac{c^4 - 4}{4c^2}$.*

Furthermore, to keep the expressions simple, in our estimates we will assume that λ_n increases as n increases for $n \notin I_{N^{\mathrm{Jac}}}^+$, see Lemma 2.4.1. Therefore, we choose N^{Jac} such that $(N_1^{\mathrm{Jac}} + 1)^2 q_1^2 \ge \frac{c}{2}$. In summary, we thus require

$$\begin{aligned} N_1^{\mathrm{Jac}} &> \frac{\left[c^2 + (\max\{0, c^4 - 4\})^{1/2}\right]^{1/2}}{2^{1/2} q_1} - 1, \\ N_2^{\mathrm{Jac}} &> \frac{(\max\{0, c^4 - 4\})^{1/2}}{2 c q_2} - 1. \end{aligned} \tag{2.9}$$

Let $\chi = \mathbb{R}^{\mathbb{N}^2}$ be the space of Fourier-cosine coefficients. Elements of χ are usually denoted by $a = \{a_n\}_{n \in \mathbb{N}^2}$. For $N \in \mathbb{N}^2$, the (Galerkin) projection Π^N of χ onto the $(N_1 + 1)(N_2 + 1)$-dimensional subspace $\pi^N \chi$ of χ is given by

$$\left(\Pi^N a\right)_n = \begin{cases} a_n & \text{if } n \in I_N^+, \\ 0 & \text{if } n \notin I_N^+. \end{cases}$$

We can identify $\Pi^N \chi$ with $\mathbb{R}^{(N_1+1)(N_2+1)}$ and linear operators on $\Pi^N \chi$ can be represented by matrices of size $(N_1 + 1)(N_2 + 1) \times (N_1 + 1)(N_2 + 1)$.

Let $\bar{a} \in \pi^{N^{\mathrm{Gal}}} \chi$ be a numerical approximate zero of F, i.e., $\bar{a}_n = 0$ for $n \notin I_{N^{\mathrm{Gal}}}$ and $\Pi^{N^{\mathrm{Gal}}} F(\bar{a}) \approx 0$. For the Newton-Kantorovich method we will need an approximation A of the inverse of the Fréchet derivative of F at $\bar{a}$. To construct such an approximation, we consider the Jacobian matrix associated to the restricted map

$F^{N^{\mathrm{Jac}}} := \pi^{N^{\mathrm{Jac}}} F\Big|_{\pi^{N^{\mathrm{Jac}}}\chi}$ evaluated at $\pi^{N^{\mathrm{Jac}}}\bar{a}$. Here N^{Jac} is not necessarily equal to N^{Gal}. We denote by $A^{N^{\mathrm{Jac}}}$ the $(N_1^{\mathrm{Jac}}+1)(N_2^{\mathrm{Jac}}+1) \times (N_1^{\mathrm{Jac}}+1)(N_2^{\mathrm{Jac}}+1)$ matrix obtained by numerically computing an approximate inverse of the Jacobian matrix $DF^{N^{\mathrm{Jac}}}(\Pi^{N^{\mathrm{Jac}}}\bar{a})$. Using $A^{N^{\mathrm{Jac}}}$ we can define the operator A as

$$(Av)_n := \begin{cases} (A^{N^{\mathrm{Jac}}}\Pi^{N^{\mathrm{Jac}}} v)_n & \text{if } n \in I^+_{N^{\mathrm{Jac}}}, \\ \lambda_n^{-1} v_n & \text{if } n \notin I^+_{N^{\mathrm{Jac}}}. \end{cases} \tag{2.10}$$

Remark 2.2.4. *When evaluating $\Pi^{N^{\mathrm{Gal}}}F(\bar{a})$ and $DF^{N^{\mathrm{Jac}}}(\Pi^{N^{\mathrm{Jac}}}\bar{a})$ we will encounter $\Pi^{N^{\mathrm{Gal}}}G(\bar{a})$ and $\Pi^{N^{\mathrm{Jac}}}G'(\bar{a})$. While we cannot compute these terms exactly, at this stage of the construction that is not a problem, since we only need numerical approximations. In Section 2.3 we delve deeper into obtaining rigorous enclosures of these terms.*

Remark 2.2.5. *For simplicity the two projection dimensions are usually chosen to be equal: $N^{\mathrm{Gal}} = N^{\mathrm{Jac}}$. In that "natural" case the Jacobian matrix used for the Newton iterations that produce $\bar{a}$ is the same as the one inverted to obtain $A^{N^{\mathrm{Jac}}}$. However, when trying to obtain a proof it is often only necessary to enlarge* either N^{Gal} or N^{Jac} *to have a successful CAP. Hence distinguishing between N^{Gal} and N^{Jac} allows us to minimize the computation time and memory usage, which is why we make the distinction explicit.*

To turn a subset of the coefficient space χ into a Banach space, we choose a weighted ℓ^1 space, where the weights are represented by $\nu = (\nu_1, \nu_2) \geq (1,1)$. Here and in what follows, for $x, \tilde{x} \in \mathbb{R}^2$ we write $x \geq \tilde{x}$ to say that both $x_1 \geq \tilde{x}_1$ and $x_2 \geq \tilde{x}_2$. Similarly, $x > \tilde{x}$ means that both $x_1 > \tilde{x}_1$ and $x_2 > \tilde{x}_2$.

We now denote by ℓ^1_ν the Banach space of elements $a \in \chi$ with finite norm

$$\|a\|_\nu := \sum_{n\in\mathbb{N}^2} |a_n|\,\omega_n,$$

with weights

$$\omega_n := \gamma_n \nu^n := \gamma_n \nu_1^{n_1} \nu_2^{n_2},$$

where we recall that γ_n is given by (2.7). The weights ω_n are such that we can also write

$$\|a\|_\nu = \sum_{n\in\mathbb{Z}^2} \left|a_{|n|}\right| \nu^{|n|},$$

where $|n| = (|n_1|, |n_2|)$. We note that for $a \in \ell^1_\nu$ with $\nu \geq 1$ the Fourier series (2.6) converges uniformly, while for $\nu > 1$ the series represents a smooth (real analytic) function. One of the other benefits of this space is that the norm satisfies the Banach algebra property, i.e.,

$$\|a * \tilde{a}\|_\nu \leq \|a\|_\nu \|\tilde{a}\|_\nu, \qquad \text{for } a, \tilde{a} \in \ell^1_\nu, \tag{2.11}$$

where the convolution product is defined as

$$(a * \tilde{a})_n = \sum_{m \in \mathbb{Z}^2} a_{|m|} \tilde{a}_{|n-m|} \qquad \text{for } n \in \mathbb{N}^2.$$

Finally, let I denote the identity map (its domain should be clear from context). We are now ready to state the existence theorem used for obtaining the CAPs in this chapter, which is based on establishing that $a \mapsto a - AF(a)$ is a contraction on a ball of appropriately chosen radius centered at $\bar{a}$.

Theorem 2.2.6 (e.g. [6]). *Let $F : X \to \hat{X}$ be a Fréchet differentiable map between Banach spaces X and $\hat{X}$. Furthermore, let $A \in B(\hat{X}, X)$ be injective, $\bar{a} \in X$ and $r^* \in (0, \infty]$. Assume that $Y, Z, W \in \mathbb{R}^+$ satisfy the bounds*

$$\|AF(\bar{a})\|_X \leq Y, \tag{2.12}$$

$$\|I - ADF(\bar{a})\|_{B(X)} \leq Z, \tag{2.13}$$

$$\|A[DF(\bar{a} + w) - DF(\bar{a})]\|_{B(X)} \leq W\|w\|_X \quad \text{for all } \|w\|_X \leq r^*. \tag{2.14}$$

If Y, Z and W satisfy

$$Z < 1;$$
$$2YW < (1 - Z)^2,$$

then, for any r satisfying

$$\frac{1 - Z - \sqrt{(1 - Z)^2 - 2YW}}{W} \leq r < \min\left(\frac{1 - Z}{W}, r^*\right)$$

there exists a unique $\hat{a} \in X$ satisfying $F(\hat{a}) = 0$ such that $\|\hat{a} - \bar{a}\|_X \leq r$.

When we apply this theorem in our setting we take $X = \ell^1_\nu$ and we can for example select $\hat{X} = \{a \in \chi : \|a\|_{\hat{X}} = \sum_{n \in \mathbb{N}^2} (|\lambda_n| + 1)^{-1} |a_n| \omega_n < \infty\}$, so that $A : \hat{X} \to X$ is a bounded operator. Concerning injectivity of A, it follows from (2.10) that it suffices to check that the matrix $A^{N^{\text{Jac}}}$ is invertible, which is not difficult to verify (for our norm it is implied by the requirement that $\|I - ADF(\bar{a})\|_{B(X)} < 1$).

2.3 Determining the Fourier coefficients of the nonlinear term

Assuming that we know $\bar{a}$, which has only finitely many nonzero terms and represents a numerical approximate zero of F, we want to calculate corresponding $\bar{b} = G(\bar{a})$, the Fourier coefficients of $\mathcal{G} \circ \bar{u}$ where $\bar{u}$ is the function with Fourier coefficients $\bar{a}$. However, we cannot calculate $\bar{b}$ exactly. One reason for this is that $\bar{b}$ has infinitely many non-vanishing Fourier coefficients, since $\mathcal{G}$ is not polynomial. But the situation is even worse, since for nonpolynomial $\mathcal{G}$ not even finitely many of the coefficients of $\bar{b}$ can be calculated exactly. Hence, in this section we perform estimates to obtain intervals containing the values of the Fourier coefficients. To do so, we follow [25] and extend the one-dimensional method outlined in [66] to higher

dimensions. To be specific, we focus on *two* dimensions, but our notation is chosen such that the generalization to dimensions three and higher is straightforward. We present the estimates for general Fourier series instead of cosine series. However, in the implementation in the code we do use the symmetries in our problem and hence we work with cosine series there. We also note that the implementation uses interval arithmetic to rigorously absorb errors due to rounding in floating point operations.

The enclosure we obtain for $\bar{b}$ is described in two steps. First, in Section 2.3.1 we derive a relatively rough bound on $|\bar{b}_n|$ that holds for all $n \in \mathbb{Z}^2$. While a bit rough, the bound decays exponentially in n, and in practice we use this bound for large n. Subsequently, we construct an improved enclosure of $\bar{b}_n$ for small $n \in \mathbb{Z}^2$ in Section 2.3.2. Here the boundary between small and large n is determined by a computational parameter $N^{\mathrm{Alias}} \in \mathbb{N}^2$. We choose $N^{\mathrm{Alias}} \geq N^{\mathrm{Jac}}$ for implementation purposes. Combining the two results, we arrive at a way of rigorously computing intervals containing $\bar{b}_n$.

2.3.1 Enclosure for the tail

Since $\bar{a} \in \chi$ has only finitely many nonvanishing terms, the corresponding function $\bar{u}(z) = \sum_{n\in\mathbb{Z}^2} \bar{a}_n e^{i(n_1 z_1 + n_2 z_2)}$ is analytic on $\mathbb{C}^2$. Note that this function is 2π-periodic in the real parts of z_1 and z_2, hence we have absorbed the frequencies (q_1, q_2) in the independent variables $z = (z_1, z_2)$. For $\bar{\rho} \in \mathbb{R}^2$ we define

$$C_{\bar{\rho}} := \frac{1}{(2\pi)^2} \int_{-\pi}^{\pi} \int_{-\pi}^{\pi} |\mathcal{G}(\bar{u}(x_1 - i\bar{\rho}_1, x_2 - i\bar{\rho}_2))| dx_1 dx_2. \tag{2.15}$$

Furthermore, for $\bar{\rho} > 0$ we set

$$\widehat{C}_{\bar{\rho}} := \max\left\{C_{\bar{\rho}_1,\bar{\rho}_2}, C_{-\bar{\rho}_1,\bar{\rho}_2}, C_{\bar{\rho}_1,-\bar{\rho}_2}, C_{-\bar{\rho}_1,-\bar{\rho}_2}\right\}. \tag{2.16}$$

Remark 2.3.1. *The constant $\widehat{C}_{\bar{\rho}}$ defined in* (2.16) *cannot be calculated exactly. However, we can rigorously and efficiently estimate it using the discrete Fourier transform and interval arithmetic. This procedure is described in Appendix 2.B.*

The following lemma controls the decay rate of the Fourier coefficients of $\mathcal{G}(\bar{u})$. The result holds more generally for any function $\bar{u}$ which is analytic on some strip

$$S_\rho := \{z \in \mathbb{C}^2 : \mathrm{Im}(z_1) < \rho_1, \mathrm{Im}(z_2) < \rho_2\}$$

of width $\rho > \bar{\rho}$ and any nonlinearity $\mathcal{G}$ which is analytic on the range of $\bar{u}|_{S_\rho}$.

Lemma 2.3.2. *Let $\mathbb{R}^2 \ni \bar{\rho} > 0$. Let $\{\bar{b}_n\}_{n\in\mathbb{Z}^2}$ denote the Fourier coefficients of $\mathcal{G} \circ \bar{u}$ and let $\bar{\nu} = (e^{\bar{\rho}_1}, e^{\bar{\rho}_2})$. Then*

$$\left|\bar{b}_n\right| \leq \frac{\widehat{C}_{\bar{\rho}}}{\bar{\nu}^{|n|}}, \quad \text{for all } n \in \mathbb{Z}^2.$$

Proof. We present the details for $n \geq 0$, which corresponds to $C_{\bar{\rho}}$. The other cases ($n < 0$ and $n_1 < 0, n_2 \geq 0$ and $n_1 \geq 0, n_2 < 0$) are dealt with in an equivalent way.

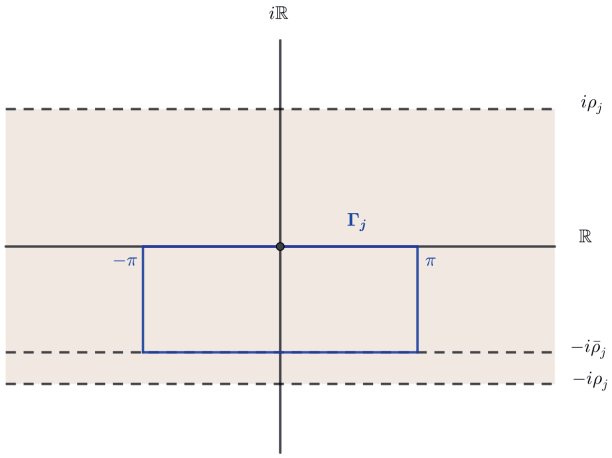


Figure 2.3.1: The placement of the strip and the contours used in the proof of Lemma 2.3.2.

Choose any $\rho > \bar{\rho}$. As $\bar{u}$ is analytic on $\mathbb{C}^2$, both $\bar{u}$ and $\mathcal{G} \circ \bar{u}$ are analytic on the strip S_ρ. Hence, for the closed contours Γ_j, $j = 1, 2$ depicted in Figure 2.3.1 we have $\iint_{\Gamma_1 \times \Gamma_2} \mathcal{G}(\bar{u}(z))dz = 0$ by Cauchy's Integral Theorem. By using periodicity of $\bar{u}$ in $\mathrm{Re}(z_j)$, we rewrite the formula for the Fourier coefficients $\bar{b}_n$ as

$$\begin{aligned}
\bar{b}_n &= \frac{1}{(2\pi)^2} \int_{-\pi}^{\pi} \int_{-\pi}^{\pi} \mathcal{G}(\bar{u}(x_1, x_2)) e^{-i(n_1 x_1 + n_2 x_2)} dx_1 dx_2 \\
&= \frac{1}{(2\pi)^2} \int_{-\pi}^{\pi} \int_{-\pi}^{\pi} \mathcal{G}(\bar{u}(x_1 - i\bar{\rho}_1, x_2 - i\bar{\rho}_2)) e^{-i(n_1 x_1 + n_2 x_2) - (n_1 \bar{\rho}_1 + n_2 \bar{\rho}_2)} dx_1 dx_2 \\
&= \frac{1}{(2\pi)^2} e^{-(n_1 \bar{\rho}_1 + n_2 \bar{\rho}_2)} \int_{-\pi}^{\pi} \int_{-\pi}^{\pi} \mathcal{G}(\bar{u}(x_1 - i\bar{\rho}_1, x_2 - i\bar{\rho}_2)) e^{-i(n_1 x_1 + n_2 x_2)} dx_1 dx_2.
\end{aligned}$$

Consequently, we obtain, for any $n \geq 0$,

$$\begin{aligned}
\left|\bar{b}_n\right| &\leq \frac{1}{(2\pi)^2 e^{n_1 \bar{\rho}_1 + n_2 \bar{\rho}_2}} \int_{-\pi}^{\pi} \int_{-\pi}^{\pi} \left|\mathcal{G}(\bar{u}(x_1 - i\bar{\rho}_1, x_2 - i\bar{\rho}_2))\right| \left|e^{-i(n_1 x_1 + n_2 x_2)}\right| dx_1 dx_2 \\
&= \frac{1}{\bar{\nu}_1^{n_1} \bar{\nu}_2^{n_2}} \frac{1}{(2\pi)^2} \int_{-\pi}^{\pi} \int_{-\pi}^{\pi} \left|\mathcal{G}(\bar{u}(x_1 - i\bar{\rho}_1, x_2 - i\bar{\rho}_2))\right| dx_1 dx_2 = \frac{C_{\bar{\rho}}}{\bar{\nu}^n}.
\end{aligned}$$

Adjusting the contour to the upper half plane where appropriate, we gather the constants for the other cases, e.g.

$$\left|\bar{b}_n\right| \leq \frac{C_{-\bar{\rho}_1, \bar{\rho}_2}}{\bar{\nu}^{|n|}} \qquad \text{for all } n_1 < 0, n_2 \geq 0.$$

Combining the different cases and using the definition of $\widehat{C}_{\bar{\rho}}$ in (2.16) proves the result. □

Remark 2.3.3. *In the case of cosine series we have $\bar{b}_n = \bar{b}_{|n|}$. We are thus only interested in $n \in \mathbb{N}^2$ and it easily follows, for example from the proof above, that $\widehat{C}_{\bar{\rho}} = C_{\bar{\rho}}$ for $\bar{\rho} > 0$.*

2.3.2 Aliasing error

In this section we aim to find tight enclosures on $\bar{b}_n$ for $n \in I_{N^{\text{Alias}}}$. The choice of the computational parameter N^{Alias} may depend on the purpose of our calculations, but will in our case be guided by the bounds we need to compute in Section 2.4. We thus fix N^{Alias} and set out to improve the general bound from Lemma 2.3.2 for $n \in I_{N^{\text{Alias}}}$. Namely, we use the *discrete* Fourier transform to calculate a numerical approximation of $\bar{b}$, which we call $\bar{b}^{\text{FFT}}$, and bound the resulting *aliasing* error via the Poisson summation formula, as explained below.

In order to calculate $\bar{b}^{\text{FFT}}$, we introduce N^{FFT} indicating how many Fourier modes are considered when doing discrete (inverse) Fourier transformations. For algorithmic reasons, we choose N_1^{FFT} and N_2^{FFT} to be powers of 2, but for the analysis that is irrelevant. In order to obtain a small aliasing error for $n \in I_{N^{\text{Alias}}}$, we require that $N^{\text{FFT}} \gg N^{\text{Alias}}$, see also Remark 2.3.6.

We introduce the index set

$$J_{N^{\text{FFT}}} := \{-N_1^{\text{FFT}} \le n_1 \le N_1^{\text{FFT}} - 1, -N_2^{\text{FFT}} \le n_2 \le N_2^{\text{FFT}} - 1\},$$

and define the uniform mesh (of the square $[-\pi, \pi] \times [-\pi, \pi]$)

$$x_{1,k_1} = \frac{\pi k_1}{N_1^{\text{FFT}}}, \quad x_{2,k_2} = \frac{\pi k_2}{N_2^{\text{FFT}}} \qquad \text{for } k \in J_{N^{\text{FFT}}}. \tag{2.17}$$

Then $\bar{b}^{\text{FFT}}$ is defined via

$$\bar{b}_n^{\text{FFT}} := \frac{1}{4N_1^{\text{FFT}} N_2^{\text{FFT}}} \sum_{k \in J_{N^{\text{FFT}}}} \mathcal{G}\left(\bar{u}\left(x_{1,k_1}, x_{2,k_2}\right)\right) e^{-i(n_1 x_{1,k_1} + n_2 x_{2,k_2})}. \tag{2.18}$$

When $\bar{u}$ has only finitely many nonvanishing Fourier coefficients, then the right-hand side of (2.18) can be evaluated rigorously via interval arithmetic for all $n \in J_{N^{\text{FFT}}}$. Before stating the bound on the aliasing error, we introduce

$$\begin{aligned} f_{\text{geo}}(\xi, N) &:= \frac{(1+\xi_1)(1+\xi_2) - (1+\xi_1 - 2\xi_1^{N_1+1})(1+\xi_2 - 2\xi_2^{N_1+1})}{(1-\xi_1)(1-\xi_2)} \\ &= \frac{2\xi_1^{N_1+1}(1+\xi_2) + 2\xi_2^{N_2+1}(1+\xi_1) - 4\xi_1^{N_1+1}\xi_2^{N_2+1}}{(1-\xi_1)(1-\xi_2)}, \end{aligned}$$

and prove an auxiliary lemma.

Lemma 2.3.4. *Let $N \in \mathbb{N}^2$ and let $\xi = (\xi_1, \xi_2)$ be such that $\xi_1, \xi_2 \in [0, 1)$. Then*

$$\sum_{n \notin I_N^+} \gamma_n \xi^{|n|} = \sum_{n \notin I_N} \xi^{|n|} = f_{\text{geo}}(\xi, N). \tag{2.19}$$

Proof. The first identity in (2.19) follows directly from the definition of γ_n in (2.7). To prove the second identity, we use the splitting

$$\sum_{n \notin I_N} \xi^{|n|} = \sum_{n \in \mathbb{Z}^2} \xi^{|n|} - \sum_{n \in I_N} \xi^{|n|}. \tag{2.20}$$

We start by rewriting the second summation as

$$\sum_{n\in I_N} \xi^{|n|} = \sum_{n_1=-N_1}^{N_1} \xi_1^{|n_1|} \sum_{n_2=-N_2}^{N_2} \xi_2^{|n_2|} = \left(2\sum_{n_1=0}^{N_1} \xi_1^{n_1} - 1\right)\left(2\sum_{n_2=0}^{N_2} \xi_2^{n_2} - 1\right)$$
$$= \left(\frac{1-2\xi_1^{N_1+1}+\xi_1}{1-\xi_1}\right)\left(\frac{1-2\xi_2^{N_2+1}+\xi_2}{1-\xi_2}\right).$$

Using this and recalling that $(\xi_1,\xi_2) < (1,1)$, we can write the first summation in (2.20) as

$$\sum_{n\in\mathbb{Z}^2} \xi^{|n|} = \lim_{(N_1,N_2)\to(\infty,\infty)} \sum_{n\in I_N} \xi^{|n|} = \left(\frac{1+\xi_1}{1-\xi_1}\right)\left(\frac{1+\xi_2}{1-\xi_2}\right).$$

Subtracting the second term from the first one and rewriting yields the assertion. □

We now present an estimate for the aliasing error, along the lines of [25].

Lemma 2.3.5. *Let $\bar\rho = (\bar\rho_1,\bar\rho_2) > 0$ and let $\widehat{C}_{\bar\rho}$ be defined in (2.16) and $\bar\nu_j = e^{\bar\rho_j}$ for $j = 1,2$. Then*

$$\left|\bar b_n - \bar b_n^{\mathrm{FFT}}\right| \le \widehat{C}_{\bar\rho}\,\bar\nu^{|n|}\, f_{\mathrm{geo}}\big(\bar\nu^{-2N^{\mathrm{FFT}}},0\big), \qquad \text{for } n \in J_{N^{\mathrm{FFT}}}. \tag{2.21}$$

Proof. The two-dimensional discrete Poisson summation formula (see Appendix 2.C) implies that

$$\bar b_n^{\mathrm{FFT}} = \bar b_n + \sum_{\substack{j\in\mathbb{Z}^2\\(j_1,j_2)\neq(0,0)}} \bar b_{n+2jN^{\mathrm{FFT}}}, \qquad \text{for } n \in J_{N^{\mathrm{FFT}}}.$$

For $n \in J_{N^{\mathrm{FFT}}}$, we then obtain

$$\begin{aligned}
\left|\bar b_n - \bar b_n^{\mathrm{FFT}}\right| &\le \sum_{\substack{j\in\mathbb{Z}^2\\(j_1,j_2)\neq(0,0)}} \left|\bar b_{n+2jN^{\mathrm{FFT}}}\right| \\
&\le \widehat{C}_{\bar\rho} \sum_{\substack{j\in\mathbb{Z}^2\\(j_1,j_2)\neq(0,0)}} \frac{1}{\bar\nu^{|2jN^{\mathrm{FFT}}|-|n|}} \qquad \text{(Lemma 2.3.2)} \\
&= \widehat{C}_{\bar\rho}\bar\nu^{|n|} \sum_{\substack{j\in\mathbb{Z}^2\\ j\notin I_0}} \big(\bar\nu^{-2N^{\mathrm{FFT}}}\big)^{|j|} \\
&= \widehat{C}_{\bar\rho}\bar\nu^{|n|} f_{\mathrm{geo}}\big(\bar\nu^{-2N^{\mathrm{FFT}}},0\big). \qquad \text{(Lemma 2.3.4)}
\end{aligned}$$

□

We now obtain enclosures on $\bar b_n$ for $n \in I_{N^{\mathrm{Alias}}}$. Combining Lemma 2.3.2 and Lemma 2.3.5 and setting

$$\bar\varepsilon_n := \bar\nu^{|n|} f_{\mathrm{geo}}\left(\bar\nu^{-2N^{\mathrm{FFT}}},0\right) = \frac{2\bar\nu^{|n|}\left(\bar\nu_1^{-2N_1^{\mathrm{FFT}}} + \bar\nu_2^{-2N_2^{\mathrm{FFT}}}\right)}{\left(1-\bar\nu_1^{-2N_1^{\mathrm{FFT}}}\right)\left(1-\bar\nu_2^{-2N_2^{\mathrm{FFT}}}\right)},$$

we can enclose $\bar{b}_n$ by intervals

$$\bar{b}_n \in \begin{cases} \bar{b}_n^{\mathrm{FFT}} + \widehat{C}_{\bar{\rho}}[-\bar{\varepsilon}_n, \bar{\varepsilon}_n] & n \in I_{N^{\mathrm{Alias}}}, \\ [-\frac{\widehat{C}_{\bar{\rho}}}{\bar{\nu}^{|n|}}, \frac{\widehat{C}_{\bar{\rho}}}{\bar{\nu}^{|n|}}] & n \notin I_{N^{\mathrm{Alias}}}. \end{cases} \tag{2.22}$$

Remark 2.3.6. *The size of the aliasing errors is thus measured by the product of* $\widehat{C}_{\log \bar{\nu}}$ *and*

$$\frac{2\bar{\nu}_1^{N_1^{\mathrm{Alias}}} \bar{\nu}_2^{N_2^{\mathrm{Alias}}} \left(\bar{\nu}_1^{-2N_1^{\mathrm{FFT}}} + \bar{\nu}_2^{-2N_2^{\mathrm{FFT}}}\right)}{\left(1 - \bar{\nu}_1^{-2N_1^{\mathrm{FFT}}}\right)\left(1 - \bar{\nu}_2^{-2N_2^{\mathrm{FFT}}}\right)},$$

which quantifies the requirement that $N^{\mathrm{FFT}} \gg N^{\mathrm{Alias}}$ *in order to obtain tight bounds.*

Remark 2.3.7. *The bounds in Theorem 2.2.6 do not only involve* $F(\bar{a})$*, but also its derivative. Hence, we also need the Fourier coefficients* $\bar{b}' = G'(\bar{a})$ *of* $\mathcal{G}' \circ \bar{u}$*. As before, the enclosing intervals are constructed using the numerical approximation obtained through the discrete Fourier transform:*

$$\bar{b}_n'^{\mathrm{FFT}} := \frac{1}{4N_1^{\mathrm{FFT}} N_2^{\mathrm{FFT}}} \sum_{k \in J_{N^{\mathrm{FFT}}}} \mathcal{G}'\left(\bar{u}\left(x_{1,k_1}, x_{2,k_2}\right)\right) e^{-i(n_1 x_{1,k_1} + n_2 x_{2,k_2})}.$$

Repeating the procedure for $\mathcal{G}'(u) = e^u - 1$ *instead of* $\mathcal{G}(u) = e^u - u - 1$*, in particular calculating* $\widehat{C}'_{\bar{\rho}}$ *from* (2.16) *with* $\mathcal{G}$ *replaced by* $\mathcal{G}'$*, we end up with*

$$\bar{b}'_n \in \begin{cases} \bar{b}_n'^{\mathrm{FFT}} + \widehat{C}'_{\bar{\rho}}[-\bar{\varepsilon}_n, \bar{\varepsilon}_n] & n \in I_{N^{\mathrm{Alias}}}, \\ [-\frac{\widehat{C}'_{\bar{\rho}}}{\bar{\nu}^{|n|}}, \frac{\widehat{C}'_{\bar{\rho}}}{\bar{\nu}^{|n|}}] & n \notin I_{N^{\mathrm{Alias}}}. \end{cases} \tag{2.23}$$

We note that one does not need to use the same N^{Alias} *(and* N^{FFT}*) for* $\mathcal{G}'$ *as for* $\mathcal{G}$*, although in our code we did.*

Finally, in Section 2.4.3 we will use the analogous construction for $\mathcal{G}''(u) = e^u$ *and* $\bar{b}'' = G''(\bar{a})$*.*

2.4 Bounds

In this section, formulas for the bounds Y, Z and W that appear in Theorem 2.2.6 are derived. All these formulas can be evaluated (or at least bounded) algorithmically using interval arithmetic. We assume that

- we have fixed N^{Gal} and computed numerically the Fourier coefficients $\bar{a}$ of an approximation of a (candidate) solution.
- we have selected N^{Jac} satisfying (2.9) and we have determined numerically a matrix $A^{N^{\mathrm{Jac}}}$ so that the operator A is defined.
- we have chosen $\bar{\rho}$ and $N^{\mathrm{Alias}} \geq N^{\mathrm{Jac}}$ and $N^{\mathrm{FFT}} \gg N^{\mathrm{Alias}}$ as introduced in Section 2.3.

2.4.1 Computing Y

The first bound appearing in Theorem 2.2.6 is the Y-bound, which should satisfy $\|AF(\bar{a})\|_\nu \leq Y$, as stated in (2.12). We can rewrite $\|AF(\bar{a})\|_\nu$ as

$$\|AF(\bar{a})\|_\nu = \sum_{n \in I^+_{N^{\text{Alias}}}} |(AF(\bar{a}))_n| \, \omega_n + \sum_{n \notin I^+_{N^{\text{Alias}}}} |(AF(\bar{a}))_n| \, \omega_n, \tag{2.24}$$

where $N^{\text{Alias}} \geq N^{\text{Jac}}$ essentially determines where we switch from relatively tight computation of terms to relatively loose estimation of the tail (which is nevertheless small in size in practice). We start with the first summation.

Case $n \in I^+_{N^{\text{Alias}}}$

Using the structure of A given in (2.10) and using (2.22), we write

$$\begin{aligned}\sum_{n \in I^+_{N^{\text{Alias}}}} |(AF(\bar{a}))_n| \, \omega_n \leq \sum_{n \in I^+_{N^{\text{Jac}}}} \left| \left(A^{N^{\text{Jac}}} F^{N^{\text{Jac}}}(\bar{a}) \right)_n \right| \omega_n \\ + \sum_{\substack{n \in I^+_{N^{\text{Alias}}} \\ n \notin I^+_{N^{\text{Jac}}}}} \frac{\left| \bar{b}_n^{\text{FFT}} \right| + \widehat{C}_{\bar{\rho}} \bar{\varepsilon}_n}{\lambda_n} \omega_n.\end{aligned}$$

Even though both terms contain finitely many terms, we are not able to compute $F^{N^{\text{Jac}}}(\bar{a})$ exactly as we have that $F_n(\bar{a}) = \lambda_n \bar{a}_n + \bar{b}_n$, where we cannot evaluate $\bar{b}_n = G_n(\bar{a})$ exactly. Therefore, we use interval arithmetic both to compensate for rounding errors and to compute intervals containing $\bar{b}_n$ given in the right-hand side of (2.22). With this interpretation of computability of $F^{N^{\text{Jac}}}(\bar{a})$, we set

$$Y^{N^{\text{Alias}}} := \sum_{n \in I^+_{N^{\text{Jac}}}} \left| \left(A^{N^{\text{Jac}}} F^{N^{\text{Jac}}}(\bar{a}) \right)_n \right| \omega_n + \sum_{\substack{n \in I^+_{N^{\text{Alias}}} \\ n \notin I^+_{N^{\text{Jac}}}}} \frac{\left| \lambda_n \bar{a}_n + \bar{b}_n^{\text{FFT}} \right| + \widehat{C}_{\bar{\rho}} \bar{\varepsilon}_n}{\lambda_n} \omega_n,$$

which bounds the first summation in (2.24).

Case $n \notin I^+_{N^{\text{Alias}}}$

We assume N^{Jac} satisfies the two inequalities in (2.9). Letting $\lceil \cdot \rceil$ denote the ceiling function, we introduce

$$\lambda_{\min}(N) := \min\{\lambda_{N_1+1,0}, \min_{0 \leq i \leq \lceil \frac{c}{q_1} \rceil} \lambda_{i,N_2+1}\},$$

which is used in the next lemma to bound the tail of A.

Lemma 2.4.1. *Let $N \in \mathbb{N}^2$ be such that $N \geq N^{\text{Jac}}$. Let λ_n be as in (2.8). Then*

$$\frac{1}{\lambda_n} \leq \frac{1}{\lambda_{\min}(N)} \qquad \text{for all } n \notin I^+_N.$$

Proof. From Remark 2.2.3, we know that λ_n is positive and increasing in both n_1 and n_2 for $n \notin I_N^+$, since $I_{N^{\mathrm{Jac}}}^+ \subset I_N^+$. Hence, the smallest values of λ_n for $n \notin I_N^+$ is attained either at $n = (N_1 + 1, 0)$ or at $n_2 = N_2 + 1$ and some $0 \leq n_1 \leq \lceil \frac{c}{q_1} \rceil$. This proves the assertion on the inverse λ_n^{-1}. □

We now bound the second summation in (2.24) as follows:

$$\begin{aligned}
\sum_{n \notin I_{N^{\mathrm{Alias}}}^+} |(AF(\bar{a}))_n| \, \omega_n &= \sum_{n \notin I_{N^{\mathrm{Alias}}}^+} \frac{|\bar{b}_n|}{\lambda_n} \gamma_n \nu^n \\
&\leq \frac{\widehat{C}_{\bar{\rho}}}{\lambda_{\min}(N^{\mathrm{Alias}})} \sum_{n \notin I_{N^{\mathrm{Alias}}}^+} \gamma_n \frac{\nu^n}{\bar{\nu}^n} \quad \text{(Lemmas 2.3.2, 2.4.1)} \\
&= \frac{\widehat{C}_{\bar{\rho}}}{\lambda_{\min}(N^{\mathrm{Alias}})} f_{\mathrm{geo}}\left(\frac{\nu}{\bar{\nu}}, N^{\mathrm{Alias}}\right) \quad \text{(Lemma 2.3.4).}
\end{aligned}$$

Both the bound above and the formula for $Y^{N^{\mathrm{Alias}}}$ are evaluated using interval arithmetic. We take the upper bound of the interval containing the sum of these to determine Y:

$$Y := \text{upperbound}\left(Y^{N^{\mathrm{Alias}}} + \frac{\widehat{C}_{\bar{\rho}}}{\lambda_{\min}(N^{\mathrm{Alias}})} f_{\mathrm{geo}}\left(\frac{\nu}{\bar{\nu}}, N^{\mathrm{Alias}}\right) \right).$$

In the next subsections we will also use interval arithmetic to compute the Z-bound and the W-bound. However, in the derivation for these bounds we will refrain from repeating that we are dealing with intervals and that we take the upper bound of the intervals in the end.

2.4.2 Computing Z

Since the norm on X is a weighted ℓ^1-norm, we can express the operator norm as (e.g. Lemma 2.13 in [6])

$$\|I - ADF(\bar{a})\|_{B(X)} = \sup_{k \in \mathbb{N}^2} \frac{\|[I - ADF(\bar{a})]e_k\|_\nu}{\|e_k\|_\nu},$$

where $(e_k)_n = \delta_{kn}$ for $k, n \in \mathbb{N}^2$ and where δ denotes the Kronecker delta. Hence, we consider the norm of the "columns" of the operator $I - ADF(\bar{a})$ imagined as an infinite matrix in order to determine the Z-bound. For that purpose, we introduce some notation. Let $\mathbb{1}_S$ be the indicator function that is 1 if S is true and 0 otherwise. We have for $k, n \in \mathbb{N}^2$

$$\begin{aligned}
(ADF(\bar{a})e_k)_n = &\sum_{j \in I_{N^{\mathrm{Jac}}}^+} A_{nj}^{N^{\mathrm{Jac}}} \lambda_j \delta_{kj} \mathbb{1}_{\{n \in I_{N^{\mathrm{Jac}}}^+\}} + \delta_{kn} \mathbb{1}_{\{n \notin I_{N^{\mathrm{Jac}}}^+\}} \\
&+ (ADG(\bar{a})e_k)_n.
\end{aligned} \tag{2.25}$$

To make the expression for $DG(\bar{a})e_k$ more explicit, we introduce some notation related to the fact that we are working with cosine series:

$$\begin{aligned} h_1(k) &:= (k_1, k_2), & h_3(k) &:= (k_1, -k_2), \\ h_2(k) &:= (-k_1, k_2), & h_4(k) &:= (-k_1, -k_2). \end{aligned}$$

Remark 2.4.2. *The definition of h_i for $i = 1, 2, 3, 4$ is chosen such that, with γ_k defined in* (2.7)*, for any $a \in \mathbb{C}^{\mathbb{Z}^2}$ such that $\sum_{n\in\mathbb{Z}^2} |a_n| < \infty$ it holds that*

$$\sum_{n\in\mathbb{Z}^2} a_n = \sum_{n\in\mathbb{N}^2} \frac{\gamma_n}{4} \sum_{i=1}^{4} a_{h_i(n)}.$$

For the derivative of the nonlinearity we have $DG(a)\tilde{a} = G'(a) * \tilde{a}$. Denoting $\bar{b}' = G'(\bar{a})$, we thus infer that $DG(\bar{a})e_k = \bar{b}' * e_k$, hence (using Remark 2.4.2) some bookkeeping leads to

$$\begin{aligned} (ADG(\bar{a})e_k)_n &= \sum_{j\in I^+_{N^{\mathrm{Jac}}}} A^{N^{\mathrm{Jac}}}_{nj} \sum_{m\in\mathbb{Z}^2} \bar{b}'_{|j-m|}(e_k)_{|m|} \mathbb{1}_{\{n\in I^+_{N^{\mathrm{Jac}}}\}} \\ &\quad + \frac{1}{\lambda_n} \sum_{m\in\mathbb{Z}^2} \bar{b}'_{|n-m|}(e_k)_{|m|} \mathbb{1}_{\{n\notin I^+_{N^{\mathrm{Jac}}}\}} \\ &= \sum_{j\in I^+_{N^{\mathrm{Jac}}}} A^{N^{\mathrm{Jac}}}_{nj} \frac{\gamma_k}{4} \sum_{i=1}^{4} \bar{b}'_{|j-h_i(k)|} \mathbb{1}_{\{n\in I^+_{N^{\mathrm{Jac}}}\}} \\ &\quad + \frac{1}{\lambda_n} \frac{\gamma_k}{4} \sum_{i=1}^{4} \bar{b}'_{|n-h_i(k)|} \mathbb{1}_{\{n\notin I^+_{N^{\mathrm{Jac}}}\}}. \end{aligned}$$

Substituting this into (2.25), we obtain

$$\begin{aligned} ([I - ADF(\bar{a})]e_k)_n = &\Bigg((e_k)_n - \sum_{j\in I^+_{N^{\mathrm{Jac}}}} A^{N^{\mathrm{Jac}}}_{nj} \lambda_j \delta_{kj} \\ &\qquad - \sum_{j\in I^+_{N^{\mathrm{Jac}}}} A^{N^{\mathrm{Jac}}}_{nj} \frac{\gamma_k}{4} \sum_{i=1}^{4} \bar{b}'_{|j-h_i(k)|} \Bigg) \mathbb{1}_{\{n\in I^+_{N^{\mathrm{Jac}}}\}} \\ &+ \left((e_k)_n - \delta_{kn} - \frac{1}{\lambda_n} \frac{\gamma_k}{4} \sum_{i=1}^{4} \bar{b}'_{|n-h_i(k)|} \right) \mathbb{1}_{\{n\notin I^+_{N^{\mathrm{Jac}}}\}}. \end{aligned}$$

Since $(e_k)_n = \delta_{kn}$ for $k, n \in \mathbb{N}$ and $\|e_k\|_\nu = \omega_k$, we infer that

$$\begin{aligned}\frac{\|\|[I - ADF(\bar{a})]e_k\|_\nu}{\|e_k\|_\nu} = \sum_{n\in I^+_{N^{\mathrm{Jac}}}} \Bigg| \delta_{kn} - \sum_{j\in I^+_{N^{\mathrm{Jac}}}} A^{N^{\mathrm{Jac}}}_{nj}\lambda_j\delta_{kj} \\ - \sum_{j\in I^+_{N^{\mathrm{Jac}}}} A^{N^{\mathrm{Jac}}}_{nj}\frac{\gamma_k}{4}\sum_{i=1}^4 \bar{b}'_{|j-h_i(k)|}\Bigg|\frac{\omega_n}{\omega_k} \\ + \sum_{n\notin I^+_{N^{\mathrm{Jac}}}} \frac{1}{\lambda_n}\left|\frac{\gamma_k}{4}\sum_{i=1}^4 \bar{b}'_{|n-h_i(k)|}\right|\frac{\omega_n}{\omega_k}. \end{aligned} \tag{2.26}$$

We estimate both summations separately, starting with the first one.

Case $n \in I^+_{N^{\mathrm{Jac}}}$

In the first summation of (2.26), the first two terms are only non-zero for $k \in I^+_{N^{\mathrm{Jac}}}$. Therefore, we rewrite the summation once more:

$$\begin{aligned}&\sum_{n\in I^+_{N^{\mathrm{Jac}}}} \Bigg| \delta_{kn} - \sum_{j\in I^+_{N^{\mathrm{Jac}}}} A^{N^{\mathrm{Jac}}}_{nj}\lambda_j\delta_{kj} - \sum_{j\in I^+_{N^{\mathrm{Jac}}}} A^{N^{\mathrm{Jac}}}_{nj}\frac{\gamma_k}{4}\sum_{i=1}^4 \bar{b}'_{|j-h_i(k)|}\Bigg|\frac{\omega_n}{\omega_k} \\ &\quad = \sum_{n\in I^+_{N^{\mathrm{Jac}}}} \Bigg|[\delta_{kn} - A^{N^{\mathrm{Jac}}}_{nk}\lambda_k]\mathbb{1}_{\{k\in I^+_{N^{\mathrm{Jac}}}\}} - \sum_{j\in I^+_{N^{\mathrm{Jac}}}} A^{N^{\mathrm{Jac}}}_{nj}\frac{\gamma_k}{4}\sum_{i=1}^4 \bar{b}'_{|j-h_i(k)|}\Bigg|\frac{\omega_n}{\omega_k}. \end{aligned} \tag{2.27}$$

The first part, denoted by $[\delta_{kn} - A^{N^{\mathrm{Jac}}}_{nk}\lambda_k]\mathbb{1}_{\{k\in I^+_{N^{\mathrm{Jac}}}\}}$, can be computed explicitly for all $n \in I^+_{N^{\mathrm{Jac}}}$. The second part, $\sum_{j\in I^+_{N^{\mathrm{Jac}}}} A^{N^{\mathrm{Jac}}}_{nj}\frac{\gamma_k}{4}\sum_{i=1}^4 \bar{b}'_{|j-h_i(k)|}$, is computed using (2.23) for "small" $k \in I^+_{N^{\mathrm{Col}}}$, whereas it is estimated for all "large" $k \notin I^+_{N^{\mathrm{Col}}}$. Here $N^{\mathrm{Col}} \geq N^{\mathrm{Jac}}$ indicates where we switch from essentially evaluating "columns" of the linear operator to uniformly estimating.

After computing the finite sum in (2.27) for all $k \in I^+_{N^{\mathrm{Col}}}$, we are left with uniformly bounding the second summation in the right-hand side of (2.27) for $k \notin I^+_{N^{\mathrm{Col}}}$. Before we proceed we analyze

$$\mu(j,k) := \frac{1}{4}\sum_{i=1}^4 \frac{1}{\bar{\nu}^{|j-h_i(k)|}\nu^k}$$

for $j \in I^+_{N^{\mathrm{Jac}}}$ and $k \notin I^+_{N^{\mathrm{Col}}}$. For any $N \in \mathbb{N}^2$ we introduce the "boundary" $\mathcal{I}_N \subset \mathbb{N}^2$ of I^+_N:

$$\mathcal{I}_N := \big\{(k_1, N_2+1) : 0 \leq k_1 \leq N_1\big\} \cup \big\{(N_1+1, k_2) : 0 \leq k_2 \leq N_2\big\}.$$

We then define

$$\widehat{\mu}(j,N) := \max_{k\in\mathcal{I}_N} \mu(j,k).$$

Lemma 2.4.3. *Let $N \in \mathbb{N}^2$ and $j \in I_N^+$. Then $\mu(j,k) \leq \widehat{\mu}(j,N)$ for all $k \notin I_N^+$,*

Proof. Fix $j \in I_N^+$. We first observe that $\mu(j,k) = \frac{1}{4}\sum_{i=1}^4 \frac{1}{\bar{\nu}^{|h_i(j)-k|_{\nu^k}}}$. Since $\bar{\nu} > \nu \geq 1$, each of the four summands decreases in k_1 for $k_1 \geq N_1$ and decreases in k_2 for $k_2 \geq N_2$. Hence the supremum of $\mu(j,k)$ over $k \notin I_N^+$ is attained for some $k \in \mathcal{I}_N$. This proves the assertion. □

We are now ready to estimate the second summation in the right-hand side of (2.27). By using (2.23) and Lemma 2.4.3, we conclude that for any $k \notin I_{N^{\mathrm{Col}}}^+$

$$\begin{aligned}\sum_{n\in I_{N^{\mathrm{Jac}}}^+}\sum_{j\in I_{N^{\mathrm{Jac}}}^+}\left|A_{nj}^{N^{\mathrm{Jac}}}\right|\left|\frac{\gamma_k}{4}\sum_{i=1}^4 \bar{b}'_{|j-h_i(k)|}\right|\frac{\omega_n}{\omega_k}&\\ \leq \sum_{n\in I_{N^{\mathrm{Jac}}}^+}\sum_{j\in I_{N^{\mathrm{Jac}}}^+}\left|A_{nj}^{N^{\mathrm{Jac}}}\right|\frac{\gamma_k}{4}\sum_{i=1}^4 \frac{\widehat{C}'_{\bar{\rho}}}{\bar{\nu}^{|j-h_i(k)|}}\frac{\omega_n}{\gamma_k\nu^k}&\\ \leq \widehat{C}'_{\bar{\rho}}\sum_{n\in I_{N^{\mathrm{Jac}}}^+}\sum_{j\in I_{N^{\mathrm{Jac}}}^+}\left|A_{nj}^{N^{\mathrm{Jac}}}\right|\widehat{\mu}(j,N^{\mathrm{Col}})\,\omega_n,&\end{aligned}$$

where we have used that $N^{\mathrm{Col}} \geq N^{\mathrm{Jac}}$. We note that the right-hand side does not depend on k and requires only a finite computation to evaluate.

Case $n \notin I_{N^{\mathrm{Jac}}}^+$

We now investigate the second summation in the right-hand side of (2.26), which is given by

$$\sum_{n\notin I_{N^{\mathrm{Jac}}}^+}\frac{1}{\lambda_n}\left|\frac{\gamma_k}{4}\sum_{i=1}^4 \bar{b}'_{|n-h_i(k)|}\right|\frac{\omega_n}{\omega_k}. \tag{2.28}$$

We start by considering "small" k, i.e., $k \in I_{N^{\mathrm{Col}}}^+$. For these values of k, we split the summation in (2.28) into "small" values of $n \in I_{N^{\mathrm{Row}}}^+$, where we simply evaluate the term, and "large" values of $n \notin I_{N^{\mathrm{Row}}}^+$, where we need an estimate. Here $N^{\mathrm{Row}} \geq N^{\mathrm{Jac}}$ indicates where we switch from explicitly calculating "rows" to estimating uniformly using the rougher enclosure of $\bar{b}'_n$. Hence we write

$$\begin{aligned}\sum_{n\notin I_{N^{\mathrm{Jac}}}^+}\frac{1}{\lambda_n}\left|\frac{\gamma_k}{4}\sum_{i=1}^4 \bar{b}'_{|n-h_i(k)|}\right|\frac{\omega_n}{\omega_k} = &\sum_{\substack{n\in I_{N^{\mathrm{Row}}}^+\\ n\notin I_{N^{\mathrm{Jac}}}^+}}\frac{1}{\lambda_n}\left|\frac{\gamma_k}{4}\sum_{i=1}^4 \bar{b}'_{|n-h_i(k)|}\right|\frac{\omega_n}{\omega_k}\\ &+\sum_{n\notin I_{N^{\mathrm{Row}}}^+}\frac{1}{\lambda_n}\left|\frac{\gamma_k}{4}\sum_{i=1}^4 \bar{b}'_{|n-h_i(k)|}\right|\frac{\omega_n}{\omega_k}.\end{aligned}$$

The first term in the right-hand side is calculated (for each $k \in I_{N^{\mathrm{Col}}}^+$). For the second term we derive an estimate. Indeed, we observe that

$$|n-h_i(k)| \geq \big||n|-|h_i(k)|\big| = \big||n|-|k|\big| \geq |n|-|k| = n-k.$$

We then apply Lemmas 2.3.2 and 2.4.1, and subsequently Lemma 2.3.4 to obtain

$$\begin{aligned}\sum_{n\notin I^+_{N^{\mathrm{Row}}}} \frac{1}{\lambda_n}\left|\frac{\gamma_k}{4}\sum_{i=1}^4 \bar{b}'_{|n-h_i(k)|}\right|\frac{\omega_n}{\omega_k} &\le \frac{1}{\lambda_{\min}(N^{\mathrm{Row}})}\sum_{n\notin I^+_{N^{\mathrm{Row}}}}\frac{1}{4}\sum_{i=1}^4 \frac{\widehat{C}'_{\bar\rho}}{\bar\nu^{|n-h_i(k)|}}\frac{\gamma_n\nu^n}{\nu^k}\\ &\le \frac{\widehat{C}'_{\bar\rho}}{\lambda_{\min}(N^{\mathrm{Row}})}\sum_{n\notin I^+_{N^{\mathrm{Row}}}}\frac{\gamma_n}{4}\sum_{i=1}^4\frac{1}{\bar\nu^{n-k}}\frac{\nu^n}{\nu^k}\\ &= \frac{\widehat{C}'_{\bar\rho}\bar\nu^k}{\lambda_{\min}(N^{\mathrm{Row}})\nu^k} f_{\mathrm{geo}}\left(\frac{\nu}{\bar\nu}, N^{\mathrm{Row}}\right).\end{aligned}$$

We note that this estimate holds for any $k\in\mathbb{N}^2$, but we will use it only for $k\in I^+_{N^{\mathrm{Col}}}$.

We are left with establishing a uniform bound on (2.28) for $k\notin I^+_{N^{\mathrm{Col}}}$. In order to take advantage of computational power to tighten the bound, we introduce another computational parameter N^{Tail} with $N^{\mathrm{Jac}}\le N^{\mathrm{Tail}}\le N^{\mathrm{Col}}$ and split

$$\begin{aligned}\sum_{n\notin I^+_{N^{\mathrm{Jac}}}} \frac{1}{\lambda_n}\left|\frac{\gamma_k}{4}\sum_{i=1}^4 \bar{b}'_{|n-h_i(k)|}\right|\frac{\omega_n}{\omega_k} &= \sum_{\substack{n\in I^+_{N^{\mathrm{Tail}}}\\ n\notin I^+_{N^{\mathrm{Jac}}}}} \frac{1}{\lambda_n}\left|\frac{\gamma_k}{4}\sum_{i=1}^4 \bar{b}'_{|n-h_i(k)|}\right|\frac{\omega_n}{\omega_k}\\ &\quad+\sum_{n\notin I^+_{N^{\mathrm{Tail}}}} \frac{1}{\lambda_n}\left|\frac{\gamma_k}{4}\sum_{i=1}^4 \bar{b}'_{|n-h_i(k)|}\right|\frac{\omega_n}{\omega_k}. \quad (2.29)\end{aligned}$$

For the first term in the right-hand side of (2.29) we proceed as in Section 2.4.2 and use Lemma 2.4.3 to obtain

$$\begin{aligned}\sum_{\substack{n\in I^+_{N^{\mathrm{Tail}}}\\ n\notin I^+_{N^{\mathrm{Jac}}}}} \frac{1}{\lambda_n}\left|\frac{\gamma_k}{4}\sum_{i=1}^4 \bar{b}'_{|n-h_i(k)|}\right|\frac{\omega_n}{\omega_k} &\le \widehat{C}'_{\bar\rho}\sum_{\substack{n\in I^+_{N^{\mathrm{Tail}}}\\ n\notin I^+_{N^{\mathrm{Jac}}}}}\frac{1}{\lambda_n}\left|\frac{1}{4}\sum_{i=1}^4\frac{1}{\bar\nu^{|n-h_i(k)|}\nu^k}\right|\omega_n\\ &\le \widehat{C}'_{\bar\rho}\sum_{\substack{n\in I^+_{N^{\mathrm{Tail}}}\\ n\notin I^+_{N^{\mathrm{Jac}}}}}\frac{\widehat{\mu}(n,N^{\mathrm{Col}})\,\omega_n}{\lambda_n}.\end{aligned}$$

For the second term in the right-hand side of (2.29) we use Lemma 2.4.1 to infer that

$$\begin{aligned}\sum_{n\notin I^+_{N^{\mathrm{Tail}}}} \frac{1}{\lambda_n}\left|\frac{\gamma_k}{4}\sum_{i=1}^4 \bar{b}'_{|n-h_i(k)|}\right|\frac{\omega_n}{\omega_k} &\le \frac{1}{\lambda_{\min}(N^{\mathrm{Tail}})}\sum_{n\in\mathbb{N}^2}\frac{1}{4}\sum_{i=1}^4\left|\bar{b}'_{|n-h_i(k)|}\right|\frac{\gamma_n\nu^n}{\nu^k}\\ &\le \frac{1}{\lambda_{\min}(N^{\mathrm{Tail}})}\sum_{n\in\mathbb{N}^2}\frac{1}{4}\sum_{i=1}^4\left|\bar{b}'_{|h_i(n)-k|}\right|\gamma_n\nu^{|n-k|}.\end{aligned}$$

Next we rewrite the sum over $n\in\mathbb{N}^2$ into a sum over $n\in\mathbb{Z}^2$ (see Remark 2.4.2)

and use (2.23) and Lemma 2.3.4 to obtain the explicit uniform estimate

$$\begin{aligned}\sum_{n\in\mathbb{N}^2}\frac{1}{4}\sum_{i=1}^{4}\left|\bar{b}'_{|h_i(n)-k|}\right|\gamma_n\nu^{|n-k|} &= \sum_{n\in\mathbb{Z}^2}\left|\bar{b}'_{|n-k|}\right|\nu^{|n-k|}\\ &= \|\bar{b}'\|_\nu\\ &= \sum_{n\in I_{N^{\mathrm{Alias}}}}|\bar{b}'_{|n|}|\nu^{|n|}+\sum_{n\notin I_{N^{\mathrm{Alias}}}}|\bar{b}'_{|n|}|\nu^{|n|}\\ &= \sum_{n\in I^+_{N^{\mathrm{Alias}}}}|\bar{b}'_n|\omega_n+\sum_{n\notin I_{N^{\mathrm{Alias}}}}\frac{\widehat{C}'_{\bar{\rho}}}{\bar{\nu}^{|n|}}\nu^{|n|}\\ &\le \sum_{n\in I^+_{N^{\mathrm{Alias}}}}|\bar{b}'_n|\omega_n+\widehat{C}'_{\bar{\rho}}f_{\mathrm{geo}}\left(\frac{\nu}{\bar{\nu}},N^{\mathrm{Alias}}\right).\end{aligned}$$

We note that this estimate again holds for all $k\in\mathbb{N}^2$, but it is used only for $k\notin I^+_{N^{\mathrm{Col}}}$.

Overall Z-bound

To summarize, to estimate the operator norm of $I-ADF(\bar{a})$ the strategy in this section has been to compute where we can and to estimate (uniformly) where we have to. We collect the results from Sections 2.4.2 and 2.4.2 for $k\in I^+_{N^{\mathrm{Col}}}$ into

$$\begin{aligned}Z^{\mathrm{Col}} := \max_{k\in I^+_{N^{\mathrm{Col}}}}\Bigg\{&\sum_{n\in I^+_{N^{\mathrm{Jac}}}}\Bigg|[\delta_{kn}-A^{N^{\mathrm{Jac}}}_{nk}\lambda_k]\mathbb{1}_{\{k\in I^+_{N^{\mathrm{Jac}}}\}}\\ &\qquad-\sum_{j\in I^+_{N^{\mathrm{Jac}}}}A^{N^{\mathrm{Jac}}}_{nj}\frac{\gamma_k}{4}\sum_{i=1}^{4}\bar{b}'_{|j-h_i(k)|}\Bigg|\frac{\omega_n}{\omega_k}\\ &+\sum_{\substack{n\in I^+_{N^{\mathrm{Row}}}\\ n\notin I^+_{N^{\mathrm{Jac}}}}}\frac{1}{\lambda_n}\left|\frac{\gamma_k}{4}\sum_{i=1}^{4}\bar{b}'_{|n-h_i(k)|}\right|\frac{\omega_n}{\omega_k}\\ &+\frac{\widehat{C}'_{\bar{\rho}}\bar{\nu}^k}{\lambda_{\min}(N^{\mathrm{Row}})\nu^k}f_{\mathrm{geo}}\left(\frac{\nu}{\bar{\nu}},N^{\mathrm{Row}}\right)\Bigg\},\end{aligned}$$

and those for $k\notin I^+_{N^{\mathrm{Col}}}$ into

$$\begin{aligned}Z^{\mathrm{Est}} := \widehat{C}'_{\bar{\rho}}\sum_{n\in I^+_{N^{\mathrm{Jac}}}}\sum_{j\in I^+_{N^{\mathrm{Jac}}}}\left|A^{N^{\mathrm{Jac}}}_{nj}\right|\widehat{\mu}(j,N^{\mathrm{Col}})\,\omega_n+\widehat{C}'_{\bar{\rho}}\sum_{\substack{n\in I^+_{N^{\mathrm{Tail}}}\\ n\notin I^+_{N^{\mathrm{Jac}}}}}\frac{\widehat{\mu}(n,N^{\mathrm{Col}})\,\omega_n}{\lambda_n}\\ +\frac{1}{\lambda_{\min}(N^{\mathrm{Tail}})}\left[\sum_{n\in I^+_{N^{\mathrm{Alias}}}}|\bar{b}'_n|\omega_n+\widehat{C}'_{\bar{\rho}}f_{\mathrm{geo}}\left(\frac{\nu}{\bar{\nu}},N^{\mathrm{Alias}}\right)\right].\end{aligned}$$

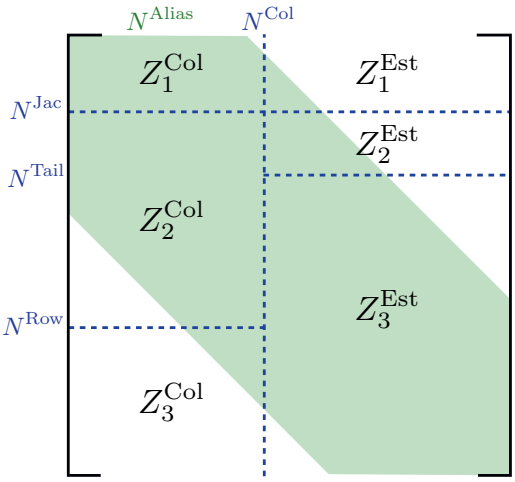


Figure 2.4.1: Schematic representation of the different blocks of $I - ADF(\bar{a})$ appearing in the analysis of $\|I - ADF(\bar{a})\|_{B(X)}$ and their relation with N^{Jac}, N^{Col}, N^{Row} and N^{Tail}. The diagonal band represents a Toeplitz matrix of width N^{Alias}, see Remark 2.4.4.

In both expressions above we evaluate $\bar{b}'_n$ in an interval arithmetic sense through (2.23). Finally, we set $Z := \max\{Z^{\text{Col}}, Z^{\text{Est}}\}$.

Remark 2.4.4. *Observe that Z^{Col} consists of three terms and Z^{Est} consists of two terms, i.e., we have $Z^{\text{Col}} := \max\{Z_{1k}^{\text{Col}} + Z_{2k}^{\text{Col}} + Z_{3k}^{\text{Col}} : k \leq N^{Col}\}$ and $Z^{\text{Est}} := Z_1^{\text{Est}} + Z_2^{\text{Est}} + Z_3^{\text{Est}}$. Essentially we have divided the estimate for the operator norm $\|I - ADF(\bar{a})\|_{B(X)}$ into analyzing the six blocks of $I - ADF(\bar{a})$ outlined schematically in Figure 2.4.1.*

We see that values $\bar{b}'_n$ appear in Z_1^{Col}, Z_2^{Col} and Z_3^{Est}. This makes sense only if for most n appearing in those summations, the values $\bar{b}'_n$ are computed via the discrete Fourier transform with tight aliasing error as described in Section 2.3.2 rather than using the rough uniform estimate from Section 2.3.1. This is trivially satisfied for the summation in Z_3^{Est}, but for Z_1^{Col} and Z_2^{Col} this implies a (mild) relation between N^{Alias} on the one hand and N^{Col} and N^{Row} on the other. This is indicated schematically by the diagonal strip of width N^{Alias}, representing the Toeplitz matrix of $\Pi^{N^{\text{Alias}}}\bar{b}'$, which is part of $DF(\bar{a})$. The diagonal strip should cover a "significant part" of the blocks corresponding to Z_1^{Col} and Z_2^{Col}. Similarly, it is a waste of computational resources to choose N^{Alias} too large and hence compute accurately values of $\bar{b}'_n$ not needed to determine Z_1^{Col} and Z_2^{Col}.

2.4.3 Computing W

Fixing $r^* > 0$, we need a $W \in \mathbb{R}^+$ such that

$$\|A[DF(\bar{a}+w) - DF(\bar{a})]\|_{B(X)} \leq W\|w\|_\nu \qquad \text{whenever } \|w\|_\nu \leq r^*.$$

For any v such that $\|v\|_\nu \le 1$, we define $g_v(w) := ADF(\bar{a}+w)v$, so that

$$g_v(w) - g_v(0) = A[DF(\bar{a}+w) - DF(\bar{a})]v,$$

and $\|A[DF(\bar{a}+w) - DF(\bar{a})]\|_{B(X)} = \sup_{\|v\|_\nu \le 1} \|g_v(w) - g_v(0)\|_\nu$. By the mean value theorem for Banach spaces (cf. Theorem 1.1.1 in [33]), it holds true that $\|g_v(w) - g_v(0)\|_\nu \le M_v \|w\|_\nu$ whenever $\|w\|_\nu \le r^*$, where

$$M_v := \sup_{\|\tilde{w}\|_\nu \le r^*} \|Dg_v(\tilde{w})\|_{B(X)}.$$

Using the definition of the operator norm, we rewrite M_v as

$$\begin{aligned} M_v &= \sup_{\substack{\|\tilde{v}\|_\nu \le 1 \\ \|\tilde{w}\|_\nu \le r^*}} \|Dg_v(\tilde{w})\tilde{v}\|_\nu = \sup_{\substack{\|\tilde{v}\|_\nu \le 1 \\ \|\tilde{w}\|_\nu \le r^*}} \|AD^2F(\bar{a}+\tilde{w})[\tilde{v}, v]\|_\nu \\ &= \sup_{\substack{\|\tilde{v}\|_\nu \le 1 \\ \|\tilde{w}\|_\nu \le r^*}} \|Ae^{\bar{a}+\tilde{w}} * \tilde{v} * v\|_\nu. \end{aligned}$$

We use the Banach algebra property as given in (2.11) to obtain, for any v with $\|v\|_\nu \le 1$,

$$\begin{aligned} \|g_v(w) - g_v(0)\|_\nu &\le \|A\|_{B(X)} \sup_{\substack{\|\tilde{v}\|_\nu \le 1 \\ \|\tilde{w}\|_\nu \le r^*}} \|e^{\bar{a}+\tilde{w}}\|_\nu \, \|\tilde{v}\|_\nu \, \|v\|_\nu \, \|w\|_\nu \\ &\le \|A\|_{B(X)} \, e^{r^*} \left\|e^{\bar{a}}\right\|_\nu \|w\|_\nu. \end{aligned}$$

Here we have used that $e^{\bar{a}+\tilde{w}} = e^{\bar{a}} * e^{\tilde{w}}$ and $\|e^{\tilde{w}}\|_\nu \le e^{\|\tilde{w}\|_\nu}$. We note that although A is described as an operator from $\hat{X}$ to X in Theorem 2.2.6, we are free to interpret it as a bounded operator from X to X here. To determine $\|A\|_{B(X)}$, we compute the matrix norm

$$\|A^{N^{\mathrm{Jac}}}\|_{B(X)} = \max_{k \in I^+_{N^{\mathrm{Jac}}}} \frac{\|A^{N^{\mathrm{Jac}}} e_k\|_\nu}{\|e_k\|_\nu},$$

and then use that (see Lemma 2.4.1)

$$\|A\|_{B(X)} = \max\left\{ \|A^{N^{\mathrm{Jac}}}\|_{B(X)}, \lambda_{\min}^{-1}(N^{\mathrm{Jac}}) \right\}. \tag{2.30}$$

To estimate $\bar{b}'' = e^{\bar{a}}$, we proceed as before to bound the Fourier coefficients of $\mathcal{G}'' \circ \bar{u}$, see Remark 2.3.7. By repeating part of the construction described in Section 2.4.1, we obtain

$$\|e^{\bar{a}}\|_\nu \le \sum_{n \in I^+_{N^{\mathrm{Alias}}}} \left(|\bar{b}_n''^{\mathrm{FFT}}| + \widehat{C}''_{\bar{\rho}} \bar{\varepsilon}_n \right) \omega_n + \widehat{C}''_{\bar{\rho}} f_{\mathrm{geo}}\left(\frac{\nu}{\bar{\nu}}, N^{\mathrm{Alias}} \right).$$

Setting

$$\widehat{W} := \|A\|_{B(X)} \left(\sum_{n \in I^+_{N^{\mathrm{Alias}}}} \left(|\bar{b}_n''^{\mathrm{FFT}}| + \widehat{C}''_{\bar{\rho}} \bar{\varepsilon}_n \right) \omega_n + \widehat{C}''_{\bar{\rho}} f_{\mathrm{geo}}\left(\frac{\nu}{\bar{\nu}}, N^{\mathrm{Alias}} \right) \right),$$

N^{Gal}	N^{Jac}	N^{Alias}	N^{FFT}	N^{Col}	N^{Row}	N^{Tail}
$(130, 130)$	$(65, 65)$	$(400, 400)$	$(1024, 1024)$	$(300, 300)$	$(800, 800)$	$(140, 140)$

Table 2.5.1: Overview of the different values of N used for proving existence of solutions to (2.3) with boundary conditions (2.5) in Theorem 2.1.1.

we conclude that we may choose, for any fixed $r^* > 0$,

$$W = \widehat{W} e^{r^*}. \tag{2.31}$$

Finally, we remark that we have used the estimate $\|e^{\bar{a}+\tilde{w}}\|_\nu \leq \|e^{\bar{a}}\|_\nu e^{r^*}$ and that this convenient property of our exponential nonlinearity leads to substantially better results than the more naive bound $\|e^{\bar{a}+\tilde{w}}\|_\nu \leq e^{\|\bar{a}\|_\nu + r^*}$.

2.5 Results

In this section, we prove existence of different solutions to (2.3) with boundary conditions (2.5). As explained in the introduction, these correspond to periodic waves on an infinite strip, traveling at speed c. The codes that are used to obtain the results can be found in [78]. All computations were carried out in MATLAB (2024a) on an Apple M1 Pro CPU with 32 GB RAM. In order to make the calculations rigorous, the interval arithmetic library Intlab [57] is used. We report floating point numbers displaying four decimals, with the precise values available in the code. At the end of this section we discuss how we found numerical approximations of solutions. We start by proving the theorem that was stated in the introduction.

Proof of Theorem 2.1.1. We set $\nu = (1+10^{-7}, 1+10^{-7})$ and $\bar{\rho} = (0.09531, 0.09531)$. The reasons for this choice and the selection of the other values of the parameters in this proof are discussed in Remark 2.5.1. The values of the different truncation parameters N are presented in Table 2.5.1. The Fourier coefficients $\bar{a}$ of the approximate solution $\bar{u}$ (depicted in Figure 2.1.1) can be found in the code. The values for the bounds are (for $r^* = 6.3605 \cdot 10^{-3}$; see Remark 2.5.2)

$$Y = 2.4708 \cdot 10^{-8}, \quad Z = 2.9545 \cdot 10^{-1}, \quad W = 1.1042 \cdot 10^{2}.$$

Let $\hat{a}$ be the zero of F obtained from Theorem 2.2.6 and let $\hat{u}$ be the corresponding solution of (2.3) with Fourier coefficients $\hat{a}$. It then follows from the error bound in Theorem 2.2.6 that

$$\|\hat{u} - \bar{u}\|_\infty \leq \|\hat{a} - \bar{a}\|_\nu \leq 3.5069 \cdot 10^{-8}. \qquad \square$$

Remark 2.5.1. *The choice of $\nu = (1 + 10^{-7}, 1 + 10^{-7})$ in the proof of Theorem 2.1.1 was made to ensure that solutions are smooth, although a straightforward bootstrap argument also allows the choice $\nu = (1, 1)$. For $\bar{\nu}$ and $\bar{\rho}$, we have the*

relationship $\bar{\nu} = (e^{\bar{\rho}_1}, e^{\bar{\rho}_2})$. *The choice for* $\bar{\nu} = (1.1, 1.1)$ *was made using experimentation, taking into account that it needs to be chosen in between* $(1, 1)$ *and* $\nu_{\bar{a}}$, *where* $\nu_{\bar{a}}$ *is the approximate decay rate of* $\bar{a}$, *i.e.* $|\bar{a}_n| \propto \nu_{\bar{a}}^{-n}$ *for moderately large* n. *Concerning the values of the different* N *that are presented in Table 2.5.1, we have chosen* N^{Gal} *(and the other values of* N*) relatively large in order to obtain a tight error bound. Somewhat smaller* N *still lead to a proof, but with an error bound that is less tight, see also the discussion below. In general, one may want to choose the different* N *as small as possible to keep the computation time manageable, but sufficiently large such that the proof is successful and all the requirements (e.g.* $N^{\mathrm{Col}} \geq N^{\mathrm{Jac}}$*) are met. An overview of the roles of the different* N *and the corresponding requirements can be found in Appendix 2.A.*

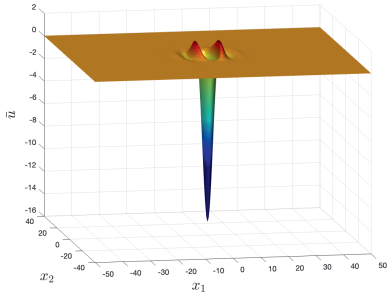
Remark 2.5.2. *Equation* (2.31) *provides a bound* $W = \widehat{W} e^{r^*}$, *which implies that for a successful proof we essentially need that* $\hat{p}(r) := \frac{1}{2}\widehat{W} e^r r^2 - (1 - Z)r + Y < 0$. *Note that this condition is related to the conditions in Theorem 2.2.6, as the lower bound on* r *in Theorem 2.2.6 is one of the roots of* $p(r) := \frac{1}{2} W r^2 - (1 - Z)r + Y$. *To obtain a negative value for* p *and to bring us strictly in the formulation of Theorem 2.2.6, we choose a value* r^* *such that* $\hat{p}(r^*)$ *is minimal (numerically). Subsequently, we check whether for this value of* r^* *and some* $r < r^*$ *it indeed holds that* $p(r) = \frac{1}{2}\widehat{W} e^{r^*} r^2 - (1 - Z)r + Y < 0$. *For the situation in Theorem 2.1.1, this procedure resulted in* $r^* = 6.3605 \cdot 10^{-3}$.

For the discussion in this section, the error bound obtained from Theorem 2.2.6 on the difference between the approximate and the true solution is denoted by $r^{\min}$. For example, in the proof of Theorem 2.1.1 we have $r^{\min} = 3.5069 \cdot 10^{-8}$. Besides Theorem 2.1.1, we present five more existence proofs to illustrate the efficacy of the method. The results are combined in Theorem 2.5.3. We discuss the different solutions found after the statement of the theorem. We note that the approximate solutions in the plots in Figure 2.5.1 are extended to domains such that a single period is visualized.

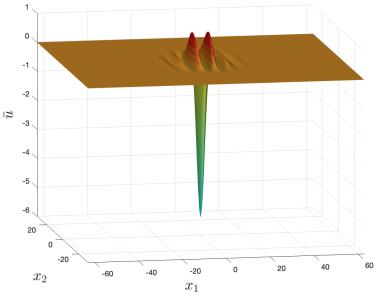
Theorem 2.5.3. *For the different combinations of* c, q *and* $r^{\min}$ *as presented in Table 2.5.2, there exists a solution* $\hat{u}$ *to* (2.3) *with boundary conditions* (2.5) *such that* $\|\hat{u} - \bar{u}\|_\infty \leq r^{\min}$. *Here* $\bar{u}$ *are the numerical approximations visualized in Figure 2.5.1. The finitely many non-vanishing Fourier-cosine coefficients of* $\bar{u}$ *can be found in the code at [78].*

Proof. The proofs of these solutions are entirely analogous to the proof of Theorem 2.1.1 presented above. The values of the parameters not presented in Table 2.5.2, such as the values of ν, $\bar{\rho}$ and the values of the other N, can be found in the code at [78]. □

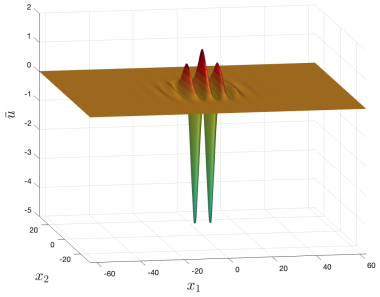
Figure 2.5.1a essentially reproduces the profile from Figure 2.1.1. In Figures 2.5.1b-2.5.1d we depict three (approximate) solutions for wave speed $c = 1.3$, which is the same value as was used in [9] for results in one dimension. The frequencies q are selected such that the solutions are convincingly localized relative to the domain size. In Figures 2.5.1b and 2.5.1c we showcase periodically localized solutions with a single peak and a double peak, respectively. We prove that we can also find a



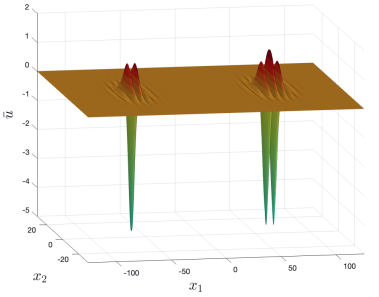
(a) Approximate solution with fewer modes for $c = 1.1$.



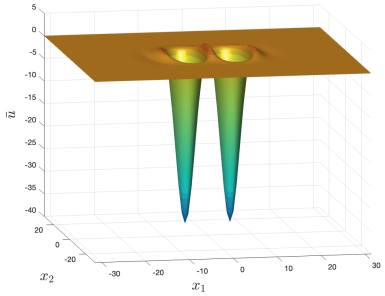
(b) Approximate one peak solution for $c = 1.3$.



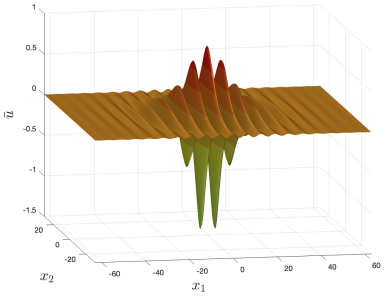
(c) Approximate two peak solution for $c = 1.3$.



(d) Approximate combination solution for $c = 1.3$.



(e) Approximate solution for low wave speed $c = 0.9$.



(f) Approximate solution for high wave speed $c = 1.4$.

Figure 2.5.1: Overview of approximate solutions to (2.3) with boundary conditions (2.5), which can be verified using the code in [78].

Figure	N^{Gal}	c	q	$r^{\min}$	time (s)
2.5.1a	$(65, 65)$	1.1	$(0.0628, 0.0785)$	$3.5069 \cdot 10^{-8}$	7979
2.5.1b	$(60, 20)$	1.3	$(0.05, 0.1)$	$2.0794 \cdot 10^{-3}$	352
2.5.1c	(100,60)	1.3	$(0.05, 0.1)$	$2.1378 \cdot 10^{-6}$	4906
2.5.1d	$(200, 49)$	1.3	$(0.025, 0.1)$	$4.2604 \cdot 10^{-6}$	44330
2.5.1e	$(60, 60)$	0.9	$(0.1, 0.1)$	$2.7351 \cdot 10^{-5}$	42935
2.5.1f	$(80, 40)$	1.4	$(0.05, 0.1)$	$4.2865 \cdot 10^{-6}$	4292

Table 2.5.2: Overview of the parameters N^{Gal}, c and q, the difference $r^{\min}$ between the approximate and true solution, and the computation time for the different (approximate) solutions plotted in Figure 2.5.1.

traveling wave solution that combines the one- and two-peak patterns, as shown in Figure 2.5.1d. Note that the first component of the frequency corresponding to Figure 2.5.1d is half of the ones in Figures 2.5.1b and 2.5.1c. One may conjecture that solutions with more peaks also exist, as well as many combinations of multi-peak patterns, but we leave this for future investigation.

While an in-depth analysis of automated or near-optimal choices of N is beyond the scope of the present chapter, we highlight some features of the presented sample results. For the solution in Figure 2.5.1b, the number of Fourier modes are chosen relatively low to minimize computation time. For that purpose, it is especially important to minimize N^{Col} and, to a lesser but still significant extent, N^{Jac}, as they heavily influence the computation time. The flip side of the coin is that the error bound $r^{\min}$ for this solution is comparatively large, although it is straightforward and computationally not too costly to decrease $r^{\min}$ by increasing N^{Gal} (and N^{Alias}). For the rest of the figures we have chosen more Fourier modes than necessary in order to obtain tighter bounds at higher computational cost.

Next, in Figures 2.5.1e and 2.5.1f we illustrate the influence of the wave speed on the size of the periodically localized pattern. For relatively low wave speed $c = 0.9$ the amplitude is large (Figure 2.5.1e), whereas for relatively large wave speed $c = 1.4$ the amplitude is much smaller and the wave is markedly less localized, see Figure 2.5.1f. For Figure 2.5.1e we choose relatively large $q = (0.1, 0.1)$ as at this low wave speed the pattern is more localized than at higher wave speeds. In general, proving solutions with a lower wave speed requires more modes, as they are needed to approximate the rather spiky solution accurately.

The approximate solutions leading to the rigorously verified solutions corresponding to Figures 2.5.1a-2.5.1f were obtained using Newton's method. Finding a suitable initial guess for Newton's method is often a nontrivial task. A systematic approach for obtaining such guesses is provided by the mountain pass algorithm (see [32]). However, implementing this algorithm can be quite challenging in practice. Therefore, we adopted an alternative strategy. As a starting point, we constructed initial guesses by extending one-dimensional solutions to the ODE (2.4), which are easier to find, into two dimensions. Specifically, these one-dimensional solutions

were embedded into a two-dimensional domain and multiplied by a smooth bump function with compact support in the X_2-direction. To obtain convergence to nontrivial two-dimensional solutions, we added random perturbations to these functions before applying Newton's method. After some trial and error we obtained a nontrivial solution of the type in Figures 2.5.1a and 2.5.1b: a pattern with one large negative peak. Once we found one solution, we used continuation in c to compute solutions of the same type for different wave speeds. By continuing in c up to approximately $c = \sqrt{2}$, we obtained a small amplitude solution u_{small}. In this parameter range, $-u_{\text{small}}$ is almost a solution as well, but this one has a different structure: it features two large negative peaks. Starting with $-u_{\text{small}}$ and decreasing c, we arrived at the solutions shown in Figures 2.5.1c, 2.5.1e and 2.5.1f. Finally, to construct a third type of solution, we combined these two types of patterns by placing them side by side, sufficiently far apart, and then we applied Newton iterations. This procedure led to the pattern shown in Figure 2.5.1d.

2.6 An alternative method: power series

Besides the procedure described in the main part of this chapter, we explored another way of proving solutions to the suspension bridge equation (2.3) with boundary conditions (2.5). This alternative method is based on the power series expansion of the exponential function

$$e^u - u - 1 = \sum_{n=2}^{\infty} \frac{u^n}{n!}. \tag{2.32}$$

By substituting (2.32) in (2.3), we end up with the zero-finding problem

$$F_n(a) := \lambda_n a_n + \sum_{k=2}^{\infty} \frac{(\overbrace{a * \cdots * a}^{k})_n}{k!} = 0 \qquad \text{for all } n \in \mathbb{N}^2,$$

where λ_n is as in (2.8). Again, we choose $X = \ell^1_\nu$ for our Banach space. Fixing some $M \in \mathbb{N}$, we split the series in F in two parts, namely $F := F^{(M)} + F^{(\infty)}$, where, for $n \in \mathbb{N}^2$,

$$F^{(M)}_n(a) := \lambda_n a_n + \sum_{k=2}^{M} \frac{(\overbrace{a * \cdots * a}^{k})_n}{k!}, \qquad F^{(\infty)}_n(a) := \sum_{k=M+1}^{\infty} \frac{(\overbrace{a * \cdots * a}^{k})_n}{k!}.$$

We can compute all nonzero components of $F^{(M)}_n(\bar{a})$ for fixed M since $F^{(M)}_n(\bar{a})$ vanishes for $n \notin I^+_{MN^{\text{Gal}}}$. The norm of the tail term $F^{(\infty)}_n(\bar{a})$ we can estimate by

$$\|F^{(\infty)}(\bar{a})\|_\nu = \left\| \sum_{k=M+1}^{\infty} \frac{(\overbrace{\bar{a} * \cdots * \bar{a}}^{k})}{k!} \right\|_\nu \le \sum_{k=M+1}^{\infty} \frac{\|\bar{a}\|^k_\nu}{k!} = e^{\|\bar{a}\|_\nu} - \sum_{k=0}^{M} \frac{\|\bar{a}\|^k_\nu}{k!}, \tag{2.33}$$

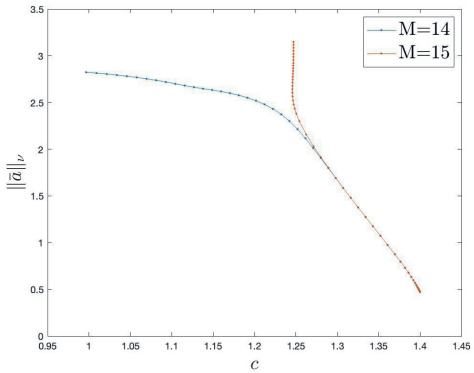


Figure 2.6.1: Influence of the parity of M. The code used to create this plot can be found in [78].

where the inequality follows from the triangle inequality and the Banach algebra property (2.11). Since $\bar{a}$ only has finitely many nonzero terms, we can compute $\|\bar{a}\|_\nu$, hence the right-hand side of (2.33) can be calculated.

Using this splitting of F, all bounds in Theorem 2.2.6 can be computed explicitly. For example, considering the Y-bound, instead of computing $\|AF(\bar{a})\|_\nu$, we use the triangle inequality to obtain

$$\begin{aligned}\|AF(\bar{a})\|_\nu &\leq \|AF^{(M)}(\bar{a})\|_\nu + \|AF^{(\infty)}(\bar{a})\|_\nu \\ &\leq \|AF^{(M)}(\bar{a})\|_\nu + \|A\|_{B(X)} \left(e^{\|\bar{a}\|_\nu} - \sum_{k=0}^{M} \frac{\|\bar{a}\|_\nu^k}{k!} \right). \end{aligned} \tag{2.34}$$

We can compute $\|AF^{(M)}(\bar{a})\|_\nu$ since $AF^{(M)}(\bar{a})$ has only finitely many nonzero terms (essentially following the same argument as for $F^{(M)}(\bar{a})$). The second term in (2.34) involves $\|A\|_{B(X)}$, which we can compute using (2.30), and the right-hand side of (2.33), which we also can compute, as explained earlier.

The computation of the Z-bound is similar to the Y-bound. First, DF is split into $DF^{(M)}$ and $DF^{(\infty)}$. The operator norm of the polynomial term $DF^{(M)}(\bar{a})$ is then evaluated by computer, whereas the norm of $DF^{(\infty)}(\bar{a})$ is estimated using the Banach algebra property. For the W-bound, we use the naive bound described in Section 2.4.3, i.e., $W = \|A\|_{B(X)} e^{\|\bar{a}\|_\nu + r^*}$.

This method is more straightforward to understand and implement in comparison with the technique using the discrete Fourier transform and the aliasing error bound in the previous sections. The method described in this section works well for wave speed values close to $\sqrt{2}$, where the amplitude of the solution is small and the Taylor expansion thus converges quickly. Approximating the solution becomes increasingly difficult for smaller values of the wave speed c, as the amplitude of the wave increases. In order to illustrate this, we created Figure 2.6.1 using numerical continuation. We depict (the norm of) the numerical approximation of a solution, where we performed the numerics with F replaced by $F^{(M)}$ for both $M = 14$ and

$M = 15$. Since the results are completely divergent for c smaller than roughly 1.25, for such values of c we know that the numerical zeros of $F^{(M)}$ are in fact not good approximations of a zero of F. Increasing M further did not improve the situation. Clearly then, approximating F by a Taylor polynomial $F^{(M)}$, which is essentially what we try to do in this section, already fails at the numerics level, hence attempting a proof based on the Taylor polynomial approximation will be futile.

We conclude that for $c \gtrsim 1.3$ the alternative approach in this section works nicely and it may even be preferable when studying solutions bifurcating from the uniform state. However, for smaller c, and corresponding larger wave profiles, the method based on the FFT is superior. Moreover, that method extends directly to analytic nonlinearities other than the exponential, and hence is more versatile in that respect as well.

Appendix 2.A Overview of computational parameters N

An overview of the different computational parameters N used throughout this chapter is presented here.

- N^{Gal}: As we can only compute finitely many Fourier coefficients, we choose a truncation dimension N^{Gal}. This determines how many (nonzero) Fourier coefficients we consider in our numerical approximation. Hence, we have that $\bar{a}_n = 0$ for $n \notin I^+_{N^{\mathrm{Gal}}}$.

- N^{Jac}: Using the computer, we calculate a finite part $D\Pi^{N^{\mathrm{Jac}}} F\left(\Pi^{N^{\mathrm{Jac}}} \bar{a}\right)$ of the full Jacobian. Increasing N^{Jac} can lead to a lower value for the Z-bound, which in turn increases the chances of obtaining a successful proof. Typically $N^{\mathrm{Jac}} = N^{\mathrm{Gal}}$ is chosen in implementations (see Remark 2.2.5), but this is not required. To solve our two-dimensional suspension bridge equation, we require that N^{Jac} satisfies the two inequalities in (2.9).

- N^{Alias}: We construct two methods for enclosing $\bar{b}_n = G_n(\bar{a})$. One of them can be used for general $n \in \mathbb{Z}^2$ (see Lemma 2.3.2) and the other one for $n \in I_{N^{\mathrm{Alias}}}$, which provides a tighter enclosure (at additional computational cost), see Lemma 2.3.5. Hence, N^{Alias} determines from which point on we use the general bound. For implementation purposes, we set $N^{\mathrm{Alias}} \geq N^{\mathrm{Jac}}$. We use the same choice of N^{Alias} for $\bar{b}$, $\bar{b}'$ and $\bar{b}''$.

- N^{FFT}: When applying the discrete (inverse) Fourier transformations we use $2N^{\mathrm{FFT}}$ discretization points or modes. In particular, this determines the size (and values) of $\bar{b}^{\mathrm{FFT}}_n$ in (2.21). We require that both N^{FFT}_1 and N^{FFT}_2 are powers of 2 for algorithmic reasons. Furthermore, we require $N^{\mathrm{FFT}} \gg N^{\mathrm{Alias}}$ to get tight enclosures on $\bar{b}_n$ for $n \in I^+_{N^{\mathrm{Alias}}}$.

- N^{Col}: We want to compute the norm $\|I - ADF(\bar{a})\|_{B(X)}$ in Section 2.4.2. For that purpose, we need to estimate $\|[I - ADF(\bar{a})]e_k\|_\nu$ for every k. We have two method for this, one for "small" k and one for "large" k. The switching point is at N^{Col}. We require that $N^{\mathrm{Col}} \geq N^{\mathrm{Jac}}$ for the analysis in Section 2.4.2.

- N^{Row}: To evaluate $\|[I - ADF(\bar{a})]e_k\|_\nu$, we analyze $([I - ADF(\bar{a})]e_k)_n$. As explained in the previous bullet point in this list, we have two ways of analyzing this depending on whether $k \in I_{N^{\mathrm{Col}}}$ or $k \notin I_{N^{\mathrm{Col}}}$. Likewise, we have two ways of analyzing $([I - ADF(\bar{a})]e_k)_n$ depending on whether n is "small" or "large" and the switching point is at N^{Row}. We require that $N^{\mathrm{Row}} \geq N^{\mathrm{Jac}}$ for the analysis in Section 2.4.2.

- N^{Tail}: When we estimate $([I - ADF(\bar{a})]e_k)_n$ uniformly for large k, we identify an intermediate range of values of n where we can use computational power to improve on the general estimate that holds for any large n. This intermediate range is denoted by N^{Tail} and we require $N^{\mathrm{Jac}} \leq N^{\mathrm{Tail}} \leq N^{\mathrm{Col}}$.

Appendix 2.B Estimation of the constant in Lemma 2.3.2

In this appendix, a lemma is proven stating an efficient procedure, based on the interval-valued discrete Fourier transform, for rigorously estimating the constant $C_{\bar\rho}$ defined in (2.15). Recalling (2.16), we can use these constants to estimate the constant $\widehat{C}_{\bar\rho}$ in Lemma 2.3.2 for bounding $\bar b_n$. Before stating the lemma and its proof, we introduce some notation.

As in Section 2.3.2 we choose a discrete Fourier transform with grid dimensions $N^{\mathrm{FFT}} \in \mathbb{N}^2$. It is not necessary that the choice is the same as in Section 2.3.2, although it is in our code. Assuming that $\bar a_n$ vanishes for $n \notin I_{N^{\mathrm{Gal}}}$, in this section we require that $N^{\mathrm{FFT}} > N^{\mathrm{Gal}}$, which is a different condition than the one in Section 2.3.2. We recall the notation

$$J_{N^{\mathrm{FFT}}} = \{-N_1^{\mathrm{FFT}} \le n_1 \le N_1^{\mathrm{FFT}} - 1, -N_2^{\mathrm{FFT}} \le n_2 \le N_2^{\mathrm{FFT}} - 1\},$$

and the uniform mesh (of the square $[-\pi,\pi]\times[-\pi,\pi]$).

$$x_{1,k_1} = \frac{\pi k_1}{N_1^{\mathrm{FFT}}}, \quad x_{2,k_2} = \frac{\pi k_2}{N_2^{\mathrm{FFT}}} \qquad \text{for } k \in J_{N^{\mathrm{FFT}}}.$$

Let $\square = \square_1 \times \square_2$ be the small rectangle with sides $\square_j = [0, \frac{\pi}{N_j^{\mathrm{FFT}}}]$, $j = 1, 2$. Then for $\delta \in \square$ we have, since $I_{N^{\mathrm{Gal}}} \subset J_{N^{\mathrm{FFT}}}$, that

$$\begin{aligned}\bar u(x_k + \delta - i\bar\rho) &= \sum_{n\in J_{N^{\mathrm{Gal}}}} \bar a_n e^{i(n_1(x_{1,k_1}+\delta_1 - i\bar\rho_1)+n_2(x_{2,k_2}+\delta_2 - i\bar\rho_2)} \\ &= \sum_{n\in J_{N^{\mathrm{FFT}}}} \bar a_n e^{n_1\bar\rho_1+n_2\bar\rho_2} e^{i(n_1\delta_1+n_2\delta_2)} e^{i(n_1 x_{1,k_1}+n_2 x_{2,k_2})}. \qquad (2.35)\end{aligned}$$

The right-hand side in (2.35) can be interpreted as the discrete Fourier transform of $\bar a^{\bar\rho,\delta}$, where

$$\bar a_n^{\bar\rho,\delta} := \bar a_n e^{n_1\bar\rho_1+n_2\bar\rho_2} e^{i(n_1\delta_1+n_2\delta_2)}.$$

By introducing the corresponding interval-valued sequence

$$\bar a_n^{\bar\rho,\square} := \bar a_n e^{n_1\bar\rho_1+n_2\bar\rho_2} e^{i(n_1\square_1+n_2\square_2)},$$

and its interval-valued discrete Fourier transform (evaluated efficiently using interval arithmetic)

$$\bar u_k^{\bar\rho,\square} := \sum_{n\in J_{N^{\mathrm{FFT}}}} \bar a_n^{\bar\rho,\square} e^{i(n_1 x_{1,k_1}+n_2 x_{2,k_2})},$$

we then have that

$$\bar u(x_k + \delta - i\bar\rho) \in \bar u_k^{\bar\rho,\square} \qquad \text{for all } \delta \in \square \quad \text{and} \quad k \in J_{N^{\mathrm{FFT}}}. \qquad (2.36)$$

We are now ready to state the lemma.

Lemma 2.B.1. *The constant $C_{\bar{\rho}}$ defined in* (2.15) *can be estimated via*

$$C_{\bar{\rho}} \leq \text{upperbound}\left(\frac{1}{4N_1^{\mathrm{FFT}}N_2^{\mathrm{FFT}}}\sum_{k\in J_{N^{\mathrm{FFT}}}}|\mathcal{G}(\bar{u}_k^{\bar{\rho},\square})|\right),$$

where the upper bound of the interval is taken.

Proof. Recalling (2.15) and (2.36), we have that

$$\begin{aligned}
C_{\bar{\rho}} &= \frac{1}{(2\pi)^2}\int_{-\pi}^{\pi}\int_{-\pi}^{\pi}|\mathcal{G}(\bar{u}(x_1-i\bar{\rho}_1,x_2-i\bar{\rho}_2))|dx_1dx_2\\
&= \frac{1}{(2\pi)^2}\sum_{k\in J_{N^{\mathrm{FFT}}}}\int_{x_{2,k_2}}^{x_{2,k_2+1}}\int_{x_{1,k_1}}^{x_{1,k_1+1}}|\mathcal{G}(\bar{u}(x_1-i\bar{\rho}_1,x_2-i\bar{\rho}_2))|dx_1dx_2\\
&\leq \frac{1}{4N_1^{\mathrm{FFT}}N_2^{\mathrm{FFT}}}\sum_{k\in J_{N^{\mathrm{FFT}}}}\sup_{\delta\in\square}\left|\mathcal{G}(\bar{u}(x_{1,k_1}+\delta_1-i\bar{\rho}_1,x_{2,k_2}+\delta_2-i\bar{\rho}_2))\right|\\
&\leq \text{upperbound}\left(\frac{1}{4N_1^{\mathrm{FFT}}N_2^{\mathrm{FFT}}}\sum_{k\in J_{N^{\mathrm{FFT}}}}|\mathcal{G}(\bar{u}_k^{\rho,\square})|\right).
\end{aligned}$$

□

Appendix 2.C Two-dimensional discrete Poisson summation formula

In this appendix, the two-dimensional discrete Poisson summation formula is proven for our case, which was used in Section 2.3.2. We assume that we are in the setting described there, hence in particular that $\mathcal{G}\circ\bar{u}$ is equal to its uniformly convergent Fourier series.

Lemma 2.C.1. *For $\bar{b}_n$, the Fourier coefficients of $\mathcal{G}\circ\bar{u}$, and $\bar{b}_n^{\mathrm{FFT}}$ as defined via* (2.18)*, we have the discrete Poisson summation formula*

$$\bar{b}_n^{\mathrm{FFT}} = \bar{b}_n + \sum_{\substack{j\in\mathbb{Z}^2\\(j_1,j_2)\neq(0,0)}}\bar{b}_{n+2jN^{\mathrm{FFT}}}, \qquad \text{for } n\in J_{N^{\mathrm{FFT}}}. \tag{2.37}$$

Proof. The proof mimics the proof for the one-dimensional variant in Section 6.2 of [11]. In our case, we consider the mesh given in (2.17). Then, we have that for $k\in J_{N^{\mathrm{FFT}}}$

$$\mathcal{G}\left(\bar{u}\left(x_{1,k_1},x_{2,k_2}\right)\right) = \sum_{j\in\mathbb{Z}^2}\bar{b}_j e^{i(j_1x_{1,k_1}+j_2x_{2,k_2})}.$$

Recalling (2.18), we obtain

$$\begin{aligned}\bar{b}_n^{\mathrm{FFT}} &= \frac{1}{4N_1^{\mathrm{FFT}}N_2^{\mathrm{FFT}}} \sum_{k\in J_{N^{\mathrm{FFT}}}} \mathcal{G}\left(\bar{u}\left(x_{1,k_1}, x_{2,k_2}\right)\right) e^{-in_1 x_{1,k_1} - in_2 x_{2,k_2}} \\ &= \frac{1}{4N_1^{\mathrm{FFT}}N_2^{\mathrm{FFT}}} \sum_{j\in\mathbb{Z}^2} \bar{b}_j \sum_{k\in J_{N^{\mathrm{FFT}}}} e^{ix_{1,k_1}(j_1-n_1)} e^{ix_{2,k_2}(j_2-n_2)} \\ &\overset{(2.17)}{=} \frac{1}{4N_1^{\mathrm{FFT}}N_2^{\mathrm{FFT}}} \sum_{j\in\mathbb{Z}^2} \bar{b}_j \sum_{k\in J_{N^{\mathrm{FFT}}}} e^{\frac{\pi i k_1}{N_1^{\mathrm{FFT}}}(j_1-n_1)} e^{\frac{\pi i k_2}{N_2^{\mathrm{FFT}}}(j_2-n_2)}.\end{aligned}$$

By using the geometric summation, we infer that $\sum_{k\in J_{N^{\mathrm{FFT}}}} e^{\frac{\pi i k_1}{N_1^{\mathrm{FFT}}}(j_1-n_1)} e^{\frac{\pi i k_2}{N_2^{\mathrm{FFT}}}(j_2-n_2)}$ vanishes unless $j_1 - n_1$ is a multiple of $2N_1^{\mathrm{FFT}}$ and $j_2 - n_2$ is a multiple of $2N_2^{\mathrm{FFT}}$. Hence,

$$\bar{b}_n^{\mathrm{FFT}} = \sum_{j\in\mathbb{Z}^2} \bar{b}_{n_1+2j_1N_1^{\mathrm{FFT}}, n_2+2j_2N_2^{\mathrm{FFT}}},$$

which can be rewritten to (2.37). □

3 Existence and orbital stability proofs of traveling wave solutions on an infinite strip for the suspension bridge equation

3.1 Introduction

The objective of this chapter is to prove the existence of traveling wave solutions of the two-dimensional suspension bridge equation on an infinite strip given by $\Omega \stackrel{\text{def}}{=} \mathbb{R} \times (-d_2, d_2)$ for $d_2 > 0$ and to prove orbital stability or instability. We let $v = v(t, X_1, X_2) : \mathbb{R}^+ \times \Omega \to \mathbb{R}$ represent the deflection in the downward direction of the surface of the bridge and we let $\Delta^2 = (\partial_{X_1}^2 + \partial_{X_2}^2)^2$. One of the systems used for modeling suspension bridges is (e.g. [20, 47])

$$\partial_t^2 v = -\Delta^2 v - e^v + 1. \tag{3.1}$$

Summaries of the historical development of different mathematical models for suspension bridges, both simplistic and advanced, are available in [23] and [28].

In the dynamics of the suspension bridge equation, traveling waves can be observed [9]. In order to look for such solutions, we introduce the parameter $c \in \mathbb{R}$ to denote the wave speed. We consider waves in the X_1-direction. Hence, we choose the traveling wave ansatz $v(t, X_1, X_2) = u(X_1 - ct, X_2) = u(x_1, x_2)$ such that the function $u : \Omega \to \mathbb{R}$ satisfies

$$\Delta^2 u + c^2 \partial_{x_1}^2 u + e^u - 1 = 0, \tag{3.2}$$

with $u(x) \to 0$ as $|x_1| \to \infty$. In the x_2 direction, we impose the following boundary conditions [79]

$$\partial_{x_2} u(\cdot, \pm d_2) = \partial_{x_2}^3 u(\cdot, \pm d_2) = 0. \tag{3.3}$$

We only consider values of c in $(0, \sqrt{2})$, because if c tends to zero, the amplitude of the waves grows to infinity, and for $c = 0$, nontrivial solutions do not longer exist [52]. Contrarily, if c approaches $\sqrt{2}$, the solutions become oscillatory as the amplitudes of the waves tend to go to zero [32].

We want to establish the existence of a solution $\tilde{u}$ to (3.2) on Ω. Numerical simulations of solutions to this equation, obtained via the Mountain Pass Algorithm,

This chapter reproduces the content of the published paper *Existence and orbital stability proofs of traveling wave solutions on an infinite strip for the suspension bridge equation* [77], co-authored with Matthieu Cadiot. Minor modifications have been made to match the formatting of this thesis.

are discussed in [32]. A rigorous existence proof for traveling wave solutions to (3.2) on finite domains, periodic in one direction and satisfying Neumann boundary conditions in the other, was later given in [79]. We combine the techniques and results outlined there with procedures developed in [16] and [17] to obtain an existence proof of a solution that decays to zero as $|x_1| \to \infty$.

Proving the existence of solutions to nonlinear partial differential equations (PDEs) on unbounded domains poses substantial analytical challenges. In particular, the loss of compactness in the resolvent of differential operators on unbounded domains complicates the application of standard existence theorems. In [49], this obstacle is overcome by rigorously controlling the spectrum of the linearization of an approximate solution resulting in methods for proving weak solutions to PDEs of second and fourth order. These methods are demonstrated for the Schrödinger equation on $\mathbb{R}^2$. That book also discusses the work of [51], where solutions to Emden's equation on an unbounded L-shaped domain are proven. Additionally, [86] verifies the existence of a weak solution to the Navier-Stokes equations on a perturbed infinite strip. While methods providing weak solutions are advantageous for certain applications, they do not naturally extend to the proof of strong solutions in the present context. We note that while strong solutions on bounded domains are addressed in [49], our focus is on the construction of strong solutions on an infinite strip.

In contrast, the previously mentioned papers [16] and [17] provide an approach for proving strong solutions on unbounded domains by introducing a new technique for constructing approximate inverses of PDE operators and proving compactness. In these works, solutions on unbounded domains are proven for equations with polynomial nonlinearities, specifically the Kawahara and Swift-Hohenberg equations. The techniques discussed in these papers need to be adjusted to be able to apply them to our suspension bridge equation that includes an exponential nonlinearity, which will be done in this chapter. Our approach is versatile in the sense that it can be extended to other analytic nonlinearities as well.

To deal with nonpolynomial terms such as the exponential term in (3.2), the method described in [25] can be used to control the aliasing error. In [66], it is demonstrated how to apply these techniques for working with nonpolynomial nonlinearities in one spatial dimension. The generalization to higher dimensions can be found in [79], in which specifically the suspension bridge equation is discussed, but only on bounded domains.

In this chapter, we construct an approximate solution $\bar{u} : \Omega \to \mathbb{R}$ to (3.2) and then prove the existence of a true solution to (3.2) in a vicinity of $\bar{u}$. An illustration of such an approximate solution $\bar{u}$, that we rigorously verify in Theorem 4.1.1, is depicted in Figure 3.1.1. The precise construction of $\bar{u}$ is explained in Section 3.3.1. The verification of such an approximate solution is done using a computer-assisted proof (CAP), a method that has gained significant interest in the rigorous verification of numerical simulations for dynamical systems over the past few decades. Early implementations of CAPs to the study of elliptic PDEs are seen in [48] and [53], stemming from 1988 and 1992, respectively. Later, advancements in the applications of CAPs to (elliptic) PDEs were made (e.g. [21, 22, 50, 62, 75, 88]).

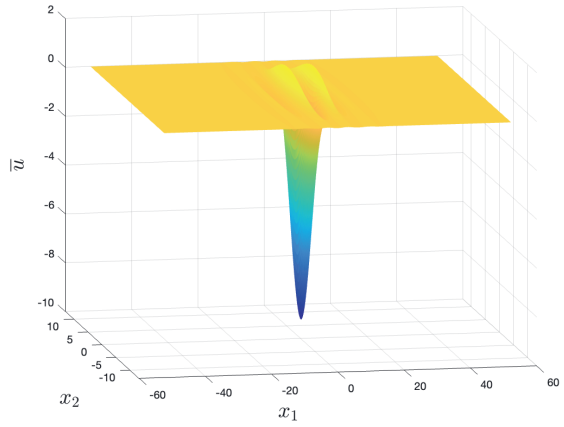


Figure 3.1.1: Visualization of an approximate solution $\bar{u}$ to (3.2) with $c = 1.2$. The approximation is truncated to a finite domain in this plot.

Comprehensive discussions on the role of CAPs in the study of PDEs are outlined in [30] and [49].

In particular, the setting in which we work allows us to utilize a Newton-Kantorovich-type theorem. These type of theorems are widely used in the construction of CAPs for PDEs and various other contexts (see for instance [8, 35, 68]). Specifically, we use a variant of this theorem called the radii polynomial theorem [22]. To prove existence on a bounded domain using this theorem, we need to compute certain bounds. To compensate for the fact that we are working on an unbounded domain, an additional bound is introduced and computed in this chapter. To guarantee the reliability of the computational components of the proof, we employ *Julia* interval arithmetic using the packages [31] and [58].

The solutions obtained in our CAPs will also be analyzed for stability. This part of the work is based on the procedure outlined in [47], where the authors investigate orbital stability of *one-dimensional* traveling wave solutions to the suspension bridge equation. Their analysis employs energy methods and spectral analysis to establish the stability results, supported by computer-assisted techniques. In two dimensions, to our knowledge, only numerical results concerning stability are available so far, which can be found in [32]. To rigorously handle the spectral properties of the higher-dimensional equation, we follow the framework proposed in [14]. Using this approach, we are able to conclude that the solution corresponding to the approximation in Figure 3.1.1 is orbitally stable.

The chapter is organized as follows. We begin by introducing notation and formulating the zero-finding problem. In Section 3.3, we present the Newton-Kantorovich theorem, which forms the foundation of our existence results. Moreover, we de-

scribe the construction of approximate solutions and provide more computational details. Section 3.4 presents the bounds required to apply the existence theorem. The set-up for the stability analysis is given in Section 3.5. Finally, the proof of the solution corresponding to the approximation shown in Figure 3.1.1 is given in Section 3.6, along with two additional existence results. All three proofs include verifications of orbital (in)stability.

3.2 Set-up

In this section, we introduce notation that will be used in the rest of the chapter. Part of the notation is borrowed from [16, 17] and adjusted to our setting of the suspension bridge equation.

3.2.1 Zero-finding problem for functions

Let $\mathbb{L}$ be the linear differential operator defined as

$$\mathbb{L} = \Delta^2 + c^2\partial_{x_1}^2 + I$$

where I is the identity and Δ is the Laplace operator. Moreover, let $\mathbb{G}$ be defined as $\mathbb{G}(u) = e^u - u - 1$. Then, (3.2) is equivalent to a zero finding problem $\mathbb{F}(u) = 0$ where

$$\mathbb{F}(u) = \mathbb{L}u + \mathbb{G}(u) = \Delta^2 u + c^2\partial_{x_1}^2 u + e^u - 1. \tag{3.4}$$

Note that by defining $\mathbb{G}$ as such we have that $\mathbb{G}(0) = 0$ and $D\mathbb{G}(0) = 0$. In particular, we look for a solution to (3.2) such that $u(x) \to 0$ as $|x_1| \to \infty$ and u satisfies boundary conditions (3.3). Taking advantage of the symmetries $u(x_1, x_2) = u(-x_1, x_2) = u(x_1, -x_2)$ allows us to represent u as a cosine series instead of a general Fourier series. Furthermore, assuming the symmetry in the x_1-direction avoids the degeneracy of the Jacobian operator that would otherwise arise from the shift invariance of the problem on the infinite strip. As a result, we choose the following ansatz

$$u(x_1, x_2) = u_0(x_1) + 2\sum_{n_2=1}^{\infty} u_{n_2}(x_1)\cos(2\pi\tilde{n}_2 x_2) \quad \text{with } \tilde{n}_2 \stackrel{\text{def}}{=} \frac{n_2}{2d_2}, \tag{3.5}$$

and where $u_{n_2} : \mathbb{R} \to \mathbb{R}$ and u_{n_2} is even. Corresponding to (3.5), we define L_e^2 as the following Hilbert space of L^2 even functions on the strip Ω:

$$L_e^2 \stackrel{\text{def}}{=} \Big\{ u \in L^2(\Omega) \mid u(x_1, x_2) = u_0(x_1) + 2\sum_{n_2 \in \mathbb{N}} u_{n_2}(x_1)\cos(2\pi\tilde{n}_2 x_2), \\ \text{subject to } u_{n_2}(x_1) = u_{n_2}(-x_1) \Big\},$$

where

$$\|u\|_2 \stackrel{\text{def}}{=} \left(\|u_0\|_{L^2(\mathbb{R})}^2 + 2\sum_{n_2 \in \mathbb{N}} \|u_{n_2}\|_{L^2(\mathbb{R})}^2 \right)^{\frac{1}{2}}.$$

Now, given $u \in L_e^2$ regular enough, we have that

$$\mathbb{L}u(x) = \mathbb{L}_0 u_0(x_1) + 2\sum_{n_2 \in \mathbb{N}} \mathbb{L}_{n_2} u_{n_2}(x_1)\cos\left(2\pi \tilde{n}_2 x_2\right)$$

for all $x \in \Omega$, where

$$\mathbb{L}_{n_2} \stackrel{\text{def}}{=} \left(-\frac{n_2^2\pi^2}{d_2^2} + \partial_{x_1}^2\right)^2 + c^2\partial_{x_1}^2 + I$$

for all $n_2 \in \mathbb{N}_0$. In particular, note that for $c \in (0, \sqrt{2})$, the symbol $l_{n_2}(\xi_1)$ is strictly positive and bounded away from zero for all $\xi_1 \in \mathbb{R}$ (see Lemma 3.A.1. Thus, $\mathbb{L}_{n_2} : H^4(\mathbb{R}) \to L^2(\mathbb{R})$ is bijective with a bounded inverse. Consequently, similarly as what was achieved in [16] and [17], we can define the Hilbert space $\mathcal{H}$ as follows:

$$\mathcal{H} \stackrel{\text{def}}{=} \{u \in L_e^2,\ \|u\|_{\mathcal{H}} \stackrel{\text{def}}{=} \|\mathbb{L}u\|_2 < \infty\}.$$

In addition, we see that

$$\|u\|_{\mathcal{H}} = \left(\|\mathbb{L}_0 u_0\|_2^2 + 2\sum_{n_2=1}^{\infty} \|\mathbb{L}_{n_2} u_{n_2}\|_2^2\right)^{\frac{1}{2}}.$$

Using the bijectivity of the individual components $\mathbb{L}_{n_2}$, we have that $\mathbb{L} : \mathcal{H} \to L_e^2$ is an isometric isomorphism and hence bijective as well. Moreover, we define $l : \mathbb{R}^2 \to \mathbb{R}$ as the symbol of $\mathbb{L}$ and $l_{n_2} : \mathbb{R} \to \mathbb{R}$ as the one of $\mathbb{L}_{n_2}$ for all $n_2 \in \mathbb{N}_0$. Specifically, we have that

$$l(\xi) \stackrel{\text{def}}{=} |2\pi\xi|^4 - c^2(2\pi\xi_1)^2 + 1 \quad \text{and} \quad l_{n_2}(\xi_1) \stackrel{\text{def}}{=} (2\pi)^4(\xi_1^2 + \tilde{n}_2^2)^2 - c^2(2\pi\xi_1)^2 + 1 \tag{3.6}$$

where we recall that $\tilde{n}_2 \stackrel{\text{def}}{=} \frac{n_2}{2d_2}$.

Remark 3.2.1. *Note that one could impose different boundary conditions in the x_2-direction. For instance, a variational formulation of* (3.2) *leads to natural "free" boundary conditions which read $\Delta u(\cdot, \pm d_2) = \partial_{x_2}\Delta u(\cdot, \pm d_2) = 0$. However, these conditions do not allow to use Fourier series in the x_2-direction (in contrast to* (3.5)*), which leads to technical and computational challenges in the current approach. This hurdle might be addressed using a different expansion in the x_2 direction (such as a polynomial expansion), and would require an adaptation of the presented analysis.*

Now, it remains to prove that $\mathbb{G} : \mathcal{H} \to L_e^2$ is well defined in order to formulate (3.2) on $\mathcal{H}$. For that purpose, we use the following result:

Lemma 3.2.2. *Let κ_1, κ_2 be defined as follows:*

$$\kappa_1 \stackrel{\text{def}}{=} \frac{1}{1 - \frac{c^4}{4}} \quad \textit{and} \quad \kappa_2 \stackrel{\text{def}}{=} \left(\left\|\frac{1}{l_0}\right\|_{L^2(\mathbb{R})}^2 + 2\sum_{n_2 \in \mathbb{N}} \left\|\frac{1}{l_{n_2}}\right\|_{L^2(\mathbb{R})}^2\right)^{\frac{1}{2}}. \tag{3.7}$$

Then, for all $u, v \in \mathcal{H}$, we have that

$$\|(e^u - 1)v\|_2 \leq \kappa_1(e^{\kappa_2\|u\|_{\mathcal{H}}} - 1)\|v\|_{\mathcal{H}}.$$

Proof. First, we notice that

$$\|(e^u - 1)v\|_2 \leq \|e^u - 1\|_\infty \|v\|_2.$$

Then, we have

$$\|e^u - 1\|_\infty \leq e^{\|u\|_\infty} - 1.$$

It remains to prove that $\|u\|_\infty \leq \kappa_2 \|u\|_{\mathcal{H}}$ and $\|v\|_2 \leq \kappa_1 \|v\|_{\mathcal{H}}$. Using the proof of Lemma 2.1 in [16], we obtain that

$$\|u\|_\infty \leq \left(\left\| \frac{1}{l_0} \right\|^2_{L^2(\mathbb{R})} + 2 \sum_{n_2 \in \mathbb{N}} \left\| \frac{1}{l_{n_2}} \right\|^2_{L^2(\mathbb{R})} \right)^{\frac{1}{2}} \|u\|_{\mathcal{H}},$$

$$\|v\|_2 \leq \max_{n_2 \in \mathbb{N}_0} \sup_{\xi_1 \in \mathbb{R}} \left| \frac{1}{l_{n_2}(\xi_1)} \right| \|v\|_{\mathcal{H}}.$$

We conclude the proof using (3.58) from Lemma 3.A.1. □

Remark 3.2.3. *In practice, for the computation of κ_2, we use Riemann summations to bound the summation up to finitely many n_2. In fact, this can be achieved using rigorous numerics (cf. [76]). To estimate the tail of the summation, we use* (3.59) *in Lemma 3.A.1.*

Using the embedding of $\mathcal{H}$ into $L^\infty(\Omega)$ established in Lemma 3.2.2 and the analyticity of the exponential function, it follows that $\mathbb{G} : \mathcal{H} \to L^2_e$ is a Fréchet differentiable mapping. Accordingly, we investigate the solution of the following zero-finding problem

$$\mathbb{F}(u) = 0 \quad \text{for } u \in \mathcal{H}, \tag{3.8}$$

where $\mathbb{F} : \mathcal{H} \to L^2_e$.

3.2.2 Fourier series representation

As described in [16], existence proofs of localized solutions can be achieved using approximations of the true solution in Fourier space. Following such an approach, we introduce notation corresponding to Fourier series, related to the ones introduced in the previous section. Let $d_1 > 0$ and let $\Omega_0 \stackrel{\text{def}}{=} (-d_1, d_1) \times (-d_2, d_2)$ be the bounded domain on which our approximate solution is constructed. We let $\mathbb{N}_0^2 = (\mathbb{N} \cup \{0\})^2$ and we define

$$\alpha_n = \alpha_{n_1,n_2} := \begin{cases} 1 & \text{for } n_1 = n_2 = 0, \\ 2 & \text{for } n_1 = 0, n_2 > 0, \\ 2 & \text{for } n_1 > 0, n_2 = 0, \\ 4 & \text{for } n_1 > 0, n_2 > 0 \end{cases} \tag{3.9}$$

for all $n \in \mathbb{N}_0^2$. The coefficients α_n appear when switching between the cosine series representation and the exponential Fourier series one. Let ℓ^p denote the Lebesgue

space for sequences defined as

$$\ell^p \stackrel{\text{def}}{=} \left\{ U = (U_n)_{n\in\mathbb{N}_0^2} : \ \|U\|_p \stackrel{\text{def}}{=} \left(\sum_{n\in\mathbb{N}_0^2} \alpha_n |U_n|^p \right)^{\frac{1}{p}} < \infty \right\}.$$

Then, operators $\mathbb{L}$ and $\mathbb{G}$ have a Fourier coefficients representation, when being considered on Ω_0 with periodicity in the x_1-direction. Indeed, defining

$$\tilde{n} = (\tilde{n}_1, \tilde{n}_2) = \left(\frac{n_1}{2d_1}, \frac{n_2}{2d_2} \right),$$

we introduce L, the Fourier coefficients representation of $\mathbb{L}$, as

$$(LU)_n = l(\tilde{n})U_n \text{ for all } n \in \mathbb{N}_0^2$$

and all $U \in \ell^2$. Then, we define $U * V$ as the discrete convolution for sequences indexed on $\mathbb{N}_0^2$, given as

$$(U * V)_n = \sum_{m\in\mathbb{Z}^2} U_{|m|} V_{|n-m|}$$

for $n \in \mathbb{N}_0^2$. Note that Young's convolution inequality holds true for this convolution product, i.e., for $U \in \ell^2$ and $V \in \ell^1$, we have that

$$\|U * V\|_2 \leq \|U\|_2 \|V\|_1. \tag{3.10}$$

Moreover, given $U \in \ell^1$, we define e^U as

$$e^U \stackrel{\text{def}}{=} \sum_{k=0}^{\infty} \frac{U^k}{k!}, \tag{3.11}$$

where $U^k = \overbrace{U * U * \cdots * U}^{k \text{ times}}$. Consequently, we define $G : \ell^1 \to \ell^2$ as the equivalent of $\mathbb{G}$ as

$$G(U) \stackrel{\text{def}}{=} e^U - U - e_0,$$

where $(e_0)_n = 1$ if $n = (0,0)$ and $(e_0)_n = 0$ for all $n \in \mathbb{N}^2 \setminus \{0,0\}$. Since ℓ^1 is a Banach algebra under the discrete convolution product and because of (3.11), $e^U \in \ell^1$, and thus in ℓ^2, for any $U \in \ell^1$, which ensures the operator is well-defined on the sequence space. Finally, we define the zero finding counterpart $F : \ell^1 \to \ell^2$ on Ω_0 as

$$F(U) \stackrel{\text{def}}{=} LU + G(U).$$

Now, as in [16] and [17], we introduce operators which allow us to switch from L_e^2 to ℓ^2 and vice versa. Therefore, we define $\gamma : L_e^2 \to \ell^2$ and $\gamma^\dagger : \ell^2 \to L_e^2$ such that

$$\begin{aligned} (\gamma(u))_n &= \frac{1}{|\Omega_0|} \int_{\Omega_0} u(x_1, x_2) e^{-2\pi i \tilde{n}\cdot x} dx \quad \text{for } n \in \mathbb{N}_0^2, \\ \gamma^\dagger(U)(x) &= \mathbb{1}_{\Omega_0}(x) \sum_{n\in\mathbb{N}_0^2} \alpha_n U_n \cos(2\pi\tilde{n}_1 x_1) \cos(2\pi\tilde{n}_2 x_2), \end{aligned}$$

where $\mathbb{1}_{\Omega_0}$ denotes the characteristic function on Ω_0.

Now, given X a Banach space, we denote $\mathcal{B}(X)$ as the set of bounded linear operators on X. Then, we define $\Gamma : \mathcal{B}(L_e^2) \to \mathcal{B}(\ell^2)$ and $\Gamma^\dagger : \mathcal{B}(\ell^2) \to \mathcal{B}(L_e^2)$ as

$$\Gamma(\mathbb{H}) = \gamma \mathbb{H} \gamma^\dagger \quad \text{and} \quad \Gamma^\dagger(H) = \gamma^\dagger H \gamma \tag{3.12}$$

for all bounded linear operators $\mathbb{H} \in \mathcal{B}(L_e^2)$ and $H \in \mathcal{B}(\ell^2)$. The map $\Gamma^\dagger$ will be useful when constructing operators on $\mathcal{B}(L_e^2)$ thanks to operators on Fourier coefficients (that is, operators on $\mathcal{B}(\ell^2)$). Furthermore, we introduce the norm $\|\cdot\|_{2,\mathcal{H}}$ to denote the operator norm for bounded linear operators $L_e^2 \to \mathcal{H}$.

Finally, given $u \in L^\infty, U \in \ell^1$, we introduce notation to denote the linear multiplication operator $\mathbb{M}_u$ related to the function u and the linear discrete convolution operator $\mathbb{M}_U$ related to the sequence U as

$$\mathbb{M}_u : L_e^2 \to L_e^2 : v \mapsto \mathbb{M}_u v = uv \quad \text{and} \quad \mathbb{M}_U : \ell^2 \to \ell^2 : V \mapsto \mathbb{M}_U V = U * V. \tag{3.13}$$

3.3 Constructive proof of existence

In this section, we present our approach for proving constructively the existence of solutions to (3.2). Our approach is based on a Newton-Kantorovich theorem. More specifically, we construct a fixed point operator for which fixed points correspond to zeros of $\mathbb{F}$.

First, we construct an approximate solution $\bar{u} \in \mathcal{H}$ thanks to its Fourier coefficients representation. The technical construction of $\bar{u}$ is described in Section 3.3.1. Given $\bar{u}$, we then construct an injective $\mathbb{A} : L_e^2 \to \mathcal{H}$ as an approximate inverse for the Fréchet derivative $D\mathbb{F}(\bar{u})$. Then, our goal is to determine a radius $r > 0$ such that $\mathbb{T}$, given as

$$\mathbb{T}(u) \stackrel{\text{def}}{=} u - \mathbb{A}\mathbb{F}(u),$$

is well defined on $\overline{B_r(\bar{u})} \to \overline{B_r(\bar{u})}$ and contracting (where $B_r(\bar{u})$ is the open ball of $\mathcal{H}$ centered at $\bar{u}$ and of radius r). The Banach fixed point theorem then provides the existence of a unique zero of $\tilde{u} \in \mathcal{H}$ of $\mathbb{F}$ in $\overline{B_r(\bar{u})}$.

In order to verify the existence of such a radius r, we make use of the following result. Its proof is for instance given in [16].

Theorem 3.3.1. *Let $\mathbb{F} : \mathcal{H} \to L_e^2$ be given as in (3.4) and let $\mathbb{A} : L_e^2 \to \mathcal{H}$ be a bounded linear operator. Assume that $\mathcal{Y}_0, \mathcal{Z}_1 \in (0, \infty)$ and let $\mathcal{Z}_2 : (0, \infty) \to [0, \infty)$ satisfy*

$$\|\mathbb{A}\mathbb{F}(\bar{u})\|_{\mathcal{H}} \leq \mathcal{Y}_0, \tag{3.14}$$

$$\|I - \mathbb{A}D\mathbb{F}(\bar{u})\|_{\mathcal{H}} \leq \mathcal{Z}_1, \tag{3.15}$$

$$\|\mathbb{A}(D\mathbb{F}(\bar{u}+h) - D\mathbb{F}(\bar{u}))\|_{\mathcal{H}} \leq \mathcal{Z}_2(r)r \quad \text{for all } h \in \overline{B_r(0)} \subset \mathcal{H} \text{ and all } r > 0. \tag{3.16}$$

If there exists $r > 0$ such that

$$\frac{1}{2}\mathcal{Z}_2(r)r^2 - (1 - \mathcal{Z}_1)r + \mathcal{Y}_0 < 0 \text{ and } \mathcal{Z}_1 + \mathcal{Z}_2(r)r < 1, \tag{3.17}$$

then there exists a unique $\tilde{u} \in \overline{B_r(\bar{u})} \subset \mathcal{H}$ *for which* $\mathbb{F}(\tilde{u}) = 0$.

Observe that we have transformed our problem into computing explicit values for the bounds $\mathcal{Y}_0, \mathcal{Z}_1, \mathcal{Z}_2$ of the previous theorem. Then, a value for the radius $r > 0$ is obtained thanks to (3.17).

The core of our approach becomes determining $\bar{u} \in \mathcal{H}$ and $\mathbb{A} : L^2_e \to \mathcal{H}$ such that the bounds of Theorem 3.3.1 can be computed explicitly. We describe the construction of these objects in the next sections.

3.3.1 Construction of an approximate solution

First, we demonstrate how to construct the approximate solution $\bar{u} \in \mathcal{H}$. Our approach is based on that presented in [15, 16, 17]. We construct $\bar{u}$ using a cosine-cosine series representation on $\Omega_0 = (-d_1, d_1) \times (-d_2, d_2)$ as

$$\bar{u}(x) \stackrel{\text{def}}{=} \mathbb{1}_{\Omega_0}(x) \sum_{n \in \mathbb{N}_0^2} \alpha_n \bar{U}_n \cos\left(2\pi \tilde{n}_1 x_1\right) \cos\left(2\pi \tilde{n}_2 x_2\right) \tag{3.18}$$

where $\bar{U} = (\bar{U}_n)_{n \in \mathbb{N}_0^2}$ is the Fourier coefficients representation of $\bar{u}$. Note that by construction $\operatorname{supp}(\bar{u}) \subset \overline{\Omega_0}$. The sequence $\bar{U}$ is determined numerically and contains a finite number of non-zero coefficients. In order to describe our numerical truncations, we define projection operators: given $\mathcal{N} = (\mathcal{N}_1, \mathcal{N}_2) \in \mathbb{N}^2$,

$$\left(\pi^{\mathcal{N}}(U)\right)_n = \begin{cases} U_n & \text{for } n \in I_{\mathcal{N}}, \\ 0 & \text{for } n \notin I_{\mathcal{N}} \end{cases} \quad \text{and} \quad \left(\pi_{\mathcal{N}}(U)\right)_n = \begin{cases} 0 & \text{for } n \in I_{\mathcal{N}}, \\ U_n & \text{for } n \notin I_{\mathcal{N}}. \end{cases} \tag{3.19}$$

where $I_{\mathcal{N}} \stackrel{\text{def}}{=} \{n \in \mathbb{N}_0^2 : 0 \le n_1 \le \mathcal{N}_1, 0 \le n_2 \le \mathcal{N}_2\}$.

Let us fix $N^0 = (N_1^0, N_2^0) \in \mathbb{N}^2$ to be the numerical truncation size of $\bar{U}$. Then, using (3.19), we assume that $\bar{U} = \pi^{N^0} \bar{U}$. That is, $\bar{U}$ has a vector representation of size $(N_1^0 + 1)(N_2^0 + 1)$.

Now, note that by construction $\bar{u} \in L^2_e$, but we do not necessarily have $\bar{u} \in \mathcal{H}$. Indeed, $\bar{u}$ might not be smooth at $x_1 = \pm d_1$. By periodicity of $\bar{u}$ on Ω_0, smoothness at $x_1 = \pm d_1$ is equivalent to smoothness only at d_1. Now, in order to obtain the required regularity for $\mathcal{H}$, we need

$$\partial_{x_1}^k \bar{u}(d_1, x_2) = 0 \text{ for all } x_2 \in (-d_2, d_2) \text{ and all } k \in \{0, 1, 2, 3\}.$$

Since $\bar{u}$ has a cosine-cosine representation, we readily have $\partial_{x_1}^k \bar{u}(d_1, x_2) = 0$ for all $x_2 \in (-d_2, d_2)$ and all $k \in \{1, 3\}$. Consequently, it remains to ensure that

$$\partial_{x_1}^k \bar{u}(d_1, x_2) = 0 \text{ for all } x_2 \in (-d_2, d_2) \text{ and all } k \in \{0, 2\}. \tag{3.20}$$

As $\bar{u}$ is represented by $\bar{U}$ on Ω_0, (3.20) can be translated to equations on $\bar{U}$:

$$\sum_{n_1 = -N_1^0}^{N_1^0} \alpha_{n_1, n_2} (-1)^{n_1} (2\pi \tilde{n}_1)^k \bar{U}_{n_1, n_2} = 0 \text{ for all } n_2 \in -N_2^0, \ldots, N_2^0 \text{ and all } k \in \{0, 2\},$$

where we have used that $\bar{U} = \pi^N \bar{U}$. Note that this is equivalent to $\bar{U} \in \mathrm{Ker}(\mathcal{T})$, where

$$\mathcal{T}\bar{U} = \begin{pmatrix} \mathcal{T}_0 \bar{U} \\ \mathcal{T}_2 \bar{U} \end{pmatrix} \overset{\text{def}}{=} \begin{pmatrix} \left(\sum_{n_1=-N_1^0}^{N_1^0} \alpha_{n_1,n_2} (-1)^{n_1} \bar{U}_{n_1,n_2} \right)_{n_2 \in -N_2^0,\dots,N_2^0} \\ \left(\sum_{n_1=-N_1^0}^{N_1^0} \alpha_{n_1,n_2} (-1)^{n_1} (2\pi \tilde{n}_1)^2 \bar{U}_{n_1,n_2} \right)_{n_2 \in -N_2^0,\dots,N_2^0} \end{pmatrix}.$$

Consequently, $\bar{U}$ needs to be projected into the kernel of the matrix $\mathcal{T}$ of size $(2N_1^0+1)(2N_2^0+1)$. Such an operation has been described in [16, 17] and is implemented in [76].

Overall, we ensure that $\bar{U} \in \mathrm{Ker}(\mathcal{T})$ and obtain that

$$\bar{u} \overset{\text{def}}{=} \gamma^\dagger \left(\bar{U} \right) \in \mathcal{H} \quad \text{and} \quad \bar{U} = \pi^N \bar{U}. \tag{3.21}$$

By construction, we have $\mathrm{supp}(\bar{u}) \subset \Omega_0$.

Now that $\bar{u}$ has been constructed, one of the major difficulties in the treatment of (3.2) is the evaluation of the nonpolynomial nonlinearity $e^{\bar{u}}$. Indeed, in order to evaluate the bound $\mathcal{Y}_0$ (3.14), we need to be able to compute rigorously such a quantity. This is the objective of the next section.

3.3.2 Computing the nonlinearity

The existence proof requires the computation of the nonlinear part given by $G(U) = e^U - U - e_0$. However, the Fourier coefficients corresponding to the exponential function cannot be determined exactly, as there are infinitely many nonzero Fourier coefficients. Moreover, even the computation of a finite number of Fourier coefficients cannot be performed exactly due to the nonpolynomial nature of the nonlinearity. For small indices, we approximate these coefficients using discrete Fourier transforms and establish an upper bound on the associated error, referred to as the aliasing error. For larger indices, we use a general bound, which is only suitable for the tail part because of the decay of the bound. To compute the Fourier coefficients of $G(\bar{U})$, we first determine the Fourier coefficients $e^{\bar{U}}$ corresponding to the function $e^{\bar{u}}$. Following the procedure outlined in Section 3 of [79], we obtain the expression:

$$\left(e^{\bar{U}} \right)_n \in \begin{cases} (e^{\bar{U}})_n^{\mathrm{FFT}} + C[-\varepsilon_n, \varepsilon_n] & \text{if } 0 \le n_1 \le N_1^0, 0 \le n_2 \le N_2^0, \\ [-\frac{C}{\nu_1^{|n_1|} \nu_2^{|n_2|}}, \frac{C}{\nu_1^{|n_1|} \nu_2^{|n_2|}}] & \text{otherwise} \end{cases} \tag{3.22}$$

where $(e^{\bar{U}})^{\mathrm{FFT}}$ is the numerical approximation of $e^{\bar{U}}$ calculated using discrete Fourier transforms, $C > 0$, $\nu_1, \nu_2 > 1$ and $\varepsilon_n > 0$ for all n. The procedure of computing C can be found in [79]. The parameters ν_1, ν_2 are related to the domain of analyticity, i.e., $\bar{U}$ is analytic on a strip $\{z \in \mathbb{C}^2 : \mathrm{Im}(z_1) < \rho_1, \mathrm{Im}(z_2) < \rho_2\}$ and $\nu_1 = e^{\rho_1 - \overline{\varepsilon}_1}$, $\nu_2 = e^{\rho_2 - \overline{\varepsilon}_2}$ for small $\overline{\varepsilon}_1, \overline{\varepsilon}_2 > 0$ (cf. Section 3.1 in [79]). Note that $G(\bar{U})$ is analytic for $\bar{U}$ analytic.

Moreover, let N^{FFT} denote how many Fourier modes are considered when doing Fourier transformations such that N_1^{FFT} and N_2^{FFT} are powers of 2 and such that

$N^{\mathrm{FFT}} \gg N^0$. Then we have

$$\varepsilon_n := \frac{2\nu_1^{|n_1|}\nu_2^{|n_2|}\left(\nu_1^{-2N_1^{\mathrm{FFT}}} + \nu_2^{-2N_2^{\mathrm{FFT}}}\right)}{\left(1-\nu_1^{-2N_1^{\mathrm{FFT}}}\right)\left(1-\nu_2^{-2N_2^{\mathrm{FFT}}}\right)}.$$

Remark 3.3.2. *Note that the support of $\bar{u}$ is on $\overline{\Omega_0}$, which is a finite domain. As a consequence, $\mathbb{G}(\bar{u})$ also has its support on $\overline{\Omega_0}$. Therefore, the actual representation of the nonlinear term is on the infinite strip, even though Fourier transformations are carried out on finite domains only.*

3.3.3 Approximate inverse

In order to be able to apply Theorem 3.3.1, it remains to construct an approximate inverse $\mathbb{A}$ for $D\mathbb{F}(\bar{u})$. For this purpose, we recall the construction established in [16]. Let $N = (N_1, N_2) \in \mathbb{N}^2$ be the numerical truncation size of our operators. In practice, we choose $N_1 \leq N_1^0$ and $N_2 \leq N_2^0$, where N^0 is the size of the numerical truncation of $\bar{U}$.

Numerically, we construct a "matrix" B^N, which approximates the inverse of $\pi^N DF(\bar{U})L^{-1}\pi^N$. In particular, B^N is finite-dimensional in the sense that we have $B^N = \pi^N B^N \pi^N$. Then, using (3.12), we define $\mathbb{B} : L^2_e \to L^2_e$ as

$$\mathbb{B} \overset{\text{def}}{=} \mathbb{1}_{\Omega\setminus\Omega_0} + \Gamma^\dagger(\pi_N + B^N).$$

Here, $\mathbb{1}_{\Omega\setminus\Omega_0}$ has to be understood as a multiplication operator by the characteristic function $\mathbb{1}_{\Omega\setminus\Omega_0}$. In particular, $\mathbb{B}$ approximates the inverse of $D\mathbb{F}(\bar{u})\mathbb{L}^{-1}$. Finally, we define $\mathbb{A}$ as

$$\mathbb{A} \overset{\text{def}}{=} \mathbb{L}^{-1}\mathbb{B} = \mathbb{L}^{-1}\left(\mathbb{1}_{\Omega\setminus\Omega_0} + \Gamma^\dagger(\pi_N + B^N)\right) : L^2_e \to \mathcal{H}. \tag{3.23}$$

Note that $\mathbb{A}$ is well defined as $\mathbb{L} : \mathcal{H} \to L^2_e$ is an isometric isomorphism. Computing the bound $\mathcal{Z}_1$ defined in (3.15), we will show that (3.23) is an accurate choice for an approximate inverse. In particular, it is well suited for our analysis since it allows us to compute the bounds of Theorem 3.3.1 explicitly. This will be the goal of the next section. We can already recall a result from [16] providing the operator norm of $\mathbb{A}$ thanks to the norm of the matrix B^N:

$$\|\mathbb{A}\|_{2,\mathcal{H}} = \|\mathbb{B}\|_2 = \max\{1, \|B^N\|_2\}. \tag{3.24}$$

3.4 Computation of the bounds

In this section, we justify our choices for the approximate objects constructed above by providing explicit formulas for the bounds of Theorem 3.3.1. Before stating the first bound, we recall that N^0 corresponds to the truncation dimension for sequences and N for operators.

Lemma 3.4.1 (Bound $\mathcal{Y}_0$). *Let $\mathcal{Y}_0$ be satisfying*

$$\mathcal{Y}_0 \geq \sqrt{2d_1}\Bigg(\|B^N F(\bar{U})\|_2^2 + \|(\pi^{N^0} - \pi^N)(L\bar{U} + G(\bar{U}))\|_2^2 + C^2 \frac{2\nu_1^{-2N_1^0-2}(1+\nu_2^{-2}) + 2\nu_2^{-2N_2^0-2}(1+\nu_1^{-2}) - 4\nu_1^{-2N_1^0-2}\nu_2^{-2N_2^0-2}}{(1-\nu_1^{-2})(1-\nu_2^{-2})}\Bigg)^{\frac{1}{2}}.$$

Then $\mathcal{Y}_0$ satisfies (3.14).

Proof. As $\mathrm{supp}(\bar{u}) \subset \overline{\Omega_0}$, we have that $\mathrm{supp}(\mathbb{G}(\bar{u})) \subset \overline{\Omega_0}$ since $e^u - u - 1 = \sum_{k=2}^{\infty} \frac{u^k}{k!}$. Hence, we can apply Parseval's identity and follow the proof of Lemma 4.11 in [16] to obtain

$$\|\mathbb{A}\mathbb{F}(\bar{u})\|_{\mathcal{H}} = \|\mathbb{L}\mathbb{A}\mathbb{F}(\bar{u})\|_2 = \|\mathbb{B}\mathbb{F}(\bar{u})\|_2 = \sqrt{2d_1}\|BF(\bar{U})\|_2$$

where

$$\|BF(\bar{U})\|_2^2 = \|B^N F(\bar{U})\|_2^2 + \|(\pi^{N^0} - \pi^N)L\bar{U} + \pi_N G(\bar{U})\|_2^2. \tag{3.25}$$

Note that the nonlinear part of $F(\bar{U})$ in $\|B^N F(\bar{U})\|_2^2$ can be calculated and bounded using (3.22).

For the second term in the right-hand side of (3.25) we write

$$\|(\pi^{N^0} - \pi^N)L\bar{U} + \pi_N G(\bar{U})\|_2^2 \leq \|(\pi^{N^0} - \pi^N)(L\bar{U} + G(\bar{U}))\|_2^2 + \sum_{n \notin I_{N^0}} \alpha_n \frac{C^2}{\nu_1^{2|n_1|}\nu_2^{2|n_2|}}.$$

The last summation can be calculated using a geometric series argument as was done in Lemma 3.4 of [79]. Hence,

$$\sum_{n \notin I_{N^0}} \alpha_n \frac{C^2}{\nu_1^{2|n_1|}\nu_2^{2|n_2|}} = C^2 \frac{2\nu_1^{-2N_1^0-2}(1+\nu_2^{-2}) + 2\nu_2^{-2N_2^0-2}(1+\nu_1^{-2}) - 4\nu_1^{-2N_1^0-2}\nu_2^{-2N_2^0-2}}{(1-\nu_1^{-2})(1-\nu_2^{-2})}.$$

□

Remark 3.4.2. *Note that for the second term in the $\mathcal{Y}_0$-bound, we can use* (3.22) *to state the interval that contains this term as follows:*

$$\|(\pi^{N^0} - \pi^N)(L\bar{U} + G(\bar{U}))\|_2^2 \in \sum_{\substack{n \in I_{N^0} \\ n \notin I_N}} \alpha_n \left(l\left(\frac{n}{2d}\right)\bar{U}_n + (e^{\bar{U}})_n^{\mathrm{FFT}} + C[-\varepsilon_n, \varepsilon_n]\right)^2.$$

The right-hand side is what is used in the (interval arithmetic) computation of the $\mathcal{Y}_0$-bound in [76].

We now turn to the computation of $\mathcal{Z}_2(r)$.

Lemma 3.4.3 (Bound $\mathcal{Z}_2$). *Let $r > 0$ and let $\mathcal{Z}_2(r)$ be satisfying*

$$\mathcal{Z}_2(r) \geq \kappa_1 \frac{e^{\kappa_2 r} - 1}{r} \max\left\{ \|Be^{\mathbb{M}_{\bar{U}}}\|_2, 1 \right\},$$

where κ_1 and κ_2 are given in Lemma 3.2.2. Then $\mathcal{Z}_2(r)$ satisfies (3.16).

Proof. Let $h \in \overline{B_r(0)}$. Since $\|u\|_{\mathcal{H}} = \|\mathbb{L}u\|_2$ and $\mathbb{A} = \mathbb{L}^{-1}\mathbb{B}$ by definition, we have that

$$\begin{aligned} \|\mathbb{A}(D\mathbb{F}(\bar{u}+h) - D\mathbb{F}(\bar{u}))\|_{\mathcal{H}} &= \|\mathbb{L}\mathbb{A}(D\mathbb{F}(\bar{u}+h) - D\mathbb{F}(\bar{u}))\|_{\mathcal{H},2} \\ &= \|\mathbb{B}(e^{\mathbb{M}_{\bar{u}+h}} - e^{\mathbb{M}_{\bar{u}}})\|_{\mathcal{H},2}. \end{aligned}$$

Then, we have

$$\|\mathbb{B}(e^{\mathbb{M}_{\bar{u}+h}} - e^{\mathbb{M}_{\bar{u}}})\|_{\mathcal{H},2} \leq \sup_{\|w\|_{\mathcal{H}}=1} \|\mathbb{B}e^{\mathbb{M}_{\bar{u}}}\|_2 \|(e^h - 1)w\|_{L^2_e}$$

where, using (3.24), we also get

$$\|\mathbb{B}e^{\mathbb{M}_{\bar{u}}}\|_2 \leq \max\left\{ \|Be^{\mathbb{M}_{\bar{U}}}\|_2, 1 \right\}.$$

We conclude the proof using Lemma 3.2.2, from which we deduce that

$$\|(e^h - 1)w\|_{L^2_e} \leq \kappa_1(e^{\kappa_2 r} - 1).$$

□

For the computation of the bound $\mathcal{Z}_1$, we first introduce some extra notation for simplicity. Let $\overline{v} \overset{\text{def}}{=} e^{\bar{u}} - 1$ and $\bar{V} \overset{\text{def}}{=} \gamma(\bar{v})$. Doing so, notice that $D\mathbb{G}(\bar{u})$ and $DG(\bar{U})$ can be expressed as

$$D\mathbb{G}(\bar{u}) = \mathbb{M}_{\bar{v}} \text{ and } DG(\bar{U}) = M_{\bar{V}},$$

where we have used the notation in (3.13). Finally, note that $\bar{V}$ is an infinite number of Fourier coefficients, as explained in Section 3.3.2. In order to exhibit finite-dimensional computations, we define $\bar{V}^N$ and $\bar{v}^N$ as

$$\bar{V}^N \overset{\text{def}}{=} \pi^N \bar{V} \text{ and } \bar{v}^N \overset{\text{def}}{=} \gamma^\dagger(\bar{V}^N).$$

That is, $\bar{V}^N$ correspond to the N first modes of $\bar{V}$. In fact, the difference $\bar{V} - \bar{V}^N$ can be controlled explicitly as a result of the analysis of Section 3.3.2. Then, we recall Lemma 3.6 from [17], providing the decomposition of $\mathcal{Z}_1$ as a Fourier coefficients computation Z_1, and a remainder $\mathcal{Z}_u$ that corresponds to the unboundedness of the domain Ω.

Lemma 3.4.4 (Bound $\mathcal{Z}_1$). *Let $\mathcal{Z}_u$ and Z_1 be bounds satisfying*

$$\begin{aligned} \|\left(\mathbb{L}^{-1} - \Gamma^\dagger(L^{-1})\right)\mathbb{M}_{\overline{v}^N}\mathbb{B}^*\|_2 &\leq \mathcal{Z}_u, \\ \|I - (B^N + \pi_N)(I + M_{\bar{V}^N}L^{-1})\|_2 &\leq Z_1. \end{aligned} \tag{3.26}$$

Then defining $\mathcal{Z}_1$ *as*

$$\mathcal{Z}_1 \overset{\text{def}}{=} Z_1 + \left(\mathcal{Z}_u + \frac{\max\{1, \|B^N\|_2\}}{1 - \frac{c^4}{4}} \|\bar{V} - \bar{V}^N\|_1 \right), \tag{3.27}$$

we get that (3.15) *holds, that is* $\|I - \mathbb{A}D\mathbb{F}(\bar{u})\|_{\mathcal{H}} \leq \mathcal{Z}_1$.

Proof. The proof is given in [17]. Note that the difference in the formulas lies in the fact that $\sup_{\xi \in \mathbb{R}^2} \frac{1}{l(\xi)} = \frac{1}{1 - \frac{c^4}{4}}$ in the case of (3.2). □

Remark 3.4.5. *In our implementation, the operator* $\mathbb{L}$ *acts as a diagonal operator. Its inverse* $\mathbb{L}^{-1}$ *is computed by dividing each Fourier coefficient by the corresponding value of the symbol* $l_{n_2}(\xi_1)$*. This operation is well-defined because the symbol is strictly positive for* $c \in (0, \sqrt{2})$.

We recall the computation of the bound Z_1, which is given in Lemma 3.9 from [17].

Lemma 3.4.6. *Let* Z_1^N *and* Z_1 *be such that*

$$\begin{gathered} \left(\|\pi^N - B^N(I_d + M_{\bar{V}^N} L^{-1})\pi^{2N}\|_2^2 + \|(\pi^{2N} - \pi^N) M_{\bar{V}^N} L^{-1} \pi^N\|_2^2 \right)^{\frac{1}{2}} \leq Z_1^N, \\ \left((Z_1^N)^2 + \|\bar{V}^N\|_1^2 \max_{n \in \mathbb{N}_0^2 \setminus I^N} \frac{1}{|l(\tilde{n})|^2} \right)^{\frac{1}{2}} \leq Z_1. \end{gathered} \tag{3.28}$$

Then we have $\left\| I_d - (B^N + \pi_N)\left(I_d + M_{\bar{V}^N} L^{-1}\right) \right\|_2 \leq Z_1$.

The above quantities are related to finite-dimensional computations, and their computation (with interval arithmetic) is presented in [76]. It remains to compute the bound $\mathcal{Z}_u$ satisfying (3.26).

Following the analysis of [16], we can write $\mathcal{Z}_u$ as

$$\mathcal{Z}_u = \max\left\{1, \|B^N\|_2\right\} \sqrt{\mathcal{Z}_{u,1}^2 + \mathcal{Z}_{u,2}^2}$$

where $\mathcal{Z}_{u,1}$ and $\mathcal{Z}_{u,2}$ are defined as follows:

$$\mathcal{Z}_{u,1} = \sup_{\|u\|_2 = 1} \left(\|\mathbb{1}_{\mathbb{R} \setminus (-d_1, d_1)} \mathbb{L}_0^{-1} (\bar{v}^N u)_0\|_2^2 + 2 \sum_{n_2 \in \mathbb{N}} \|\mathbb{1}_{\mathbb{R} \setminus (-d_1, d_1)} \mathbb{L}_{n_2}^{-1} (\bar{v}^N u)_{n_2}\|_2^2 \right)^{\frac{1}{2}},$$

$$\mathcal{Z}_{u,2} = \sup_{\|u\|_2 = 1} \left(\|\mathbb{1}_{(-d_1, d_1)} (\mathbb{L}_0^{-1} - \Gamma^\dagger(L_0^{-1}))(\bar{v}^N u)_0\|_2^2 \right.$$
$$\left. + 2 \sum_{n_2 \in \mathbb{N}} \|\mathbb{1}_{(-d_1, d_1)} (\mathbb{L}_{n_2}^{-1} - \Gamma^\dagger(L_{n_2}^{-1}))(\bar{v}^N u)_{n_2}\|_2^2 \right)^{\frac{1}{2}}.$$

In particular, we have that $\mathbb{L}_{n_2}^{-1}$ is a convolution operator associated to the function $f_{n_2} \stackrel{\text{def}}{=} \mathcal{F}^{-1}\left(\frac{1}{l_{n_2}}\right)$. Indeed, we have that

$$\mathbb{L}_{n_2} u = \mathcal{F}^{-1}\left(\mathcal{F}(\mathbb{L}_{n_2} u)\right) = \mathcal{F}^{-1}\left(\frac{1}{l_{n_2}} \hat{u}\right) = f_{n_2} * u.$$

The results derived in [16] require the computation of constants $C_{n_2} > 0$ and $a_{n_2} > 0$ such that

$$|f_{n_2}(x)| \leq C_{n_2} e^{-a_{n_2}|x|}, \quad \text{for all } x \in \mathbb{R}. \tag{3.29}$$

If we can obtain explicit constants satisfying the above, then [16] provides explicit formulas for the computation of $\mathcal{Z}_{u,1}$ and $\mathcal{Z}_{u,2}$. We derive such a result in the following lemma.

Lemma 3.4.7. *Let $n_2 \in \mathbb{N}_0$, and let us define a_{n_2}, b_{n_2} and C_{n_2} as*

$$a_{n_2} \stackrel{\text{def}}{=} \frac{\sqrt{4(1+\tilde{n}_2^2 c^2) - c^4}}{2\sqrt{c^2 - 2\tilde{n}_2^2 + \sqrt{(c^2 - 2\tilde{n}_2^2)^2 + 4(1 + c^2\tilde{n}_2^2) - c^4}}}, \tag{3.30}$$

$$b_{n_2} \stackrel{\text{def}}{=} \frac{1}{2}\sqrt{c^2 - 2\tilde{n}_2^2 + \sqrt{(c^2 - 2\tilde{n}_2^2)^2 + 4(1 + c^2\tilde{n}_2^2) - c^4}}, \tag{3.31}$$

$$C_{n_2} \stackrel{\text{def}}{=} \frac{1}{2(a_{n_2}^2 + b_{n_2}^2)^{\frac{1}{2}} \pi \sqrt{4(1+\tilde{n}_2^2 c^2) - c^4}}. \tag{3.32}$$

Then, we obtain that C_{n_2} and a_{n_2} satisfy (3.29).

Proof. Let $n_2 \in \mathbb{N}_0$ and let us compute the inverse Fourier transform of $\frac{1}{l_{n_2}}$. We have

$$f_{n_2}(x) = \int_{\mathbb{R}} \frac{1}{l_{n_2}(\xi)} e^{2\pi i \xi x} d\xi = \frac{1}{2\pi} \int_{\mathbb{R}} \frac{1}{l_{n_2}(\frac{\xi}{2\pi})} e^{i\xi x} d\xi.$$

Now, notice that $\xi \mapsto l_{n_2}(\frac{\xi}{2\pi})$ has four roots given by $\pm\xi_1$ and $\pm\overline{\xi_1}$ where

$$\xi_1 \stackrel{\text{def}}{=} b_{n_2} - i a_{n_2}.$$

In particular, we have that

$$\frac{1}{l_{n_2}(\frac{\xi}{2\pi})} = \frac{1}{i\sqrt{4(1+\tilde{n}_2^2 c^2) - c^4}} \left(\frac{1}{\xi^2 - \xi_1^2} - \frac{1}{\xi^2 - \overline{\xi_1}^2} \right).$$

Using Section 2.3.14 in [55], we obtain that

$$\begin{aligned} f_{n_2}(x) &= \frac{1}{2\pi} \frac{1}{i\sqrt{4(1+\tilde{n}_2^2 c^2) - c^4}} \int_{\mathbb{R}} \left(\frac{1}{\xi^2 - \xi_1^2} - \frac{1}{\xi^2 - \overline{\xi_1}^2} \right) e^{i\xi x} d\xi \\ &= \frac{1}{4\pi} \frac{1}{i\sqrt{4(1+\tilde{n}_2^2 c^2) - c^4}} \left(\frac{e^{-i\xi_1|x|}}{i\xi_1} - \frac{e^{-i\overline{\xi_1}|x|}}{i\overline{\xi_1}} \right) \end{aligned}$$

for all $x \in \mathbb{R}$. Then, we have that

$$f_{n_2}(x) = \frac{e^{-a_{n_2}|x|}}{4(a_{n_2}^2 + b_{n_2}^2)i\pi\sqrt{4(1+\tilde{n}_2^2c^2)-c^4}} \left(e^{-ib_{n_2}|x|}(a_{n_2} - ib_{n_2}) - e^{ib_{n_2}|x|}(a_{n_2} + ib_{n_2})\right)$$
$$= -\frac{e^{-a_{n_2}|x|}}{2(a_{n_2}^2 + b_{n_2}^2)\pi\sqrt{4(1+\tilde{n}_2^2c^2)-c^4}} \left(a_{n_2}\mathrm{sign}(x)\sin(b_{n_2}x) + b_{n_2}\cos(b_{n_2}x)\right).$$

Notice that $x \mapsto f_{n_2}(x)$ is an even function and that f_{n_2} is smooth on $[0,\infty)$. In particular, we have that C_{n_2} and a_{n_2} satisfy (3.29). □

Using the above, we obtain an explicit formula for $\mathcal{Z}_u$.

Lemma 3.4.8. *Let $E \in \ell^2$ the sequence of Fourier coefficients given as*

$$E_n \stackrel{\text{def}}{=} \frac{(C_{n_2})^2 a_{n_2}(-1)^{n_1}(1 - e^{-4a_{n_2}d_1})}{d_1(4a_{n_2}^2 + (2\pi\tilde{n}_1)^2)} \tag{3.33}$$

for all $n \in \mathbb{N}_0^2$. Moreover, let a and $C(d_1)$ be defined as

$$a \stackrel{\text{def}}{=} \inf_{n_2 \in \mathbb{N}_0} a_{n_2} \quad \text{and} \quad C(d_1) \stackrel{\text{def}}{=} 4d_1 + \frac{4e^{-ad_1}}{a(1 - e^{-\frac{3}{2}ad_1})} + \frac{2}{a(1 - e^{-2ad_1})}.$$

Then, we obtain that

$$\mathcal{Z}_{u,1} \leq \left(2d_1(\bar{V}^N, \bar{V}^N * E)_2\right)^{\frac{1}{2}},$$
$$\mathcal{Z}_{u,2} \leq \left(2d_1(\bar{V}^N, V^N * E)_2 + C(d_1)e^{-2ad_1}(\bar{V}^N, \bar{V}^N * E)_2\right)^{\frac{1}{2}},$$

and that $\mathcal{Z}_u = \max\left\{1, \|B^N\|_2\right\}\sqrt{\mathcal{Z}_{u,1}^2 + \mathcal{Z}_{u,2}^2}$ satisfies (3.26).

Proof. Let $u \in L_e^2$ such that $\|u\|_{L_e^2} = 1$ and let $v \stackrel{\text{def}}{=} \bar{v}^N u$. Using the proof of Theorem 3.9 in [16], we have

$$\|\mathbb{1}_{\mathbb{R}\setminus(-d_1,d_1)}\mathbb{L}_{n_2}^{-1}v_{n_2}\|_2^2 \leq C_{n_2}^2 \int_{\mathbb{R}\setminus(-d_1,d_1)} \left(\int_{-d_1}^{d_1} e^{-a_{n_2}|x-y|}|v_{n_2}(x)|dx\right)^2 dy \tag{3.34}$$

for all $n_2 \in \mathbb{N}_0$, where we have used (3.29). Noting that $v = \bar{v}^N u$, we have

$$v_{n_2} = \sum_{k\in\mathbb{Z}} \bar{v}_{|n_2-k|}^N u_{|k|}.$$

for all $n_2 \in \mathbb{N}_0$. Going back to (3.34), we get

$$\|\mathbb{1}_{\mathbb{R}\setminus(-d_1,d_1)}\mathbb{L}_{n_2}^{-1}v_{n_2}\|_2^2$$
$$\leq C_{n_2}^2 \int_{\mathbb{R}\setminus(-d_1,d_1)} \left(\sum_{k\in\mathbb{Z}} \int_{-d_1}^{d_1} e^{-a_{n_2}|x-y|}|\bar{v}_{|n_2-k|}^N(x)u_{|k|}(x)|dx\right)^2 dy.$$

Now, applying the Cauchy-Schwarz inequality, we get

$$\begin{aligned}
&\|\mathbb{1}_{\mathbb{R}\setminus(-d_1,d_1)}\mathbb{L}_{n_2}^{-1}v_{n_2}\|_2^2 \\
\leq\ & C_{n_2}^2\int_{\mathbb{R}\setminus(-d_1,d_1)}\left(\sum_{k\in\mathbb{Z}}\int_{-d_1}^{d_1}e^{-2a_{n_2}|x-y|}|\bar{v}_{|n_2-k|}^N(x)|^2dx\right)\left(\sum_{k\in\mathbb{Z}}\int_{-d_1}^{d_1}|u_{|k|}(x)|^2dx\right)dy \\
\leq\ & C_{n_2}^2\int_{\mathbb{R}\setminus(-d_1,d_1)}\sum_{k\in\mathbb{Z}}\int_{-d_1}^{d_1}e^{-2a_{n_2}|x-y|}|\bar{v}_{|n_2-k|}^N(x)|^2dxdy \qquad (3.35)
\end{aligned}$$

since $\|u\|_2 = 1$. Employing Fubini's theorem, we have

$$\begin{aligned}
&\int_{\mathbb{R}\setminus(-d_1,d_1)}\sum_{k\in\mathbb{Z}}\int_{-d_1}^{d_1}e^{-2a_{n_2}|x-y|}|\bar{v}_{|n_2-k|}^N(x)|^2dxdy \\
&\quad=\int_{-d_1}^{d_1}\sum_{k\in\mathbb{Z}}|\bar{v}_{|n_2-k|}^N(x)|^2\int_{\mathbb{R}\setminus(-d_1,d_1)}e^{-2a_{n_2}|x-y|}dydx.
\end{aligned}$$

Recalling the proof of Theorem 3.9 from [16], we get

$$\int_{\mathbb{R}\setminus(-d_1,d_1)}e^{-2a_{n_2}|x-y|}dy=\frac{e^{-2a_{n_2}d_1}\cosh(2a_{n_2}x)}{a_{n_2}}.$$

In particular, using Lemma 4.6 in [13], we obtain that $x\to\frac{e^{-2a_{n_2}d_1}\cosh(2a_{n_2}x)}{a_{n_2}}$ has a Fourier coefficients representation on $(-d_1,d_1)$ given by the sequence $\tilde{E}$, where

$$\tilde{E}_{n_1}\overset{\text{def}}{=}\frac{a_{n_2}(-1)^{n_1}(1-e^{-4a_{n_2}d_1})}{d_1(4a_{n_2}^2+(2\pi\tilde{n}_1)^2)}$$

for all $n_1\in\mathbb{N}_0$ and all $n_2\in\mathbb{N}_0$. Applying Parseval's identity, this implies that

$$\begin{aligned}
\mathcal{Z}_{u,1}^2&\leq\sum_{k\in\mathbb{Z}}\sum_{n_2\in\mathbb{Z}}\int_{-d_1}^{d_1}|\bar{v}_{|n_2-k|}^N(x)|^2\frac{C_{|n_2|}^2e^{-2a_{n_2}d_1}\cosh(2a_{n_2}x)}{a_{n_2}}dx \\
&=2d_1(\bar{V}^N,\bar{V}^N*E)_2. \qquad (3.36)
\end{aligned}$$

This concludes the inequality for $\mathcal{Z}_{u,1}$.

For the computation of $\mathcal{Z}_{u,2}$ we use the formulas provided in [16]. Indeed, applying the proof of Theorem 3.9 again, we can define g_n as

$$g_n\overset{\text{def}}{=}\frac{1}{2d_1}\int_{-d_1}^{d_1}\mathbb{L}_{n_2}v_{n_2}(x)e^{-2\pi i\tilde{n}_1x}dx$$

for all $n\in\mathbb{Z}^2$, where $v_{n_2}=v_{-n_2}$ if $n_2<0$. Utilizing the proof of Theorem 3.9 in [16], we have that

$$\mathcal{Z}_{u,2}^2=2d_1\sum_{n\in\mathbb{Z}^2}|g_n|^2=\int_{\mathbb{R}\setminus((-d_1,d_1)\cup(-d_1,d_1)+2d_1n_1)}\mathbb{L}_{n_2}v_{n_2}(x)\mathbb{L}_{n_2}v_{n_2}(x-2d_1n_1)dx.$$

In particular, note that for $n_1 = 0$, we have

$$\sum_{n_2\in\mathbb{Z}} \int_{\mathbb{R}\setminus((-d_1,d_1)\cup(-d_1,d_1)+2d_1n_1)} \mathbb{L}_{n_2}v_{n_2}(x)\mathbb{L}_{n_2}v_{n_2}(x-2d_1n_1)dx$$
$$= \sum_{n_2\in\mathbb{Z}} \int_{\mathbb{R}\setminus((-d_1,d_1)} |\mathbb{L}_{n_2}v_{n_2}(x)|^2\, dx = \mathcal{Z}_{u,1}^2.$$

With the help of the proof of Lemma 6.5 in [16], we obtain that

$$\mathcal{Z}_{u,2}^2 \le \mathcal{Z}_{u,1}^2 + \sum_{n\in\mathbb{Z}^2, n_1\neq 0} C_{n_2}^2 \int_{(-d_1,d_1)^2} |v_{n_2}(x)v_{n_2}(z)| I_n(x,z)dxdz$$

where

$$I_n(x,z) \stackrel{\text{def}}{=} \int_{\mathbb{R}\setminus((-d_1,d_1)\cup(-d_1,d_1)+2d_1n_1)} e^{-a_{n_2}|y-x|}e^{-a_{n_2}|2d_1n_1+z-y|}dy.$$

We conclude the proof following the steps of the proof of Lemma 6.5 in [16] and using the above computations concerning the bound $\mathcal{Z}_{u,1}$. □

3.5 Stability Analysis

In this section, we aim at investigating the stability of traveling wave solutions to (3.2) with boundary conditions (3.3), which is the traveling wave formulation associated with (3.1). The existence of these traveling waves will be constructively established in Section 3.6. In particular, we assume that we know the existence of a solution $\tilde{u} \in \mathcal{H}$ to (3.2) such that

$$\|\tilde{u} - \bar{u}\|_{\mathcal{H}} \le r_0, \tag{3.37}$$

where $\bar{u}$ is an approximate solution constructed as in (3.21) and r_0 is explicit. In order to study stability, we heavily rely on the framework developed in [47]. In fact, the authors of [47] investigated the orbital stability of traveling wave solutions in the 1D version of (3.2). One can easily show that the analysis of Sections 3 and 4 of [47] generalizes to the 2D version (3.2). We recall some notations for completeness.

Let $\Omega \stackrel{\text{def}}{=} \mathbb{R}\times(-d_2,d_2)$ be our spatial domain. Then, let $X \stackrel{\text{def}}{=} H^2(\Omega)\times L^2(\Omega)$ and let $X^* \stackrel{\text{def}}{=} H^{-2}(\Omega)\times L^2(\Omega)$ be its dual. Moreover, let us define the functional $E : X \to \mathbb{R}$ as

$$E\begin{pmatrix}u\\v\end{pmatrix} \stackrel{\text{def}}{=} \int_\Omega \left[\frac{1}{2}v(x)^2 + \frac{1}{2}(\Delta u(x))^2 + e^{u(x)} - u(x) - 1\right]dx \tag{3.38}$$

Then, (3.1) can be written in the form

$$\frac{d}{dt}U = JE'(U) \tag{3.39}$$

where $U = \begin{pmatrix} u \\ v \end{pmatrix}$, $J : L^2(\Omega) \times H^2(\Omega) \to X$ defined by $J\begin{pmatrix} u \\ v \end{pmatrix} = \begin{pmatrix} v \\ -u \end{pmatrix}$ and $E'\begin{pmatrix} u \\ v \end{pmatrix} = \begin{pmatrix} \Delta^2 u + e^u - 1 \\ v \end{pmatrix} \in X^*$. Let $T(s) : X \to X$ be the translation by $s \in \mathbb{R}$ in the direction x_1, that is $T(s)U(x) = U(x_1 + s, x_2)$. Defining the so-called bound state

$$\tilde{U} \stackrel{\text{def}}{=} \begin{pmatrix} \tilde{u} \\ c\partial_{x_1}\tilde{u} \end{pmatrix}, \tag{3.40}$$

we find that $U(t) := T(ct)\tilde{U}$ provides a solution to (3.39).

We are now in a position to introduce the notation of orbital stability used in [47].

Definition 3.5.1. Let $\tilde{u}$ be a traveling wave solution to (3.2) in $\mathcal{H}$ and let $\tilde{U}$ be defined as in (3.40). Then $\tilde{u}$ is said to be *orbitally stable* if the solution U to (3.39) with initial condition $U(0) = U_0$ exists for all positive times and if for all $\epsilon > 0$, there exists $\delta > 0$ such that if $\|U_0 - \tilde{U}\|_X < \delta$, then $\inf_{s\in\mathbb{R}} \|U(t) - T(s)\tilde{U}\|_X < \epsilon$. Furthermore, $\tilde{u}$ is called *orbitally unstable* if it is not orbitally stable.

Let $n(D\mathbb{F}(\tilde{u}))$ be the number of negative eigenvalues of $D\mathbb{F}(\tilde{u})$, counted with multiplicity. Then, the authors of [47] derived in Theorem 1 sufficient conditions under which orbital (in)stability is achieved. This result naturally generalizes to the 2D case, since the steps of the proof are essentially the same, as also observed by the authors in [47]. We state the two-dimensional version in the following lemma.

Lemma 3.5.1. *Let $\tilde{w} \in \mathcal{H}$ be defined as*

$$\tilde{w} = -2cD\mathbb{F}(\tilde{u})^{-1}\partial_{x_1}^2\tilde{u}. \tag{3.41}$$

Moreover, define the constant θ as follows

$$\theta \stackrel{\text{def}}{=} \int_\Omega (\tilde{u} + 2c\tilde{w})\partial_{x_1}^2\tilde{u}. \tag{3.42}$$

If $n(D\mathbb{F}(\tilde{u})) = 0$, or if $\theta > 0$ and $n(D\mathbb{F}(\tilde{u})) = 1$, then $\tilde{u}$ is orbitally stable. If $\theta > 0$ and $n(D\mathbb{F}(\tilde{u}))$ is even, or if $\theta < 0$ and $n(D\mathbb{F}(\tilde{u}))$ is odd, then $\tilde{u}$ is orbitally unstable.

Remark 3.5.2. *A solution is not only valid for a fixed parameter c, but also persists under variations of c. Differentiating with respect to c yields $\tilde{w}$ in Lemma 3.5.1, which is called v_c in [47]. To determine (in)stability, the authors of [47] introduce a functional $d(c)$ and compute its second derivative $d''(c)$ in Section 4.3 of their paper, which corresponds to θ in our Lemma 3.5.1 after applying integrations by parts.*

The previous lemma provides sufficient conditions for proving (in)stability, which depend on the spectrum of the Jacobian $D\mathbb{F}(\tilde{u})$ and on the sign of θ. Consequently, our objective is now to enclose the spectrum of $D\mathbb{F}(\tilde{u})$ and to provide a computer-assisted approach for enclosing the value of θ.

3.5.1 Enclosure of the spectrum of $D\mathbb{F}(\tilde{u})$

In this section, we present a computer-assisted strategy for the enclosure of the spectrum of $D\mathbb{F}(\tilde{u}) : \mathcal{H} \to L^2(\Omega)$, denoted as $\sigma(D\mathbb{F}(\tilde{u}))$. First, notice that $D\mathbb{F}(\tilde{u})$ viewed as an operator on $L^2(\Omega)$ with domain $\mathcal{H}$ is self-adjoint. This implies that its spectrum is real-valued. Consequently, we restrict our study of the spectrum to the real line.

In order to obtain explicit enclosures on $\sigma(D\mathbb{F}(\tilde{u}))$, we follow the set-up introduced in [14]. In particular, we want to construct a homotopy allowing the study of the spectrum of $D\mathbb{F}(\tilde{u})$ based on the one of $DF(\bar{U})$.

To begin with, we control the essential part $\sigma_{ess}(D\mathbb{F}(\tilde{u})$ of the spectrum. In particular, using [14], we have that the essential spectrum can be computed using the Fourier transform of $\mathbb{L}$ as follows:

$$\sigma_{ess}(D\mathbb{F}(\tilde{u})) = \{l_{n_2}(\xi),\ \xi \in \mathbb{R}, n_2 \in \mathbb{N}_0\} \subset \left[1 - \frac{c^4}{4}, \infty\right).$$

Then, using Lemma 2.2 of [14], we have the following decomposition of the spectrum

$$\sigma(D\mathbb{F}(\tilde{u})) = \sigma_{ess}(D\mathbb{F}(\tilde{u})) \cup Eig(D\mathbb{F}(\tilde{u})). \tag{3.43}$$

Consequently, it remains to control the eigenvalues of $D\mathbb{F}(\tilde{u})$ away from the essential spectrum. First, we construct a lower bound for the eigenvalues.

Lemma 3.5.3. *Let λ_{min} be defined as*

$$\lambda_{min} \stackrel{\text{def}}{=} -e^{\kappa_2 r_0}\|e^{\bar{U}}\|_1 - \frac{c^4}{4}. \tag{3.44}$$

Then $(-\infty, 1 - \frac{c^4}{4}) \cap Eig(D\mathbb{F}(\tilde{u})) \subset [\lambda_{min}, 1 - \frac{c^4}{4})$.

Proof. Let $\lambda \in (-\infty, 1 - \frac{c^4}{4}) \cap Eig(D\mathbb{F}(\tilde{u}))$. Then, there exists $u \in \mathcal{H}$, $u \neq 0$, such that

$$\mathbb{L}u + (e^{\tilde{u}} - 1)u = \lambda u.$$

Using that $\lambda < 1 - \frac{c^4}{4}$, we have that $|l_{n_2}(\xi) - \lambda| \geq |1 - \frac{c^4}{4} - \lambda|$ for all $\xi \in \mathbb{R}$ and all $n_2 \in \mathbb{N}_0$. This implies that

$$|1 - \frac{c^4}{4} - \lambda|\|u\|_2 \leq \|\mathbb{L}u - \lambda u\|_2 \leq \|e^{\tilde{u}}u - u\|_2 \leq \|e^{\tilde{u}}u\|_2 + \|u\|_2.$$

Now, we have

$$\begin{aligned}\|e^{\tilde{u}}u\|_2 = \|e^{\tilde{u}-\bar{u}}e^{\bar{u}}u\|_2 &\leq \|e^{\tilde{u}-\bar{u}}\|_\infty \|e^{\bar{u}}\|_\infty \|u\|_2 \\ &\leq e^{\kappa_2\|\tilde{u}-\bar{u}\|_{\mathcal{H}}}\|e^{\bar{U}}\|_1\|u\|_2 \\ &\leq e^{\kappa_2 r_0}\|e^{\bar{U}}\|_1\|u\|_2.\end{aligned}$$

This concludes the proof after a short algebraic manipulation. □

Having established the lower bound $\lambda_{\min}$, we now restrict our work to the interval $\mathcal{J} \stackrel{\text{def}}{=} [\lambda_{min}, \delta_0]$ where $0 < \delta_0 < 1 - \frac{c^4}{4}$. Then, the above results provide that the negative eigenvalues of $D\mathbb{F}(\tilde{u})$ must be contained in $\mathcal{J}$. Using the analysis derived in [14], we provide rigorous enclosures for the set $\mathcal{J} \cap Eig(D\mathbb{F}(\tilde{u}))$, based on the spectrum of $DF(\bar{U})$. Our approach is computer-assisted and follows the methodology derived in Sections 3 and 4 of [14]. Before presenting such an approach, we present a simplification by separating even and odd subspaces.

Using the ideas of Section 5.1 in [14], we notice that L^2 can be decomposed as follows

$$L^2 = L^2_e \oplus L^2_o,$$

where

$$L^2_o \stackrel{\text{def}}{=} \left\{ u \in L^2,\ u(x_1, x_2) = -u(-x_1, x_2) \text{ for all } x \in \mathbb{R}^2 \right\}. \tag{3.45}$$

Moreover, given $\tilde{u} \in \mathcal{H}$, we have that

$$D\mathbb{F}(\tilde{u}) v_i \in L^2_i$$

for all $v_i \in L^2_i$ and all $i \in \{e, o\}$. This implies that if $u \in L^2$ satisfies

$$D\mathbb{F}(\tilde{u}) u = \lambda u$$

and we decompose $u = u_e + u_o$, where $u_i \in L^2_i$, then

$$D\mathbb{F}(\tilde{u}) u_i = \lambda u_i$$

for all $i \in \{e, o\}$. Consequently, we investigate the spectrum of $D\mathbb{F}_i(\tilde{u}) : L^2_i \to L^2_i$, the restriction of $D\mathbb{F}(\tilde{u})$ to $L^2_i \to L^2_i$, for all $i \in \{e, o\}$ and obtain the following decomposition

$$\sigma\left(D\mathbb{F}(\tilde{u})\right) = \sigma\left(D\mathbb{F}_e(\tilde{u})\right) \cup \sigma\left(D\mathbb{F}_o(\tilde{u})\right). \tag{3.46}$$

Then, in practice, we control the spectrum of each $D\mathbb{F}_i(\tilde{u})$ and use the identity (3.46) to conclude. This disjunction allows to optimize numerical memory usage by considering smaller operators.

Going back to our strategy for enclosing the eigenvalues of $D\mathbb{F}(\tilde{u})$, we introduce a pseudo-diagonalization for $DF(\bar{U})$ given as

$$\mathcal{D} \stackrel{\text{def}}{=} P^{-1} DF(\bar{U}) P,$$

for some invertible infinite matrix $P = P^N + \pi_N$, with $P^N = \pi^N P^N \pi^N$, whose inverse is given as $P^{-1} = \pi^N (P^N)^{-1} \pi^N + \pi_N$. $(P^N)^{-1}$ has to be understood as the inverse of $P^N : \pi^N \ell^2 \to \pi^N \ell^2$. In practice, columns of P are approximate eigenvectors of $DF(\bar{U})$, so that $\mathcal{D}$ is close to being diagonal. We define S as the diagonal part of the matrix $\mathcal{D}$ and $R = \mathcal{D} - S$. Moreover, we define λ_k as the diagonal entries of S, that is,

$$(SU)_k = \lambda_k U_k \text{ for all } k \in \mathbb{N}_0^2. \tag{3.47}$$

Our goal will be to prove that the eigenvalues of $D\mathbb{F}(\tilde{u})$ are contained in a neighborhood of the sequence (λ_k).

Before delving further into the enclosure of the spectrum of $D\mathbb{F}(\tilde{u})$, we introduce the following auxiliary lemma, which will be useful for our estimations.

Lemma 3.5.4. *Let $n_2 \in \mathbb{N}_0$, and let us define $a_{n_2}(\mathcal{J})$, $b_{n_2}(\mathcal{J})$ and $C_{n_2}(\mathcal{J})$ as (cf. Lemma 3.4.7)*

$$a_{n_2}(\mathcal{J}) \stackrel{\text{def}}{=} \frac{\sqrt{4(1+\tilde{n}_2^2c^2-\delta_0)-c^4}}{2\sqrt{c^2-2\tilde{n}_2^2+\sqrt{(c^2-2\tilde{n}_2^2)^2+4(1+c^2\tilde{n}_2^2-\delta_0)}-c^4}}, \tag{3.48}$$

$$b_{n_2}(\mathcal{J}) \stackrel{\text{def}}{=} \frac{1}{2}\sqrt{c^2-2\tilde{n}_2^2+\sqrt{(c^2-2\tilde{n}_2^2)^2+4(1+c^2\tilde{n}_2^2-\delta_0)}-c^4}, \tag{3.49}$$

$$C_{n_2}(\mathcal{J}) \stackrel{\text{def}}{=} \frac{1}{2(a_{n_2}(\mathcal{J})^2+b_{n_2}(\mathcal{J})^2)^{\frac{1}{2}}\pi\sqrt{4(1+\tilde{n}_2^2c^2-\delta_0)-c^4}}. \tag{3.50}$$

Given $\mu \in \mathcal{J}$, we define $f_{n_2,\mu} \stackrel{\text{def}}{=} \mathcal{F}^{-1}(\frac{1}{l_{n_2}-\mu})$. Then, we obtain that

$$\sup_{\mu\in\mathcal{J}} |f_{n_2,\mu}(x)| \leq C_{n_2}(\mathcal{J})e^{-a_{n_2}(\mathcal{J})|x|}, \quad \textit{for all } x \in \mathbb{R}. \tag{3.51}$$

Proof. The proof is very similar to the one of Lemma 3.4.7. Indeed, we compute $f_{n_2,\mu}$ as in the proof of Lemma 3.4.7, and obtain that

$$|f_{n_2,\mu}(x)| \leq C_{n_2}(\mu)e^{-a_{n_2}(\mu)|x|}, \quad \text{for all } x \in \mathbb{R}$$

where

$$a_{n_2}(\mu) \stackrel{\text{def}}{=} \frac{\sqrt{4(1+\tilde{n}_2^2c^2-\mu)-c^4}}{2\sqrt{c^2-2\tilde{n}_2^2+\sqrt{(c^2-2\tilde{n}_2^2)^2+4(1+c^2\tilde{n}_2^2-\mu)}-c^4}},$$

$$b_{n_2}(\mu) \stackrel{\text{def}}{=} \frac{1}{2}\sqrt{c^2-2\tilde{n}_2^2+\sqrt{(c^2-2\tilde{n}_2^2)^2+4(1+c^2\tilde{n}_2^2-\mu)}-c^4},$$

$$C_{n_2}(\mu) \stackrel{\text{def}}{=} \frac{1}{2(a_{n_2}(\mu)^2+b_{n_2}(\mu)^2)^{\frac{1}{2}}\pi\sqrt{4(1+\tilde{n}_2^2c^2-\mu)-c^4}}.$$

Subsequently, one can prove that both a_{n_2} and b_{n_2} are decreasing functions of μ, leading to the desired result. □

Next, we aim at applying Theorem 4.3 from [14] in order to enclose the eigenvalues of $D\mathbb{F}(\tilde{u})$ in intervals centered at the λ_k's. Note that the set-up is slightly different since [14] focuses on the domain $\mathbb{R}^m$, where (3.2) is posed on $\Omega = \mathbb{R} \times (-d_2, d_2)$. However, a very similar analysis applies and we summarize the main result of [14] in the case of Ω.

Lemma 3.5.5. *Let $t > -\lambda_{min}$ and let $\mathcal{J} = [\lambda_{min}, \delta_0]$. We define $E = (E_n)_{n\in\mathbb{N}_0^2}$ as*

$$E_n \stackrel{\text{def}}{=} \frac{(C_{n_2}(\mathcal{J}))^2 a_{n_2}(\mathcal{J})(-1)^{n_1}(1-e^{-4a_{n_2}(\mathcal{J})d_1})}{d_1(4a_{n_2}(\mathcal{J})^2+(2\pi\tilde{n}_1)^2)}. \tag{3.52}$$

Furthermore, define $a(\mathcal{J})$ *and* $C(d_1)$ *as*

$$a(\mathcal{J}) \stackrel{\text{def}}{=} \inf_{n_2 \in \mathbb{N}_0} a_{n_2}(\mathcal{J}),$$
$$C(d_1) \stackrel{\text{def}}{=} 4d_1 + \frac{4e^{-a(\mathcal{J})d_1}}{a(\mathcal{J})(1-e^{-\frac{3}{2}a(\mathcal{J})d_1})} + \frac{2}{a(\mathcal{J})(1-e^{-2a(\mathcal{J})d_1})}.$$

We introduce various constants satisfying the following inequalities:

$$\begin{aligned}
\mathcal{Z}_{u,1} &\geq 4d_1(\bar{V}, \bar{V} * E),\\
\mathcal{Z}_{u,2} &\geq 4d_1(\bar{V}, \bar{V}*, E)_2 + 2C(d_1)e^{-2a(\mathcal{J})d_1}(\bar{V}, \bar{V} * E)_2\\
\mathcal{Z}_{u,3} &\geq \|\pi^N(S+tI)^{-1}P^{-1}(L-\delta_0 I)\|_2 \mathcal{Z}_{u,2},\\
\mathcal{C}_1 &\geq \frac{\|e^{\bar{U}}\|_1}{1-\delta_0-\frac{c^4}{4}}\frac{e^{\kappa_2 r_0}-1}{r_0},\\
\mathcal{C}_2 &\geq \|e^{\bar{U}}\|_1 \frac{\|\pi^N(S+tI)^{-1}P^{-1}(L-\delta_0 I)\|_2}{1-\delta_0-\frac{c^4}{4}}\frac{e^{\kappa_2 r_0}-1}{r_0},\\
Z_{1,1} &\geq \frac{1}{1-\delta_0-\frac{c^4}{4}}\|\pi_N(L-\delta_0 I)^{-1}R\pi^N\|_2,\\
Z_{1,2} &\geq \frac{1}{1-\delta_0-\frac{c^4}{4}}\|\pi_N(L-\delta_0 I)^{-1}R\pi_N\|_2,\\
Z_{1,3} &\geq \|\pi^N(S+tI)^{-1}R\pi^N\|_2, \qquad Z_{1,4} \geq \|\pi^N(S+tI)^{-1}R\pi_N\|_2.
\end{aligned}$$

Assuming

$$\mathcal{C}_1 r_0 < 1, \tag{3.53}$$

we define β_1 *as* $\beta_1 \stackrel{\text{def}}{=} \frac{\mathcal{Z}_{u,1}+\mathcal{C}_1 r_0}{1-\mathcal{C}_1 r_0}$. *Furthermore, we assume that*

$$1 - Z_{1,2} - \mathcal{Z}_{u,2} - (1+\beta_1^2)^{\frac{1}{2}}\mathcal{C}_1 r_0 > 0. \tag{3.54}$$

Then, we define

$$\begin{aligned}
\beta_2 &\stackrel{\text{def}}{=} \frac{Z_{1,1} + (\mathcal{Z}_{u,2} + (1+\beta_1^2)^{\frac{1}{2}}\mathcal{C}_1 r_0)\|P^N\|_2}{1 - Z_{1,2} - \mathcal{Z}_{u,2} - (1+\beta_1^2)^{\frac{1}{2}}\mathcal{C}_1 r_0},\\
\epsilon_n^{(q)} &\stackrel{\text{def}}{=} |\lambda_n + t|\Bigg(Z_{1,3} + Z_{1,4}\frac{Z_{1,1} + \mathcal{Z}_{u,2}\|P^N\|_2}{1 - Z_{1,2} - \mathcal{Z}_{u,2}}\\
&\qquad + \mathcal{Z}_{u,3}\left(\|P^N\|_2 + \frac{Z_{1,1} + \mathcal{Z}_{u,2}\|P^N\|_2}{1 - Z_{1,2} - \mathcal{Z}_{u,2}}\right)\Bigg),\\
\epsilon_n^{(\infty)} &\stackrel{\text{def}}{=} |\lambda_n + t|\left(Z_{1,3} + Z_{1,4}\beta_2 + \left(\mathcal{Z}_{u,3} + \mathcal{C}_2 r_0(1+\beta_1^2)^{\frac{1}{2}}\right)\left(\|P^N\|_2 + \beta_2\right)\right),\\
\epsilon_n &\stackrel{\text{def}}{=} \max\{\epsilon_n^{(q)}, \epsilon_n^{(\infty)}\}
\end{aligned}$$

for all $n \in \mathbb{N}_0^2$. *Let* $k \in \mathbb{N}$ *and* $I \subset \mathbb{N}_0^2$ *such that* $|I| = k$. *If*

$$\bigcup_{n\in I}[\lambda_n - \epsilon_n, \lambda_n + \epsilon_n] \subset \mathcal{J} \quad \textit{and}$$
$$\left(\bigcup_{n\in I}[\lambda_n - \epsilon_n, \lambda_n + \epsilon_n]\right) \cap \left(\bigcup_{n\in \mathbb{N}_0^2\setminus I}[\lambda_n - \epsilon_n, \lambda_n + \epsilon_n]\right) = \varnothing,$$

then there are exactly k *eigenvalues of* $D\mathbb{F}(\tilde{u})$ *in* $\cup_{n\in I}[\lambda_n-\epsilon_n, \lambda_n+\epsilon_n] \subset \mathcal{J}$ *counted with multiplicity.*

Proof. The proof of the lemma follows the ones of Lemmas 4.1 and 4.2 in [14]. Following Lemma 4.1 in [14], we want to compute $\mathcal{Z}_{u,1}, \mathcal{Z}_{u,2}$ such that

$$\mathcal{Z}_{u,1} \geq \sup_{\mu\in\mathcal{J}} \left\| \mathbb{1}_{\Omega\setminus\Omega_0} \left(\mathbb{L} - \mu I\right)^{-1} D\mathbb{G}(\bar{u}) \right\|_2,$$
$$\mathcal{Z}_{u,2} \geq \sup_{\mu\in\mathcal{J}} \|\mathbb{1}_{\Omega_0} \left(\Gamma^\dagger \left((L-\mu I)^{-1}\right) - \left(\mathbb{L} - \mu I\right)^{-1}\right) D\mathbb{G}(\bar{u})\|_2.$$

Noticing that $\left(\mathbb{L}_{n_2} - \mu I\right)^{-1}$ is the convolution operator associated to the function $f_{n_2,\mu}$ defined in Lemma 3.5.4, we combine Lemma 3.4.8 and Lemma 3.5.4 to obtain that

$$2d_1(\bar{V}, \bar{V} * E) \geq \sup_{\mu\in\mathcal{J}} \left\|\mathbb{1}_{\Omega\setminus\Omega_0}(\mathbb{L} - \mu I)^{-1} D\mathbb{G}(\bar{u})\right\|_2,$$
$$\left[2d_1 + C(d_1)e^{-2ad_1}\right](\bar{V}, \bar{V} * E)_2 \geq \sup_{\mu\in\mathcal{J}} \left\| \mathbb{1}_{\Omega_0} \left(\Gamma^\dagger \left((L-\mu I)^{-1}\right) - \left(\mathbb{L} - \mu I\right)^{-1}\right) D\mathbb{G}(\bar{u}) \right\|_2.$$

In particular, this validates our choice for $\mathcal{Z}_{u,1}, \mathcal{Z}_{u,2}$. In fact, as explained in the proof of Theorem 5.2 in [14], the extra factor 2 in the bounds $\mathcal{Z}_{u,1}, \mathcal{Z}_{u,2}$ allows them to satisfy the inequalities for $\mathcal{Z}_{u,1}^{(q)}, \mathcal{Z}_{u,2}^{(q)}$ in Lemma 4.2 in [14]. This means that we can choose $\mathcal{Z}_{u,1}^{(q)} = \mathcal{Z}_{u,1}$ and $\mathcal{Z}_{u,2}^{(q)} = \mathcal{Z}_{u,2}$ in the aforementioned lemma. For the bound $\mathcal{Z}_{u,3}$, we need

$$\mathcal{Z}_{u,3} \geq \sup_{\mu\in\mathcal{J}} \Big(\left\|\pi^N (S+tI)^{-1} P^{-1} (L - \mu I)\right\|_2 \cdot \left\| \mathbb{1}_{\Omega_0} \left(\Gamma^\dagger((L-\mu I)^{-1}) - \left(\mathbb{L} - \mu I\right)^{-1}\right) D\mathbb{G}(\bar{u}) \right\|_2 \Big).$$

For a fixed $\mu \in \mathcal{J}$, the first factor on the right-hand side is bounded by

$$\left\|\pi^N (S+tI)^{-1} P^{-1} (L - \mu I)\right\|_2 \leq \left\|\pi^N (S+tI)^{-1} P^{-1} (L - \delta_0 I)\right\|_2 \cdot \left\|(L-\delta_0 I)^{-1}(L-\mu I)\right\|_2.$$

Next, we derive

$$\|(L-\delta_0 I)^{-1}(L-\mu I)\|_2 = \sup_{n\in\mathbb{N}_0^2} \frac{l(\tilde{n}) - \mu}{l(\tilde{n}) - \delta_0} = \sup_{n\in\mathbb{N}_0^2} 1 + \frac{\delta_0 - \mu}{l(\tilde{n}) - \delta_0} = \frac{1 - \frac{c^4}{4} - \mu}{1 - \frac{c^4}{4} - \delta_0}$$

using Lemma 3.A.1. Then, recalling $C_{n_2}(\mu)$ from the proof of Lemma 3.5.4, one can prove that $\mu \mapsto C_{n_2}(\mu)\frac{1-\frac{c^4}{4}-\mu}{1-\frac{c^4}{4}-\delta_0}$ is increasing in μ and consequently the maximum is

reached at $\mu = \delta_0$ when considering $\mu \in \mathcal{J}$. This concludes the inequality for $\mathcal{Z}_{u,3}$. The computations of $\mathcal{C}_1$ and $\mathcal{C}_2$ follow directly from the proof of Lemma 3.4.3. In particular, we also use that $\|(\mathbb{L} - \mu I)^{-1}\|_2 \leq \frac{1}{1-\frac{c^4}{4}-\delta_0}$ for all $\mu \in \mathcal{J}$. The rest of the proof follows from [14]. □

The previous lemma provides explicit formulas for the computation of intervals, called Gershgorin intervals, $[\lambda_j - \epsilon_j, \lambda_j + \epsilon_j]$ containing the eigenvalues of $D\mathbb{F}(\tilde{u})$. In fact, it also allows to count the number of eigenvalues in a union of such intervals (if disjoint from the rest of the intervals). This enables us to exactly count the number of negative eigenvalues of $D\mathbb{F}(\tilde{u})$, having in mind the application of Lemma 3.5.1.

3.5.2 Enclosure of θ

In this section, we provide a computer-assisted strategy for enclosing the value of θ defined in Lemma 3.5.1. In fact, we derive the following result.

Lemma 3.5.6. *Let $r_0 > 0$ and let $\tilde{u} \in \mathcal{H}$ be a solution to (3.2) such that $\|\tilde{u} - \bar{u}\|_{\mathcal{H}} \leq r_0$, where $\bar{u} \in \mathcal{H}$ is constructed as in (3.21). Choose $\overline{W} \in \pi^N \ell^2$ such that $\overline{w} \stackrel{\text{def}}{=} \gamma^\dagger(\overline{W}) \in \mathcal{H}$. Let $\epsilon_0, \epsilon > 0$ be defined as*

$$\epsilon_0 \stackrel{\text{def}}{=} \kappa_1 r_0 + 4c^2 \|D\mathbb{F}(\tilde{u})^{-1}\|_2 \left(\|\partial_{x_1} \bar{u} + \frac{1}{2c} D\mathbb{F}(\bar{u})\overline{w}\|_2 + \frac{r_0}{2-c^2} + \frac{1}{2c}(1 - e^{\kappa_2 r_0})\|e^{\bar{U}} \overline{W}\|_1 \right),$$

$$\epsilon \stackrel{\text{def}}{=} \|\bar{u} + 2c\overline{w}\|_2 \|\partial_{x_1}^2 \mathbb{L}^{-1}\|_2 r_0 + \epsilon_0 \left(\|\partial_{x_1}^2 \bar{u}\|_2 + \frac{r_0}{2-c^2} \right). \tag{3.55}$$

Then, we obtain that

$$\theta \in [\theta_0 - \epsilon, \theta_0 + \epsilon], \tag{3.56}$$

where

$$\theta_0 \stackrel{\text{def}}{=} |\Omega_0| \left((\bar{U} + 2c\overline{W}), \partial_{x_1}^2 \bar{U} \right)_2,$$

in which the coefficients of the second derivative are given by $(\partial_{x_1}^2 \bar{U})_n = -\frac{n_1^2 \pi^2}{d_1^2} \bar{U}_n$ for all $(n_1, n_2) \in \mathbb{N}_0^2$.

Proof. Recalling the definition of θ in (3.42), we have

$$\theta = \int_\Omega (\bar{u} + 2c\overline{w}) \partial_{x_1}^2 \bar{u} + \int_\Omega (\bar{u} + 2c\overline{w}) \partial_{x_1}^2 (\tilde{u} - \bar{u}) + \int_\Omega (\tilde{u} - \overline{u} + 2c\tilde{w} - 2c\overline{w}) \partial_{x_1}^2 \tilde{u},$$

where $\overline{w} \in \mathcal{H}$ is an approximation of $\tilde{w}$. In particular, employing Cauchy-Schwarz inequality, we have for the second term

$$\begin{aligned} \left| \int_\Omega (\bar{u} + 2c\overline{w}) \partial_{x_1}^2 (\tilde{u} - \bar{u}) \right| &\leq \|\bar{u} + 2c\overline{w}\|_2 \|\partial_{x_1}^2 (\tilde{u} - \bar{u})\|_2 \\ &\leq \|\bar{u} + 2c\overline{w}\|_2 \|\partial_{x_1}^2 \mathbb{L}^{-1}\|_2 \|\mathbb{L}(\tilde{u} - \bar{u})\|_2 \\ &\leq \|\bar{u} + 2c\overline{w}\|_2 \|\partial_{x_1}^2 \mathbb{L}^{-1}\|_2 r_0 \end{aligned}$$

using that $\|\mathbb{L}(\tilde{u}-\bar{u})\|_2 = \|\tilde{u}-\bar{u}\|_{\mathcal{H}} \leq r_0$. Applying the Fourier transform, we have for the second norm on the right-hand side that

$$\|\partial_{x_1}^2 \mathbb{L}^{-1}\|_2 \leq \sup_{\xi\in\mathbb{R}^2} \frac{(2\pi\xi_1)^2}{l(\xi)} \leq \frac{1}{2-c^2}.$$

Furthermore, we have for the third term of θ that

$$\begin{aligned}\left|\int_\Omega (\tilde{u}-\overline{u}+2c\tilde{w}-2c\overline{w})\partial_{x_1}^2\tilde{u}\right| &\leq \|\tilde{u}-\overline{u}+2c\tilde{w}-2c\overline{w}\|_2\|\partial_{x_1}^2\tilde{u}\|_2\\ &\leq (\|\tilde{u}-\overline{u}\|_2+2c\|\tilde{w}-\overline{w}\|_2)(\|\partial_{x_1}^2\bar{u}\|_2\\ &\quad+\|\partial_{x_1}^2(\tilde{u}-\bar{u})\|_2)\\ &\leq (\kappa_1 r_0+2c\|\tilde{w}-\overline{w}\|_2)\left(\|\partial_{x_1}^2\bar{u}\|_2+\tfrac{r_0}{2-c^2}\right).\end{aligned}$$

It remains to estimate $\|\tilde{w}-\overline{w}\|_2$. By definition of $\tilde{w}$ in (3.41), we have

$$\|\tilde{w}-\overline{w}\|_2 = \|-2cD\mathbb{F}(\tilde{u})\partial_{x_1}^2\tilde{u}-\overline{w}\|_2 \leq 2c\|D\mathbb{F}(\tilde{u})^{-1}\|_2\|\partial_{x_1}\tilde{u}+\tfrac{1}{2c}D\mathbb{F}(\tilde{u})\overline{w}\|_2.$$

For the second norm on the right-hand side

$$\begin{aligned}\|\partial_{x_1}\tilde{u}+\frac{1}{2c}D\mathbb{F}(\tilde{u})\overline{w}\|_2 \leq \|\partial_{x_1}\bar{u}+\frac{1}{2c}D\mathbb{F}(\bar{u})\overline{w}\|_2 &+ \left\|\partial_{x_1}^2(\bar{u}-\tilde{u})\right\|_2\\ &+\frac{1}{2c}\|D\mathbb{F}(\bar{u})\overline{w}-D\mathbb{F}(\tilde{u})\overline{w}\|_2.\end{aligned}$$

For the last term, we estimate

$$\begin{aligned}\|D\mathbb{F}(\bar{u})\overline{w}-D\mathbb{F}(\tilde{u})\overline{w}\|_2 = \|(e^{\bar{u}}-e^{\tilde{u}})\overline{w}\|_2 &\leq \|1-e^{\tilde{u}-\bar{u}}\|_2\|e^{\bar{u}}\overline{w}\|_\infty\\ &\leq (1-e^{\kappa_2 r_0})\|e^{\bar{U}}\overline{W}\|_1.\end{aligned}$$

Finally, using $\bar{u}=\gamma^\dagger(\bar{U})$ and $\overline{w}=\gamma^\dagger(\overline{W})$, we apply Parseval's identity to get

$$\int_\Omega (\bar{u}+2c\overline{w})\partial_{x_1}^2\bar{u} = |\Omega_0|\left((\bar{U}+2c\overline{W}),\partial_{x_1}^2\bar{U}\right)_2,$$

where $(\partial_{x_1}^2\bar{U})_n = -\frac{n_1^2\pi^2}{d_1^2}\bar{U}_n$ for all $(n_1,n_2)\in\mathbb{N}_0^2$. After algebraic manipulation, this concludes the proof. □

Using the previous result, we obtain a computer-assisted strategy for the enclosure of the value of θ. Indeed, the constant ϵ depends on finite-dimensional computations, which can be handled using rigorous numerics (cf. [76]). In particular, this allows us to conclude about the stability of $\tilde{u}$.

Remark 3.5.7. *We emphasize that the orbital stability established here is restricted to the subspace of perturbations that are symmetric with respect to x_2. While we explicitly decomposed the space $L^2(\Omega)$ into even and odd subspaces with respect to the x_1-direction (see* (3.45)*), our choice of ansatz in* (3.5) *restricts the analysis to functions that are even in x_2. Consequently, the analysis does not*

rule out the potential existence of unstable functions that are antisymmetric in x_2, which may still satisfy the boundary conditions (3.3). *To prove stability against the full class of admissible perturbations satisfying* (3.3), *one can employ a domain doubling technique in the x_2-direction and mirror and shift the solution, as demonstrated in [65].*

3.6 Results

In this section, we present computer-assisted proofs for the existence of solutions to (3.2) with boundary conditions (3.3). To do so, we begin with approximate solutions obtained by Newton's method and initialized with carefully constructed guesses based on approximations in the periodic setting described in [79]. To extend the initial guesses in the periodic case to the infinite setting, we project them into the kernel of matrix $\mathcal{T}$, as described in Section 3.3.1.

By combining these new approximations with the estimates established in the previous section, we obtain a validated proof of existence for solutions to the suspension bridge equation within explicitly controlled error bounds. This leads to the following theorem statement:

Theorem 3.6.1. *For $c = 1.2$, $d = (\frac{\pi}{0.06}, \frac{\pi}{0.24})$, $N_0 = (150, 80)$, $N = (40, 40)$, there exists a solution $\tilde{u} \in \mathcal{H} \cap C^\infty(\Omega)$ to* (3.2) *on Ω with boundary conditions* (3.3) *in the x_2-direction such that*

$$\|\tilde{u} - \bar{u}\|_{\mathcal{H}} \leq 9.5 \cdot 10^{-8},$$

where $\bar{u}$ is a numerically computed approximation visualized in Figure 3.1.1. Moreover, $D\mathbb{F}(\tilde{u}) : \mathcal{H} \to L^2(\Omega)$ possesses exactly one negative eigenvalue and $\theta > 0$, where θ is given in (3.42). *Finally, $\tilde{u}$ is orbitally stable.*

Proof. Recall that ν and N^{FFT} are defined in Section 3.3.2. Furthermore, we choose $\nu = (1.1, 1.1)$ and $N^{\mathrm{FFT}} = (512, 512)$. Finitely many cosine coefficients of the approximate solution $\bar{u}$, visualized in Figure 3.1.1, can be found in the code in [76]. We report the values for the bounds in floating point numbers displaying finitely many decimals. We have

$$\mathcal{Y}_0 = 6.0005 \cdot 10^{-8}, \quad \mathcal{Z}_1 = 3.6608 \cdot 10^{-1}, \quad \mathcal{Z}_2 = 22.7926.$$

Letting $\tilde{u}$ denote the zero of $\mathbb{F}$, we apply Theorem 3.3.1 to obtain the error bound

$$\|\tilde{u} - \bar{u}\|_{\mathcal{H}} \leq 9.4657 \cdot 10^{-8}.$$

Note that the regularity of $\tilde{u}$ (and the fact that it is infinitely differentiable) is a direct consequence of Proposition 2.5 in [16]. Concerning the enclosure of the spectrum, we apply the analysis derived in Section 3.5.1. In particular, we apply Lemma 3.5.5 and prove that $D\mathbb{F}_e(\tilde{u})$ possesses exactly one negative eigenvalue and the rest of its spectrum is purely positive. Indeed, we prove that one Gershgorin interval $[\lambda_0 - \epsilon_0, \lambda_0 + \epsilon_0] \subset [-0.1743, -0.1286]$ of Lemma 3.5.5 is fully contained in

the negative part of $\mathbb{R}$, and the rest of the intervals are disjoint from $[\lambda_0-\epsilon_0, \lambda_0+\epsilon_0]$ and fully located in the positive part of $\mathbb{R}$.

Moreover, for $D\mathbb{F}_o(\tilde{u})$, we obtain an interval $[\lambda_0 - \epsilon_0, \lambda_0 + \epsilon_0] \subset [-0.0364, 0.0119]$ (using the notation of Lemma 3.5.5) which is disjoint from the rest of the intervals and which contains the number 0. We also prove that the rest of the spectrum is purely positive. Consequently, there exists an eigenvalue λ, of undetermined sign, in $[\lambda_0 - \epsilon_0, \lambda_0 + \epsilon_0]$. However, we prove that $\lambda = 0$ is an eigenvalue. Indeed, since $\tilde{u}$ is a zero of $\mathbb{F}$, we have

$$0 = \partial_{x_1}\mathbb{F}(\tilde{u}) = D\mathbb{F}(\tilde{u})\partial_{x_1}\tilde{u}. \tag{3.57}$$

This implies that $\partial_{x_1}\tilde{u}$ is in the kernel of $D\mathbb{F}(\tilde{u})$. Moreover, since $\tilde{u} \in \mathcal{H}$, then $\partial_{x_1}\tilde{u} \in L^2_o$, using the notation of (3.45). In particular, since $\tilde{u} \neq 0$, we obtain that $0 \in Eig(D\mathbb{F}_o(\tilde{u}))$. This implies that $\lambda = 0$. Concerning the sign of θ, we use Lemma 3.5.6 and prove that $\theta > 0$. Finally, we conclude the proof using Lemma 3.5.1. □

The code used to obtain the above result, as well as the results presented later in this section, can be found in [76]. The computations were carried out in Julia (v1.10.4) on an Apple M1 Pro CPU with 32 GB RAM. We heavily relied on interval arithmetic using the packages IntervalArithmetic.jl ([58]) and RadiiPolynomial.jl ([31]) to ensure that the computations are rigorous.

The method developed in this chapter is versatile and can also be applied to rigorously prove existence of solutions on infinite strips for other parameter values (e.g. different c, d_1, d_2) and with alternative spatial patterns. Two illustrative examples are presented in Figure 3.6.1. In contrast to the approximation shown in Figure 3.1.1, which contains a single prominent peak at the bottom, the approximations in Figure 3.6.1 show an alternative spatial pattern characterized by two dominant peaks at the bottom. In Figure 3.6.1a, the parameter c is slightly increased relative to the value used in Theorem 4.1.1, while in Figure 3.6.1b, it is decreased. The plots indicate that reducing the value of c leads to an increase in the amplitude of the resulting wave patterns.

The existence theorems and corresponding proofs, with stability analysis, of the two alternative patterns are given below.

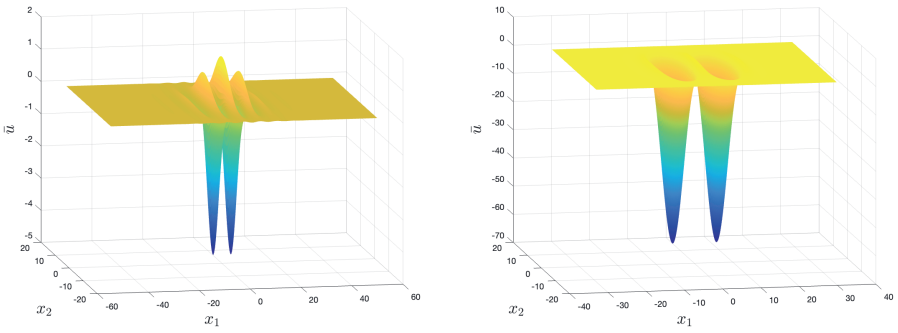
Theorem 3.6.2. *For $c = 1.3$, $d = (\frac{\pi}{0.06}, \frac{\pi}{0.2})$, $N_0 = (100, 60)$, $N = (60, 60)$, there exists a solution $\tilde{u} \in \mathcal{H} \cap C^\infty(\Omega)$ to (3.2) on Ω with boundary conditions (3.3) in the x_2-direction such that*

$$\|\tilde{u} - \bar{u}\|_{\mathcal{H}} \leq 3.1 \cdot 10^{-6},$$

where $\bar{u}$ is a numerically computed approximation visualized in Figure 3.6.1a. Moreover, $D\mathbb{F}(\tilde{u}) : \mathcal{H} \to L^2(\Omega)$ possesses exactly two negative eigenvalues and $\theta > 0$, where θ is given in (3.42). Finally, $\tilde{u}$ is orbitally unstable.

Proof. We choose $\nu = (1.1, 1.1)$ and $N^{\text{FFT}} = (512, 512)$. We have

$$\mathcal{Y}_0 = 2.4835 \cdot 10^{-6}, \quad \mathcal{Z}_1 = 1.792 \cdot 10^{-1}, \quad \mathcal{Z}_2 = 40.3926.$$



(a) Approximate solution for $c = 1.3$. (b) Approximate solution for $c = 0.8$.

Figure 3.6.1: Visualization of approximate two-peak solutions $\bar{u}$ to (3.2). The approximations are truncated to a finite domain in these plots.

Letting $\tilde{u}$ denote the zero of $\mathbb{F}$, we apply Theorem 3.3.1 to obtain the error bound

$$\|\tilde{u} - \bar{u}\|_{\mathcal{H}} \leq 3.0256 \cdot 10^{-6}.$$

The stability part follows similarly as the one presented in the proof of Theorem 4.1.1. In this case, we provide the existence of exactly two negative eigenvalues by proving that two Gershgorin intervals of Lemma 3.5.5 are in the negative part of $\mathbb{R}$, disjoint from one another, and disjoint from the rest of the intervals. □

The next theorem and its proof are very similar to the previous ones. However, the stability analysis is more involved, so we choose to present the full proof again.

Theorem 3.6.3. *For $c = 0.8$, $d = (\frac{\pi}{0.1}, \frac{\pi}{0.2})$, $N_0 = (80, 60)$, $N = (80, 60)$, there exists a solution $\tilde{u} \in \mathcal{H} \cap C^\infty(\Omega)$ to (3.2) on Ω with boundary conditions (3.3) in the x_2-direction such that*

$$\|\tilde{u} - \bar{u}\|_{\mathcal{H}} \leq 4.0 \cdot 10^{-5},$$

where $\bar{u}$ is a numerically computed approximation visualized in Figure 3.6.1b. Moreover, $D\mathbb{F}(\tilde{u}) : \mathcal{H} \to L^2(\Omega)$ possesses exactly two negative eigenvalues and $\theta > 0$, where θ is given in (3.42). Finally, $\tilde{u}$ is orbitally unstable.

Proof. We choose $\nu = (1.1, 1.1)$ and $N^{\mathrm{FFT}} = (512, 512)$. We have

$$\mathcal{Y}_0 = 3.3557 \cdot 10^{-5}, \quad \mathcal{Z}_1 = 1.4034 \cdot 10^{-1}, \quad \mathcal{Z}_2 = 65.7018.$$

Letting $\tilde{u}$ denote the zero of $\mathbb{F}$, we apply Theorem 3.3.1 to obtain the error bound

$$\|\tilde{u} - \bar{u}\|_{\mathcal{H}} \leq 3.9094 \cdot 10^{-5}.$$

For the stability part, we obtain $\lambda_{min} \approx -15$, using the notation of Lemma 3.5.3. Then, we choose $t > \lambda_{min}$ in Lemma 3.5.5 and compute the bounds of the lemma to compute the Gershgorin intervals $\overline{B_{\epsilon_j}(\lambda_j)}$. We obtained intersecting intervals and could not conclude about the localization of negative eigenvalues. However, we obtained that the union of all the intervals was contained in $(-0.4, \infty)$. This implies that we can improve our choice for λ_{min} and choose $\lambda_{min} = -0.45$. Choosing $t = 0.5$ in Lemma 3.5.3 and computing the bounds again, we get tighter radii for the Gershgorin intervals and obtain disjoint intervals on the negative part of $\mathbb{R}$.

The stability part then follows similarly as the one presented in the proof of Theorem 4.1.1. In this case, we provide the existence of exactly two negative eigenvalues by proving that two Gershgorin intervals of Lemma 3.5.5 are in the negative part of $\mathbb{R}$, disjoint from one another, and disjoint from the rest of the intervals. □

The computation time to obtain the result in Theorem 4.1.1 was 892 seconds, including the stability proof. The computation times corresponding to the results in Theorems 3.6.2 and 3.6.3 were 420 and 586 seconds, respectively. The increased computation time associated with our first theorem arises from selecting a larger value for N_0, which in turn yields a tighter error bound.

Appendix 3.A Technical results

In the next lemma we provide some technical results about l_n, where we recall from (3.6) that

$$l_{n_2}(\xi_1) = (2\pi)^4(\xi_1^2 + \tilde{n}_2^2)^2 - c^2(2\pi\xi_1)^2 + 1$$

and that $\tilde{n}_2 = \frac{n_2}{2d_2}$.

Lemma 3.A.1. *We have*

$$\min_{\xi_1 \in \mathbb{R}} l_{n_2}(\xi_1) = \begin{cases} c^2\tilde{n}_2^2 + 1 - \frac{c^4}{4} & \text{if } 0 \le n_2 \le \frac{d_2 c}{\pi\sqrt{2}} \\ \tilde{n}_2^4 + 1 & \text{otherwise.} \end{cases} \tag{3.58}$$

Furthermore, given $n_2 \ge \frac{d_2 c}{\pi}$, we have

$$l_{n_2}(\xi_1) \ge \frac{(2\pi)^4}{2}(\tilde{n}_2^2 + \xi_1^2)^2$$

for all $\xi \in \mathbb{R}$. In particular, given $N \in \mathbb{N}$ such that $N > \frac{d_2 c}{\pi}$, this implies that

$$\sum_{n_2=N+1}^{\infty} \left\| \frac{1}{l_{n_2}} \right\|_2^2 \le \frac{5(2d_2)^7}{48(2\pi)^7 N^6}. \tag{3.59}$$

Proof. Denoting $x = (2\pi\xi_1)^2$ and $\alpha = (2\pi\xi_2)^2$, we have

$$l(\xi_1, \xi_2) = (x + \alpha)^2 - c^2 x + 1 \stackrel{\text{def}}{=} p_\alpha(x).$$

Studying the variations of p_α, we have that p_α has a global minimum at $x = \frac{c^2}{2} - \alpha$. In particular, this implies that

$$l(\xi_1, \xi_2) \geq \begin{cases} (2\pi\xi_2)^2 c^2 + 1 - \frac{c^4}{4} & \text{if } \frac{c^2}{2} \geq (2\pi\xi_2)^2 \\ (2\pi\xi_2)^4 + 1 & \text{otherwise.} \end{cases}$$

Choosing $\xi_2 = \frac{n_2}{2d_2}$, we obtain the desired result. To prove the remaining statement, notice that

$$\begin{aligned} l_{n_2}(\xi_1) - \frac{1}{2}((2\pi\tilde{n}_2)^2 + (2\pi\xi_1)^2)^2 &= \frac{1}{2}((2\pi\tilde{n}_2)^2 + x)^2 - c^2 x + 1 \\ &= \frac{1}{2}((2\pi\tilde{n}_2)^4 + 2(2\pi\tilde{n}_2)^2 x + x^2) - c^2 x + 1 \end{aligned}$$

where $x = (2\pi\xi_1)^2$. Consequently, we have that $l_{n_2}(\xi_1) - \frac{1}{2}((2\pi\tilde{n}_2)^2 + (2\pi\xi_1)^2)^2 \geq 0$ if $2\pi\tilde{n}_2 \geq c$. Now, we have

$$\left\| \frac{1}{l_{n_2}} \right\|_2^2 \leq \frac{4}{(2\pi)^8} \int_{\mathbb{R}} \frac{1}{(\tilde{n}_2^2 + \xi_1^2)^4} d\xi_1 = \frac{20\pi}{16(2\pi)^8 \tilde{n}_2^7} = \frac{5}{8(2\pi\tilde{n}_2)^7}.$$

Moreover, we get

$$\sum_{n_2=N+1}^{\infty} \frac{1}{\tilde{n}_2^7} = (2d_2)^7 \sum_{n_2=N+1}^{\infty} \frac{1}{n_2^7} \leq (2d_2)^7 \int_N^{\infty} \frac{1}{x^7} dx = \frac{(2d_2)^7}{6N^6}.$$

Noticing that $2\pi\tilde{n}_2 \geq c$ is equivalent to $n_2 \geq \frac{d_2 c}{\pi}$, we have

$$\sum_{n_2=N+1}^{\infty} \left\| \frac{1}{l_{n_2}} \right\|_2^2 \leq \frac{(2d_2)^7}{6N^6} \frac{5}{8(2\pi)^7}$$

where $N \in \mathbb{N}$ such that $N > \frac{d_2 c}{\pi}$. □

4 Traveling wave solutions in the three-dimensional Navier-Stokes equations

4.1 Introduction

The Navier-Stokes equations, which describe the motion of viscous fluids, remain among the most significant and challenging systems in mathematical physics [24, 34]. Derived from Newton's second law of motion and the conservation of mass, these nonlinear partial differential equations govern how a fluid's flow reacts to viscous friction, pressure gradients and external forces.

To formulate this in a three-dimensional domain, we describe the fluid motion in terms of the velocity field $U = U(X_1, X_2, X_3, T)$ and the kinematic pressure $p(X_1, X_2, X_3, T) = \frac{P}{\rho}$, where P is the pressure and ρ denotes the constant fluid density. Additionally, let ν be the kinematic viscosity and $f = f(X_1, X_2, X_3)$ represent a time-independent external forcing. The Navier-Stokes equations for incompressible fluids are given by

$$\begin{cases} \partial_T U + (U \cdot \nabla)U - \nu \Delta U + \nabla p = f, \\ \nabla \cdot U = 0. \end{cases} \tag{4.1}$$

We restrict our spatial domain to the three-dimensional torus $\mathbb{T}^3 = (\mathbb{R}/2\pi\mathbb{Z})^3$, which we identify with the fundamental domain $[-\pi, \pi]^3$ equipped with periodic boundary conditions. Furthermore, we choose f as the Taylor-Green forcing

$$f = \begin{pmatrix} 2 \sin X_1 \cos X_2 \\ -2 \cos X_1 \sin X_2 \\ 0 \end{pmatrix}.$$

The forcing f has a zero spatial mean, i.e., $\int_{\mathbb{T}^3} f \, dx = 0$. This condition is necessary to guarantee the existence of bounded solutions. If we integrate the incompressible Navier-Stokes equations over the periodic domain $\mathbb{T}^3$, all terms involving spatial derivatives exactly vanish due to the periodic boundary conditions. This leaves us with $\frac{d}{dt} \int_{\mathbb{T}^3} u \, dx = \int_{\mathbb{T}^3} f \, dx$. Consequently, any net constant forcing would cause the spatial integral of the velocity field to grow linearly in time. This would exclude the existence of bounded traveling wave solutions.

Using the ansatz for traveling waves

$$U(X_1, X_2, X_3, T) = u(X_1, X_2, X_3 - cT) = u(x_1, x_2, x_3) = u(x) = u,$$

where c denotes the wave speed, we can rewrite (4.1) as the stationary system

$$\begin{cases} -c\partial_{x_3} u + (u \cdot \nabla)u - \nu \Delta u + \nabla p = f, \\ \nabla \cdot u = 0. \end{cases} \tag{4.2}$$

Due to the nonlinearity of the advection term $(u \cdot \nabla)u$, finding explicit analytical solutions to (4.2) is generally complicated. Historically, researchers have relied on standard numerical simulations to approximate fluid behavior, but these methods can struggle to isolate unstable solution profiles. Recently, machine learning techniques, specifically Physics-Informed Neural Networks (PINNs), have emerged as an alternative approach for discovering such complicated fluid structures. PINNs incorporate the partial differential equations directly into the loss function of a neural network, guiding the algorithm to find approximate solutions that obey the underlying physics. For instance, PINNs have been successfully used to discover families of unstable singularities in the three-dimensional Euler equations [81], representing the inviscid limit of the Navier-Stokes equations.

While [81] focuses on unstable singularities in nonlinear fluid systems other than the viscous Navier-Stokes equations, it highlights a broader challenge in fluid dynamics: solutions are often exceedingly difficult to detect and verify using standard numerical simulations or classical analysis alone. Validating the existence of such specific solutions, whether they be singular profiles in the three-dimensional Euler equations or, as in our case, traveling waves in the Navier-Stokes equations, requires moving to rigorous mathematical verification. For this purpose we employ Computer-Assisted Proofs (CAP).

As discussed in previous chapters, these methods typically rely on a Newton-Kantorovich type argument, where the differential equation is formulated as a zero-finding problem $F(u) = 0$ in a suitable Banach space. By computing an approximate inverse for the linearized operator, one derives rigorous error bounds that guarantee the existence of a true solution within a small, explicitly quantifiable neighborhood of the numerical approximation. For a broad overview of these techniques in the context of partial differential equations, we refer the reader to the survey [30] and the book [49].

As discussed in the general introduction of this thesis in Chapter 1, CAPs have established themselves as a powerful tool for rigorously verifying fluid behaviors that are otherwise difficult to isolate. This methodology has been successfully applied to a wide spectrum of Navier-Stokes problems, ranging from foundational planar stationary states [84] and hydrodynamic instabilities [38, 83] to nonlinear phenomena such as Hopf bifurcations [5] and spontaneous periodic orbits [68].

More recently, the research on CAPs has shifted toward the analytical challenges posed by three-dimensional spatial dynamics and nontrivial geometries [41, 82, 86]. In this chapter, we build upon this trajectory by proving the existence of a traveling wave solution for the three-dimensional system (4.2). While our proof strategy is heavily inspired by the framework established in [68] for periodic orbits, the shift to a three-dimensional traveling wave introduces computational and analytical hurdles mainly caused by the expansion in the number of Fourier modes needed.

We apply this framework to prove the existence of a traveling wave solution for (4.2). The main theorem of this chapter is as follows:

Theorem 4.1.1. *For viscosity $\nu = 0.2069$ and wave speed $c = -2.5805$, there exists a traveling wave solution $(\tilde{u}, \tilde{p})$ to the Navier-Stokes equations* (4.2)*. Specif-*

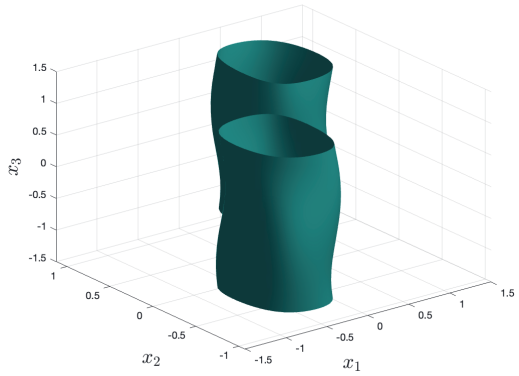


Figure 4.1.1: Level set at value 4 of the vorticity of the third component of the numerical approximation $\overline{u}$ to (4.2), of which finitely many Fourier coefficients can be found in [73].

ically, there exists a divergence-free velocity field $\tilde{u}$ in the Banach space $\mathcal{X}$ (defined in Section 4.4) and an associated pressure profile $\tilde{p}$, such that

$$\|\tilde{u} - \overline{u}\|_{\mathcal{X}} \leq 4.7 \cdot 10^{-5},$$

where $\overline{u}$ is a numerically computed approximation. The finite set of nonzero Fourier coefficients defining $\overline{u}$ is available in [73] and a level set of the third component of its vorticity $\nabla \times \bar{u}$ is visualized in Figure 4.1.1.

While [68] focused on periodic dynamics in two spatial dimensions, our work considers the three-dimensional Navier-Stokes equations. By employing a traveling wave ansatz, we reduce this space-time problem into a stationary three-dimensional one, analogous to the effective dimensionality of the two-dimensional time-periodic case. However, the novelty of this chapter lies in overcoming the analytical and computational challenges introduced by this shift. Unlike in two dimensions, we must control three nontrivial vorticity components. Furthermore, the lower viscosity ($\nu = 0.2069$) considered here necessitates a substantially larger number of Fourier modes to accurately represent numerical approximations. This increase in modes drastically expands the problem, resulting in a validation that requires approximately three weeks of computation time. It should be emphasized that achieving this three-week execution time was possible only after implementing the further computational reductions detailed in Remark 4.5.1.

The rest of the chapter is organized as follows. We start by discussing the setup of the problem leading to our zero-finding problem formulation in Section 4.2. In Section 4.3, the symmetries are discussed that will be taken advantage of to manage the computational load. The existence theorem is stated in Section 4.4 and the corresponding bounds are given in Section 4.5. Finally, the main result consisting of the proof of Theorem 4.1.1 will be given in Section 4.6.

4.2 Setup

We follow the notation and procedure described in [68] to derive a zero-finding problem in terms of Fourier coefficients. To this end, we introduce the vorticity $\omega = \nabla \times u$ and take the curl of the velocity equation (4.2). This operation eliminates the pressure gradient, since the curl of any gradient field vanishes, i.e., $\nabla \times \nabla p = 0$. When evaluating the curl of the nonlinear advection term $(u \cdot \nabla)u$, we apply vector identities to obtain $(u \cdot \nabla)\omega - (\omega \cdot \nabla)u + \omega(\nabla \cdot u) - u(\nabla \cdot \omega)$. The incompressibility condition causes the last two terms to vanish. This results in the stationary vorticity equation:

$$-c\partial_{x_3}\omega + (u \cdot \nabla)\omega - (\omega \cdot \nabla)u - \nu\Delta\omega = f^{\omega}, \tag{4.3}$$

where f^{ω} denotes $\nabla \times f$.

Furthermore, the incompressibility condition plays a second crucial role: it is required to uniquely recover u from the vorticity ω. As the curl of a gradient is always zero, multiple velocity fields can share the same vorticity. For example, adding an arbitrary gradient field or a constant vector to the velocity field leaves the resulting vorticity completely unchanged. However, by requiring that u is divergence-free (incompressible) and has a spatial mean of zero, we eliminate these extra possibilities, ensuring a one-to-one mapping between the velocity and vorticity fields.

To transform the problem into Fourier space, we first introduce the Fourier series representation of the vorticity field

$$\omega = \sum_{n \in \mathbb{Z}^3_*} \omega_n e^{i(n_1 x_1 + n_2 x_2 + n_3 x_3)},$$

where $n = (n_1, n_2, n_3)$. Furthermore, $\mathbb{Z}^3_* := \mathbb{Z}^3 \backslash \{0\}$ is defined to explicitly exclude the zeroth Fourier coefficient of the vorticity ω_0. Since $\omega = \nabla \times u$, its Fourier representation is given by $\omega_n = in \times u_n$. Evaluating this at $n = 0$ trivially yields $\omega_0 = 0$ for any velocity field. As this zeroth coefficient is not actually an unknown variable, it is entirely omitted from the zero-finding problem, allowing us to restrict ourselves to indices in $\mathbb{Z}^3_*$.

Let $n^2 = n_1^2 + n_2^2 + n_3^2$. In Fourier space, the relationship between the velocity and vorticity is expressed as $u_n = M_n \omega_n$, where M_n is defined, following [68], as

$$M_n = \begin{cases} \dfrac{i}{n^2} \begin{pmatrix} 0 & -n_3 & n_2 \\ n_3 & 0 & -n_1 \\ -n_2 & n_1 & 0 \end{pmatrix} & n \neq 0, \\ 0 & n = 0. \end{cases}$$

To translate the nonlinear advection terms of (4.3) into Fourier space, we must define the convolution of sequences. Let the convolution product of Fourier sequences $a = (a_n)$, $b = (b_n)$ in $\mathbb{C}^{\mathbb{Z}^3}$ be defined as

$$(a * b)_n = \sum_{l \in \mathbb{Z}^3} a_l b_{n-l}.$$

Furthermore, let $v^{(m)} \in \mathbb{C}^{\mathbb{Z}^3}$, for $m \in \{1,2,3\}$, be the Fourier sequence of the m'th component of v. We define the sequence $D_m v$ corresponding to the partial derivatives of v with respect to x_m, up to a factor i, as

$$(D_m v)_n = n_m v_n$$

for $n \in \mathbb{Z}^3$. Using these definitions, we define for $v, w \in (\mathbb{C}^3)^{\mathbb{Z}^3}$

$$\left[(v \star \tilde{D})w\right]^{(m)} = \sum_{p=1}^{3} v^{(p)} * \left(D_p w^{(m)}\right).$$

We can now formulate the main component of our zero-finding problem. For this purpose, we define

$$F_n(W) = -ci n_3 \omega_n + \Psi_n(\omega) + \nu n^2 \omega_n - f_n^{\omega},$$

for variables $W = \begin{pmatrix} c \\ (\omega_n)_{n \in \mathbb{Z}^3_*} \end{pmatrix}$ and where

$$\Psi_n(\omega) := i\left[\left(M\omega \star \tilde{D}\right)\omega\right]_n - i\left[\left(\omega \star \tilde{D}\right)M\omega\right]_n.$$

Remark 4.2.1. *Only the first term of F_n differs in comparison to the one in [68].*

As for the phase condition, we consider

$$\int_{\mathbb{T}^3} \omega(x) \cdot \partial_{x_3} \hat{\omega}(x) dx = 0,$$

where $\mathbb{T}^3$ indicates the 3-torus with side length 2π and $\hat{\omega}$ represents an approximate periodic orbit. To implement this computationally, we impose the phase condition

$$F_c(W) = i \sum_{m=1}^{3} \sum_{n \in \mathbb{Z}^3} \omega_n^{(m)} n_3 \left(\hat{\omega}_n^{(m)}\right)^*,$$

in which * denotes the complex conjugation. We remark that the subscript c in F_c does not indicate that the phase condition depends on the wave speed. Instead, it denotes that this phase condition is appended to the system to account for the additional unknown c. Then, the full zero-finding problem becomes $\mathcal{F} = 0$ where

$$\mathcal{F} = \begin{pmatrix} F_c \\ (F_n)_{n \in \mathbb{Z}^3_*} \end{pmatrix}. \tag{4.4}$$

Solving this infinite-dimensional system results in the Fourier coefficients and wave speed of a traveling wave solution. As illustrated in the bifurcation diagram in Figure 1.3.3 of Chapter 1, numerical continuation reveals that the second bifurcation point (the light blue dot at $\nu \approx 0.2112$) gives rise to a branch of traveling waves propagating in the x_3-direction. By applying our radii polynomial framework to $\mathcal{F}$, we will prove the existence of a traveling wave solution on this specific branch, located just past the bifurcation point.

4.3 Symmetries

To manage the computational time and memory necessary for the CAP, we take advantage of symmetries. The symmetries described in [68] focus on essentially two-dimensional solutions of the Navier-Stokes equations, characterized by the absence of dependence on the x_3-variable. For traveling wave solutions, the symmetry structure is largely analogous. However, the temporal symmetries are replaced by spatial symmetries in the x_3-direction, as the traveling wave ansatz implies a dependence on $X_3 - cT = x_3$. In what follows, we list the symmetries satisfied by the Fourier coefficients ω_n for our traveling wave solution.

4.3.1 Reflection symmetry in x_1 and x_2 (Sx_1Sx_2)

The system admits a symmetry with respect to both the x_1 and x_2 axes, resulting in a reflection in the origin. This symmetry acts on the Fourier coefficients by mapping $n_1 \to -n_1$ and $n_2 \to -n_2$. For the vorticity components, the coefficients satisfy:

$$\begin{aligned}
\omega^{(1)}_{n_1,n_2,n_3} &= -\omega^{(1)}_{-n_1,-n_2,n_3},\\
\omega^{(2)}_{n_1,n_2,n_3} &= -\omega^{(2)}_{-n_1,-n_2,n_3},\\
\omega^{(3)}_{n_1,n_2,n_3} &= \ \ \omega^{(3)}_{-n_1,-n_2,n_3}.
\end{aligned}$$

This implies that the vertical component $\omega^{(3)}$ is invariant under this reflection, whereas the horizontal components $\omega^{(1)}$ and $\omega^{(2)}$ change sign.

4.3.2 Shift and reflection symmetry in x_1 (DSx_1)

The second symmetry combines a reflection in the x_1-direction with a spatial shift of half a period in the (x_1, x_2)-plane. Specifically, the Fourier coefficients satisfy the relation:

$$\begin{aligned}
\omega^{(1)}_{n_1,n_2,n_3} &= \ \ (-1)^{n_1+n_2}\omega^{(1)}_{-n_1,n_2,n_3},\\
\omega^{(2)}_{n_1,n_2,n_3} &= -(-1)^{n_1+n_2}\omega^{(2)}_{-n_1,n_2,n_3},\\
\omega^{(3)}_{n_1,n_2,n_3} &= -(-1)^{n_1+n_2}\omega^{(3)}_{-n_1,n_2,n_3}.
\end{aligned}$$

Here, the factor $(-1)^{n_1+n_2} = e^{i\pi(n_1+n_2)}$ corresponds to the spatial translation by (π, π) in the (x_1, x_2)-plane.

4.3.3 Rotation and shift symmetry (P_4Sx_1R)

This symmetry involves a permutation of the spatial coordinates x_1 and x_2, combined with a phase shift in the x_3-direction. In the essentially two-dimensional case, this shift acted on the temporal variable, while for traveling waves, it acts on n_3. The symmetry relates the first and second components of the vorticity as

follows:

$$\omega^{(1)}_{n_1,n_2,n_3} = -(-1)^{n_2} i^{n_3} \omega^{(2)}_{n_2,n_1,n_3},$$
$$\omega^{(2)}_{n_1,n_2,n_3} = -(-1)^{n_2} i^{n_3} \omega^{(1)}_{n_2,n_1,n_3}.$$

For the third component, the relationship is

$$\omega^{(3)}_{n_1,n_2,n_3} = -(-1)^{n_2} i^{n_3} \omega^{(3)}_{n_2,n_1,n_3}.$$

As the symmetries of the system form a group, the solution must also be invariant under the repeated application of any symmetry. Applying the $P_4 S x_1 R$ transformation twice, by substituting the expression for $\omega^{(2)}$ back into the expression for $\omega^{(1)}$, yields

$$\begin{aligned}\omega^{(1)}_{n_1,n_2,n_3} &= -(-1)^{n_2} i^{n_3} \left(-(-1)^{n_1} i^{n_3} \omega^{(1)}_{n_1,n_2,n_3}\right) \\ &= (-1)^{n_1+n_2+n_3} \omega^{(1)}_{n_1,n_2,n_3}.\end{aligned}$$

A similar derivation holds for $\omega^{(2)}$ and $\omega^{(3)}$. Hence, the solutions satisfy a parity constraint defined by the sum of the indices. The Fourier coefficients vanish unless the sum of the indices is even. i.e.,

$$\omega_n = 0 \quad \text{if } n_1 + n_2 + n_3 \text{ is odd.}$$

This condition corresponds to $\omega_n = (-1)^{n_1+n_2+n_3}\omega_n$, which results in a checkerboard-like structure on the non-zero Fourier modes.

4.4 Existence theorem

Before we turn to the statement of the existence theorem and the derivation of the corresponding bounds, we need to introduce more notation. Let A and $\widehat{A}$ be operators approximating $\left(DF(\bar{W})\right)^{-1}$ and $DF(\bar{W})$, respectively, evaluated at a numerically computed approximate solution $\bar{W}$. As the system is infinite-dimensional, these operators are constructed by combining a finite-dimensional dense block for the low frequencies with a diagonal tail for the high frequencies. The size of the finite-dimensional block is determined by a truncation parameter $N^\dagger \in \mathbb{N}$. Adjusting the notation from [68] to our specific setting, we define

$$\lambda_n = \frac{1}{\nu n^2 - i\bar{c} n_3}, \quad \mu_n = \frac{1}{|\lambda_n|}, \quad \mathcal{E}(N) = \{n \in \mathbb{Z}^3_* : \mu_n \le N\}, \quad \mathcal{E}^\dagger = \mathcal{E}(N^\dagger).$$

Recall from Section 4.2 that we explicitly exclude the zeroth Fourier mode. Therefore, we work with sequences for $a \in \mathbb{C}^{\mathbb{Z}^3_*}$. The Galerkin projection $\Pi^{N^\dagger}$ onto the finite-dimensional computational domain is given by

$$\Pi^{N^\dagger} a = (a_n)_{n \in \mathcal{E}^\dagger}.$$

Let $A^{N^\dagger}$ and $\widehat{A}^{N^\dagger}$ denote the finite-dimensional square matrices. The infinite-dimensional operators $\widehat{A}$ and A act on a sequence $v = (v_n) \in \mathbb{C}^{\mathbb{Z}^3_*}$ component-wise as

$$(\widehat{A}v)_n = \begin{cases} \left(\widehat{A}^{N^\dagger}\Pi^{N^\dagger}v\right)_n & n \in \mathcal{E}^\dagger, \\ \lambda_n^{-1}v_n & n \notin \mathcal{E}^\dagger, \end{cases}$$

$$(Av)_n = \begin{cases} \left(A^{N^\dagger}\Pi^{N^\dagger}v\right)_n & n \in \mathcal{E}^\dagger, \\ \lambda_n v_n & n \notin \mathcal{E}^\dagger. \end{cases}$$

Furthermore, we let $\eta > 1$ and let $\ell^1_\eta(\mathbb{C})$ represent the subspace of sequences $a \in \mathbb{C}^{\mathbb{Z}^3_*}$ endowed with the norm

$$\|a\|_{\ell^1_\eta} = \sum_{n\in\mathbb{Z}^3_*} |a_n|\eta^{|n|_1}$$

where $|n|_1 = |n_1| + |n_2| + |n_3|$. Then, we define $\mathcal{X} = \mathbb{C} \times \left(\ell^1_\eta(\mathbb{C})\right)^3$ equipped with the norm

$$\|W\|_{\mathcal{X}} = |c| + \sum_{m=1}^{3} \|\omega^{(m)}\|_{\ell^1_\eta}.$$

Note that we did not introduce weights for the norm of c, i.e., we have set the weights equal to one there. Following Definition 2.14 in [68], we define

$$\mathcal{X}^\dagger = \{W \in \mathcal{X} : \omega_n = 0, \quad \forall n \notin \mathcal{E}^\dagger\}.$$

Remark 4.4.1. *Although the wave speed c is a physical, real-valued quantity, we treat it here as a complex variable ($c \in \mathbb{C}$) so that $\mathcal{X}$ constitutes a complex Banach space and the zero-finding problem is well-defined. The symmetries of the system ensure that the actual solution $\tilde{c}$ we find has a vanishing imaginary part, resulting in a real wave speed.*

We are now ready to present the existence theorem.

Theorem 4.4.2 (cf. Theorem 2.15 in [68])**.** *Assume that $\eta > 1$ and that there exists $\bar{W} = (\bar{c}, \bar{\omega})^T \in \mathcal{X}$ such that the divergence-free condition $\sum_{m=1}^{3} D_m\bar{\omega}^{(m)} = 0$ holds. Furthermore, let Y_0, Z_0, Z_1 and Z_2 be non-negative constants satisfying*

$$\left\|A\mathcal{F}(\bar{W})\right\|_{\mathcal{X}} \leq Y_0 \tag{4.5}$$

$$\left\|I - A\hat{A}\right\|_{B(\mathcal{X},\mathcal{X})} \leq Z_0 \tag{4.6}$$

$$\left\|A\left(D\mathcal{F}(\bar{W}) - \hat{A}\right)\right\|_{B(\mathcal{X},\mathcal{X})} \leq Z_1 \tag{4.7}$$

$$\left\|A(D\mathcal{F}(W) - D\mathcal{F}(\bar{W}))\right\|_{B(\mathcal{X},\mathcal{X})} \leq Z_2\left\|W - \bar{W}\right\|_{\mathcal{X}}, \quad \textit{for all } W \in \mathcal{X}. \tag{4.8}$$

If

$$Z_0 + Z_1 < 1 \qquad \text{and} \qquad 2Y_0Z_2 < \left(1 - (Z_0 + Z_1)\right)^2, \tag{4.9}$$

then, for all $r \in [r_{\min}, r_{\max})$ *there exists a unique* $\tilde{W} = (\tilde{c}, \tilde{\omega})^T \in \mathcal{B}_{\mathcal{X}}(\bar{W}, r)$ *such that* $\mathcal{F}(\tilde{W}) = 0$*, where* $\mathcal{B}_{\mathcal{X}}(\bar{W}, r)$ *is the closed ball of* $\mathcal{X}$*, centered at* $\bar{W}$ *and of radius* r*, and*

$$r_{\min} := \frac{1 - (Z_0 + Z_1) - \sqrt{\left(1 - (Z_0 + Z_1)\right)^2 - 2Y_0Z_2}}{Z_2}, \qquad r_{\max} := \frac{1 - (Z_0 + Z_1)}{Z_2}.$$

Besides, for this unique $\tilde{W}$*, the condition* $\sum_{m=1}^{3} D_m \tilde{\omega}^{(m)} = 0$ *is satisfied for the vorticity field. Finally, defining* $u = M\tilde{\omega}$*, there exists a pressure function* p *such that* (u, p) *is a* $\frac{2\pi}{\tilde{c}}$*-periodic, real-valued and analytic solution of* (4.1)*.*

Proof. The proof of Theorem 4.4.2 relies on a Newton-Kantorovich type argument and is highly analogous to the proof of Theorem 2.15 in [68]. By reformulating the zero-finding problem $\mathcal{F}(W) = 0$ as an equivalent fixed-point problem $T(W) = W - \widehat{A}\mathcal{F}(W)$, the conditions defined in (4.5)-(4.8) ensure that T maps the closed ball $\mathcal{B}_{\mathcal{X}}(\bar{W}, r)$ into itself and acts as a strict contraction. The contraction mapping theorem then guarantees the existence of a unique fixed point $\tilde{W}$ within this neighborhood. □

Remark 4.4.3. *Crucially, the theorem assumes that the numerical approximation* $\bar{\omega}$ *is strictly divergence-free in Fourier space (*$\sum_{m=1}^{3} D_m \bar{\omega}^{(m)} = 0$*). Recall from Section 4.2 that since vorticity is defined as the curl of a vector field (*$\omega = \nabla \times u$*), the vector identity* $\nabla \cdot (\nabla \times u) = 0$ *dictates that any physically valid vorticity field must be divergence-free. Therefore, by ensuring our approximation lies in the divergence-free subspace (cf. the space* $\mathcal{X}^{\text{div}}$ *in Section 2.2 of [68]), the contraction mapping converges to a locally unique solution* $\tilde{\omega}$ *that also satisfies* $\nabla \cdot \tilde{\omega} = 0$*. Hence, we can use* $u = M\tilde{\omega}$ *to uniquely recover the velocity field. A more detailed explanation can be found in Section 2 of [68].*

4.4.1 Symmetry-reduced existence theorem

Instead of working in the full space $\mathcal{X}$, we can significantly reduce the computational load by restricting our analysis to a symmetry-reduced subspace. Let G denote the group of symmetries defined in Section 4.3. The action of these symmetries partitions $\mathbb{Z}_*^3 \times \{1, 2, 3\}$ into disjoint equivalence classes, which we call orbits. For any pair (n, m), its orbit $G.(n, m)$ consists of all indices generated by applying the symmetry transformations to (n, m). As the Fourier coefficients and components within the same orbit are algebraically linked up to a known sign or phase, we only need to solve for one representative coefficient per orbit.

Let $J^{\text{Red}} \subset \mathbb{Z}_*^3 \times \{1, 2, 3\}$ represent this symmetry-reduced index set, chosen such that it contains exactly one representative index from each orbit (an exact algorithmic definition of this selection can be found in Section 4.4 of [68]). Similarly,

let J_c denote the index corresponding to the wave speed c and its associated phase condition $F_c = 0$. We then define the complete symmetry-reduced index set as

$$\mathcal{J}^{\mathrm{Red}} = J_c \cup J^{\mathrm{Red}}.$$

We define the norm of $\mathcal{X}$ in the symmetric case as

$$\|W\|_{\mathcal{X},\mathrm{Red}} = |c| + \sum_{(n,m)\in J^{\mathrm{Red}}} \xi^s_{n,m} |\omega_n^{(m)}|.$$

The factor $\xi^s_{n,m}$ is introduced to ensure that the reduced norm matches the norm in the full space $\mathcal{X}$. Specifically, it includes both the algebraic weight and the multiplication by the size of the orbit, i.e., $\xi^s_{n,m} = \eta^{|n|_1} |G.(n,m)|$, where $|G.(n,m)|$ denotes the number of elements in the symmetry orbit of the pair (n,m).

Furthermore, we introduce symmetry-reduced versions $\bar{W}^{\mathrm{Red}}$, A^{Red}, $\hat{A}^{\mathrm{Red}}$, F^{Red} and $\mathcal{F}^{\mathrm{Red}}$ of W, A, $\hat{A}$, F and $\mathcal{F}$, respectively. These operators and elements act strictly on the components defined by $\mathcal{J}^{\mathrm{Red}}$. The existence theorem in this symmetric setting is then stated as follows:

Theorem 4.4.4 (cf. Theorem 4.23 in [68]). *Assume that $\eta > 1$ and that there exists $\bar{W}^{\mathrm{Red}} \in \mathcal{X}^{\mathrm{Red}}$ such that the divergence-free condition $\sum_{m=1}^{3} D_m \left(\bar{\omega}^{\mathrm{Red}}\right)^{(m)} = 0$ holds. Furthermore, let Y_0^{Red}, Z_0^{Red}, Z_1^{Red} and Z_2^{Red} be non-negative constants satisfying*

$$\left\|A^{\mathrm{Red}} \mathcal{F}^{\mathrm{Red}}(\bar{W}^{\mathrm{Red}})\right\|_{\mathcal{X}^{\mathrm{Red}}} \le Y_0^{\mathrm{Red}} \tag{4.10}$$

$$\left\|I - A^{\mathrm{Red}} \hat{A}^{\mathrm{Red}}\right\|_{B(\mathcal{X}^{\mathrm{Red}},\mathcal{X}^{\mathrm{Red}})} \le Z_0^{\mathrm{Red}} \tag{4.11}$$

$$\left\|A^{\mathrm{Red}} \left(D\mathcal{F}^{\mathrm{Red}}(\bar{W}^{\mathrm{Red}}) - \hat{A}^{\mathrm{Red}}\right)\right\|_{B(\mathcal{X}^{\mathrm{Red}},\mathcal{X}^{\mathrm{Red}})} \le Z_1^{\mathrm{Red}} \tag{4.12}$$

$$\begin{aligned}\left\|A^{\mathrm{Red}}(D\mathcal{F}^{\mathrm{Red}}(W^{\mathrm{Red}}) - D\mathcal{F}^{\mathrm{Red}}(\bar{W}^{\mathrm{Red}}))\right\|_{B(\mathcal{X}^{\mathrm{Red}},\mathcal{X}^{\mathrm{Red}})} \\ \le Z_2^{\mathrm{Red}} \left\|W^{\mathrm{Red}} - \bar{W}^{\mathrm{Red}}\right\|_{\mathcal{X}^{\mathrm{Red}}}, \quad \text{for all } W^{\mathrm{Red}} \in \mathcal{X}^{\mathrm{Red}}.\end{aligned} \tag{4.13}$$

If

$$Z_0^{\mathrm{Red}} + Z_1^{\mathrm{Red}} < 1 \qquad \text{and} \qquad 2Y_0^{\mathrm{Red}} Z_2^{\mathrm{Red}} < \left(1 - (Z_0^{\mathrm{Red}} + Z_1^{\mathrm{Red}})\right)^2, \tag{4.14}$$

then, for all $r \in [r_{\min}, r_{\max})$ there exists a unique $\tilde{W}^{\mathrm{Red}} \in \mathcal{B}_{\mathcal{X}^{\mathrm{Red}}}(\bar{W}^{\mathrm{Red}}, r)$ such that $\mathcal{F}^{\mathrm{Red}}(\tilde{W}^{\mathrm{Red}}) = 0$, where $\mathcal{B}_{\mathcal{X}^{\mathrm{Red}}}(\bar{W}^{\mathrm{Red}}, r)$ is the closed ball of $\mathcal{X}^{\mathrm{Red}}$, centered at $\bar{W}^{\mathrm{Red}}$ and of radius r, and

$$r_{\min} := \frac{1 - (Z_0^{\mathrm{Red}} + Z_1^{\mathrm{Red}}) - \sqrt{\left(1 - (Z_0^{\mathrm{Red}} + Z_1^{\mathrm{Red}})\right)^2 - 2Y_0^{\mathrm{Red}} Z_2^{\mathrm{Red}}}}{Z_2^{\mathrm{Red}}},$$

$$r_{\max} := \frac{1 - (Z_0^{\mathrm{Red}} + Z_1^{\mathrm{Red}})}{Z_2^{\mathrm{Red}}}.$$

Besides, for this unique $\tilde{W}^{\mathrm{Red}}$*, the condition* $\sum_{m=1}^{3} D_m \left(\tilde{\omega}^{\mathrm{Red}}\right)^{(m)} = 0$ *is satisfied for the vorticity field. Finally, defining* $u = M\tilde{\omega}^{\mathrm{Red}}$*, there exists a pressure function* p *such that* (u, p) *is a* $\frac{2\pi}{\tilde{c}}$*-periodic, real-valued and analytic solution of* (4.1) *that possesses the symmetries defined in Section 4.3.*

Proof. The proof is heavily analogous to the full-space existence proof of Theorem 4.4.2. How to deal with the symmetries is detailed in the proof of Theorem 4.23 in [68]. □

4.5 Bounds

To derive the bounds necessary to apply Theorem 4.4.2 or Theorem 4.4.4, we must derive bounds for Y_0, Z_0, Z_1 and Z_2. While our general estimation strategy follows Section 3 in [68], we must systematically adapt the bounds to account for the specific structure of our F. As we are solving a three-dimensional traveling wave problem, rather than a two-dimensional time-periodic problem, the differential structure of our operator differs from the one analyzed in [68]. Consequently, this alters our definition of λ_n and A, which impacts the computation of the bounds.

4.5.1 Y_0-bound

Recall from Theorem 4.4.2 that the constant Y_0 bounds the residual error of our approximate solution via $\|A\mathcal{F}(\bar{W})\|_{\mathcal{X}} \leq Y_0$. To derive a computable expression for this bound, let $\mathcal{S}^{\mathrm{sol}}$ be a finite set of indices in $\mathbb{Z}^3_*$ such that $\bar{\omega}_n = 0$ for all $n \notin \mathcal{S}^{\mathrm{sol}}$. Following Proposition 3.5 in [68], we set

$$\begin{aligned} Y_0 &= \|A^{N^\dagger}\Pi^{N^\dagger}\mathcal{F}(\bar{W})\|_{\mathcal{X}} + \sum_{n\in(\mathcal{S}^{\mathrm{sol}}+\mathcal{S}^{\mathrm{sol}})\setminus\mathcal{E}^\dagger}\sum_{m=1}^{3} |\lambda_n| \left|F_n^{(m)}(\bar{W})\right| \eta^{|n|_1} \\ &= \left|\left(A^{N^\dagger}\Pi^{N^\dagger}\mathcal{F}(\bar{W})\right)_c\right| + \sum_{n\in\mathcal{E}^\dagger}\sum_{m=1}^{3} \left|\left(A^{N^\dagger}\Pi^{N^\dagger}\mathcal{F}(\bar{W})\right)_n^{(m)}\right| \eta^{|n|_1} \\ &\quad + \sum_{n\in(\mathcal{S}^{\mathrm{sol}}+\mathcal{S}^{\mathrm{sol}})\setminus\mathcal{E}^\dagger}\sum_{m=1}^{3} |\lambda_n| \left|F_n^{(m)}(\bar{W})\right| \eta^{|n|_1}. \end{aligned}$$

Recall that the subscript c denotes the scalar component of the vector in $\mathcal{X}$ corresponding to the phase condition.

Symmetry-reduced Y_0-bound

Including symmetries, we have

$$\begin{aligned} Y_0^{\mathrm{Red}} &= \|A^{\mathrm{Red},N^\dagger}\Pi^{N^\dagger}\mathcal{F}^{\mathrm{Red}}(\bar{W}^{\mathrm{Red}})\|_{\mathcal{X},\mathrm{Red}} \\ &\quad + \sum_{\substack{n\in(\mathcal{S}^{\mathrm{sol}}+\mathcal{S}^{\mathrm{sol}})\setminus\mathcal{E}^\dagger \\ (n,m)\in J^{\mathrm{Red}}}} \xi^s_{n,m}|\lambda_n|\left|\left(F_n^{\mathrm{Red}}(\bar{W}^{\mathrm{Red}})\right)^{(m)}\right| \\ &= \left|\left(A^{\mathrm{Red},N^\dagger}\Pi^{N^\dagger}\mathcal{F}^{\mathrm{Red}}(\bar{W}^{\mathrm{Red}})\right)_c\right| \\ &\quad + \sum_{\substack{n\in\mathcal{E}^\dagger \\ (n,m)\in J^{\mathrm{Red}}}} \xi^s_{n,m}\left|\left(A^{\mathrm{Red},N^\dagger}\Pi^{N^\dagger}\mathcal{F}^{\mathrm{Red}}(\bar{W}^{\mathrm{Red}})\right)_n^{(m)}\right| \\ &\quad + \sum_{\substack{n\in(\mathcal{S}^{\mathrm{sol}}+\mathcal{S}^{\mathrm{sol}})\setminus\mathcal{E}^\dagger \\ (n,m)\in J^{\mathrm{Red}}}} \xi^s_{n,m}|\lambda_n|\left|\left(F_n^{\mathrm{Red}}(\bar{W}^{\mathrm{Red}})\right)^{(m)}\right|. \end{aligned}$$

As our symmetry-reduced index set $J^{\mathrm{Red}} \subset \mathbb{Z}^3_* \times \{1,2,3\}$ includes the vector components, the symmetry-reduced Y_0^{Red}-bound reflects this structure by summing over the representative Fourier mode-component pairs $(n,m) \in J^{\mathrm{Red}}$, weighted by $\xi^s_{n,m}$ to account for the sizes of the corresponding orbits.

To avoid redundancy, we omit the explicit derivations of the symmetry-reduced bounds for Z_0, Z_1 and Z_2. These bounds can be constructed directly from their full-space counterparts in a manner analogous to the Y_0-bound.

4.5.2 Z_0-bound

As in Proposition 3.6 in [68], we set

$$Z_0 = \|I - A^{N^\dagger}\hat{A}^{N^\dagger}\|_{B(\mathcal{X},\mathcal{X})}.$$

Note that the tails of A and $\hat{A}$ are exact inverses of each other and thus Z_0 can be computed by considering finitely many elements.

4.5.3 Z_1-bound

The constant Z_1 bounds the error of the approximate inverse, represented by the operator norm $\left\|A\left(D\mathcal{F}(\bar{W}) - \widehat{A}\right)\right\|_{B(\mathcal{X},\mathcal{X})}$. Since our Banach space $\mathcal{X}$ is equipped with a weighted ℓ^1-norm, the induced operator norm corresponds to the supremum over the ℓ^1-norms of the operator's columns. As a result, we can partition the computation of Z_1 into three distinct components: the single column associated with the derivative with respect to the scalar wave speed c, the finite block of columns corresponding to the computed low-frequency Fourier modes of the vorticity, and the infinite tail of columns corresponding to the high-frequency modes. To separate the low- and high-frequency modes, we introduce a computational parameter

$\tilde{N} \in \mathbb{N}$, with $\tilde{N} \geq N^{\dagger}$, following Proposition 3.10 in [68]. We then evaluate the overall bound as the maximum over these three parts:

$$Z_1 = \max\left(\left\|A[D\mathcal{F}(\bar{W}) - \widehat{A}]^{(\cdot,c)}\right\|_{\mathcal{X}}, \max_{1\leq m\leq 3}\left(Z_1^{\text{finite}}\right)^{(m)}, \max_{1\leq m\leq 3}\left(Z_1^{\text{tail}}\right)^{(m)}\right),$$

where the finite low-frequency block is computed over the set of modes $\tilde{\mathcal{S}}^{\text{sol}}(\tilde{N})$ as

$$\left(Z_1^{\text{finite}}\right)^{(m)} = \max_{n\in\tilde{\mathcal{S}}^{\text{sol}}(\tilde{N})} \frac{1}{\eta^{|n|_1}} \left\|A[D\mathcal{F}(\bar{W}) - \widehat{A}]^{(\cdot,m)}_{\cdot,n}\right\|_{\mathcal{X}},$$

and the infinite high-frequency tail is controlled by $\left(Z_1^{\text{tail}}\right)^{(m)}$. Following Proposition 3.10 in [68], we derive the tail bound by introducing $C = D\mathcal{F}(\bar{W}) - \widehat{A}$. For high frequencies, the nonzero elements of C correspond to the derivative of the nonlinear term $D\Psi(\bar{\omega})$. Evaluating this derivative for a general variation ω yields four distinct components for each Fourier mode n:

$$\begin{aligned}&(D\Psi(\bar{\omega})\omega)_n\\ &\quad= i\left([(M\bar{\omega}\star\tilde{D})\omega]_n - [(\omega\star\tilde{D})M\bar{\omega}]_n + [(M\omega\star\tilde{D})\bar{\omega}]_n - [(\bar{\omega}\star\tilde{D})M\omega]_n\right).\end{aligned}$$

To establish the bound, we evaluate the column norms of AC by multiplying the high-frequency tail of the approximate inverse, given by $|\lambda_n|$, into each of the four terms. The unbounded spatial derivatives are balanced by the decay rate of $|\lambda_n|$ using Lemma 4.5.2. For the first term, applying vector identities to factor out the spatial derivative from the convolution yields a multiplier n_p, which is bounded by $\sup|\lambda_n||n_p| \leq \frac{1}{\sqrt{\nu\tilde{N}}}$. This results in the factor $\frac{\sqrt{3}}{\sqrt{\nu\tilde{N}}}\|\max_{1\leq p\leq 3}(M\bar{\omega})^{(p)}\|_{\ell^1_\eta}$. In the second and third terms, the derivatives apply to the computed numerical approximations ($M\bar{\omega}$ and $\bar{\omega}$), resulting in finite sequences. In the fourth term, the spatial derivative acts on $M\omega$. However, because the operator M_n scales as $\mathcal{O}(n^{-1})$, the combined operation $n_p M_n^{(l,m)}$ is bounded by a constant. Hence, the last three terms are controlled using $\sup|\lambda_n| \leq \frac{1}{\tilde{N}}$. Summing these bounds across all dimensions yields the final estimate:

$$\begin{aligned}\left(Z_1^{\text{tail}}\right)^{(m)} = \frac{\sqrt{3}}{\sqrt{\nu\tilde{N}}}\left\|\max_{1\leq p\leq 3}(M\bar{\omega})^{(p)}\right\|_{\ell^1_\eta} + \frac{1}{\tilde{N}}\left(\frac{3}{2}\sum_{p=1}^{3}\left\|\bar{\omega}^{(p)}\right\|_{\ell^1_\eta} - \frac{1}{2}\left\|\bar{\omega}^{(m)}\right\|_{\ell^1_\eta}\right)\\ + \frac{1}{\tilde{N}}\sum_{l=1}^{3}\left(\left\|D_m(M\bar{\omega})^{(l)}\right\|_{\ell^1_\eta} + \sum_{p=1}^{3}\left\|D_p\bar{\omega}^{(l)}\right\|_{\ell^1_\eta} - \left\|D_m\bar{\omega}^{(l)}\right\|_{\ell^1_\eta}\right).\end{aligned} \tag{4.15}$$

The interaction between the truncation parameter $N^{\dagger}$ and the parameter for the tail bound $\tilde{N}$ allows us to balance computational cost with the sharpness of the bounds. Specifically, increasing $\tilde{N}$ incorporates more modes into the explicit finite computation, which directly decreases the magnitude of the tail bound Z_1^{tail} (due to the $\frac{1}{N}$ decay rates). Conversely, increasing $N^{\dagger}$ expands the size of the approximate inverse $\widehat{A}$, which reduces the error across the finite block Z_1^{finite}.

Remark 4.5.1. *To improve the computational efficiency of Z_1^{finite}, we exploited the submultiplicativity of the norm to avoid expensive matrix-vector multiplications whenever possible. We started by precomputing the operator norm $\|A\|_{B(\mathcal{X},\mathcal{X})}$ just once. Then, for each column index n and component m, we first computed the product $\|A\|_{B(\mathcal{X},\mathcal{X})} \cdot \|[D\mathcal{F}(\bar{W}) - \hat{A}]_{:,n}^{(:,m)}\|_{\mathcal{X}}$. If this value remained below a predetermined threshold, we accepted it as our bound for that column and component. We only evaluated the more computationally expensive expression $\left\|A[D\mathcal{F}(\bar{W}) - \hat{A}]_{:,n}^{(:,m)}\right\|_{\mathcal{X}}$ if the cheaper bound failed the threshold test. This strategy allowed for a substantial reduction in computation time.*

4.5.4 Z_2-bound

Before formulating our final bound, we state the following lemma:

Lemma 4.5.2 (cf. Lemma 3.1 in [68])**.** *For $m \in \{1,2,3\}$, we have that*

$$\sup_{n \notin \mathcal{E}(N^\dagger)} |\lambda_n||n_m| \leq \frac{1}{\sqrt{\nu N^\dagger}}.$$

Proof. Using the definition of λ_n, we write

$$|\lambda_n| = \frac{1}{|\nu n^2 - icn_3|} = \frac{1}{\sqrt{(\nu n^2)^2 + (cn_3)^2}} \leq \frac{1}{\nu n^2}.$$

Hence, $n^2 \leq \frac{1}{\nu|\lambda_n|}$. As for $m \in \{1,2,3\}$, it holds that $n^2 = n_1^2 + n_2^2 + n_3^2 \geq n_m^2$, so we obtain that $n_m^2 \leq \frac{1}{\nu|\lambda_n|}$. Taking the square root on both sides and multiplying both sides by $|\lambda_n|$, we acquire that

$$|\lambda_n||n_m| \leq \sqrt{\frac{|\lambda_n|}{\nu}}.$$

Using that $|\lambda_n| = \frac{1}{\mu_n}$ and the definition of $\mathcal{E}(N^\dagger)$, we conclude the proof. □

Recall that Z_2 must satisfy $\left\|A(D\mathcal{F}(W) - D\mathcal{F}(\bar{W}))\right\|_{B(\mathcal{X},\mathcal{X})} \leq Z_2 \left\|W - \bar{W}\right\|_{\mathcal{X}}$ for all $W \in \mathcal{X}$. Analogous to Proposition 3.12 in [68], we set

$$Z_2 = (4+\sqrt{2}) \max\left[\max_{1\leq m\leq 3} \max_{n\in\mathcal{E}^\dagger} \frac{|n|_\infty}{\eta^{|n|_1}} \left\|A_{:,n}^{(:,m)}\right\|_{\mathcal{X}}, \frac{1}{\sqrt{\nu N^\dagger}}\right].$$

When examining $D\mathcal{F}(W) - D\mathcal{F}(\bar{W})$, all purely linear terms in $\mathcal{F}$ cancel out entirely. As the Navier-Stokes equations only have up to quadratic nonlinearities, the bound Z_2 therefore relies exclusively on controlling the remaining quadratic components of $\mathcal{F}$: the nonlinear advection term and the term $-cin_3\omega_n$ involving the wave speed.

The formula for Z_2 is built from a constant factor and a maximum. The constant factor $4+\sqrt{2}$ arises from summing the bounds of these quadratic components. A

factor 1 originates from the mixed derivatives of the wave speed term and a factor $3+\sqrt{2}$ arises from bounding the expanded products of the advection term.

Furthermore, because the advection term contains a spatial derivative, this introduces a multiplication by the wave number in Fourier space. To bound the combined effect of the approximate inverse A and this spatial derivative, we split the evaluation into two parts:

- **The finite part:** For the explicitly computed low frequencies ($n \in \mathcal{E}^\dagger$), we calculate the maximum weighted column sums of the finite matrix A, scaled by the derivative magnitude $|n|_\infty$.
- **The tail part:** For the high frequencies ($n \notin \mathcal{E}^\dagger$), the operator A acts diagonally by multiplying by λ_n. Combined with the spatial derivative n_m, we must bound the product $|\lambda_n||n_m|$. This bound is provided by Lemma 4.5.2.

Since Lemma 4.5.2 applies equally to n_1, n_2 and n_3, we can use it to estimate the entire tail of the matrix A. Therefore, unlike the setting in [68], where a separate estimate is required for the additional variable n_4, no such distinction is necessary in our case.

4.6 Results

With the bounds established in the previous section, we are ready to present the proof of the main result of this chapter, given in Theorem 4.1.1. We report the values for the bounds in floating point numbers displaying four decimals.

Proof of Theorem 4.1.1. Let $\eta = 1 + 10^{-7}$, $\nu = 0.2069$ and $c = -2.5805$. Furthermore, we set $N = (22, 22, 8)$, $N^\dagger = 300$ and $\tilde{N} = 700$. All nonzero Fourier coefficients of the approximate solution $\overline{u}$ can be found in the code in [73]. The bounds are as follows:

$$Y_0 = 3.6256 \cdot 10^{-6}, \quad Z_0 = 7.77508 \cdot 10^{-12},$$
$$Z_1 = 8.9719 \cdot 10^{-1}, \quad Z_2 = 1.0633 \cdot 10^{3}.$$

Letting $\tilde{u}$ denote the zero of F, we apply Theorem 4.4.2 to obtain the error bound

$$\|\tilde{u} - \overline{u}\|_{\mathcal{X}} \leq 4.6403 \cdot 10^{-5}.$$

□

Remark 4.6.1. *The parameter $\eta = 1+10^{-7}$ is selected to ensure regularity of the solution. Nevertheless, the same result could be obtained with the simpler choice $\eta = 1$, using a standard bootstrap argument to establish smoothness. The values of $N^\dagger$ and $\tilde{N}$ are selected to balance computational efficiency with achieving a sufficiently small value of Z_1. Increasing $\tilde{N}$ lowers Z_1^{tail} and increasing $N^\dagger$ lowers Z_1^{finite}, making their selection a trade-off between precision and computational cost.*

The choice of the truncation parameter $N = (22, 22, 8)$ *is chosen such that a balance between computational load and capturing the mathematical structure of the approximation is obtained. The fact that* N *consists of only three parameters reflects the fundamental reduction of the system: by moving to a traveling wave setting, the time-dependence is absorbed into the spatial coordinate* x_3*, reducing the originally four-dimensional space-time problem into an effectively three-dimensional stationary one. Furthermore, the Taylor-Green forcing acts exclusively in the* x_1 *and* x_2 *directions, generating vorticity structures that require a relatively high resolution of* 22 *Fourier modes to be sufficiently represented. In contrast, the dynamics in the* x_3*-direction, the direction of the wave propagation, exhibit a smoother profile that can be adequately captured with only* 8 *modes.*

The code used to obtain the above result can be found in [73]. The computations were carried out in MATLAB (2024a) on an Intel Xeon W-2191B CPU with 256 GB RAM. We used the interval arithmetic library Intlab ([57]) to ensure that the computations are rigorous. The computation time is approximately 20 days (1765740 seconds). This computation time is relatively long, even though an optimized version of the code was implemented (see Remark 4.5.1).

4.7 Acknowledgements

The author would like to gratefully acknowledge Lennaert van Veen for their valuable assistance in conducting the numerical explorations for this chapter, specifically for helping to identify the precise viscosity value at which the traveling wave solutions became visible.

5 Hopf bifurcation analysis in Navier-Stokes equations

5.1 Introduction

In the previous chapter, we successfully verified the existence of a periodic traveling wave solution on a branch emerging from a Hopf bifurcation. As illustrated in the bifurcation diagram displayed in the introduction of this thesis in Figure 1.3.3, the stationary and periodic solutions of the three-dimensional Navier-Stokes equations form a rich bifurcation structure, where various branches of solutions originate from bifurcation points. While our prior analysis focused on verifying a specific state along one of these branches, we will now shift to the analysis of one of the bifurcation points itself, as well as the families of periodic solutions that arise from it.

5.1.1 Context and motivation

In the context of fluid dynamics, a Hopf bifurcation represents the critical threshold at which steady fluid flow transitions into an oscillatory state. This transition is characterized by a pair of complex conjugate eigenvalues of the linearized system crossing the imaginary axis, leading to a limit cycle. A classic example is the onset of vortex shedding that leads to the formation of a von Kármán vortex street [36].

Locating a Hopf bifurcation requires finding a critical parameter value (in our case, the viscosity ν) at which the linearized operator of the system, evaluated at an equilibrium solution, possesses a pair of purely imaginary eigenvalues $\pm i\Omega$. Proving the existence of this bifurcation point provides a strong analytical foundation, as it indicates the transition from stationary to periodic dynamics. Furthermore, it serves as the basis for analyzing the continuous branches of periodic orbits that emerge from the bifurcation points.

5.1.2 Chapter roadmap and objectives

The primary objective of this chapter is to develop a rigorous mathematical and computational framework capable of verifying both the exact Hopf bifurcation point and the branch of three-dimensional periodic solutions appearing from it. To achieve this, the chapter is structured as follows.

In Section 5.2, we formulate the zero-finding problem to prove the existence of the Hopf bifurcation point in the three-dimensional Navier-Stokes equations. We set up the eigenvalue problem in a fully spatial Fourier domain and derive the necessary bounds (Y_0, Z_1 and Z_2) for the radii polynomial approach. While the final execution of this proof is currently constrained by hardware memory limits, the complete theoretical and computational framework is established.

Finally, in Section 5.3, we present the theoretical blueprint for proving the existence of three-dimensional periodic solutions away from the bifurcation point. We outline a strategy, based on the connection with the Jacobian matrix of the Hopf bifurcation problem, to construct an approximate inverse and verify the Newton-Kantorovich conditions, preparing the setting for future computer-assisted proofs in fully three-dimensional fluid dynamics.

5.2 Proof of the Hopf bifurcation point

As in the previous chapter, we consider the Navier-Stokes equations on a periodic domain. Let $u = u(x_1, x_2, x_3, t)$ represent the velocity and $p = \frac{P(x_1,x_2,x_3,t)}{\rho}$ the pressure scaled by the (constant) density ρ. Furthermore, let ν be the kinematic viscosity and f the time-independent Taylor-Green forcing

$$f = \begin{pmatrix} 2\sin x_1 \cos x_2 \\ -2\cos x_1 \sin x_2 \\ 0 \end{pmatrix}.$$

Then we can state the Navier-Stokes equations, governing the motion of incompressible viscous fluids, as

$$\begin{cases} \partial_t u + (u \cdot \nabla)u - \nu\Delta u + \nabla p = f, \\ \nabla \cdot u = 0. \end{cases} \tag{5.1}$$

In this section, we focus on the proof of the third symmetry-breaking Hopf bifurcation point corresponding to the third light blue dot in the bifurcation diagram in Figure 1.3.3. Numerically, we observed that this bifurcation occurs around viscosity $\nu = 0.1234$. As stated in the introduction of this thesis, this $O(2)$-symmetric Hopf bifurcation generically leads to the simultaneous emergence of branches of both standing and traveling waves.

5.2.1 Setup

Following the procedures in [70] and [72], we will formulate the Hopf bifurcation problem, which serves as the groundwork for computing a branch of periodic orbits. While the Navier-Stokes equations are formulated in terms of velocity and pressure, it is highly advantageous to eliminate the pressure gradient. By taking the curl of the velocity field, we transition to an equivalent formulation based entirely on the vorticity $\omega = \nabla \times u$.

The family of periodic solutions emerging from the bifurcation point can be parameterized by an amplitude parameter ε. Consequently, along this branch, the viscosity ν, the frequency Ω and the vorticity ω all become functions of ε. We expand the periodic solutions along this branch as

$$\omega(\varepsilon, t) = \tilde{\omega}\left(\nu(\varepsilon)\right) + \varepsilon\bar{\omega}(t) + \mathcal{O}(\varepsilon^2), \tag{5.2}$$

where $\tilde{\omega}(\nu)$ is the analytically known equilibrium solution, explicitly given by (see [68])

$$\tilde{\omega}(\nu) = \frac{1}{2\nu} f^{\omega}, \tag{5.3}$$

with $f^{\omega} = \nabla \times f$. At the Hopf bifurcation point, we have $\varepsilon = 0$, and we denote the parameter values as $\nu(0) = \nu_0$ and $\Omega(0) = \Omega_0$. We are interested in finding the 2π-periodic function $\bar{\omega}(t)$ in order to find $\omega(\varepsilon, t)$ for small ε.

To this end, we expand the vorticity in a Fourier series. Introducing $\mathbb{Z}^4_* := \mathbb{Z}^4 \backslash \{0\}$, we set

$$\bar{\omega} = \sum_{n \in \mathbb{Z}^4_*} \bar{\omega}_n e^{i(n_1 x_1 + n_2 x_2 + n_3 x_3 + n_4 \Omega_0 t)}. \tag{5.4}$$

We defined $\mathbb{Z}^4_*$ to exclude the zero mode $\bar{\omega}_0$, as it can always be set to zero and therefore does not need to be solved for (see Section 4.2 for a more elaborate explanation).

Furthermore, we set $\tilde{n} = (n_1, n_2, n_3)$ and $\tilde{n}^2 = n_1^2 + n_2^2 + n_3^2$. The relation between the velocity and vorticity is given by $\bar{u}_n = M_n \bar{\omega}_n$, where

$$M_n = \begin{cases} \dfrac{i}{\tilde{n}^2} \begin{pmatrix} 0 & -n_3 & n_2 \\ n_3 & 0 & -n_1 \\ -n_2 & n_1 & 0 \end{pmatrix} & \tilde{n} \neq 0, \\ 0 & \tilde{n} = 0. \end{cases}$$

To formulate the zero-finding problem, we utilize the convolution and derivative definitions established in the previous chapter and in [68]. Recall that for sequences $a, b \in \mathbb{C}^{\mathbb{Z}^4}$, the convolution is $(a * b)_n = \sum_{m \in \mathbb{Z}^3} a_m b_{n-m}$ and that the derivative operator is defined as $(D_l v)_n = n_l v_n$. The nonlinear term is captured by the operator Ψ given by

$$\Psi_n(\omega) = i \left[(M\omega \star \tilde{D})\omega \right]_n - i \left[(\omega \star \tilde{D}) M\omega \right]_n, \tag{5.5}$$

where $\left[(v \star \tilde{D}) w \right]^{(l)} = \sum_{p=1}^{3} v^{(p)} * (D_p w^{(l)})$.

We use (5.4) to obtain the zero-finding problem

$$F_n(W) = i\Omega n_4 \omega_n + \Psi_n(\omega) + \nu \tilde{n}^2 \omega_n - f_n^{\omega} = 0, \tag{5.6}$$

for variables $W = \begin{pmatrix} ((\omega(\varepsilon))_n)_{n \in \mathbb{Z}^4_*} \\ \Omega(\varepsilon) \\ \nu(\varepsilon) \end{pmatrix}$.

To extract the linearization at the Hopf bifurcation point, we substitute the expansion (5.2) into (5.6). Using that the parameter branches are locally quadratic, meaning $\nu'(0) = 0$ and $\Omega'(0) = 0$, the substitution yields

$$\begin{aligned} &i\Omega_0 n_4 (\tilde{\omega}_n(\nu_0) + \varepsilon \bar{\omega}_n) + \Psi_n(\tilde{\omega}(\nu_0) + \varepsilon \bar{\omega}) + \nu_0 \tilde{n}^2 (\tilde{\omega}_n(\nu_0) + \varepsilon \bar{\omega}_n) \\ &\quad - f_n^{\omega} + \mathcal{O}(\varepsilon^2) = 0. \end{aligned} \tag{5.7}$$

As $\tilde{\omega}(\nu)$ is an equilibrium solution, using (5.5), we transform (5.7) into

$$\varepsilon\Big(i\Omega_0 n_4\bar{\omega}_n + i\left[(M\tilde{\omega}(\nu_0)\star\tilde{D})\bar{\omega} + (M\bar{\omega}\star\tilde{D})\tilde{\omega}(\nu_0)\right]_n \\ - i\left[(\bar{\omega}\star\tilde{D})M\tilde{\omega}(\nu_0) + (\tilde{\omega}(\nu_0)\star\tilde{D})M\bar{\omega}\right]_n + \nu_0\tilde{n}^2\bar{\omega}_n\Big) + \mathcal{O}(\varepsilon^2) = 0.$$

Dividing by ε and taking the limit $\varepsilon \to 0$, we end up with

$$i\Omega_0 n_4\bar{\omega}_n + i\left[(M\tilde{\omega}(\nu_0)\star\tilde{D})\bar{\omega} + (M\bar{\omega}\star\tilde{D})\tilde{\omega}(\nu_0)\right]_n \\ - i\left[(\bar{\omega}\star\tilde{D})M\tilde{\omega}(\nu_0) + (\tilde{\omega}(\nu_0)\star\tilde{D})M\bar{\omega}\right]_n + \nu_0\tilde{n}^2\bar{\omega}_n = 0.$$

For ease of notation in the remainder of this chapter, we will drop the zero subscript and simply write ν and Ω to denote the parameters at the bifurcation point.

Normalization condition

To guarantee that the solution is isolated and non-trivial ($\bar{\omega} \neq 0$), we must impose a normalization condition. Let w^* be a row vector of complex conjugates of an approximation of the eigenvector. We set

$$w^*\bar{\omega} - 1 = 0.$$

This single complex condition provides the two real constraints needed to isolate the solution. The real part fixes the amplitude and the imaginary part fixes the phase of the eigenvector. By imposing this normalization condition, we ensure uniqueness of the eigenvector up to the choice of w.

Full system

Linearizing around a stationary solution naturally decouples the temporal frequencies. This property allows us to frame the analysis as an eigenvalue problem and isolate a single fundamental temporal mode.

As we are specifically computing the onset of the bifurcation, the temporal evolution of the perturbation is driven entirely by the purely imaginary eigenvalues $\pm i\Omega$. To naturally align the resulting zero-finding problem with the standard spatial eigenvalue formulation (where $Jv = i\Omega v$), we restrict our analysis to the fundamental temporal mode by setting $n_4 = -1$. Combining the linearized equation and the normalization condition, we obtain the purely spatial system for $n \in \mathbb{Z}^3_*$:

$$\begin{cases} -i\Omega\bar{\omega}_n + i\left[(M\tilde{\omega}(\nu)\star\tilde{D})\bar{\omega} + (M\bar{\omega}\star\tilde{D})\tilde{\omega}(\nu)\right]_n \\ \quad - i\left[(\bar{\omega}\star\tilde{D})M\tilde{\omega}(\nu) + (\tilde{\omega}(\nu)\star\tilde{D})M\bar{\omega}\right]_n + \nu\tilde{n}^2\bar{\omega}_n = 0, \\ w^*\bar{\omega} - 1 = 0. \end{cases} \tag{5.8}$$

As $\tilde{\omega}$ depends only on the first two spatial coordinates, the convolution operators in (5.8) do not couple different n_3-modes of $\bar{\omega}$. This implies that the full system decouples and can be solved independently for each n_3. Our numerical

explorations showed that the eigenvector responsible for this specific bifurcation has nonzero elements occurring exclusively at $n_3 = \pm 2$ for the bifurcation point near the viscosity value $\nu = 0.1234$. The system dictates that the Fourier modes at $n_3 = 2$ and $n_3 = -2$ are linked via a symmetry transformation. As finding the eigenvector for one automatically yields the other, we evaluate (5.8) strictly at $n_3 = 2$, which results in the eigenvalue problem outlined in the next section.

Remark 5.2.1. *We emphasize that by isolating the temporal evolution of the perturbation into the purely imaginary eigenvalue $i\Omega$ (captured by $n_4 = -1$), the determination of the Hopf bifurcation reduces to a purely spatial eigenvalue problem for the corresponding eigenfunctions. Consequently, in the formulation of the eigenvalue problem and in the computation and implementation of the bounds, no temporal grid is required.*

5.2.2 Eigenvalue problem

In this section, we formulate the eigenvalue problem for the eigenvector v, which captures the active Fourier modes of the perturbation $\bar{\omega}$ at $n_3 = 2$. As the third spatial coordinate is now fixed ($n_3 = 2$), we redefine $n = (n_1, n_2) \in \mathbb{Z}^2$. Hence, $v_n = \omega_{n,2,1}$ for $n \in \mathbb{Z}^2$. The equation corresponding to the eigenvalue problem is $Jv - i\Omega v = 0$, where $J = J(\tilde{\omega}, \nu)$ is the Fréchet derivative of F evaluated at the equilibrium solution $\tilde{\omega}$ and where Ω is the time frequency.

To simplify notation throughout this chapter, we define the diagonal operator $D_{\tilde{n}^2} := \operatorname{diag}(\tilde{n}^2)$. Due to our restriction to $n_3 = 2$, its diagonal entries are given by $\tilde{n}^2 = n_1^2 + n_2^2 + 4$ for $n \in \mathbb{Z}^2$.

Since the dependence on Ω is explicit in the eigenvalue formulation, we define J as the spatial operator

$$[J(\tilde{\omega}, \nu)]\, q = [D_\omega F(\tilde{\omega}, \nu)]\, q = \nu D_{\tilde{n}^2} q + [D\Psi\,(\tilde{\omega})]\, q,$$

for vector q. Here, the action of the advection derivative is given by

$$([D\Psi\,(\omega)]\, q)_n = i\left([(M\omega \star \tilde{D})q]_n - [(q \star \tilde{D})M\omega]_n + [(Mq \star \tilde{D})\omega]_n - [(\omega \star \tilde{D})Mq]_n\right).$$

To fix the scaling and phase of the eigenvector, we impose the normalization condition $w^* v - 1 = 0$, where w is a fixed approximation of the eigenvector and w^* denotes its conjugate transpose. Adding this normalization condition yields the full complex zero-finding problem

$$\begin{cases} J(\tilde{\omega}(\nu), \nu)v - i\Omega v & = 0, \\ w^* v - 1 & = 0. \end{cases} \tag{5.9}$$

Developing a framework to validate this system directly in a complex setting leads to functional analytic challenges due to the fact that our unknowns consist of a mix of complex variables (the eigenvector v) and strictly real parameters (the temporal frequency Ω and the kinematic viscosity ν). To circumvent these complications, we decompose the system into its real and imaginary part. This maps the entire

problem to a real vector space, ensuring that Ω and ν are naturally restricted to the real line.

Therefore, we decompose the eigenvector as $v = x + iy$, where the components are given by $x = \mathrm{Re}(v)$ and $y = \mathrm{Im}(v)$. Similarly, we decompose both the spatial Jacobian and w into their real and imaginary components via $J = J_r + iJ_i$ and $w = \mathrm{Re}(w) + i\,\mathrm{Im}(w)$. Substituting these into (5.9) and separating the real and imaginary terms, we obtain the real zero-finding problem

$$\begin{cases} J_r x - J_i y + \Omega y = 0, \\ J_i x + J_r y - \Omega x = 0, \\ (\mathrm{Re}(w))^T x + (\mathrm{Im}(w))^T y - 1 = 0, \\ (\mathrm{Re}(w))^T y - (\mathrm{Im}(w))^T x = 0. \end{cases} \tag{5.10}$$

Letting $G = \begin{pmatrix} G_1 \\ G_2 \\ G_3 \\ G_4 \end{pmatrix}$ denote the left-hand side of (5.10), we denote the eigenvalue problem as $G = 0$. Its Jacobian matrix is

$$DG = \begin{pmatrix} \frac{\partial G_1}{\partial x} & \frac{\partial G_1}{\partial y} & \frac{\partial G_1}{\partial \Omega} & \frac{\partial G_1}{\partial \nu} \\ \frac{\partial G_2}{\partial x} & \frac{\partial G_2}{\partial y} & \frac{\partial G_2}{\partial \Omega} & \frac{\partial G_2}{\partial \nu} \\ \frac{\partial G_3}{\partial x} & \frac{\partial G_3}{\partial y} & \frac{\partial G_3}{\partial \Omega} & \frac{\partial G_3}{\partial \nu} \\ \frac{\partial G_4}{\partial x} & \frac{\partial G_4}{\partial y} & \frac{\partial G_4}{\partial \Omega} & \frac{\partial G_4}{\partial \nu} \end{pmatrix}$$

$$= \left(\begin{array}{c|c|c|c} J_r & -J_i + \Omega & y & \frac{dJ_r}{d\nu}x - \frac{dJ_i}{d\nu}y \\ \hline J_i - \Omega & J_r & -x & \frac{dJ_i}{d\nu}x + \frac{dJ_r}{d\nu}y \\ \hline (\mathrm{Re}(w))^T & (\mathrm{Im}(w))^T & 0 & 0 \\ \hline -(\mathrm{Im}(w))^T & (\mathrm{Re}(w))^T & 0 & 0 \end{array}\right),$$

where

$$\begin{aligned} J_r &= \nu D_{\tilde{n}^2} + \mathrm{Re}\left(D\Psi(\tilde{\omega})\right), \\ J_i &= \mathrm{Im}\left(D\Psi(\tilde{\omega})\right), \\ \frac{dJ_r}{d\nu} &= \frac{\partial J_r}{\partial \nu} + \frac{\partial J_r}{\partial \tilde{\omega}}\frac{\partial \tilde{\omega}}{\partial \nu}, \\ \frac{dJ_i}{d\nu} &= \frac{\partial J_i}{\partial \nu} + \frac{\partial J_i}{\partial \tilde{\omega}}\frac{\partial \tilde{\omega}}{\partial \nu}, \end{aligned}$$

and, using (5.3), for which we have

$$\begin{aligned}
&\frac{\partial J_r}{\partial \nu} = D_{\tilde{n}^2},\\
&\frac{\partial J_r}{\partial \tilde{\omega}}\frac{\partial \tilde{\omega}}{\partial \nu} = \mathrm{Re}\left(D\Psi(\frac{\partial \tilde{\omega}}{\partial \nu})\right),\\
&\frac{\partial \tilde{\omega}}{\partial \nu} = \frac{\partial}{\partial \nu}\left(\frac{1}{2\nu}f^{\omega}\right) = -\frac{1}{2\nu^2}f^{\omega},\\
&\frac{\partial J_i}{\partial \nu} = 0,\\
&\frac{\partial J_i}{\partial \tilde{\omega}}\frac{\partial \tilde{\omega}}{\partial \nu} = \mathrm{Im}\left(D\Psi(\frac{\partial \tilde{\omega}}{\partial \nu})\right).
\end{aligned}$$

To construct the approximate inverse of the Jacobian matrix, we decompose our function space into a finite-dimensional computational part and an infinite-dimensional tail. Let $\mathcal{N}$ denote the finite set of Fourier modes used in the numerical Galerkin projection, and let $\mathcal{T} = \mathbb{Z}^2_* \setminus \mathcal{N}$ denote the infinite set of tail modes.

Accordingly, we partition the spatial sequences into their finite and infinite components: $x = (x^{(N)}, x^{(T)})$ and $y = (y^{(N)}, y^{(T)})$. Using a bar to indicate the numerical approximations, we assume that the numerically computed approximate inverse $A^N = \left(DG(\bar{x}, \bar{y}, \bar{\Omega}, \bar{\nu})\right)^{-1}$ acts exclusively on the finite-dimensional space and is decomposed into blocks A^N_{ij} of appropriate sizes.

For the infinite-dimensional tail, the linear operator is strongly dominated by the diagonal Laplacian term. Therefore, on the tail $\mathcal{T}$, the approximate inverse is defined purely by the inverse of this dominant linear term. We define the infinite-dimensional diagonal operator $D^{(T)}$ acting on the tail sequences such that its diagonal elements are

$$D^{(T)}_n = \frac{1}{\bar{\nu}\tilde{n}^2} \quad \text{for } n \in \mathcal{T}.$$

The infinite-dimensional approximate inverse operator A acting on the structured vector $(x^{(N)}, x^{(T)}, y^{(N)}, y^{(T)}, \Omega, \nu)^T$ is then defined as the block matrix

$$A = \left(\begin{array}{cc|cc|cc}
A^N_{11} & 0 & A^N_{12} & 0 & A^N_{13} & A^N_{14}\\
0 & D^{(T)} & 0 & 0 & 0 & 0\\
\hline
A^N_{21} & 0 & A^N_{22} & 0 & A^N_{23} & A^N_{24}\\
0 & 0 & 0 & D^{(T)} & 0 & 0\\
\hline
A^N_{31} & 0 & A^N_{32} & 0 & 0 & 0\\
\hline
A^N_{41} & 0 & A^N_{42} & 0 & 0 & 0
\end{array}\right). \tag{5.11}$$

Remark 5.2.2. *As discussed in the introduction of this thesis in Section 1.3.2, the $O(2)$ symmetry of the Navier-Stokes equations with reflection in the x_3-direction dictates that the Hopf bifurcations lead to two distinct primary branches: a traveling wave (which breaks the reflectional symmetry) and a standing wave (a genuine*

three-dimensional periodic solution that preserves it). While the theoretical and computational framework developed here is completely general and applicable to both the second and third bifurcation points, our analysis is dedicated to the three-dimensional periodic branch emerging from the third bifurcation point, where the critical spatial mode is $n_3 = 2$. This focus was guided by our numerical continuation.

However, it is worth noting that applying this framework to validate the branches at the second bifurcation point, where the critical mode shifts to $n_3 = 1$, would be computationally less expensive. The higher kinematic viscosity at that point typically necessitates fewer Fourier coefficients to accurately represent the numerical solution, thereby reducing the finite-dimensional projection required for the computer-assisted proof. More about this can be read in Remark 5.2.9.

5.2.3 Spaces and existence theorem

For $\eta > 1$, let ℓ^1_η represent the subspace of sequences $a = (a^{(1)}, a^{(2)}, a^{(3)}) \in (\mathbb{R}^3)^{\mathbb{Z}^2}$ equipped with the norm

$$\|a\|_{\ell^1_\eta} = \sum_{l=1}^{3} \sum_{n\in\mathbb{Z}^2} |a^{(l)}_n| \eta^{|n|_1}$$

for $|n|_1 = |n_1| + |n_2|$. Furthermore, we let $\mathbb{R}^\Omega$ and $\mathbb{R}^\nu$ denote one-dimensional real spaces (copies of $\mathbb{R}$) with respective weights $\eta_\Omega, \eta_\nu > 1$. Then, we define the Banach space $\mathcal{X} = \ell^1_\eta(\mathbb{R}) \times \ell^1_\eta(\mathbb{R}) \times \mathbb{R}^\Omega \times \mathbb{R}^\nu$ endowed with the norm

$$\|X\|_{\mathcal{X}} = \|x\|_{\ell^1_\eta} + \|y\|_{\ell^1_\eta} + |\Omega|\eta_\Omega + |\nu|\eta_\nu$$

for $X = (x, y, \Omega, \nu) \in \mathcal{X}$. We are now ready to state the existence theorem.

Theorem 5.2.3 ([68])**.** *Assume that $\eta > 1$ and $\eta_\Omega, \eta_\nu \geq 1$ and that there exists $\bar{X} = (\bar{x}, \bar{y}, \bar{\Omega}, \bar{\nu}) \in \mathcal{X}$ such that non-negative constants Y_0, Z_1 and Z_2 satisfying*

$$\left\|AG(\bar{X})\right\|_{\mathcal{X}} \leq Y_0 \tag{5.12}$$

$$\left\|I - ADG(\bar{X})\right\|_{B(\mathcal{X},\mathcal{X})} \leq Z_1 \tag{5.13}$$

$$\left\|A(DG(X) - DG(\bar{X}))\right\|_{B(\mathcal{X},\mathcal{X})} \leq Z_2 \left\|X - \bar{X}\right\|_{\mathcal{X}}, \quad \text{for all } X \in \mathcal{X}. \tag{5.14}$$

If

$$Z_1 < 1 \qquad \text{and} \qquad 2Y_0Z_2 < (1 - Z_1)^2, \tag{5.15}$$

then, for all $r \in [r_{\min}, r_{\max})$ there exists a unique $\hat{X} = (\hat{x}, \hat{y}, \hat{\Omega}, \hat{\nu}) \in \mathcal{B}_{\mathcal{X}}(\bar{X}, r)$ such that $G(\hat{X}) = 0$, where $\mathcal{B}_{\mathcal{X}}(\bar{X}, r)$ is the closed ball of $\mathcal{X}$, centered at $\bar{X}$ and of radius r, and

$$r_{\min} := \frac{1 - Z_1 - \sqrt{(1 - Z_1)^2 - 2Y_0Z_2}}{Z_2}, \qquad r_{\max} := \frac{1 - Z_1}{Z_2}.$$

Proof. The proof is analogous to the proof of Theorem 2.15 in [68], with the main difference being that we combined the Z_0- and Z_1-bound here, as is for example done in Theorem 2.2.6 in Chapter 2 of this thesis. □

Remark 5.2.4. *By analogy with the symmetry-reduced existence theorem of Chapter 4 (Theorem 4.4.4), Theorem 5.2.3 naturally extends to incorporate symmetries in the x_1- and x_2-directions.*

5.2.4 Bounds

For the derivation of the bounds, it is important to clarify the structure of our index sets. As we are analyzing a specific bifurcation point, our computational grid is effectively two-dimensional. Whenever the general formulation from [68] or the previous chapter uses a four-dimensional index $n = (n_1, n_2, n_3, n_4) \in \mathbb{Z}^4$, we evaluate it at $n_3 = 2$ and $n_4 = -1$. Hence, our index set is reduced to $n = (n_1, n_2) \in \mathbb{Z}^2$.

Furthermore, since the velocity and vorticity fields consist of three components, a complete index is given by a mode-component pair (n, m), where $m \in \{1, 2, 3\}$. This corresponds to the index set $J = \mathbb{Z}^4_* \times \{1, 2, 3\}$ defined in Section 4.3 in [68], reduced to our setting.

We now introduce the parameter $N^\dagger \in \mathbb{N}$, which determines the size of the finite-dimensional block of A. Following the notation in [68], adjusted to our setting, we introduce the index sets $\mathcal{S}^{\mathrm{sol}}$ and $\mathcal{E}(N)$. We let $\mathcal{S}^{\mathrm{sol}}$ be a finite set of indices in $\mathbb{Z}^2$ such that $\bar{x}_n = 0$ and $\bar{y}_n = 0$ for all $n \notin \mathcal{S}^{\mathrm{sol}}$. For $\mathcal{E}(N)$ we recall that $\tilde{n}^2 = n_1^2 + n_2^2 + 4$ for $n \in \mathbb{Z}^2$ and our fixed $n_3 = 2$. Moreover, we define

$$\mathcal{E}(N) = \{n \in \mathbb{Z}^2 : |\nu \tilde{n}^2| \leq N\}, \quad \mathcal{E}^\dagger = \mathcal{E}(N^\dagger).$$

Since the functional analytic framework for computing the bounds closely mirrors the one established in Chapter 4, we adapt the estimates for the extended Hopf system without reproducing the algebraic derivations.

Y_0-bound

We aim to compute a constant $Y_0 \geq 0$ such that

$$\left\| AG(\bar{X}) \right\|_{\mathcal{X}} \leq Y_0.$$

Let $\eta > 1$ be the weight used in the ℓ^1_η-norm.

Lemma 5.2.5. *The Y_0-bound is given by*

$$Y_0 = \|A^N G^N(\bar{X})\|_{\mathcal{X}} + \sum_{n \in (\mathcal{S}^{\mathrm{sol}} + \mathcal{S}^{\mathrm{sol}}) \setminus \mathcal{E}^\dagger} \sum_{m=1}^{3} \left| \frac{1}{\bar{\nu} \tilde{n}^2} (G_1(\bar{X}))_n^{(m)} \right| \eta^{|\tilde{n}|_1}$$
$$+ \sum_{n \in (\mathcal{S}^{\mathrm{sol}} + \mathcal{S}^{\mathrm{sol}}) \setminus \mathcal{E}^\dagger} \sum_{m=1}^{3} \left| \frac{1}{\bar{\nu} \tilde{n}^2} (G_2(\bar{X}))_n^{(m)} \right| \eta^{|\tilde{n}|_1}.$$

Proof. The bound is calculated by splitting the residual into a finite computational part and an analytic tail. Following the same procedure as in Chapter 4 and [68], the result follows immediately. □

Y_0-bound: symmetric case

Recall from the previous chapter and from [68] that J^{Red} represents the set of symmetry-reduced indices, including the vector components, and that $\xi^s_{n,m}$ incorporates both the orbit size and the exponential weight for Fourier mode-component pairs $(n,m) \in J^{\mathrm{Red}}$. The symmetry-reduced norm is defined as in Section 4.4.1. Imposing these symmetry conditions yields

$$Y_0^{\mathrm{Red}} = \|A^N_{\mathrm{Red}} G^N_{\mathrm{Red}}(\bar{X})\|_{\mathcal{X},\mathrm{Red}} + \sum_{\substack{n \in (\mathcal{S}^{\mathrm{sol}} + \mathcal{S}^{\mathrm{sol}}) \setminus \mathcal{E}^\dagger \\ (n,m) \in J^{\mathrm{Red}}}} \xi^s_{n,m} \left| \frac{1}{\bar{\nu}\tilde{n}^2} (G_{1,\mathrm{Red}}(\bar{X}))_n \right| + \sum_{\substack{n \in (\mathcal{S}^{\mathrm{sol}} + \mathcal{S}^{\mathrm{sol}}) \setminus \mathcal{E}^\dagger \\ (n,m) \in J^{\mathrm{Red}}}} \xi^s_{n,m} \left| \frac{1}{\bar{\nu}\tilde{n}^2} (G_{2,\mathrm{Red}}(\bar{X}))_n \right|.$$

To avoid repetition, the explicit derivations of the symmetry-reduced bounds for Z_1 and Z_2 are omitted. These bounds follow from their full-space counterparts using a method analogous to the one of the Y_0-bound.

Z_1-bound

We require a constant Z_1 such that

$$\left\| I - ADG(\bar{X}) \right\|_{B(\mathcal{X},\mathcal{X})} \leq Z_1.$$

Before deriving this bound, we introduce $\tilde{N} \in \mathbb{N}$ as a parameter determining the tail split of Z_1. Recall that $N^\dagger$ determines the size of the finite part of A. We choose $\tilde{N}$ and $N^\dagger$ such that $\tilde{N} \geq N^\dagger$. Following the notation in [68], we set $\tilde{\mathcal{S}}^{\mathrm{sol}}(\tilde{N}) = \mathcal{E}(\tilde{N}) + \mathcal{S}^{\mathrm{sol}}$. The bound is formulated in the following lemma.

Lemma 5.2.6.

$$Z_1 = \max\left\{ \max_{1 \leq m \leq 3} \left(Z_1^{\mathrm{finite}}\right)^{(m)}, \max_{1 \leq m \leq 3} \left(Z_1^{\mathrm{tail}}\right)^{(m)} \right\}$$

where the finite part is

$$\left(Z_1^{\mathrm{finite}}\right)^{(m)} = \max_{n \in \tilde{\mathcal{S}}^{\mathrm{sol}}(\tilde{N})} \frac{1}{\eta^{|n|_1}} \left\| \left(I^N - A^N [DG^N(\bar{X})]^{(\cdot,m)} \right) e_n \right\|_{\mathcal{X}},$$

and the tail part is given by

$$
\begin{aligned}
\left(Z_1^{\mathrm{tail}}\right)^{(m)} &= 4\Bigg(\frac{\sqrt{3}}{\sqrt{\nu\tilde{N}}}\|\max_{1\le p\le 3}(M\tilde{\omega})^{(p)}\|_{\ell^1_\eta} + \sum_{l=1}^{3}\frac{1}{\tilde{N}}\|D_m(M\tilde{\omega})^{(l)}\|_{\ell^1_\eta} \\
&+ \frac{1}{\tilde{N}}\sum_{l=1}^{3}\left(\sum_{p=1}^{3}\|D_p\tilde{\omega}^{(l)}\|_{\ell^1_\eta} - \|D_m\tilde{\omega}^{(l)}\|_{\ell^1_\eta}\right) \\
&+ \frac{1}{\tilde{N}}\left(\frac{3}{2}\sum_{p=1}^{3}\|\tilde{\omega}^{(p)}\|_{\ell^1_\eta} - \frac{1}{2}\|\tilde{\omega}^{(m)}\|_{\ell^1_\eta}\right)\Bigg) + 2\frac{\bar{\Omega}}{\tilde{N}} \\
&+ \frac{1}{\eta_\nu}\sum_{k\notin\mathcal{E}^\dagger}\frac{1}{\bar{\nu}\tilde{k}^2}\sum_{l=1}^{3}\left|\left(\left(\mathrm{Re}\left(D\Psi(\frac{\partial\tilde{\omega}}{\partial\nu})\right)\bar{x}\right)^{(l)} - \left(\mathrm{Im}\left(D\Psi(\frac{\partial\tilde{\omega}}{\partial\nu})\right)\bar{y}\right)^{(l)}\right)_k\right|\eta^{|\tilde{k}|_1} \\
&+ \frac{1}{\eta_\nu}\sum_{k\notin\mathcal{E}^\dagger}\frac{1}{\bar{\nu}\tilde{k}^2}\sum_{l=1}^{3}\left|\left(\left(\mathrm{Im}\left(D\Psi(\frac{\partial\tilde{\omega}}{\partial\nu})\right)\bar{x}\right)^{(l)} + \left(\mathrm{Re}\left(D\Psi(\frac{\partial\tilde{\omega}}{\partial\nu})\right)\bar{y}\right)^{(l)}\right)_k\right|\eta^{|\tilde{k}|_1}.
\end{aligned}
$$

Remark 5.2.7. *We can actually replace $\sqrt{3}$ by $\sqrt{2}$ in the first term of $\left(Z_1^{\mathrm{tail}}\right)^{(m)}$ because our equilibrium $\tilde{\omega}$ is strictly two-dimensional. Furthermore, increasing $\tilde{N}$ lowers Z_1^{tail}, while increasing $N^\dagger$ lowers Z_1^{finite}, presenting a trade-off between bound tightness and computational cost.*

Proof. To bound Z_1, we must estimate the operator norm $\|I - ADG(\bar{X})\|_{B(\mathcal{X},\mathcal{X})}$. Since the chosen Banach space is equipped with a weighted ℓ^1-norm, the induced operator norm corresponds to the supremum of the weighted column sums. Therefore, we estimate the operator norm column-wise. For $1 \le m \le 3$, we investigate

$$\sup_n \frac{\|I - A[DG(\bar{X})]^{(\cdot,m)}e_n\|_{\ell^1_\eta}}{\|e_n\|_{\ell^1_\eta}}.$$

As the index set of Fourier modes is infinite, we cannot compute this supremum entirely by machine. We must therefore partition the supremum into a finite computational part and an infinite analytical tail, using the block structure of A defined in (5.11).

For the modes inside the computational part given by $n \in \tilde{\mathcal{S}}^{\mathrm{sol}}(\tilde{N})$, the operator A acts via the dense numerical matrix A^N. Hence, we consider the finite computation

$$\left(Z_1^{\mathrm{finite}}\right)^{(m)} = \max_{n\in\tilde{\mathcal{S}}^{\mathrm{sol}}(\tilde{N})}\frac{1}{\eta^{|n|_1}}\|I^N - A^N[DG^N(\bar{X})]^{(\cdot,m)}e_n\|_{\ell^1_\eta}.$$

For the infinite tail $n \notin \tilde{\mathcal{S}}^{\mathrm{sol}}(\tilde{N})$, we let I_{ij} represent identity blocks corresponding with the size of A_{ij} and we consider $\sup_{n\notin\tilde{\mathcal{S}}^{\mathrm{sol}}(\tilde{N})}\frac{\|I_{ij} - A_{ii}[DG_{ij}(\bar{X})]^{(\cdot,m)}e_n\|}{\|e_n\|}$ for indices $i = 1, 2$ and $1 \le j \le 4$. Note that for $i = 3, 4$ the tail parts vanish entirely.

While part of the bounds directly parallel the derivations in Chapter 4 and [68], we outline the derivation of the terms unique to the extended Hopf formulation. For

the block DG_{11}, the unbounded growth of the spatial derivatives is neutralized by the quadratic decay of the approximate inverse, as established in the derivation of (4.15). By applying bounds on the convolution terms, we obtain

$$\begin{aligned}
&\sup_{n\notin\tilde{\mathcal{S}}^{\mathrm{sol}}(\tilde{N})} \frac{\|I_{11}-A_{11}[DG_{11}(\bar{X})]^{(\cdot,m)}e_n\|}{\|e_n\|} \\
&\quad= \sup_{n\notin\tilde{\mathcal{S}}^{\mathrm{sol}}(\tilde{N})} \frac{1}{\eta^{|n|_1}}\sum_{l=1}^{3}\sum_{k\notin\mathcal{E}^\dagger}\frac{1}{\bar{\nu}\tilde{k}^2}\left|\mathrm{Re}\left(D\Psi(\tilde{\omega})\right)\right)_{kn}^{(l,m)}\Big|\,\eta^{|k|_1} \\
&\quad\le \frac{\sqrt{3}}{\sqrt{\bar{\nu}\tilde{N}}}\|\max_{1\le p\le 3}(M\tilde{\omega})^{(p)}\|_{\ell^1_\eta} + \sum_{l=1}^{3}\frac{1}{\tilde{N}}\|D_m(M\tilde{\omega})^{(l)}\|_{\ell^1_\eta} \\
&\quad+ \frac{1}{\tilde{N}}\sum_{l=1}^{3}\sum_{p=1}^{3}(1-\delta_{pm})\|D_p\tilde{\omega}^{(l)}\|_{\ell^1_\eta} + \frac{1}{\tilde{N}}\sum_{p=1}^{3}\left(1+\frac{1}{2}(1-\delta_{pm})\right)\|\tilde{\omega}^{(p)}\|_{\ell^1_\eta}.
\end{aligned}$$

Recall from (5.3) that we have an explicit expression for the equilibrium given by $\tilde{\omega}(\bar{\nu}) = \frac{1}{2\bar{\nu}}f^{\omega}$, which has finitely many nonzero modes and thus can be computed.

In contrast to this purely spatial term, the block corresponding to DG_{12} contains an additional scaling term due to the variable Ω. Splitting the supremum into a spatial and a frequency part, the spatial part is bounded analogously to DG_{11}. The frequency part arises from the derivative of the linear term Ωy with respect to y, multiplied by the tail of the approximate inverse. Therefore, we have the following bound:

$$\begin{aligned}
&\sup_{n\notin\tilde{\mathcal{S}}^{\mathrm{sol}}(\tilde{N})} \frac{\|I_{12}-A_{11}[DG_{12}(\bar{X})]^{(\cdot,m)}e_n\|}{\|e_n\|} \\
&\quad\le \sup_{n\notin\tilde{\mathcal{S}}^{\mathrm{sol}}(\tilde{N})} \frac{1}{\eta^{|n|_1}}\sum_{l=1}^{3}\sum_{k\notin\mathcal{E}^\dagger}\frac{1}{\bar{\nu}\tilde{k}^2}\left|\mathrm{Im}\left(D\Psi(\tilde{\omega})\right)\right)_{kn}^{(l,m)}\Big|\,\eta^{|k|_1} + \frac{\bar{\Omega}}{\tilde{N}},
\end{aligned}$$

where we used the definition of $\tilde{\mathcal{S}}^{\mathrm{sol}}(\tilde{N})$ for the second term.

Next, note that because $DG_{13}(\bar{X})$ acts only on the parameter Ω, it vanishes entirely in the tail part of the Z_1-bound.

New in this extended system are the derivatives with respect to the viscosity, represented by the columns DG_{14} and DG_{24}. For the first block, we evaluate

$$\begin{aligned}
&\|I_{14}-A_{11}[DG_{14}(\bar{X})]^{(l)}\| \\
&\quad= \frac{1}{\eta_\nu}\sum_{k\notin\mathcal{E}^\dagger}\frac{1}{\bar{\nu}\tilde{k}^2}\sum_{l=1}^{3}\left|\left(\mathrm{Re}\left(D\Psi(\frac{\partial\tilde{\omega}}{\partial\nu})\right)\bar{x}\right)^{(l)} - \left(\mathrm{Im}\left(D\Psi(\frac{\partial\tilde{\omega}}{\partial\nu})\right)\bar{y}\right)^{(l)}\right|_k \eta^{|k|_1}.
\end{aligned}$$

As the two-dimensional equilibrium $\tilde{\omega}$ possesses finitely many nonzero modes, its derivative $\frac{\partial\tilde{\omega}}{\partial\nu}$ also has strict finite support. Consequently, the resulting discrete convolution has finitely many nonzero terms, reducing this infinite tail norm to a finite summation that can be evaluated in MATLAB using interval arithmetic.

Applying an identical block-wise procedure to the second block row of the system (corresponding to $i = 2$, which is associated with G_2), we extract the corresponding spatial bounds for DG_{21} and DG_{22}, alongside the exact same $\frac{\bar{\Omega}}{\bar{N}}$ term. Likewise, DG_{23} vanishes and the ν-derivative evaluates to

$$\begin{aligned}&\|I_{24} - A_{22}[DG_{24}(\bar{X})]^{(l)}\| \\ &\quad = \frac{1}{\eta_\nu} \sum_{k \notin \mathcal{E}^\dagger} \frac{1}{\bar{\nu}\tilde{k}^2} \sum_{l=1}^{3} \left| \left(\mathrm{Im}\left(D\Psi(\frac{\partial \tilde{\omega}}{\partial \nu}) \right) \bar{x} \right)^{(l)} + \left(\mathrm{Re}\left(D\Psi(\frac{\partial \tilde{\omega}}{\partial \nu}) \right) \bar{y} \right)^{(l)} \right|_k \eta^{|k|_1},\end{aligned}$$

which, again, consists of finitely many nonzero terms. Summing the respective components completes the proof. □

Z_2-bound

To apply the radii polynomial approach, we need to determine a bound Z_2 such that

$$\|A[DG(\bar{X} + X_1) - DG(\bar{X})]\|_{B(\mathcal{X})} \leq Z_2 \|X_1\|_{\mathcal{X}}$$

for all $\|X_1\|_{\mathcal{X}} \leq r^*$.

Before stating the bound, we introduce extra notation. Define $\ell^1_{\eta,-1,-1}$ together with the norm

$$\|x\|_{\ell^1_{\eta,-1,-1}} = \sum_{n \in \mathbb{Z}^2} |x_n| \frac{\eta^{|n|_1}}{|n|_\infty}.$$

The division by $|n|_\infty = \max\{|n_1|, |n_2|, 2\}$ compensates for the multiplication by n as a consequence of the derivative operator. Using this norm, we set

$$\mathcal{X}_{-1,-1} = \ell^1_{\eta,-1,-1}(\mathbb{R}) \times \ell^1_{\eta,-1,-1}(\mathbb{R}) \times \mathbb{R} \times \mathbb{R}.$$

The Z_2- bound is formalized in the lemma below.

Lemma 5.2.8. *Let $\mathcal{Y}_1 = \mathcal{Y}_2 = \ell^1_\eta$, $\mathcal{Y}_3 = \mathbb{R}^\Omega$, and $\mathcal{Y}_4 = \mathbb{R}^\nu$, where we recall the norm definitions in Section 5.2.3. The Z_2-bound is given by*

$$Z_2 = \sum_{j=1}^{2} \sum_{i=1}^{4} \left[\frac{2}{\eta_\nu} \|A^N_{ij} \Pi^N D_{\tilde{n}^2}\|_{B(\ell^1_{\eta,-1,-1}, \mathcal{Y}_i)} + \frac{2}{\bar{\nu}\eta_\nu} + C_Z \|A_{ij}\|_{B(\ell^1_{\eta,-1,-1}, \mathcal{Y}_i)} \right],$$

where the constant C_Z is defined as

$$\begin{aligned}C_Z = &\frac{8(3+\sqrt{2})\eta^2}{\left(\bar{\nu} - \frac{r^*}{\eta_\nu}\right)^2 \eta_\nu} + \frac{2}{\eta_\Omega} \\ &+ \frac{4(3+\sqrt{2})\eta^2}{\eta_\nu^2} \left(\|\bar{x}\|_{\ell^1_\eta} + \|\bar{y}\|_{\ell^1_\eta} + 2r^* \right) \left(\frac{1}{\left(\bar{\nu} - \frac{r^*}{\eta_\nu}\right)^3} + \frac{1}{4\left(\bar{\nu} - \frac{r^*}{\eta_\nu}\right)^4} \right).\end{aligned}$$

Proof. By the mean value theorem for Banach spaces, we can bound Z_2 via the second derivative. For any X_1 such that $\|X_1\|_{\mathcal{X}} \leq r^*$, it holds that

$$\begin{aligned}&\|A[DG(\bar{X}+X_1) - DG(\bar{X})]\|_{B(\mathcal{X})} \\ &\quad\leq \left(\sup_{\|\hat{X}\|_{\mathcal{X}}\leq r^*} \|AD^2G(\bar{X}+\hat{X})\|_{B(\mathcal{X}\times\mathcal{X},\mathcal{X})}\right)\|X_1\|_{\mathcal{X}}.\end{aligned}$$

Therefore, we can determine the bound Z_2 by estimating this supremum. The norm of AD^2G evaluated at $\bar{X}+\hat{X}$ is defined by taking the supremum over two arbitrary unit vectors $X_2, X_3 \in \mathcal{X}$:

$$\|AD^2G(\bar{X}+\hat{X})\|_{B(\mathcal{X}\times\mathcal{X},\mathcal{X})} = \sup_{\substack{\|X_2\|_{\mathcal{X}}\leq 1\\ \|X_3\|_{\mathcal{X}}\leq 1}} \|AD^2G(\bar{X}+\hat{X})[X_2,X_3]\|_{\mathcal{X}}.$$

Combining these, we seek a constant Z_2 such that

$$\sup_{\|\hat{X}\|_{\mathcal{X}}\leq r^*} \sup_{\substack{\|X_2\|_{\mathcal{X}}\leq 1\\ \|X_3\|_{\mathcal{X}}\leq 1}} \|AD^2G(\bar{X}+\hat{X})[X_2,X_3]\|_{\mathcal{X}} \leq Z_2.$$

To evaluate D^2G, we investigate its nonzero partial derivatives. Furthermore, note that mixed partials commute (e.g. $D_\nu D_x G = D_x D_\nu G$).

Z_2-bound: derivatives of G_1

We begin with the second derivatives of G_1. Note that $D_{xx}G_1$, $D_yD_xG_1$ and $D_\Omega D_x G_1$ all vanish. The first non-trivial term is $D_\nu D_x G_1[x_2,\nu_3]$, which, using (5.3), reads

$$D_\nu D_x G_1(\bar{X}+\hat{X})[x_2,\nu_3] = \left[D_{\tilde{n}^2}x_2 + \mathrm{Re}\left(D\Psi\left(-\frac{1}{2(\bar{\nu}+\hat{\nu})^2}f^\omega\right) * x_2\right)\right]\nu_3.$$

Multiplying by A_{11} and taking the norm of the first part, we find

$$\begin{aligned}&\|A_{11}\left[D_{\tilde{n}^2}x_2\right]\nu_3\|_{\ell^1_\eta} \\ &\leq \left(\|A_{11}^N\Pi^N D_{\tilde{n}^2}\|_{B(\ell^1_{\eta,-1,-1},\ell^1_\eta)} + \|\Pi^\infty \operatorname{diag}(\bar{\nu}^{-1})\|_{B(\ell^1_{\eta,-1,-1},\ell^1_\eta)}\right)\|x_2\|_{\ell^1_\eta}\nu_3 \\ &\leq \left(\|A_{11}^N\Pi^N D_{\tilde{n}^2}\|_{B(\ell^1_{\eta,-1,-1},\ell^1_\eta)} + \frac{1}{\bar{\nu}}\right)\frac{1}{\eta_\nu}.\end{aligned}$$

For the nonlinear convolution term, we follow the procedure in [68]. We bound the components of $(D\Psi(f)^\omega x_2)_k$ by expanding the terms. First, noting that f^ω has a single nonzero mode in the third component (consisting of four terms of magnitude 1), its norm evaluates exactly to $\|f^{\omega,(3)}\|_{\ell^1_\eta} = 4\eta^2$.

To evaluate the resulting convolutions, we mirror the derivations for the Z_2-bound in Section 3.5 of [68]. For the first two terms, applying Lemma 2.2 of [68] allows us to factor out the advective derivative, which is subsequently absorbed by the

$\ell^1_{\eta,-1,-1}$ norm. Combined with the Banach algebra property and the estimate $\sum_{p=1}^3 \|(Mx_2)^{(p)}\|_{\ell^1_\eta} \le \sum_{p=1}^3 \|x_2^{(p)}\|_{\ell^1_\eta} \le 1$, this yields

$$\|(Mf \star \tilde{D})x_2\|_{\ell^1_{\eta,-1,-1}} \le 4\eta^2,$$
$$\|(Mx_2 \star \tilde{D})f^\omega\|_{\ell^1_{\eta,-1,-1}} \le 4\eta^2.$$

For the remaining two terms, we utilize the following estimate from Section 3.5 in [68]: $\|(u \star \tilde{D})Mv\|_{\ell^1_{\eta,-1,-1}} \le \frac{1+\sqrt{2}}{2}\|u\|_{\ell^1_\eta}\|v\|_{\ell^1_\eta}$. Applying this to our convolutions gives

$$\|(x_2 \star \tilde{D})Mf^\omega\|_{\ell^1_{\eta,-1,-1}} \le 2(1+\sqrt{2})\eta^2,$$
$$\|(f \star \tilde{D})Mx_2\|_{\ell^1_{\eta,-1,-1}} \le 2(1+\sqrt{2})\eta^2.$$

Combining these and observing that $\frac{1}{2(\bar{\nu}+\hat{\nu})^2} \le \frac{1}{2(\bar{\nu}-\frac{r^*}{\eta_\nu})^2}$, we obtain

$$\begin{aligned}&\|A_{11}D_\nu D_x G_1(\bar{X}+\hat{X})[x_2,\nu_3]\|_{\ell^1_\eta}\\ &\quad\le \left(\|A_{11}^N \Pi^N D_{\tilde{n}^2}\|_B + \frac{1}{\bar{\nu}} + \|A_{11}\|_B \frac{2(3+\sqrt{2})\eta^2}{(\bar{\nu}-\frac{r^*}{\eta_\nu})^2}\right)\frac{1}{\eta_\nu},\end{aligned}$$

where B denotes the bounded operator space $B(\ell^1_{\eta,-1,-1}, \ell^1_\eta)$.

To evaluate the operator norms $\|A_{i1}\|_B$ and its finite-dimensional projections, we rely on the standard approach for approximate inverses in this weighted ℓ^1-setting. Following (3.14) in [68], the norm of an operator A acting on these spaces can be explicitly bounded:

$$\|A\|_{B(\mathcal{X}_{-1,-1},\mathcal{X})} \le \max\left\{\max_{1\le m\le 3}\max_{n\in\mathcal{E}^\dagger}\frac{|n|_\infty}{\eta^{|n|_1}}\|A^{(\cdot,m)}e_n\|_{\mathcal{X}}, \frac{1}{\sqrt{\bar{\nu}\tilde{N}^\dagger}}\right\}. \tag{5.16}$$

Applying (5.16) to the respective block components, analogous bounds are immediately obtained for the multipliers A_{21}, A_{31}, and A_{41}:

$$\begin{aligned}&\|A_{21}D_\nu D_x G_1(\bar{X}+\hat{X})[x_2,\nu_3]\|_{\ell^1_\eta}\\ &\quad\le \frac{1}{\eta_\nu}\left(\|A_{21}^N \Pi^N D_{\tilde{n}^2}\|_B + \frac{1}{\bar{\nu}} + \|A_{21}\|_B \frac{2(3+\sqrt{2})\eta^2}{(\bar{\nu}-\frac{r^*}{\eta_\nu})^2}\right),\\ &\|A_{31}D_\nu D_x G_1(\bar{X}+\hat{X})[x_2,\nu_3]\|_{\mathbb{R}^\Omega}\\ &\quad\le \frac{1}{\eta_\nu}\left(\|A_{31}^N \Pi^N D_{\tilde{n}^2}\|_{B'} + \frac{1}{\bar{\nu}} + \|A_{31}\|_{B'} \frac{2(3+\sqrt{2})\eta^2}{(\bar{\nu}-\frac{r^*}{\eta_\nu})^2}\right),\\ &\|A_{41}D_\nu D_x G_1(\bar{X}+\hat{X})[x_2,\nu_3]\|_{\mathbb{R}^\nu}\\ &\quad\le \frac{1}{\eta_\nu}\left(\|A_{41}^N \Pi^N D_{\tilde{n}^2}\|_{B''} + \frac{1}{\bar{\nu}} + \|A_{41}\|_{B''} \frac{2(3+\sqrt{2})\eta^2}{(\bar{\nu}-\frac{r^*}{\eta_\nu})^2}\right),\end{aligned}$$

where B' and B'' denote the spaces $B(\ell^1_{\eta,-1,-1}, \mathbb{R}^\Omega)$ and $B(\ell^1_{\eta,-1,-1}, \mathbb{R}^\nu)$, respectively.

For the derivative with respect to y, since $D_{yy}G_1 = D_xD_yG_1 = 0$, the only remaining nonzero mixed partial derivative is

$$D_\nu D_y G_1(\bar{X}+\hat{X})[y_2,\nu_3] = \left[\mathrm{Im}\left(D\Psi\left(-\frac{1}{2(\bar{\nu}+\hat{\nu})^2}f^\omega\right) * y_2\right)\right]\nu_3.$$

Its evaluation is identical to $D_\nu D_x G_1$, but acts on the imaginary component. Applying the same estimates yields identical bounds proportional to $\|A_{i1}\|\frac{2(3+\sqrt{2})\eta^2}{(\bar{\nu}-\frac{r^*}{\eta_\nu})^2\eta_\nu}$.

For the derivatives involving Ω, the only nonvanishing term is $D_yD_\Omega G_1[\Omega_2, y_3]$, which acts as the identity on y_3. Dividing by the input weight η_Ω yields the bound

$$\|A_{i1}D_yD_\Omega G_1[\Omega_2,y_3]\| \le \|A_{i1}\|\frac{1}{\eta_\Omega}.$$

Finally, we evaluate the twice-differentiated ν term. Since $\tilde{\omega}(\nu) = \frac{1}{2\nu}f^\omega$, applying the chain rule generates components proportional to ν^{-3} and ν^{-4}. Application of the convolution bounds results in

$$\begin{aligned}&\|A_{i1}D_\nu D_\nu G_1(\bar{X}+\hat{X})[\nu_2,\nu_3]\|_{\ell^1_\eta}\\ &\quad\le \|A_{i1}\|\frac{4(3+\sqrt{2})\eta^2}{\eta_\nu^2}\left(\|\bar{x}\|_{\ell^1_\eta}+\|\bar{y}\|_{\ell^1_\eta}+2r^*\right)\left(\frac{1}{(\bar{\nu}-\frac{r^*}{\eta_\nu})^3}+\frac{1}{4(\bar{\nu}-\frac{r^*}{\eta_\nu})^4}\right).\end{aligned}$$

Z_2-bound: derivatives of G_2, G_3, and G_4

When computing the bound for the full operator AD^2G, the block-matrix product expands row-wise as $\sum_{j=1}^4 A_{ij}D^2G_j$. The structure of G_2 is symmetric to G_1 (exchanging real and imaginary parts and minus signs). Thus, the estimates for D^2G_2 follow the same approach, substituting the appropriate block matrices A_{i2} in place of A_{i1}. Furthermore, G_3 and G_4 are linear with respect to the relevant variables, meaning all second derivatives D^2G_3 and D^2G_4 vanish. This justifies why the summation over the column blocks j in the definition of the Z_2-bound in the statement of our lemma ranges strictly from $j=1$ to $j=2$, entirely omitting the parameter blocks $j=3$ and $j=4$. □

5.2.5 Results

While the rigorous framework for a computer-assisted proof of the Hopf bifurcation has been fully established in this chapter, its final execution is currently constrained by hardware limits. Evaluated in MATLAB (2024a) on an Intel Xeon W-2191B CPU with 256 GB RAM, we implemented the symmetry-reduced formulation. Taking advantage of the fact that we only take $n_3 = 2$ and $n_4 = -1$ into account, we reduced the computational grid to $(2N_{x_1}+1)\times(2N_{x_2}+1)\times 1\times 1\times 3$.

We initially set $N_{x_1} = 30$, $N_{x_2} = 30$, $N^\dagger = 800$ and $\tilde{N} = 1600$, alongside the Banach space weights $\eta = 1+10^{-7}$, $\eta_\Omega = 1$ and $\eta_\nu = 70$. However, even without

the use of interval arithmetic, evaluating the bounds at this scale turned out to be exceptionally demanding. Executing the finite and tail bound computations of the Z_1-bound exceeded the available 256 GB of memory. By parallelizing the computations of Z_1^{finite}, the program successfully executed in approximately 77.2 hours, yielding a finite bound of $Z_1^{\text{finite}} \approx 5.4$ and a tail bound of $Z_1^{\text{tail}} \approx 3.6$.

However, for the Newton-Kantorovich contraction argument to succeed, we strictly require the Z_1-bound to be less than 1. Using our code, we deduced that achieving a valid tail bound (e.g. $Z_1^{\text{tail}} \approx 0.9$) would require increasing the tail parameter to at least $\tilde{N} = 24084$. Indeed, increasing the value of $\tilde{N}$ to 24084 results in $Z_1^{\text{tail}} = 0.9004$, together with $Y_0 = 1.9656 \cdot 10^{-4}$ and $Z_2 = 9.5734 \cdot 10^3$ for $r^* = 10^{-3}$. Nevertheless, combining this increased value of $\tilde{N}$ with a significantly larger value of $N^\dagger$ to decrease Z_1^{finite}, exhausts our currently available memory. Attempting to circumvent this memory limit pushes the computation time well beyond feasible limits. Since these floating-point evaluations already hit a hardware wall, including interval arithmetic is not possible at this scale.

Consequently, the existence of the Hopf bifurcation cannot be concluded here. A successful proof will likely require either a significantly larger computational tool or further optimization of the Z_1-bound. The code corresponding to the analysis of the Hopf bifurcation problem is available in [74].

Remark 5.2.9. *As stated in Remark 5.2.2, applying the framework to the second bifurcation point should be computationally less expensive. To verify this, we executed the validation for the onset of the second Hopf bifurcation point without interval arithmetic, which led to a successful computation. For this evaluation, we set* $N_{x_1} = 30$, $N_{x_2} = 30$, $N^\dagger = 300$ *and* $\tilde{N} = 4500$, *alongside the Banach space weights* $\eta = 1 + 10^{-7}$, $\eta_\Omega = 1$ *and* $\eta_\nu = 70$.

*Requiring approximately two weeks of computation (*1151195 *seconds), the execution yielded the following bounds, represented with four decimal places:*

$$Y_0 = 2.3371 \cdot 10^{-10},$$
$$Z_1 = 8.9937 \cdot 10^{-1},$$
$$Z_2 = 1.9299 \cdot 10^3 \text{ for } r^* = 2.3225 \cdot 10^{-9}.$$

The resulting existence radius is $2.3225 \cdot 10^{-9}$. *While a mathematical proof requires re-executing these evaluations utilizing interval arithmetic, these successful floating-point results provide confidence.*

5.3 Toward three-dimensional solutions away from the bifurcation

In the previous section, we formulated the zero-finding problem and established the computational framework to prove the existence of a Hopf bifurcation point. Although the execution of the final proof is currently constrained by available computational resources, the theoretical foundation can be built upon. We do so by shifting our focus to the parameter-dependent dynamics of the three-dimensional

Navier-Stokes equations. The goal of this section is to set up the basis of the rigorous mathematical framework required to prove the existence of a continuous branch of periodic solutions emerging from the bifurcation point. In two spatial dimensions, a similar validation is successfully achieved in [5], providing a strong precedent for extending these techniques into three spatial dimensions.

5.3.1 The zero-finding formulation

We isolate the bifurcating branch by expanding the vorticity field around the two-dimensional equilibrium $\omega_0(x_1, x_2)(\nu)$, which depends on the viscosity ν, and has the explicit form given in (5.3). We substitute the following ansatz into the vorticity equation:

$$\begin{aligned}\omega(x_1, x_2, x_3, t) &= \sum_{(k,m)\in(\mathbb{Z}^2\times\mathbb{Z}^2)_*} \sum_{n\in\mathbb{N}_0} \varepsilon^n \omega_{nkm} e^{i(k_1x_1+k_2x_2+m_1x_3+\Omega m_2 t)} \\ &= \omega_0(x_1, x_2)(\nu) + \varepsilon\tilde{\omega}(\varepsilon, x_1, x_2, x_3, t),\end{aligned} \tag{5.17}$$

where $\varepsilon > 0$ parametrizes the branch and the perturbation $\tilde{\omega}$ is $\frac{2\pi}{\Omega(\varepsilon)}$-periodic in time and nonzero at $\varepsilon = 0$. Furthermore, $\tilde{\omega}$ is expanded as a Taylor series in ε with coefficients $\tilde{\omega}_{nkm}$. Note that we have split the Fourier indices such that $k = (k_1, k_2) \in \mathbb{Z}^2$ corresponds to the first two spatial dimensions and such that $m = (m_1, m_2) \in \mathbb{Z}^2$ corresponds to the third spatial dimension and time. Moreover, we write $|k|^2 = k_1^2 + k_2^2$.

To define the zero-finding problem, we introduce the bilinear form $B(u, v)$ associated with Ψ defined in (5.5):

$$B(u, v) := i\left[(Mu \star \tilde{D})v\right] - i\left[(u \star \tilde{D})Mv\right]. \tag{5.18}$$

By definition, the nonlinearity can be expressed as $\Psi(\omega) = B(\omega, \omega)$.

Substituting the ansatz (5.17) into the vorticity equation, expanding the bilinear form and isolating the Taylor-Fourier coefficients yields $F^\omega(\tilde{\omega}, \Omega, \nu) = 0$. Recalling that the subscript $*$ denotes the exclusion of the zero mode, the components for $n \in \mathbb{N}_0$ and $(k, m) \in \left(\mathbb{Z}^2 \times \mathbb{Z}^2\right)_*$ are given by

$$\begin{aligned}F^\omega_{nkm} = im_2 \sum_{j=0}^{n} \Omega_j \tilde{\omega}_{(n-j)km} + (|k|^2 + m_1^2) \sum_{j=0}^{n} \nu_j \tilde{\omega}_{(n-j)km} \\ + \left[B(\omega_0, \tilde{\omega})\right]_{nkm} + \left[B(\tilde{\omega}, \omega_0)\right]_{nkm} + \left[B(\tilde{\omega}, \tilde{\omega})\right]_{(n-1)km}.\end{aligned} \tag{5.19}$$

Here, $[\dots]_{nkm}$ represents the extraction of the n-th order Taylor coefficient and the (k, m)-th Fourier mode. The last term arises from matching powers of ε. Specifically, the quadratic perturbation generates a multiplier ε through the ansatz (5.17), which causes its contribution to the n-th order equation to be dependent on the $(n-1)$-th order coefficient of the bilinear form. Since the Taylor expansion contains strictly non-negative powers, the quadratic term vanishes when we evaluate (5.19) at $n = 0$, as this leads to a Taylor index of -1.

Remark 5.3.1. *There are two ways to interpret the ε-dependence in this chapter. The first approach treats Ω, ν and $\tilde{\omega}$ as power series evaluated at a fixed $\varepsilon > 0$. In this perspective, the unknowns are the evaluated scalar and vector quantities: the temporal frequency $\Omega = \Omega(\varepsilon)$, the viscosity $\nu = \nu(\varepsilon)$ and the perturbation Fourier coefficients $\tilde{\omega} = \tilde{\omega}(\varepsilon)$. The second approach, which we predominantly use to formulate our zero-finding problem, treats the infinite sequence of the n-th order Taylor coefficients (i.e., Ω_n, ν_n and $\tilde{\omega}_{nkm}$) as the unknowns. This second approach captures the analytical dependency of the solution branch on the bifurcation parameter. Nevertheless, the series interpretation for a fixed ε remains a valuable perspective that will occasionally be used throughout the chapter.*

Remark 5.3.2. *The connection between this continuation setup and the setup of the onset of the bifurcation point is explicitly embedded in* (5.19)*. By evaluating the system at $n = 0$, the nonlinear perturbation term $[B(\tilde{\omega}, \tilde{\omega})]_{(n-1)km}$ vanishes, as the Taylor indices must be non-negative. The remaining four terms in* (5.19) *constitute the action of the spatial Jacobian matrix $J(\omega_0, \nu)$ evaluated at the Hopf bifurcation point, shifted by the frequency term $i\Omega m_2$. Thus, at $n = 0$, the zero-finding problem $F^{\omega}(\varepsilon) = 0$ naturally reduces to the linearized eigenvalue problem defined in Section 5.2.1.*

To uniquely determine Ω and ν, we require two supplementary scalar equations at each Taylor order. As we will restrict our function space to a subspace that adheres to the symmetry in x_3, we do not require a spatial phase condition. We therefore impose only a phase condition to eliminate the temporal translation symmetry and an amplitude condition to fix the parameterization scaling. To formulate these conditions, let w denote the numerical approximation associated with the Hopf bifurcation point (as introduced in Section 5.2.2), adjusted to our symmetric setting. Since w captures the specific critical modes of the bifurcation, its Fourier coefficients are nonzero only at $m = (2, 1)$ and $m = (2, -1)$.

Letting * denote the complex conjugate and δ_{n0} denote the Kronecker delta (which is 1 for $n = 0$ and 0 otherwise), we set (cf. Section 2.3 in [72])

$$F_n^{\text{phase}} = \sum_{l=1}^{3} \sum_{(k,m)\in(\mathbb{Z}^2\times\mathbb{Z}^2)_*} i m_2 \tilde{\omega}_{nkm}^{(l)} \left(w_{km}^{(l)}\right)^* = 0,$$

$$F_n^{\text{amp}} = \sum_{l=1}^{3} \sum_{(k,m)\in(\mathbb{Z}^2\times\mathbb{Z}^2)_*} m_2^2 \tilde{\omega}_{nkm}^{(l)} \left(w_{km}^{(l)}\right)^* - \delta_{n0} = 0,$$

for all $n \in \mathbb{N}_0$. To analyze this system, we initially formulate the function spaces over the complex field. We introduce the complex weighted ℓ^1-space $\mathcal{X}_{\mathbb{C}}^{\omega} = \ell^1_{\varepsilon,\eta}(\mathbb{C})$. For a fixed continuation step size ε and weights $\eta > 1$, the norm of the perturbation $\tilde{\omega}$ is defined as

$$\|\tilde{\omega}\|_{\mathcal{X}_{\mathbb{C}}^{\omega}} = \sum_{l=1}^{3} \sum_{n=0}^{\infty} \sum_{(k,m)\in(\mathbb{Z}^2\times\mathbb{Z}^2)_*} |\tilde{\omega}_{nkm}^{(l)}| \varepsilon^n \eta^{|k_1|+|k_2|+|m_1|+|m_2|}.$$

Similarly, we define the parameter sequence spaces $\mathcal{X}_{\mathbb{C}}^{\Omega}$ and $\mathcal{X}_{\mathbb{C}}^{\nu}$ equipped with the norms $\|\Omega\|_{\mathcal{X}_{\mathbb{C}}^{\Omega}} = \sum_{n=0}^{\infty} |\Omega_n| \varepsilon^n \eta_\Omega$ and $\|\nu\|_{\mathcal{X}_{\mathbb{C}}^{\nu}} = \sum_{n=0}^{\infty} |\nu_n| \varepsilon^n \eta_\nu$, where $\eta_\Omega, \eta_\nu \geq 1$.

We reduce the required set of Fourier indices by exploiting the spatial symmetries of the equations. We enforce a reflection symmetry in the x_3-direction, under which the third vorticity component remains unchanged and the first two components undergo a sign change. Introducing the reflection matrix $R_z = \mathrm{diag}(-1, -1, 1)$ (see C_{g1} in [68]), the symmetry is expressed as $\omega(x_1, x_2, -x_3, t) = R_z\omega(x_1, x_2, x_3, t)$. In the Fourier domain, this links the negative and positive x_3-frequencies, resulting in the constraint

$$\tilde{\omega}_{n,k,(-m_1,m_2)} = R_z\tilde{\omega}_{n,k,(m_1,m_2)}.$$

Since the coefficients for $-m_1$ are entirely dependent on the corresponding positive modes, this symmetry halves the number of unknowns in the x_3-direction and allows us to restrict our analysis to the modes where $m_1 \geq 0$.

Therefore, we formulate our zero-finding problem on the symmetry-reduced Banach space $\mathcal{X}$ defined by

$$\mathcal{X} = \mathcal{X}_{\mathbb{C}}^{\Omega} \times \mathcal{X}_{\mathbb{C}}^{\nu} \times \Big\{\tilde{\omega} \in \mathcal{X}_{\mathbb{C}}^{\omega} : \tilde{\omega}_{n,k,(-m_1,m_2)} = R_z\tilde{\omega}_{n,k,(m_1,m_2)} \\ \text{for all } n \in \mathbb{N}_0, (k, m) \in (\mathbb{Z}^2 \times \mathbb{Z}^2)_*\Big\},$$

equipped with the product norm

$$\|(\Omega, \nu, \tilde{\omega})\|_{\mathcal{X}} = \|\Omega\|_{\mathcal{X}_{\mathbb{C}}^{\Omega}} + \|\nu\|_{\mathcal{X}_{\mathbb{C}}^{\nu}} + \|\tilde{\omega}\|_{\mathcal{X}_{\mathbb{C}}^{\omega}}.$$

The full zero-finding problem is thus defined as finding the root of the operator $\mathcal{F} : \mathcal{X} \to \mathcal{X}$, given by

$$\mathcal{F}(\Omega, \nu, \tilde{\omega}) = \begin{pmatrix} \left(F_n^{\text{phase}}\right)_{n\in\mathbb{N}_0} \\ \left(F_n^{\text{amp}}\right)_{n\in\mathbb{N}_0} \\ \left(F_{nkm}^{\omega}\right)_{n\in\mathbb{N}_0,(k,m)\in(\mathbb{Z}^2\times\mathbb{Z}^2)_*} \end{pmatrix} = 0.$$

While the Fourier coefficients are naturally complex, the physical context of the Navier-Stokes equations imposes real-valued constraints. Specifically, Ω and ν must be strictly real parameters and the physical vorticity field $\omega(x, t)$ must be a real-valued vector field. Rather than imposing these conditions directly as constraints on the complex variables, we recover the real-valued nature of the solutions through an *a posteriori* symmetry argument as done in [68]. By ensuring that the numerical approximations are constrained by the conjugate symmetry condition $\tilde{\omega}_{n,-k,-m} = (\tilde{\omega}_{nkm})^*$, the validated solutions are guaranteed to preserve this symmetry, resulting in real-valued solutions.

Remark 5.3.3. *Another valid approach to guarantee that the zero-finding problem is defined entirely over the real field would be to explicitly decompose all the complex equations and sequences into their real and imaginary parts, analogous to the strategy used for the eigenvalue problem in Section 5.2.2.*

5.3.2 The Jacobian matrix

To apply the existence theorem, we compute the Fréchet derivative of $\mathcal{F}$. The block structure of the Jacobian matrix $D\mathcal{F}$ is:

$$D\mathcal{F}(\Omega,\nu,\tilde{\omega}) = \begin{pmatrix} D_\Omega F^{\text{phase}} & D_\nu F^{\text{phase}} & D_{\tilde{\omega}} F^{\text{phase}} \\ D_\Omega F^{\text{amp}} & D_\nu F^{\text{amp}} & D_{\tilde{\omega}} F^{\text{amp}} \\ D_\Omega F^{\omega} & D_\nu F^{\omega} & D_{\tilde{\omega}} F^{\omega} \end{pmatrix}.$$

Note that $D_\Omega F^{\text{phase}}$, $D_\nu F^{\text{phase}}$, $D_\Omega F^{\text{amp}}$ and $D_\nu F^{\text{amp}}$ are all zero because the supplementary conditions are independent of the scalar parameters.

We define the full Fréchet derivative explicitly by the action of the operator blocks on a perturbation vector $h = (\hat{\Omega}, \hat{\nu}, \hat{\omega}) \in \mathcal{X}$:

$$D\mathcal{F}(\Omega,\nu,\tilde{\omega})[\hat{\Omega},\hat{\nu},\hat{\omega}] = \begin{pmatrix} D_{\tilde{\omega}} F^{\text{phase}}[\hat{\omega}] \\ D_{\tilde{\omega}} F^{\text{amp}}[\hat{\omega}] \\ D_\Omega F^{\omega}[\hat{\Omega}] + D_\nu F^{\omega}[\hat{\nu}] + D_{\tilde{\omega}} F^{\omega}[\hat{\omega}] \end{pmatrix}.$$

The directional derivatives of the scalar constraints for a given Taylor order $n \in \mathbb{N}_0$ are given by

$$D_{\tilde{\omega}} F_n^{\text{phase}}[\hat{\omega}] = \sum_{l=1}^{3} \sum_{(k,m)\in(\mathbb{Z}^2\times\mathbb{Z}^2)_*} i m_2 \hat{\omega}_{nkm}^{(l)} \left(w_{km}^{(l)}\right)^*,$$

$$D_{\tilde{\omega}} F_n^{\text{amp}}[\hat{\omega}] = \sum_{l=1}^{3} \sum_{(k,m)\in(\mathbb{Z}^2\times\mathbb{Z}^2)_*} m_2^2 \hat{\omega}_{nkm}^{(l)} \left(w_{km}^{(l)}\right)^*.$$

For the vorticity derivative, we evaluate the action of the partial derivatives for each mode $n \in \mathbb{N}_0$ and $(k,m) \in (\mathbb{Z}^2 \times \mathbb{Z}^2)_*$. The derivative with respect to the temporal frequency yields

$$D_\Omega F_{nkm}^{\omega}[\hat{\Omega}] = i m_2 \sum_{j=0}^{n} \hat{\Omega}_j \tilde{\omega}_{(n-j)km}.$$

When differentiating with respect to the kinematic viscosity ν, we must account for the explicit dependence of the two-dimensional equilibrium ω_0 on ν. Applying the chain rule to the bilinear advection terms yields

$$\begin{aligned} D_\nu F_{nkm}^{\omega}[\hat{\nu}] = {} & (|k|^2 + m_1^2) \sum_{j=0}^{n} \hat{\nu}_j \tilde{\omega}_{(n-j)km} \\ & + \hat{\nu}_0 \left(\left[B\left(\frac{\partial \omega_0}{\partial \nu_0}, \tilde{\omega} \right) \right]_{nkm} + \left[B\left(\tilde{\omega}, \frac{\partial \omega_0}{\partial \nu_0} \right) \right]_{nkm} \right), \end{aligned}$$

where $\frac{\partial \omega_0}{\partial \nu_0} = -\frac{1}{2\nu_0^2} f^\omega = -\frac{1}{\nu_0}\omega_0$.

Finally, the Fréchet derivative with respect to the perturbation field $\tilde{\omega}$ acting on the direction $\hat{\omega}$ is given by linearizing the remaining terms in (5.19):

$$D_{\tilde{\omega}} F^{\omega}_{nkm}[\hat{\omega}] = im_2 \sum_{j=0}^{n} \Omega_j \hat{\omega}_{(n-j)km} + (|k|^2 + m_1^2) \sum_{j=0}^{n} \nu_j \hat{\omega}_{(n-j)km} + [B(\omega_0, \hat{\omega})]_{nkm} + [B(\hat{\omega}, \omega_0)]_{nkm} + [B(\tilde{\omega}, \hat{\omega}) + B(\hat{\omega}, \tilde{\omega})]_{(n-1)km} .$$

Together, these explicit block actions fully define the linear operator $D\mathcal{F}(\Omega, \nu, \tilde{\omega})$ required to construct the approximate inverse.

5.3.3 The approximate inverse A

To apply a Newton-Kantorovich type existence theorem, we must construct an injective linear operator A, which serves as an approximate inverse to the Jacobian matrix $D\mathcal{F}(\bar{X})$. For the approximate solution $\bar{X} = (\bar{\Omega}, \bar{\nu}, \bar{\tilde{\omega}})$, we evaluate the system at the onset of the bifurcation. From the series perspective (see Remark 5.3.1), this corresponds to setting $\varepsilon = 0$. In our Taylor coefficient formulation, this means we choose $\bar{\Omega}$, $\bar{\nu}$ and $\bar{\tilde{\omega}}$ such that they are nonzero only for $n = 0$, which corresponds to the solution of the Hopf bifurcation problem, adjusted to adhere to the spatial symmetries of our chosen function space.

Recall that the scalar constraints contain no explicit ε-dependence in the series perspective, meaning that the perturbation acts only within the vorticity block. We decompose the vorticity block of the Jacobian matrix into an unperturbed operator J_0 and an $\mathcal{O}(\varepsilon)$ perturbation operator J_1:

$$D_{\tilde{\omega}} F^{\omega}(\bar{X}) = J_0 + \varepsilon J_1.$$

For sufficiently small ε, the operator J_1 acts as a small perturbation. Therefore, we construct the approximate inverse A exclusively using the unperturbed block operator J_0.

Here, J_0 represents the linearization around the two-dimensional equilibrium ω_0. As ω_0 depends only on the spatial variables x_1 and x_2, the convolution products in J_0 do not couple different modes in the x_3- and t-directions. Consequently, the operator J_0 is strictly block-diagonal with respect to the pairs $m = (m_1, m_2)$.

To express this block-diagonal structure explicitly, we introduce the restricted two-dimensional bilinear operator $\tilde{B}$, which operates solely on the k-modes associated with x_1 and x_2. As the two-dimensional equilibrium ω_0 depends only on x_1 and x_2, its Fourier coefficients vanish for all $m \neq (0, 0)$. Hence, the convolution sum over the m-indices collapses to a single term where $(0, 0) + m = m$.

Consequently, the full three-dimensional bilinear form $B(\omega_0, v)$ decouples completely across the different m-slices. For any given m-slice of a vector field v, denoted v_m, the full convolution simplifies to a two-dimensional operation:

$$[B(\omega_0, v)]_{km} = \left[\tilde{B}(\omega_0, v_m)\right]_k . \tag{5.20}$$

Using this restricted operator, the action of J_0 on the Fourier modes is given by

$$(J_0 v)_{km} = \left(im_2\bar{\Omega} + \bar{\nu}(|k|^2 + m_1^2)\right) v_{km} + \left[\tilde{B}(\omega_0, v_m)\right]_k + \left[\tilde{B}(v_m, \omega_0)\right]_k .$$

The operator J_1 captures the purely quadratic interactions involving $\bar{\tilde{\omega}}$. This operator relies on the full three-dimensional bilinear form B:

$$(J_1 v)_{km} = B_{km}(\bar{\tilde{\omega}}, v) + B_{km}(v, \bar{\tilde{\omega}}).$$

The block-diagonal structure of J_0 allows us to define the approximate inverse block by block. To establish this, we introduce the spatial Jacobian operator J_{Hopf}. While conceptually analogous to the full spatial Jacobian analyzed at the onset of the bifurcation in Section 5.2.1, we define J_{Hopf} here as a lower-dimensional operator acting on two-dimensional $v = (v_k)_{k\in\mathbb{Z}^2}$. Utilizing the restricted bilinear operator $\tilde{B}$, its action is given by

$$(J_{\text{Hopf}} v)_k = \bar{\nu}(|k|^2 + 4)v_k + \left[\tilde{B}(\omega_0, v)\right]_k + \left[\tilde{B}(v, \omega_0)\right]_k .$$

By comparing J_0 and J_{Hopf}, we can express the unperturbed Jacobian matrix J_0 restricted to any fixed pair $m = (m_1, m_2)$ as a diagonal shift of the Hopf spatial operator:

$$J_0^{(m)} = J_{\text{Hopf}} + \left(im_2\bar{\Omega} + \bar{\nu}(m_1^2 - 4)\right) I. \tag{5.21}$$

This structural relation significantly reduces the computational complexity, as it allows us to evaluate the action $(J_0 v)_{km} = (J_0^{(m)} v_m)_k$ by recycling the analytical bounds and numerical computations from Section 5.2.

To construct the approximate inverse A, we first formulate its block-diagonal structure by decomposing our Banach space. Let $M_{\text{crit}} = \{(2,1), (2,-1)\}$ denote the set of critical modes associated with the Hopf bifurcation. In addition, let $\mathcal{X}^{(m)}$ represent the subspace of $\mathcal{X}_{\mathbb{C}}^{\omega}$ restricted to a fixed mode pair $m = (m_1, m_2)$, i.e., the space equipped with the norm

$$\|\tilde{\omega}\|_{\mathcal{X}^{(m)}} = \sum_{l=1}^{3} \sum_{n=0}^{\infty} \sum_{\substack{k\in\mathbb{Z}^2 \\ (k,m)\neq(0,0,0,0)}} |\tilde{\omega}_{nkm}^{(l)}| \varepsilon^n \eta^{|k_1|+|k_2|+|m_1|+|m_2|}.$$

We isolate the subspace containing the parameter spaces and the critical modes by defining

$$\mathcal{X}^{\text{crit}} = \mathcal{X}_{\mathbb{C}}^{\Omega} \times \mathcal{X}_{\mathbb{C}}^{\nu} \times \mathcal{X}^{(2,1)} \times \mathcal{X}^{(2,-1)}.$$

This allows us to express the full Banach space as the product

$$\mathcal{X} = \mathcal{X}^{\text{crit}} \times \prod_{m\notin M_{\text{crit}}} \mathcal{X}^{(m)}.$$

For any sequence $x = \left(x^{\text{crit}}, (x^{(m)})_{m \notin M_{\text{crit}}}\right) \in \mathcal{X}$, the approximate inverse operator A is then defined to act componentwise as

$$\begin{aligned}(Ax)^{\text{crit}} &= A^{\text{crit}} x^{\text{crit}},\\ (Ax)^{(m)} &= A^{(m)} x^{(m)} \quad \text{for } m \notin M_{\text{crit}}.\end{aligned}$$

To explicitly define the block operators A^{crit} and $A^{(m)}$, we introduce a finite index set

$$\mathbb{M} = \{m \in \mathbb{Z}^2 : |m_1| \leq M_1, |m_2| \leq M_2\}$$

for integers $M_1, M_2 > 0$. While the restrictions on choosing M_1 and M_2 and the construction of the resulting matrices are detailed in the subsequent sections, we introduce the three categories of A here:

1. **The critical operator A^{crit}:** Since the critical modes $m \in M_{\text{crit}}$ correspond to the spatial-temporal frequency of the Hopf bifurcation, the approximate inverse on this subspace cannot be constructed by standard matrix inversion of $J_0^{(m)}$. Instead, A^{crit} must be addressed using a bordered matrix formulation that couples the critical modes with the phase and amplitude equations. This coupling is valid because of our natural choice of the eigenvector approximation w, whose support is restricted to these critical modes.

2. **The non-critical operator $A^{(m)}$ for the infinite tail:** For all large modes, the operator is dominated by its linear diffusion term. For this infinite tail, the corresponding operators $A^{(m)}$ are defined explicitly as diagonal operators representing the inverse of the dominant linear terms.

3. **The non-critical operator $A^{(m)}$ for finite m:** For the remainder of the finite computational domain, the unperturbed block operator $J_0^{(m)}$ is theoretically invertible. The approximate inverses $A^{(m)}$ are composed of a numerical matrix inverse on a finite spatial grid and an exact diagonal inverse on the infinite spatial tail.

The critical block

We must explicitly handle the critical subspace M_{crit}, which contains the critical Hopf bifurcation modes, i.e., the wave patterns that go unstable first and drive new oscillatory flow. The scalar continuation variables (Ω, ν) are bound exclusively to this subspace via the phase and amplitude conditions F^{phase} and F^{amp}.

To construct an approximate inverse A^{crit} on this subspace, we choose to partition the spatial frequencies into a finite computational domain and an infinite tail. Since Ω and ν are scalars with no spatial frequencies, they are entirely contained within the finite domain.

For the finite part, we augment the restricted unperturbed Jacobian matrix with the corresponding Fréchet derivatives of the supplementary conditions. Evaluated at the approximate solution $\bar{X}$ and truncated to the finite spatial grid, indicated

by $|_{\text{fin}}$, this results in the finite-dimensional bordered matrix J_{crit} given by

$$J_{\text{crit}}(\bar{X}) = \begin{pmatrix} 0 & 0 & D_{\tilde{\omega}} F^{\text{phase}}(\bar{X})|_{\text{fin}} \\ 0 & 0 & D_{\tilde{\omega}} F^{\text{amp}}(\bar{X})|_{\text{fin}} \\ D_\Omega F^\omega(\bar{X})|_{\text{fin}} & D_\nu F^\omega(\bar{X})|_{\text{fin}} & J_0|_{\text{fin}} \end{pmatrix}.$$

We define the finite block of the approximate inverse, $A_{\text{fin}}^{\text{crit}}$, as a numerically computed inverse of this matrix: $A_{\text{fin}}^{\text{crit}} \approx \left(J_{\text{crit}}(\bar{X})\right)^{-1}$.

For the infinite spatial tail of the critical modes, the supplementary conditions and parameter derivatives vanish. We define the tail block A_∞^{crit} as the exact inverse of the diagonal part of this operator evaluated on the tail.

The complete approximate inverse for the critical subspace is then defined as follows:

$$A^{\text{crit}} = \begin{pmatrix} A_{\text{fin}}^{\text{crit}} & 0 \\ 0 & A_\infty^{\text{crit}} \end{pmatrix}.$$

The noncritical blocks

For all noncritical blocks $m \in \mathbb{M} \setminus M_{\text{crit}}$, we define the corresponding block operator $A^{(m)}$ as the exact inverse of the unperturbed Jacobian restricted to that m. Note that this implies that A is independent of ε in the notation of the power series perspective explained in 5.3.1. We set

$$A^{(m)} = \left(J_0^{(m)}\right)^{-1}.$$

However, at this stage of the analysis, we cannot assume the theoretical existence of this exact inverse. Instead, its existence must be validated using Neumann series techniques. In particular, if we can construct an approximate inverse $\hat{A}^{(m)}$ that satisfies

$$\|I - \hat{A}^{(m)} J_0^{(m)}\|_{B(\mathcal{X}^{(m)})} < 1,$$

we guarantee that $J_0^{(m)}$ is invertible for this m, making the exact inverse $A^{(m)}$ theoretically well-defined.

Finding $\hat{A}^{(m)}$ can be done using various strategies. We choose to construct it via a Galerkin projection, as was done for the critical block. Therefore, we partition the spatial frequencies into a finite computational domain and an infinite tail.

We first compute a numerical matrix inverse, which serves as the finite block $\hat{A}_{\text{fin}}^{(m)} \approx \left(J_0^{(m)}|_{\text{fin}}\right)^{-1}$ and define the tail block $\hat{A}_\infty^{(m)}$ as the exact inverse of the diagonal part of $J_0^{(m)}$ evaluated on the tail.

The composed approximate inverse is then given by

$$\hat{A}^{(m)} = \begin{pmatrix} \hat{A}_{\text{fin}}^{(m)} & 0 \\ 0 & \hat{A}_\infty^{(m)} \end{pmatrix}.$$

Tail bounds and bounding the approximate inverse

To guarantee that A is a bounded linear operator on $\mathcal{X}$, we must bound its global operator norm. Since the theoretical existence of A depends on validating $\hat{A}$ via Neumann series, this requires combining computational matrix norms on the finite domains with an analytical bound on the infinite high-frequency components.

The infinite part consists of two distinct regimes: tail blocks, where the x_3 and temporal frequencies fall outside the finite set ($m \notin \mathbb{M}$) and the spatial tail within the finite set ($m \in \mathbb{M}$), where the x_1 and x_2 frequencies fall outside the computational domain.

We first address the tail blocks $m \notin \mathbb{M}$. To derive this bound, we split the unperturbed block operator $J_0^{(m)}$ into its purely diagonal part $D^{(m)}$ and its dense convolution part $\hat{B}$:

$$J_0^{(m)} = D^{(m)} + \hat{B},$$

where $D^{(m)} = \operatorname{diag}(\lambda_{km})$ with $\lambda_{km} = im_2\bar{\Omega} + \bar{\nu}(|k|^2 + m_1^2)$. As ω_0 depends only on the coordinates x_1 and x_2, the bilinear interactions do not couple different m-modes. Using the restricted two-dimensional operator $\tilde{B}$ defined in (5.20), the action simplifies to

$$(\hat{B}v_m)_k = \left[\tilde{B}(\omega_0, v_m)\right]_k + \left[\tilde{B}(v_m, \omega_0)\right]_k.$$

Recall that for these large modes, we defined the approximate inverse as the inverse of the diagonal diffusion terms: $\hat{A}^{(m)} = \left(D^{(m)}\right)^{-1}$. To validate that this is a suitable inverse, we evaluate

$$I - \hat{A}^{(m)} J_0^{(m)} = I - \left(D^{(m)}\right)^{-1} \left(D^{(m)} + \hat{B}\right) = -\left(D^{(m)}\right)^{-1} \hat{B}.$$

Since the bilinear advection operator $\hat{B}$ involves first-order spatial derivatives, it is not uniformly bounded as an operator from $\mathcal{X}$ to $\mathcal{X}$. Its action introduces a factor that grows with the spatial frequencies. However, this unboundedness does not result in a mathematical obstruction, because the analysis only evaluates the composed operator $\left(D^{(m)}\right)^{-1} \hat{B}$. The diagonal diffusion operator $\left(D^{(m)}\right)^{-1}$ decays asymptotically as $\mathcal{O}\left((|k|^2 + m_1^2)^{-1}\right)$, providing second-order spatial smoothing that fully absorbs the first-order derivative growth of $\hat{B}$. To simplify the presentation of the idea for the tail estimates, we write out the bounds as if the operator $\hat{B}$ were uniformly bounded by a constant C_{ω_0}. How to actually deal with the unboundedness can be seen in Section 5.2.4. To guarantee that $J_0^{(m)}$ is theoretically invertible on these tail blocks, we require

$$\left\| \left(D^{(m)}\right)^{-1} \hat{B} \right\| \leq C_{\omega_0} \left\| \left(D^{(m)}\right)^{-1} \right\| < 1. \tag{5.22}$$

We achieve this bound by analyzing the decay of the diagonal inverse. We choose a threshold constant $M^\dagger > C_{\omega_0}$ and we set the truncation bounds M_1 and M_2 large

enough such that our finite computational domain $\mathbb{M}$ contains the set of modes where this threshold is not met:

$$\{m \in \mathbb{Z}^2 : |im_2\bar{\Omega} + \bar{\nu}m_1^2| < M^\dagger\} \subset \mathbb{M}.$$

Noting that the supremum of the diagonal elements is attained at the lowest possible spatial frequencies ($k = (0,0)$), the operator norm of the tail block inverse is then uniformly bounded by

$$\left\|\hat{A}^{(m)}\right\| = \left\|\left(D^{(m)}\right)^{-1}\right\| = \sup_{k\in\mathbb{Z}^2} \frac{1}{|im_2\bar{\Omega} + \bar{\nu}(|k|^2 + m_1^2)|} \leq \frac{1}{|im_2\bar{\Omega} + \bar{\nu}m_1^2|} \leq \frac{1}{M^\dagger}.$$

Provided $M^\dagger > C_{\omega_0}$, the condition in (5.22) holds. The Neumann series then guarantees that the exact unperturbed inverse $A^{(m)} = \left(J_0^{(m)}\right)^{-1}$ is well-defined on these tail blocks, with a uniform upper bound given by

$$\left\|A^{(m)}\right\| = \left\|\left(J_0^{(m)}\right)^{-1}\right\| \leq \frac{\left\|\left(D^{(m)}\right)^{-1}\right\|}{1 - C_{\omega_0}\left\|\left(D^{(m)}\right)^{-1}\right\|} \leq \frac{1}{M^\dagger - C_{\omega_0}} =: C_{\text{tail}}.$$

For the finitely many remaining $m \in \mathbb{M}$, the bounded norm depends on $\hat{A}$. For the noncritical blocks ($m \in \mathbb{M} \setminus M_{\text{crit}}$), bounding the exact mathematical inverses $A^{(m)}$ is a two-step process.

First, we bound $\hat{A}^{(m)}$ by combining the norm of the finite computational matrix $\hat{A}^{(m)}_{\text{fin}}$ with the norm of the tail part $\hat{A}^{(m)}_{\infty}$. Therefore, we need to construct the finite spatial computational domain $\mathbb{K}_m$ on which $\hat{A}^{(m)}_{\text{fin}}$ is computed. This domain is defined as

$$\mathbb{K}_m = \{k \in \mathbb{Z}^2 : |k_1| \leq K_1, |k_2| \leq K_2\},$$

for integers $K_1, K_2 > 0$. The origin is excluded for the $m = (0,0)$ slice, yielding $\mathbb{K}_{(0,0)} = \{k \in \mathbb{Z}^2 \setminus \{(0,0)\} : |k_1| \leq K_1, |k_2| \leq K_2\}$. As the spatial truncation is chosen to be identical for both critical modes in M_{crit}, we denote their shared finite spatial domain by $\mathbb{K}_{M_{\text{crit}}}$. We compute a numerical matrix inverse to serve as the finite block $\hat{A}^{(m)}_{\text{fin}} \approx \left(J_0^{(m)}|_{\mathbb{K}_m}\right)^{-1}$ and define the tail block $\hat{A}^{(m)}_{\infty}$ as the exact inverse of the diagonal part of $J_0^{(m)}$ evaluated on the tail.

Second, we apply the Neumann series bounds. We define $\Delta_m = I - \hat{A}^{(m)}J_0^{(m)}$. By choosing the spatial truncation thresholds K_1 and K_2 sufficiently large, we push the boundary of our computational domain into a setting where diffusion dominates advection. This guarantees that $\|\Delta_m\| \leq \kappa_m < 1$. We then rewrite the unperturbed Jacobian as $J_0^{(m)} = (\hat{A}^{(m)})^{-1}(I - \Delta_m)$. Inverting both sides yields

$$A^{(m)} = \left(J_0^{(m)}\right)^{-1} = (I - \Delta_m)^{-1}\hat{A}^{(m)}.$$

Using that $\|(I - \Delta_m)^{-1}\| \leq \frac{1}{1-\|\Delta_m\|}$, the exact mathematical inverse is then bounded by

$$\|A^{(m)}\| \leq \frac{\|\hat{A}^{(m)}\|}{1 - \kappa_m} =: C_m.$$

The critical part A^{crit} is bounded using an analogous combination of its bordered finite matrix and its tail part.

Combining these three regimes, we obtain a bound on the operator norm $\|A\|$. It is evaluated by taking the maximum over the different partitions of our operator: the critical block, the noncritical computational blocks and the infinite tail. We define the global bound as

$$\|A\| \leq \max\left\{ \left\|A^{\text{crit}}\right\|, \max_{m \in \mathbb{M} \setminus M_{\text{crit}}} C_m, C_{\text{tail}} \right\} =: C_A.$$

This bound facilitates the continuation of the bifurcating branch as by establishing a bounded global inverse A, we can determine the bounds Y_0, Z_1 and Z_2. This will be shown in the next section.

5.3.4 Bounds

Assuming we found a C_A such that the global norm of A is bounded, the next step for applying the existence theorem (Theorem 5.2.3 adapted to our framework) is to establish the bounds Y_0, Z_1 and Z_2.

Y_0-bound

To determine the value of the bound Y_0, we evaluate $\mathcal{F}$ at an approximate solution $\bar{X} = (\bar{\Omega}, \bar{\nu}, \bar{\tilde{\omega}})$. Recall that this approximate solution is derived directly from the onset of the bifurcation, meaning $\bar{\tilde{\omega}}$ consists exclusively of the numerically computed (symmetric) Hopf eigenvector. Hence, the only nonzero Taylor-Fourier coefficients of $\bar{\tilde{\omega}}_{nkm}$ occur at the zeroth Taylor order $n = 0$ and at the critical modes $m = (2, 1)$ and $m = (2, -1)$.

When evaluating the residual $\mathcal{F}(\bar{X})$, the equations decouple across the Taylor index n. At the zeroth order ($n = 0$), the residual corresponds to the one of the linearized Hopf eigenvalue problem. We bound the norm of the action on this specific zeroth-order residual ($\|A\mathcal{F}(\bar{X})\|$ for $n = 0$) by a numerically computable constant Y_0^{Hopf}, which represents the residual bound of the critical modes corresponding to the analysis of the onset of the bifurcation. The validity of the entire continuation bound assumes that the numerical validation of the onset point was highly accurate, ensuring that Y_0^{Hopf} is already very small.

The only other nonvanishing terms in the residual arise from the nonlinear advection term. As the approximate solution $\bar{\tilde{\omega}}$ is zero for all $n \geq 1$, this term evaluated at $\bar{X}$ yields only a single nonzero term: the interaction of the zeroth-order modes $B_{0km}(\bar{\tilde{\omega}}, \bar{\tilde{\omega}})$. Since $\bar{\tilde{\omega}}$ contains exclusively $n = 0$ terms at modes $m = (2, 1)$ and

$m = (2, -1)$, this quadratic interaction produces a residual solely at the first Taylor order $n = 1$ in the vorticity part of the equation. Due to the restriction of our function space to $m_1 \geq 0$, the convolution of these critical modes generates nonzero residual modes only at $m_1 \in \{0, 4\}$ with temporal frequencies $m_2 \in \{-2, 0, 2\}$.

As the two-dimensional equilibrium ω_0 and the approximate eigenvector $\bar{\tilde{\omega}}$ both consist of finitely many nonzero modes, the entire residual $\mathcal{F}(\bar{X})$ has finite support. Furthermore, because the approximate inverse A is block-diagonal with respect to m, its action on $B_{0km}(\bar{\tilde{\omega}}, \bar{\tilde{\omega}})$ can be evaluated block by block.

In the definition of the $\mathcal{X}$-norm, the n-th Taylor coefficient is weighted by ε^n. Therefore, the total Y_0-bound splits into the zeroth and first-order contributions:

$$\|A\mathcal{F}(\bar{X})\|_{\mathcal{X}} \leq Y_0^{\text{Hopf}} + \varepsilon C_{\text{nonlinear}} =: Y_0.$$

By exploiting the block structure of A, we can make the constant $C_{\text{nonlinear}}$ more explicit. This constant is defined by computing the operator norms of the respective finite approximate inverse blocks and multiplying them by the $\mathcal{X}^\omega$-norm of the quadratic residual at the specific interacting modes:

$$C_{\text{nonlinear}} = \sum_{m_1 \in \{0,4\}} \sum_{m_2 \in \{-2,0,2\}} C_{(m_1,m_2)} \, \|B_{0,\cdot,m}(\bar{\tilde{\omega}}, \bar{\tilde{\omega}})\|_{\mathcal{X}^\omega} .$$

By choosing ε to be sufficiently small, the $\mathcal{O}(\varepsilon)$ term of the Y_0-bound becomes arbitrarily small. Combined with the assumption that Y_0^{Hopf} is small, this guarantees that Y_0 is small enough to satisfy the conditions of the radii polynomial in the existence theorem.

Z_1-bound

For the Z_1-bound, we require

$$\|I - AD\mathcal{F}(\bar{X})\|_{B(\mathcal{X},\mathcal{X})} \leq Z_1 < 1.$$

Considering the series perspective (see Remark 5.3.1), we know from Section 5.3.2 that the derivatives of the phase condition and the amplitude condition, as well as the derivatives with respect to the scalar parameters (Ω, ν), contain no explicit ε terms. The only ε-dependence in the Jacobian matrix is found in the perturbation operator J_1 within the vorticity block: $D_{\tilde{\omega}} F^\omega(\bar{X}) = J_0 + \varepsilon J_1$.

Consequently, the Fréchet derivative can be decomposed as

$$D\mathcal{F}(\bar{X}) = \mathcal{J}_0 + \varepsilon \mathcal{J}_1,$$

where $\mathcal{J}_0$ and $\mathcal{J}_1$ denote the unperturbed Jacobian operator and the perturbed Jacobian operator, respectively, both evaluated at the numerical approximation $\bar{X}$. As a linear mapping on the space $\mathcal{X}$, the operator $\mathcal{J}_1$ isolates the quadratic interactions involving the approximate (symmetric) solution of the Hopf bifurcation problem. In the 3×3 block structure of the full space $\mathcal{X}$, it is given by

$$\mathcal{J}_1 = \begin{pmatrix} 0 & 0 & 0 \\ 0 & 0 & 0 \\ 0 & 0 & J_1 \end{pmatrix}.$$

To examine how these quadratic interactions behave across the Taylor indices, we evaluate the products inside J_1. Since the approximation $\bar{\tilde{\omega}}$ exists only at the zeroth Taylor order ($n = 0$), the products map a perturbation at order n to an interaction at order n. Therefore, $\mathcal{J}_1$ itself does not shift the order. Instead, the multiplier ε can be reinterpreted as a shift operator. Due to the ε^n weight in the definition of the $\mathcal{X}$-norm, this shift operator corresponds to an operator norm of exactly ε. Hence, $\varepsilon\mathcal{J}_1$ maps an input perturbation at order n to a residual at order $n + 1$.

Substituting the decomposition into $I - AD\mathcal{F}(\bar{X})$ yields

$$\begin{aligned} I - AD\mathcal{F}(\bar{X}) &= I - A(\mathcal{J}_0 + \varepsilon\mathcal{J}_1) \\ &= (I - A\mathcal{J}_0) - \varepsilon A\mathcal{J}_1. \end{aligned}$$

To bound the first term, we exploit the fact that the action of $I - A\mathcal{J}_0$ can be evaluated block by block:

- **Noncritical blocks ($m \notin M_{\text{crit}}$):** Recall that for all noncritical blocks, we used Neumann series bounds to validate the theoretical existence of the exact inverse $A^{(m)} = \left(\mathcal{J}_0^{(m)}\right)^{-1}$. Since $A^{(m)}$ is the exact inverse of the unperturbed operator on these subspaces, the action cancels across the entire block, yielding $I - A^{(m)}\mathcal{J}_0^{(m)} = 0$.
- **Critical block ($m \in M_{\text{crit}}$):** On this subspace, the finite-dimensional matrix $J_{\text{crit}}(\bar{X})$ is inverted computationally, while its infinite-dimensional extension is bounded analytically. Consequently, the action of the approximate inverse on the exact unperturbed operator produces a defect $I - A^{\text{crit}}\mathcal{J}_0|_{M_{\text{crit}}}$ that consists of both a finite computational part and an infinite analytical tail part. Bounding the norm of this combined defect is analogous to the computation of the full Z_1-bound for the Hopf bifurcation problem established in Section 5.2.4, adapting the techniques to our symmetry-reduced space and to the phase and amplitude conditions formulated in Section 5.3.1. We denote the resulting computable bound as Z_1^{Hopf}.

Combining the results of the block-by-block evaluation, the norm of the unperturbed part is bounded by the Hopf constant: $\|I - A\mathcal{J}_0\|_{B(\mathcal{X},\mathcal{X})} \leq Z_1^{\text{Hopf}}$.

For the $\mathcal{O}(\varepsilon)$ perturbation term, the operator $\mathcal{J}_1$ acts only within the vorticity block via $J_1(v) = B(\bar{\tilde{\omega}}, v) + B(v, \bar{\tilde{\omega}})$. Evaluating it on a perturbation $v \in \mathcal{X}^\omega$ introduces a first-order spatial derivative (∇). Consequently, its action introduces a factor that grows linearly with the spatial wave numbers. However, analogous to our approach in the tail bounds analysis, this unboundedness does not result in a mathematical barrier because we solely evaluate the composed operator $A\mathcal{J}_1$. The approximate inverse A acts roughly as the inverse of a second-order operator whose smoothing fully absorbs the single derivative lost to advection, making the composed action a well-defined, bounded linear operator on $\mathcal{X}$. To compute the norm of this composed operator, we refer to the convolution estimates detailed in Section 5.2.4, in which it is shown how to manage the unbounded derivative terms during the norm evaluations. However, here we mirror the simplified presentation

in the tail bounds analysis in Section 5.3.3. This results in the following upper bound for the composed operator:

$$\|A\mathcal{J}_1\|_{B(\mathcal{X},\mathcal{X})} \leq C_{AJ_1}.$$

The full Z_1-bound is then given by

$$Z_1 = Z_1^{\text{Hopf}} + \varepsilon C_{AJ_1}.$$

Assuming that the proof of the onset of the Hopf bifurcation problem was successful, we naturally have $Z_1^{\text{Hopf}} < 1$. Thus, the overall contraction condition $Z_1 < 1$ can be satisfied by choosing the continuation step size ε to be sufficiently small.

Z_2-bound

To extend the local linear contraction to a neighborhood of $\bar{X}$, we must bound the nonlinear terms. Let $s = (\Omega, \nu)$ denote the vector of scalar continuation parameters with the unperturbed state $\bar{s} = (\bar{\Omega}, \bar{\nu})$ and perturbation $w_s = (w_\Omega, w_\nu)$. Let $\mathcal{X}^s = \mathcal{X}_{\mathbb{C}}^{\Omega} \times \mathcal{X}_{\mathbb{C}}^{\nu}$ denote its corresponding product space. Furthermore, fix the *a priori* radius bound r^*.

Since the phase and amplitude equations are linear, their second derivatives vanish. Therefore, the only nonzero nonlinear contributions arise within the vorticity equation F^ω. As A acts on the full space $\mathcal{X}$, we implicitly extend the vorticity variations to match its dimensions by setting their scalar components to zero. Then we need to establish constants $Z_2^{\omega\omega}$, $Z_2^{\omega s}$ and Z_2^{ss} such that for all $W = (w_s, w_\omega)$ with $\|W\|_{\mathcal{X}} \leq r^*$, the following bounds hold:

$$\begin{aligned}
\|A[D_{\tilde{\omega}} F^\omega(\bar{s}, \bar{\tilde{\omega}} + w_\omega) - D_{\tilde{\omega}} F^\omega(\bar{s}, \bar{\tilde{\omega}})]\|_{B(\mathcal{X}^\omega, \mathcal{X})} &\leq Z_2^{\omega\omega} \|w_\omega\|_{\mathcal{X}^\omega}, \\
\|A[D_s F^\omega(\bar{s}, \bar{\tilde{\omega}} + w_\omega) - D_s F^\omega(\bar{s}, \bar{\tilde{\omega}})]\|_{B(\mathcal{X}^s, \mathcal{X})} &\leq Z_2^{\omega s} \|w_\omega\|_{\mathcal{X}^\omega}, \\
\|A[D_s F^\omega(\bar{s} + w_s, \bar{\tilde{\omega}}) - D_s F^\omega(\bar{s}, \bar{\tilde{\omega}})]\|_{B(\mathcal{X}^s, \mathcal{X})} &\leq Z_2^{ss} \|w_s\|_{\mathcal{X}^s}.
\end{aligned}$$

Note that we should also consider the bound $Z_2^{s\omega}$, but we omit its explanation as it is analogous to $Z_2^{\omega s}$.

Since the Navier-Stokes equations feature a purely quadratic nonlinearity, the second Fréchet derivative $D^2_{\tilde{\omega}\tilde{\omega}} F^\omega$ is a constant operator governed by the bilinear form B. Consequently, bounding the difference reduces to bounding the composed action $A\,[B(w_\omega, \cdot) + B(\cdot, w_\omega)]$.

As discussed in the tail bounds analysis, the bilinear advection operator B involves a first-order spatial derivative, meaning its isolated action introduces a factor that grows linearly with the spatial wave numbers. However, this unboundedness does not imply a mathematical obstruction because the analysis only evaluates the composed operator. The approximate inverse A acts as a second-order smoothing operator that fully absorbs this derivative. To compute the constant $Z_2^{\omega\omega}$ explicitly, we do not separate the operators. Instead, we apply the weighted convolution estimates detailed in the derivation of the Z_2-bound in Section 5.2.4 directly to the composed operator.

For the parameter-dependent bound $Z_2^{\omega s}$, we take the derivative of F^ω with respect to the viscosity ν, which isolates the Laplacian term $\Delta\tilde{\omega}$. Evaluated at the difference w_ω, this produces Δw_ω, which is a second-order spatial derivative. Similarly, the derivative with respect to Ω isolates a term that scales linearly with the temporal mode m_2. Therefore, the parameter derivatives are unbounded.

Once again, we must rely on the smoothing properties of the approximate inverse. Since A is built using the inverse of the diffusion operator, its $\mathcal{O}(|k|^{-2})$ decay counteracts the $\mathcal{O}(|k|^2)$ growth of the Laplacian difference and the linear growth of the temporal derivative. Consequently, the composed action is bounded and $Z_2^{\omega s}$ can be evaluated using techniques established in Section 5.2.4.

Finally, by evaluating the difference $D_s F^\omega(\bar{s} + w_s, \bar{\tilde{\omega}}) - D_s F^\omega(\bar{s}, \bar{\tilde{\omega}})$, the bound Z_2^{ss} is determined. The only surviving terms in this difference are the advection interactions that depend explicitly on the derivative of the equilibrium denoted by $\partial_\nu \omega_0(\nu)$. Subtracting these terms evaluated at the perturbed viscosity $\bar{\nu} + w_\nu$ and the unperturbed viscosity $\bar{\nu}$ results in the second derivative $\partial^2_{\nu\nu}\omega_0 = \frac{1}{\nu^3} f^\omega$. Analogous to the analysis of the Hopf bifurcation onset (see Section 5.2.4), the Z_2^{ss}-bound includes denominator terms involving $\left(\bar{\nu} - \frac{r^*}{\eta_\nu}\right)$.

Validation

Ultimately, the proof of existence reduces to verifying the discriminant condition of the radii polynomial:

$$2Y_0 Z_2 < (1 - Z_1)^2. \tag{5.23}$$

By computing the finite inverses and analytic estimates to establish the bound $\|A\| \leq C_A$, and choosing the bifurcation parameter ε small enough, the contraction condition $Z_1 < 1$ can be satisfied. Crucially, because the components of the total bounds rely on the unperturbed critical bounds, satisfying (5.23) assumes the prior successful validation of the onset of the Hopf bifurcation (ensuring Y_0^{Hopf} and Z_1^{Hopf} are small). If the bounds satisfy (5.23), the existence theorem (i.e., Theorem 5.2.3 adapted to our setting) guarantees the existence of a unique solution $\hat{X}$ representing the three-dimensional bifurcation branch.

5.3.5 Future work

It is important to emphasize that the strategy outlined in this section serves as a theoretical and computational blueprint, rather than a complete proof. While the structure of a possible approximate inverse A has been defined, the rigorous evaluation of the bounds Y_0, Z_1 and Z_2 for the fully three-dimensional Navier-Stokes equations away from the bifurcation remains to be carried out.

Executing this proof in practice requires completing several analytical and computational tasks. Analytically, one must make the bounding of the constants fully explicit. This entails deriving the bound C_{ω_0}, as well as establishing the explicit weighted convolution estimates to evaluate the constant C_{AJ_1} and the second-derivative bounds $Z_2^{\omega\omega}$, $Z_2^{\omega s}$ and Z_2^{ss}.

Alongside these analytical derivations, significant computational effort is required to perform the interval arithmetic evaluations. In practice, we must explicitly compute the approximate inverse for the bordered critical matrix $J_{\text{crit}}(\bar{X})$. Additionally, for the noncritical modes, the inverses $\left(J_0^{(m)}|_{\mathbb{K}_m}\right)^{-1}$ need to be determined. Furthermore, the computational domains $\mathbb{M}$ and $\mathbb{K}_m$ must be chosen large enough, and the continuation step size ε small enough, to guarantee the contraction condition $Z_1 < 1$ and satisfy the radii polynomial.

Remark 5.3.4. *While the fully three-dimensional formulation appears computationally discouraging, the block-diagonal structure of the unperturbed operator J_0 offers a massive computational advantage. As the dense bilinear interactions do not couple distinct m-slices, the required finite matrix inversions $A^{(m)}$ reduce entirely to independent two-dimensional operations. As a result, these heavy computational tasks can be parallelized. However, as discussed in Section 5.2, even these isolated two-dimensional projections require large computational domains to achieve the necessary accuracy, demanding optimized implementations.*

Nevertheless, by deriving the zero-finding formulation, identifying the connection to the Jacobian matrix corresponding to the Hopf bifurcation problem, analyzing the bounds and showing how the asymptotic scaling guarantees convergence for $\varepsilon \ll 1$, the mathematical foundation is available. It is our hope that this groundwork will serve as the starting point for future research aimed at completing the computer-assisted proof of three-dimensional solutions in the Navier-Stokes equations.

Remark 5.3.5. *Finally, recall from Remark 5.2.2 that the $O(2)$ symmetry of the system leads to two main bifurcating branches: standing waves and traveling waves. While our analysis focuses on standing waves which exploits the x_3-reflection symmetry R_z, this continuation framework can also be adapted for traveling waves.*

For a traveling wave moving along the x_3-direction, space and time are coupled into a single coordinate. In Fourier space, this simplifies the two-dimensional grid of frequencies (m_1, m_2) into a single index m, which makes the number of required finite matrix inversions significantly smaller.

However, because a traveling wave moves in a specific direction, it breaks the reflectional symmetry. Hence, we can no longer restrict our analysis to $m_1 \geq 0$. The underlying Banach space $\mathcal{X}$ must therefore be adjusted to include both positive and negative x_3-frequencies.

Summary

This thesis focuses on the rigorous mathematical verification of traveling wave solutions and bifurcation structures in nonlinear partial differential equations, spanning both structural mechanics and fluid dynamics. As explicit analytical solutions to these systems are often impossible to find and standard numerical simulations lack absolute mathematical certainty, this research employs computer-assisted proofs. By framing the differential equations as zero-finding problems in appropriate Banach spaces and utilizing Newton-Kantorovich type arguments, this thesis guarantees the existence of solutions with explicit error bounds.

The first part of this thesis explores structural mechanics. In particular, Chapters 2 and 3 apply computer-assisted techniques to the two-dimensional suspension bridge equation. Chapter 2 proves the existence of periodic, localized traveling waves on a large bounded domain by developing computable bounds to control the aliasing error introduced by the equation's exponential nonlinearity. Chapter 3 extends this analysis to an unbounded domain, specifically an infinite strip defined as $\Omega = \mathbb{R} \times (-d_2, d_2)$ for $d_2 > 0$. Moving beyond existence proofs, it introduces a rigorous method to determine the orbital stability of the waves. By enclosing the spectrum of a linearized operator and counting its negative eigenvalues, we establish the orbital (in)stability of the solutions.

Chapters 4 and 5 transition to fluid dynamics by analyzing the three-dimensional Navier-Stokes equations. Chapter 4 applies the computer-assisted proof approach to prove the existence of a traveling wave. To manage the computational load, spatial symmetries such as reflection and rotation are imposed, reducing the size of the system. Chapter 5 shifts to the system's bifurcation structure by focusing on the proof of a Hopf bifurcation. Moreover, this chapter outlines the method to prove the existence of a branch of periodic solutions emerging from the bifurcation point.

Hence, this thesis demonstrates that computer-assisted proofs can be extended to handle nonpolynomial nonlinearities, unbounded domains and fluid systems, all in multiple spatial dimensions. It offers a robust framework for verifying dynamical phenomena that are out of reach for classical analytical methods.

Bibliography

[1] O. H. Amann, T. von Kármán, and G. B. Woodruff. The Failure of the Tacoma Narrows Bridge. *Federal Works Agency*, 1941.

[2] G. Arioli and F. Gazzola. Torsional instability in suspension bridges: The Tacoma Narrows Bridge case. *Communications in Nonlinear Science and Numerical Simulation*, 42:342–357, 2017.

[3] G. Arioli and H. Koch. Computer-assisted methods for the study of stationary solutions in dissipative systems, applied to the kuramoto–sivashinski equation. *Archive for Rational Mechanics and Analysis*, 197:1033–1051, 2010.

[4] G. Arioli and H. Koch. Integration of dissipative partial differential equations: a case study. *SIAM Journal on Applied Dynamical Systems*, 8(3):1119–1133, 2010.

[5] G. Arioli and H. Koch. A Hopf bifurcation in the planar Navier-Stokes equations. *Journal of Mathematical Fluid Mechanics*, 23(3), 2022.

[6] M. Breden. A posteriori validation of generalized polynomial chaos expansions. *SIAM Journal on Applied Dynamical Systems*, 22(2):765–801, 2023.

[7] M. Breden and J.-P. Lessard. Polynomial interpolation and a priori bootstrap for computer-assisted proofs in nonlinear ODEs. *Discrete and Continuous Dynamical Systems - B*, 23(7):2825–2858, 2018.

[8] M. Breden, J.-P. Lessard, and J. D. Mireles-James. Computation of maximal local (un)stable manifold patches by the parameterization method. *Indagationes Mathematicae*, 27(1):340–367, 2016.

[9] B. Breuer, J. Horák, P. J. McKenna, and M. Plum. A computer-assisted existence and multiplicity proof for travelling waves in a nonlinearly supported beam. *Journal of Differential Equations*, 224(1):60–97, 2006.

[10] B. Breuer, P. J. McKenna, and M. Plum. Multiple solutions for a semilinear boundary value problem: a computational multiplicity proof. *Journal of Differential Equations*, 195:243–269, 2000.

[11] W. L. Briggs and V. E. Henson. *The DFT: An owner's manual for the discrete Fourier transform*. Society for Industrial and Applied Mathematics (SIAM), Philadelphia, PA, 1995. An owner's manual for the discrete Fourier transform.

[12] T. Buckmaster, G. Cao-Labora, and J. Gómez-Serrano. Smooth imploding solutions for 3D compressible fluids. *Forum of Mathematics, Pi*, 13:e6, 2025.

[13] M. Cadiot. Constructive proofs of existence and stability of solitary waves in the Whitham and capillary–gravity Whitham equations. *Nonlinearity*, 38(3):035021, 2025.

[14] M. Cadiot. Stability analysis for localized solutions in PDEs and nonlocal equations on $\mathbb{R}^m$, 2025.

[15] M. Cadiot and D. Blanco. The 2d gray–scott system of equations: constructive proofs of existence of localized stationary patterns. *Nonlinearity*, 38(4):045016, mar 2025.

[16] M. Cadiot, J.-P. Lessard, and J.-C. Nave. Rigorous computation of solutions of semilinear PDEs on unbounded domains via spectral methods. *SIAM J. Appl. Dyn. Syst.*, 23(3):1966–2017, 2024.

[17] M. Cadiot, J.-P. Lessard, and J.-C. Nave. Stationary non-radial localized patterns in the planar Swift-Hohenberg PDE: constructive proofs of existence. *J. Differential Equations*, 414:555–608, 2025.

[18] R. Castelli, M. Gameiro, and J.-P. Lessard. Rigorous Numerics for ill-posed PDEs: Periodic Orbits in the Boussinesq Equation. *Arch. Rational Mech. Anal.*, 228:129–157, 2018.

[19] A. Castro, D. Córdoba, C. Fefferman, F. Gancedo, and J. Gómez-Serrano. Finite time singularities for the free boundary incompressible Euler equations. *Annals of Mathematics*, 178(3):1061–134, 2013.

[20] Y. Chen and P. J. McKenna. Travelling Waves in a Nonlinearly Suspended Beam: Some Computational Results and Four Open Questions. *Philosophical Transactions: Mathematical, Physical and Engineering Sciences*, 355, 1997.

[21] J. Cyranka. Existence of globally attracting fixed points of viscous Burgers equation with constant forcing. A computer assisted proof. *Topol. Methods Nonlinear Anal.*, 45(2):655–697, 2015.

[22] S. Day, J.-P. Lessard, and K. Mischaikow. Validated continuation for equilibria of PDEs. *SIAM Journal on Numerical Analysis*, 45(4):1398–1424, 2007.

[23] P. Drábek, G. Holubová, A. Matas, and P. Nečesal. Nonlinear models of suspension bridges: discussion of the results. *Application of Mathematics*, 48(6):497–514, 2003.

[24] C. Fefferman. Existence and smoothness of the Navier-Stokes equation. *The Millennium Prize Problems*, 2006.

[25] J.-L. Figueras, A. Haro, and A. Luque. Rigorous Computer-Assisted Application of KAM Theory: A Modern Approach. *Found Comput Math*, 17:1123–1193, 2017.

[26] M. Gameiro and J.-P. Lessard. Analytic estimates and rigorous continuation for equilibria of higher-dimensional PDEs. *Journal of Differential Equations*, 249(9):2237–2269, 2010.

[27] M. Gameiro and J.-P. Lessard. A posteriori verification of invariant objects of evolution equations: Periodic orbits in the Kuramoto-Sivashinsky PDE. *Siam Journal on Applied Dynamical Systems*, 16(2):834–852, 2017.

[28] F. Gazzola. Nonlinearity in oscillating bridges. *Electronic Journal of Differential Equations*, 211:1–47, 2013.

[29] M. Golubitsky, I. Stewart, and D. G. Schaeffer. *Singularities and Groups in Bifurcation Theory: Volume II*, volume 69 of *Applied Mathematical Sciences*. Springer-Verlag, 1988.

[30] J. Gómez-Serrano. Computer-assisted proofs in PDE: a survey. *SeMA Journal*, 76(3):459–484, 2019.

[31] O. Hénot. Radiipolynomial.jl, 2021. Available at `https://github.com/OlivierHnt/RadiiPolynomial.jl`.

[32] J. Horák and P. J. McKenna. Traveling Waves in Nonlinearly Supported Beams and Plates. *Progress in Nonlinear Differential Equations and their Applications*, 54:197–215, 2003.

[33] L. Hörmander. *The Analysis of Linear Partial Differential Operators I*. Springer-Verlag Berlin Heidelberg, 1990.

[34] T. Y. Hou. Blow-up or no blow-up? A unified computational and analytic approach to 3D incompressible Euler and Navier–Stokes equations. *Acta Numerica*, 18:277–346, 2009.

[35] A. Hungria, J.-P. Lessard, and J. M. James. Rigorous numerics for analytic solutions of differential equations: the radii polynomial approach. *Mathematics of Computation*, 85:1427–1459, 2016.

[36] C. Jackson. A finite-element study of the onset of vortex shedding in flow past variously shapes bodies. *J. Fluid Mech.*, 182:23–45, 1987.

[37] J. Jaquette, J. B. van den Berg, and J. D. Mireles-James. Validated Numerical Approximation of Stable Manifolds for Parabolic Partial Differential Equations. *Journal of Dynamics and Differential Equations*, 35:3589–3649, 2022.

[38] J.-R. Lahmann and M. Plum. A computer-assisted instability proof for the Orr-Sommerfeld equation with Blasius profile. *ZAMM - Journal of Applied Mathematics and Mechanics*, 84(3):188–204, 2004.

[39] O. E. Lanford. A computer-assisted proof of the Feigenbaum conjectures. *Bulletin of the American Mathematical Society (N.S.)*, 6(3):427–434, 1982.

[40] J.-P. Lessard, J. D. Mireles-James, and C. Reinhardt. Computer assisted proof of transverse saddle-to-saddle connecting orbits for first order vector fields. *Journal of Dynamics and Differential Equations*, 26(2):267–313, 2014.

[41] X. Liu, M. T. Nakao, and S. Oishi. Computer-assisted proof for the stationary solution existence of the Navier-Stokes equation over 3D domains. *Communications in Nonlinear Science and Numerical Simulation*, 108, 2022.

[42] P. J. McKenna and C. O. Tuama. Large torsional oscillations in suspension bridges visited again: Vertical forcing creates torsional response. *The American Mathematical Monthly*, 108(8):738–745, 2001.

[43] P. J. McKenna and W. Walter. Travelling waves in a suspension bridge. *SIAM Journal on Applied Mathematics*, 50:703–715, 1990.

[44] K. Mischaikow and M. Mrozek. Chaos in the Lorenz equations: A computer-assisted proof. 39(3):329–258, 2002.

[45] K. S. Moore. Large Torsional Oscillations in a Suspension Bridge: Multiple Periodic Solutions to a Nonlinear Wave Equation. *SIAM Journal on Mathematical Analysis*, 33(6):1411–1429, 2002.

[46] R. Moore and F. Bierbaum. *Methods and applications of interval analysis*, volume 2. Society for Industrial and Applied Mathematics, 1979.

[47] K. Nagatou, M. Plum, and P. J. McKenna. Orbital stability investigations for travelling waves in a nonlinearly supported beam. *Journal of Differential Equations*, 268:80–114, 2019.

[48] M. T. Nakao. A numerical approach to the proof of existence of solutions for elliptic problems. *Japan Journal of Applied Mathematics*, 5(2):313–332, 1988.

[49] M. T. Nakao, M. Plum, and Y. Watanabe. *Numerical Verification Methods and Computer-Assisted Proofs for Partial Differential Equations*, volume 53 of *Springer Series in Computational Mathematics*. Springer Singapore, 2019.

[50] S. Oishi. Numerical verification of existence and inclusion of solutions for nonlinear operator equations. *Journal of Computational and Applied Mathematics*, 60(1-2):171–185, 1995.

[51] F. Pacella, M. Plum, and D. Rütters. A computer-assisted existence proof for Emden's equation on an unbounded L-shaped domain. *Communications in Contemporary Mathematics*, 19(02):1750005, 2017.

[52] L. Peletier and W. Troy. Multibump periodic travelling waves in suspension bridges. *Proceedings of the Royal Society of Edinburgh: Section A Mathematics*, 128(3):631–659, 1998.

[53] M. Plum. Explicit H2-estimates and pointwise bounds for solutions of second-order elliptic boundary value problems. *Journal of Mathematical Analysis and Applications*, 165(1):36–61, 1992.

[54] M. Plum. Existence and enclosure results for continua of solutions of parameter-dependent nonlinear boundary value problems. *J. Comput. Appl. Math.*, 60(1-2):187–200, 1995.

[55] A. D. Poularikas, editor. *Transforms and applications handbook*. The Electrical Engineering Handbook Series. CRC Press, Boca Raton, FL, third edition, 2010.

[56] C. Reinhardt and J. D. Mireles-James. Fourier-Taylor parameterization of unstable manifolds for parabolic partial differential equations: Formalism, implementation and rigorous validation. *Indagationes Mathematicae*, 30(1):39–80, 2019.

[57] S. Rump. INTLAB - INTerval LABoratory. In T. Csendes, editor, *Developments in Reliable Computing*, pages 77–104. Kluwer Academic Publishers, Dordrecht, 1999. `http://www.tuhh.de/ti3/rump/`.

[58] D. P. Sanders and L. Benet. Intervalarithmetic.jl, 2014. Available at `https://github.com/JuliaIntervals/IntervalArithmetic.jl`.

[59] S. Santra. On the Lazer-McKenna conjecture and its applications. *Proceedings of the American Mathematical Society*, 143(10):4361–4372, 2015.

[60] S. Santra and J. Wei. Homoclinic solutions for fourth order traveling wave equations. *SIAM Journal on Mathematical Analysis*, 41(5):2038–2056, 2009.

[61] D. Smets and J. B. van den Berg. Homoclinic solutions for Swift-Hohenberg and suspension bridge type equations. *Journal of Differential Equations*, 184:78–96, 2002.

[62] A. Takayasu, X. Liu, and S. Oishi. Verified computations to semilinear elliptic boundary value problems on arbitrary polygonal domains. *Nonlinear Theory and Its Applications, IEICE*, 4(1):34–61, 2013.

[63] W. Tucker. A Rigorous ODE Solver and Smale's 14th Problem. *Found. Comput. Math.*, 2:53–117, 2002.

[64] W. Tucker. *Validated Numerics: A Short Introduction to Rigorous Computations*. Princeton University Press, 2011.

[65] J. B. van den Berg and M. Breden. A simple rigorous integrator for semilinear parabolic PDEs, 2026.

[66] J. B. van den Berg, M. Breden, J.-P. Lessard, and J. D. Mireles-James. Computer-assisted proofs in nonlinear dynamics: a spectral approach based on fourier analysis, 2024. In preparation.

[67] J. B. van den Berg, M. Breden, J.-P. Lessard, and M. Murray. Continuation of homoclinic orbits in the suspension bridge equation: a computer-assisted proof. *Journal of Differential Equations*, 264(5):3086–3130, 2010.

[68] J. B. van den Berg, M. Breden, J.-P. Lessard, and L. van Veen. Spontaneous Periodic Orbits in the Navier–Stokes Flow. *Journal of nonlinear science*, 31(2):1–64, apr 2021.

[69] J. B. van den Berg, M. Breden, and R. Sheombarsing. Validated integration of semilinear parabolic PDEs, 2023. Preprint arXiv:2305.08221v1.

[70] J. B. van den Berg, J.-P. Lessard, and E. Queirolo. Rigorous verification of Hopf bifurcations via desingularization and continuation. *SIAM Journal on Applied Dynamical Systems*, 20(2):573–607, 2021.

[71] J. B. van den Berg, J. D. Mireles-James, J.-P. Lessard, and K. Mischaikow. Rigorous numerics for symmetric connecting orbits: even homoclinics of the Gray-Scott equation. *SIAM Journal on Mathematical Analysis*, 43(4):1557–1594, 2011.

[72] J. B. van den Berg and E. Queirolo. Rigorous validation of a Hopf bifurcation in the Kuramoto–Sivashinsky PDE. *Communications in Nonlinear Science and Numerical Simulation*, 108:1–22, 2022.

[73] J. B. van den Berg and L. van der Aalst. MATLAB code for existence proof of traveling wave in Navier-Stokes equations. 2025. `https://github.com/ljwvda/WaveProof_nu0207`.

[74] J. B. van den Berg and L. van der Aalst. MATLAB code for Hopf bifurcation proof in Navier-Stokes equations. 2026. `https://github.com/ljwvda/HopfBifurcationProof`.

[75] J. B. van den Berg and J. F. Williams. Rigorously computing symmetric stationary states of the Ohta-Kawasaki problem in three dimensions. *SIAM Journal on Mathematical Analysis*, 51(1):131–158, 2019.

[76] L. van der Aalst and M. Cadiot. SBInfiniteStrip.jl. 2025. `https://github.com/ljwvda/SBInfiniteStrip`.

[77] L. van der Aalst and M. Cadiot. Existence and orbital stability proofs of traveling wave solutions on an infinite strip for the suspension bridge equation. *Physica D: Nonlinear Phenomena*, 493, 2026.

[78] L. van der Aalst, J. B. van den Berg, and J.-P. Lessard. MATLAB code corresponding to the paper "Periodic localized traveling waves in the two-dimensional suspension bridge equation". 2024. `https://github.com/ljwvda/SuspensionBridge2D.git`.

[79] L. van der Aalst, J. B. van den Berg, and J.-P. Lessard. Periodic localized traveling waves in the two-dimensional suspension bridge equation. *Nonlinearity*, 38(7), 2025.

[80] G. S. Vincent. Golden gate bridge vibration studies. *Journal of the Structural Division*, 84(6):1817–1–1817–40, 1958.

[81] Y. Wang, M. Bennani, J. Martens, S. Racanière, S. Blackwell, et al. Discovery of Unstable Singularities. *arXiv preprint arXiv:2509.14185*, 2025.

[82] Y. Watanabe and S. Cai. A computer-assisted proof for solutions of Elkouh's equation related to Navier-Stokes equations. *Fixed Point Theory and Algorithms for Sciences and Engineering*, 7, 2025.

[83] Y. Watanabe, M. Plum, and M. T. Nakao. A computer-assisted instability proof for the Orr-Sommerfeld problem with Poiseuille flow. *ZAMM - Journal of Applied Mathematics and Mechanics*, 89(1):5–18, 2009.

[84] Y. Watanabe, N. Yamamoto, and M. T. Nakao. A numerical verification method of solutions for the Navier-Stokes equations. *Reliable Computing*, 5:347–357, 1999.

[85] D. Wilczak and P. Zgliczyński. A geometric method for infinite-dimensional chaos: Symbolic dynamics for the Kuramoto-Sivashinsky PDE on the line. *Journal of Differential Equations*, 269:8509–8548, 2020.

[86] J. M. Wunderlich. *Computer-assisted Existence Proofs for Navier-Stokes Equations on an Unbounded Strip with Obstacle*. PhD thesis, Karlsruher Institut für Technologie (KIT), 2022.

[87] N. Yamamoto. A numerical verification method for solutions of boundary value problems with local uniqueness by banach's fixed-point theorem. *SIAM Journal on Numerical Analysis*, 35(5):2004–2013, 1998.

[88] P. Zgliczyński. Attracting Fixed Points for the Kuramoto-Sivashinsky Equation: A Computer Assisted Proof. *SIAM Journal on Applied Dynamical Systems [electronic only]*, 1, 01 2002.

[89] P. Zgliczyński. Rigorous Numerics for Dissipative Partial Differential Equations II. Periodic Orbit for the Kuramoto–Sivashinsky PDE—A Computer-Assisted Proof. *Foundations of Computational Mathematics*, 4(2):157–185, 2004.

[90] P. Zgliczyński. Covering relations, cone conditions and the stable manifold theorem. *J. Differential Equations*, 246:1774–1819, 2009.